The $^{12}C+^{12}C$ fusion cross-section at sub-coulomb barrier energies

Jose Gustavo Vega Romero

Doctor of Philosophy

University of York
Department of Physics
September, 2022.

Abstract

The study of the fusion reaction process of the carbon 12 isotope is not only relevant to get a better understanding of the nucleosynthesis process but also given that it is through this process in which stars obtain their main source of energy.

Measuring the fusion cross-sections of production reactions that form chemical elements is at the centre of interest regarding some astrophysical scenarios. The processes of nucleosynthesis give birth to heavier elements and, in the carbon scenario, can develop into supernovae type IA explosions or superbursts from accreting neutron stars. In particular, given the significance of carbon to life in general, the reaction $^{12}C+^{12}C$ is vitally important to understand and has therefore long been studied. However, previous theoretical and experimental efforts show considerable discrepancies as the energy approaches that of the Coulomb barrier, resulting in differing values obtained for the astrophysical S-factor. Particularly at low energies, these discrepancies lead to vastly differing hypotheses to describe this phenomenon.

In this work, a direct measurement of the $^{12}C+^{12}C$ fusion reaction cross-section is performed via coincidences from the evaporated charged particles and the gamma particles produced from the de-excitation of the daughter nucleus, using the STELLA (STELar LAboratory) at IPN (Institut de Physique Nucléaire), Orsay, France.

Contents

List of Figures

List of Tables

List of abbreviations

STELLA	STELlar LAboratory
IPN	Institut de Physique Nucléaire d’Orsay
PMT	Photomultiplier Tube
DSSD	Double Sided Silicon Strip Detector
S3B	S3 Backward Detector
S3F	S3 Forward Detector
FATIMA	FAst TIming Array
DAQ	Digital AcQuisition
CM	Centre of Mass

Acknowledgements

In the first place, I would like to thank and dedicate this work to my mother, father, and sister. Without their love, support, and encouragement I wouldn't be anywhere close to where I am now. Also, thanks to my family that made me feel home was not very far although I was more than 8000 km away from you. ¡Gracias!

I would also like to thank my supervisor Prof. David Jenkins and the people from the collaboration of STELLA who made this project possible. A special mention to Dr. Christian Diget and Prof. Alison Laird for their help and support.

Thanks to all my friends who made my time in York one of the best episodes of my life and with whom I spent not only the most incredible times but also helped me get through hard times. Thanks to the old friends Álvaro, Ale, Erick, Eduardo, with whom I was able to keep the friendship; and to the new ones Ruth, Pierre, Sonia, Javier, and the Mexican/Latin gang whom I was incredibly lucky to meet. Thanks to my band, Reina de Cumbias, for giving me the strength to continue on this journey and discover something I also love to do. I'm probably not mentioning everyone here cause I'll probably need another thesis to express my gratitude to all the people who were significant in this journey. Cheers to all of you!

Last but not least, a special mention to Ervin Ferreira who encouraged and guided me to continue not only this but all the enterprises I'm involved in and helped me get through the toughest times.

Seguimos ...

This project was supported by the National Council of Science and Technology of Mexico CONACyT

CONACYT
Consejo Nacional de Ciencia y Tecnología

Author’s declaration

I declare that this thesis is a presentation of original work and that I am the sole author. This work has not previously been presented for an award at this university or at any other. All sources are acknowledged as references.

Chapter 1

Introduction

The need for understanding our surroundings and harnessing that knowledge to our advantage has prevailed since the emergence of intelligent life. In particular, this quest has given birth to astronomy and its determination to understand the vast outer space with its constituent entities. On the other hand, a need arose to comprehend the universe on a significantly smaller scale, leading to the development of quantum mechanics as the discipline tasked with exploring this realm. Nuclear astrophysics lies at the intersection of these two essential areas of physics, where one of the paramount objectives is furthering our understanding. Nuclear synthesis process is the production of chemical elements via nuclear reactions, which take place in stellar sites. This can occur in quiescent burning cycles or in violent explosive scenarios. Depending on the particular circumstances and initial conditions, these processes can span from mere seconds to billions of years. The present study aims to improve our understanding of the nucleosynthesis process, with a specific focus on elucidating the behaviour of the ^{12}C isotope relevant to astrophysics scenarios.

Nuclear reactions happening at the core of stars define their posterior life [20] and the initial temperature and mass govern their evolution. For example, it can result in a massive explosion such as a Supernova or lightly fade out, ending up as a White Dwarf [26, 101]. One key reaction is the ^{12}C+^{12}C fusion reaction, given not only its importance to the study of the reaction itself, but it is also a turning point in the fuel-burning phase of stars affecting their life and death [28]. Some of the scenarios more relevant to carbon burning[1] include the ones that occur when the initial mass of the star is above the Chandrasekhar limit (1.44 $M_\odot$), and which can lead to an explosive scenario of a Supernova type II (for stars with mass between 8-10 $M_\odot$) [8, 6, 7, 79, 41, 18]; or for binary systems involving a White

[1] Burning refers to the fusion process of a particular chemical element. In this work, Carbon burning is of particular interest.

Dwarf and a main sequence star[2], in which it ends up in a Supernova type Ia [80, 91, 84]; or another binary system involving a Neutron star with a main sequence star and can lead to an X-Ray burst type I [29]. A more detailed description of where the C burning is most relevant in astrophysical scenarios will be given in the next chapter. In light of these considerations, there have been numerous experimental and theoretical efforts to determine the carbon fusion cross-section. However, discrepancies arise in the determination of the cross-section and, consequently, the astrophysical S-factor, which prevents us from achieving an accurate description of the carbon-burning process.

Nuclear astrophysics presents a range of significant experimental challenges, arising from several factors. Firstly, nuclear reactions involving stable nuclei under thermal equilibrium conditions occur at energies below the Coulomb barrier. Furthermore, nuclei with short half-lives add complexity to the experimental scenarios. The presence of overwhelming impurities in target probes also contributes to dominating background signals within the detection systems. Practical limitations, such as vanishing reaction probabilities and long data acquisition periods, must be considered for the difficulties faced.

Hence, it becomes essential to undertake rigorous and meticulous experimental efforts to procure reliable data regarding the properties of nuclear astrophysics reactions. Specifically, the fusion reaction involving ^{12}C occurs below the Coulomb barrier. Consequently, the measurement of its cross-section encounters particular intricacies. While advancements in instrumentation and data processing, including background reduction, have been made, discrepancies persist among different efforts to quantify the cross-section [1]. These persistent discrepancies emphasize the continued need to acquire data that is both reliable and accurate. Doing so is vital not only for comprehending the intricacies of carbon fusion itself but also for advancing our understanding of the overall nucleosynthesis process.

In this work, the fusion reaction ^{12}C+^{12}C was studied by measuring in coincidence the resulting gamma-rays with the evaporated light-charged particles from the compound nucleus, and the emitted gamma-rays from the de-excitation of the daughter nuclei, using the STELLA (STELla LAboratory) experimental station at the Andromede facility at the Institut de Physique Nucleaire (IPN), Orsay, France [47] in an international collaboration. The facility consists of a 4 MV Pelletron accelerator which can provide a carbon 12 beam of up to 10μA in a 2+ and 3+ charge state, within an energy range of E_{lab} =7.9 to 4.38 MeV and intensities ranging from 30 pnA to 2pμA (current as if all ions in the beam were single charged). This range of energy was specifically selected given that, as it will be shown in the next section, the Coulomb barrier for the $^{12}C + ^{12}C$ system is $E_C \approx 6.3$MeV. This energy is considerably higher than the Gamow peak energy (energy at which it is most probable a certain reaction to happen). Hence, it was of utter importance to go below the Coulomb barrier energy and within a reasonable range of the Gamow Peak Energy.

[2]A Main Sequence star refers to the one that it is in its He burning cycle.

The carbon beam then would interact with carbon target foils with thicknesses varying from 20 to 70 $\mu g/cm^2$, which were placed in a rotating target mechanism that can achieve up to 1000 rpm in order to dissipate heat from the beam spot. This array was placed inside an ultra-high vacuum chamber that can achieve pressures of 10^{-8} mbar in an ultra-low outgassing environment, in order to avoid carbon buildup at the beam spot position.

For the detection system, charged particles were detected using 2 annular DSSD (Double Sided Strip Silicon Detectors) located at the forward and backward position with respect of the target, where each DSSSD consists of 24 strips [36]. Along with the DSSDs, gamma particles were detected using an array of 36 lanthanum bromide ($LaBr_3$ (Ce)) scintillating detectors, which are part of the UK FATIMA (FAst TIMing Array) collaboration [87]. Additionally, the fact that the detectors can work on the nanosecond regime allows the possibility to reduce background mainly from the self-activity of the gamma particle detectors and allow time for coincidences between the charged and gamma particles. In conclusion, the setup is designed for performing stable and most accurate fusion cross-section measurements at high beam intensity over periods of weeks with efficient background reduction from nanosecond gating on coincident charged particles and gammas.

Chapter 2 will talk about the background theory regarding the $^{12}C+^{12}C$ reaction, including the quantum mechanics concepts used not only as background but as tools that will help the analysis made for determining the cross-section of this reaction.

Chapter 3, a brief compilation of some of the previous efforts to measure this fusion reaction will be shown.

Chapter 4 will show the experimental setup at IPN that was used for this experiment.

Chapter 5 will show the results obtained from the experimental campaign such as energy spectra, angular distribution and differential cross-section plots, as well as the tools used for making the data analysis.

Finally, conclusions about this work will be shown in chapter 6.

Chapter 2

Nuclear Astrophysics

2.1 Nucleosynthesis

One of the objectives of nuclear astrophysics is to use the tools provided by nuclear physics from the quantum realm and by astronomy to explain elemental questions regarding our surroundings in a macro scale.

Models about the origin and evolution of astronomical objects developed a key milestone with the discovery of the role thermonuclear reactions had, not only on stellar energy production but in their life cycle itself. This discovery served as a starting point on the way stellar evolution is understood and processes, like nucleosynthesis, are described.

It is understood that the life cycle of stars starts as a cluster of interstellar dust begins to contract through the gravitational force, this contraction reaches a point in which the matter contained starts a process of nuclear reactions to balance out the gravitational collapse, then depending on the mass of the star, it will determine the star's death and some of this matter if not all will return to the interstellar space to give birth to the cycle of a new star [51].

The nucleosynthesis process, proposed by Burbidge, Burbidge, Fowler [21], and Cameron [22], introduces the idea that a cyclic process of nuclear reactions between different particles, right in the centre of stars, gives birth to the chemical elements commencing with the simplest atoms of Hydrogen and Helium. Once the primary isotopes or fuel, H and He combine at the core of Main Sequence stars, heavier elements such as Carbon and Oxygen are produced to recombine once again obtaining heavier atoms such as Na, Mg, Al, and even going to heavier elements like Fe, Ni, and Co. However, this chain of nuclear reactions can only provide a limited amount of energy and it will come to an end when the "fuel" finishes or nuclear reactions cannot occur anymore, as described by fig. 2.1.

Once the star's core is fundamentally formed of iron group elements, hence the binding energy per nucleon reaches the limit, it follows a gravitational collapse of the core, and a Supernova explosion takes place. This type of Supernova explosion is known as Type II Supernova Explosion [11, 52, 35]. A more detailed discussion will be done further in this chapter.

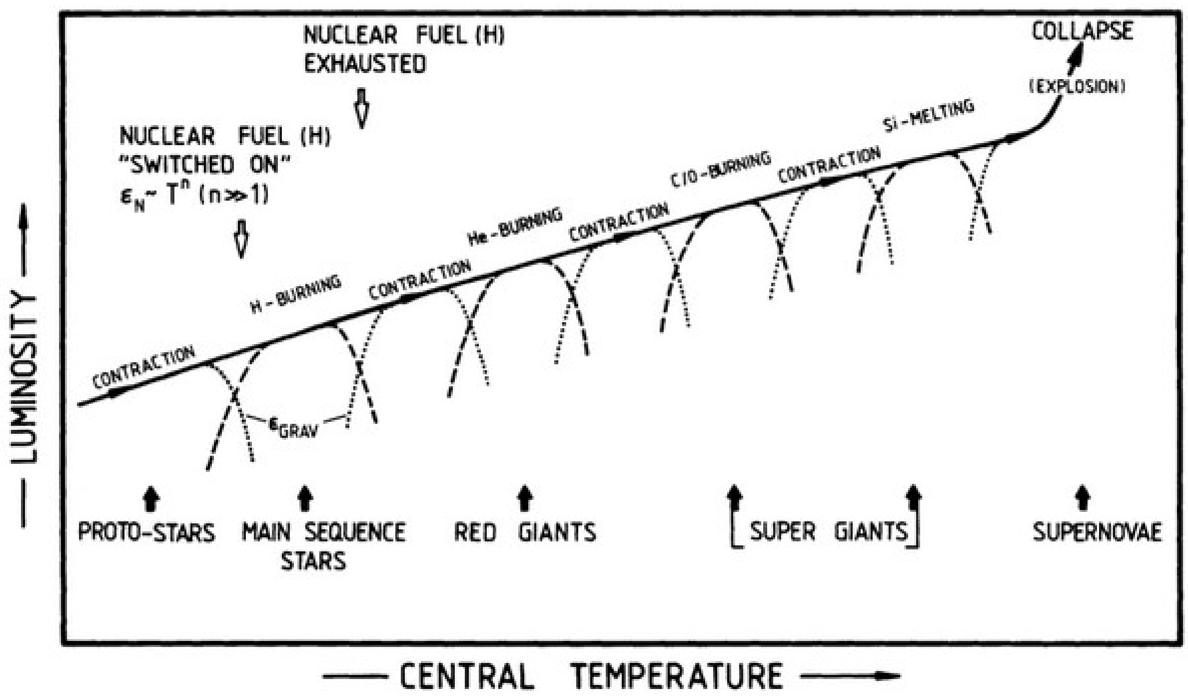

Figure 2.1: H-R diagram of a massive star , $M \geq 8M_{\odot}$, showing the nucleosynthesis process throughout its life. The process begins when a proto-star, or cumulus of interstellar matter, starts to form ending in a Supernova explosion as a result of its core collapse. Diagram taken from [94]

The first stages of fuel burning of a star start with the thermonuclear reactions of Hydrogen and Helium that will produce heavier elements and more tightly bound elements such as Carbon. Moreover, these nuclear reactions will prevent the gravitational collapse of the star, and depending on the initial conditions of the star, it will determine the star's fate. In particular, there are several conditions required to start the Carbon burning phase as not all stars reach this point given the huge dependence on the initial mass of the star, e. g. if the star has an initial mass below the Chandrasekhar mass limit ($1.4M_{\odot}$) it will likely end up as a White Dwarf, hence not reaching the carbon burning phase. Other conditions include temperatures of $\sim 10^8$ K and densities of $\sim 10^5 g/cm^3$ at the core of the star [21]. The Chandrasekhar mass limit was proposed by Landau, Chandrasekhar, et. al., for the stellar evolution framework, regarding the mass of the star of interest, when relativistic and non-relativistic scenarios are taken into account [65, 23, 24]. The Chandrasekhar limit results from the relation between mass, pressure, and density where hydrostatic equilibrium is achieved. This limit is $M_c \leq 1.4 M_{\odot}$ [25, 27]. As a consequence, it was found that no stars above this limit can survive without a gravitational collapse if there are no other ways of fighting this process other than the electron degeneracy pressure. This was discovered by Chandrasekhar and Landau and it was particularly established for White Dwarfs. Further on, it will be seen that the Chandrasekhar limit is helpful not only for White Dwarfs but it will be used for the theory of stellar evolution.

During the Hydrogen burning phase, the stage known as the CNO cycle begins. This is when carbon reactions become relevant and can also give place to other reactions involving heavier isotopes such as Silicon, and if the mass is massive enough, it could die with a Supernova explosion.

Red Giant Stars are considered to be the ones that produce most of the intergalactic ^{12}C and ^{16}O.

^{12}C	+	^{12}C	$\rightarrow$	^{20}Ne	+	α	Q=4.62 MeV
^{12}C	+	^{12}C	$\rightarrow$	^{23}Na	+	p	Q=2.24 MeV
^{12}C	+	^{12}C	$\rightarrow$	^{23}Mg	+	n	Q=-2.62 MeV

Table 2.1: Carbon fusion exit channels.

Table 2.1 shows the exit channels with their respective Q value of the fusion of 2 ^{12}C nuclei. This group of 3 reactions is known to be the “Carbon burning” [94].
The Q value provides information about whether the fusion reaction will produce energy when it happens or requires energy to take place, as this Q value is defined by the difference in nuclear masses by equation 2.1.

$$Q = (m_1 + m_2 - m_3 - m_4)c^2 \tag{2.1}$$

where m_1, m_2, m_3, m_4 are the nuclear masses of the projectile (1), target (2), and reaction products (3,4). Nuclear masses can be obtained from mass tables [108, 81].

Moreover, when the carbon burning stage takes place, the first 2 ^{12}C nuclei fuse to form an excited ^{24}Mg compound nucleus (Q=13.93 MeV), followed by its decay into excited states of ^{20}Ne, ^{23}Na, and ^{23}Mg; and it’s precisely the associated particles, α’s for Neon and protons for sodium in addition to their characteristic gamma’s as a result of their de-excitation, that are measured in the laboratory to determine the properties of the fusion reaction. The exit channels with positive Q-value are the ones of interest for measuring the fusion cross-section.

Nonetheless, other secondary reactions such as ^{23}Na(p,α)^{20}Ne or involving heavier ions as ^{12}C+^{16}O and ^{12}C+^{20}Ne can take place during this phase. Aluminum and silicon can also be produced in smaller amounts [7]; these reactions happen thanks to the ashes of a previous burning phase and to newly formed nuclei, respectively.

As previously stated, this carbon burning happens if, due to the gravitational attraction, the core of the star reaches sufficiently high temperature and density to begin the thermonuclear reactions regarding the oxygen and carbon ashes from the previous burning stages [86, 35]. Helium burning leaves as fuel for the carbon burning phase mainly ^{12}C and ^{16}O, and it is crucial for the carbon burning to happen that the mass of the star is above the Chandrasekhar limit ($M = 1.4M_{\odot}$). Otherwise, the star's temperature will not be high enough to begin and maintain the nuclear reactions processes ($\approx 20 \times 10^6 K$ [94]) and further stages like the oxygen burning or the s and r neutron capture processes will not occur. Consequently, no heavier elements will be synthesised, so that any star with initial mass below the Chandrasekhar limit, after the helium burning phase, will not undergo any further evolution. Furthermore, there would be a competition between the gravitational collapse and electron degeneracy pressure to stabilise the star. The type of stars that exhaust the nuclear fuel after helium burning are known as White Dwarfs.

However, stars with an initial mass greater than $10M_{\odot}$ finish with a mass greater than the Chandrasekhar mass limit allowing further burning stages, where even the silicon burning stage can be reached. This last stage of nucleosynthesis has as its main products iron and nickel. At this point of the evolution, the core is mainly formed by the elements previously mentioned.

If the mass of the star exceeds the Chandrasekhar mass limit, the electron degeneracy pressure will not suffice to overcome the gravitational contraction, starting the contraction of the core, and raising its temperature. The core contraction is also enhanced by the fact that the binding energy per nucleon reaches a maximum for elements with atomic mass ~ 58, such as iron (^{58}Fe) and nickel (^{52}Ni), hence the fusion energy for elements above this maximum produces no significant energy to help prevent the core contraction. Moreover, neutrino emission by neutron capture helps the core contraction process as significant amounts of energy are lost through the reaction $^{A}_{Z+1}X + e^- \rightarrow ^{A}_{Z} Y + \nu$.
Not only does photo-disintegration of iron and other elements into neutrons and alpha particles take place by the electromagnetic radiation emitted thanks to the high temperatures, but also α's can be disintegrated causing a drastic decrease of the temperature of the star and provoking a catastrophic collapse. The rise in density favours the combination of free electrons with protons ($e^- + p \rightarrow n + \nu$) leaving an enormous amount of neutrons. Since the elements conforming to the star cannot be compressed indefinitely, the mechanism to overcome this great pressure is to generate a decompressing wave or explosion that will release this pressure and expel the components of exterior layers of the

star, leaving in its core a *neutron star* or a *black hole*, depending on the initial mass of the star. This type of explosion in which the carbon burning phase is also crucial, is known as *Supernova type II*.

Not only on individual stars where nucleosynthesis takes place, binary systems allow this process as well although the way they can obtain the necessary fuel to start the ignition process might be different from the one of an individual star. Binary systems are rather common around the galaxy and consist on a pair of stars revolving at a common centre of gravity[94].
Regarding carbon fusion, a relevant scenario involving the binary systems is when one of the stars is a White Dwarf that accretes material from the other star, which can be a main sequence star, another White Dwarf, or a Red Giant. If the White Dwarf's mass, formed mainly from carbon, and the mass acquired from the second star is enough to surpass the Chandrasekhar mass limit, carbon burning can be reignited. In this scenario, if the carbon burning starts before the electron degeneracy stops due to high mass transfer rates, the energy generated would be enough to produce an explosion that will destroy the binary system. This type of explosion is known as *Supernovas type Ia*.

2.2 Quantum Mechanics of the Reaction

2.2.1 Reaction Rate and Cross-section

One key aspect to understanding the process of nucleosynthesis is the stellar reaction rate which can be written as:

$$r = N_x N_y \langle \sigma(v) v \rangle (1 + \delta_{XY})^{-1} \tag{2.2}$$

where N_x are the number of X particles (nucleus), N_y are the number of Y particles (nucleus), v is the relative velocity between X and Y particles, $\sigma(v)$ is the cross section for a single target nucleus, and δ_{XY} is the Kronecker delta.

Equation 2.2 comes from taking into account several considerations. First, the interaction between N_X and N_Y particles in a stellar gas occurs when one of the types of particles is arbitrarily chosen at rest (for instance, the X particles), hence the Y type of particles approaches at the X particles with a velocity v.
Followed by the multiplication of the number of particles, $N_X N_Y$ times $v\sigma(v)$ comes from the fact that, on one side the effective interaction area that the particle moving towards the targets is the number of targets times the cross-section of a single target, $N_Y \sigma(v)$. On the other hand, the reaction rate also depends on the flux of incoming particles towards the target given by $N_X v$.

The factor involving the Kronecker delta is introduced because it is important to consider if the particles are of the same type or not. Otherwise, for identical particles, the reaction rate would be twice as the actual rate.

Finally, it has to be considered that quantum mechanic effects take place in the interaction. Hence, the cross-section, instead of be considered classically as the effective area of interaction given by the geometry of a particular system, $\sigma = \pi R^2$, it has to be written in terms of the de Broglie wave function λ as

$$\sigma = \pi \left(\frac{m_{projectile} m_{target}}{m_{target}} \frac{\hbar}{(2 m_{projectile} E_{lab})^{1/2}} \right)^2$$

It is important to mention that since the cross-section now includes the energy of the incoming particle, E_{lab}, it will be a function that depends directly on the relative velocity between target and nucleus, i.e., $\sigma \to \sigma(v)$.

Alongside the dependency on the velocity of the cross-section, in a stellar gas, the particles' velocities vary over a range of values and have a probability of having a particular velocity between v and $v+dv$ given by the probability function $\phi(v)$. This probability function is then evaluated through all the possible values and normalised, giving as a result

$$\int_0^\infty \phi(v) dv = 1 \tag{2.3}$$

transforming the product $\sigma(v)v$ into the reaction rate per particle pair averaged over the velocity distribution as equation 2.4:

$$\langle \sigma v \rangle = \int_0^\infty \phi(v) v \sigma(v) dv \tag{2.4}$$

Once the reaction rate per particle pair is obtained, the next key aspect is the velocity distribution function given by

$$\phi(v) = 4\pi v^2 \left(\frac{m}{2\pi kT} \right)^{3/2} \exp\left(-\frac{mv^2}{2kT} \right) \tag{2.5}$$

where k is the Boltzmann constant, m is the mass of the nucleus of interest, and T the temperature of the stellar gas.

Equation 2.5 is known to be the Maxwell-Boltzmann velocity distribution function for a non-degenerate gas and with non-relativistic velocities. Moreover, considering two interacting nuclei with a relative velocity between them v and V as the centre of mass velocity, the velocity distribution functions for v and V can be written as

$$\phi(v) = 4\pi v^2 \left(\frac{\mu}{2\pi kT}\right)^{3/2} \exp\left(-\frac{\mu v^2}{2kT}\right) \tag{2.6}$$

where $\mu = \frac{m_x m_y}{m_x + m_y}$ is the reduced mass of the x and y nuclei.

$$\phi(V) = 4\pi V^2 \left(\frac{M}{2\pi kT}\right)^{3/2} \exp\left(-\frac{MV^2}{2kT}\right) \tag{2.7}$$

where $M = m_x + m_y$ is the total mass of the system.

If the velocity distribution functions are taken into account for the interacting nuclei in stellar gas of the characteristics mentioned above, the reaction rate can be rewritten as

$$\langle \sigma v \rangle = \int_0^\infty \int_0^\infty \phi(V)\phi(v)\sigma(v) v dV dv \tag{2.8}$$

and considering the normalisation over V given by equation 2.3, it is possible to get the reaction rate in terms of v

$$\langle \sigma v \rangle = \int_0^\infty \phi(v)\sigma(v) v dv \tag{2.9}$$

Coupling equations 2.6 and 2.7 with equation 2.9, in addition to the fact that the exponential term in the velocity distribution function $\phi(v)$ can be seen as the kinetic energy in the centre of mass system $E = \frac{1}{2}mv^2$, it is finally obtained the reaction rate $\langle \sigma v \rangle$ as

$$\langle \sigma v \rangle = \left(\frac{8}{\pi\mu}\right)^{1/2} \frac{1}{(kT)^{3/2}} \int_0^\infty \sigma(E) E \exp\left(-\frac{E}{kT}\right) dE \tag{2.10}$$

2.2.2 Coulomb Barrier and Tunnel Effect

The next fundamental subject matter is the Coulomb barrier and its relation to the tunnel effect as this is key for the fusion process to occur. The Coulomb potential has the form

$$V_C(r) = \frac{Z_1 Z_2 e^2}{r} \tag{2.11}$$

where Z_1 and Z_2 are the charge of the nuclei involved, e the electron charge, and r the distance between them.

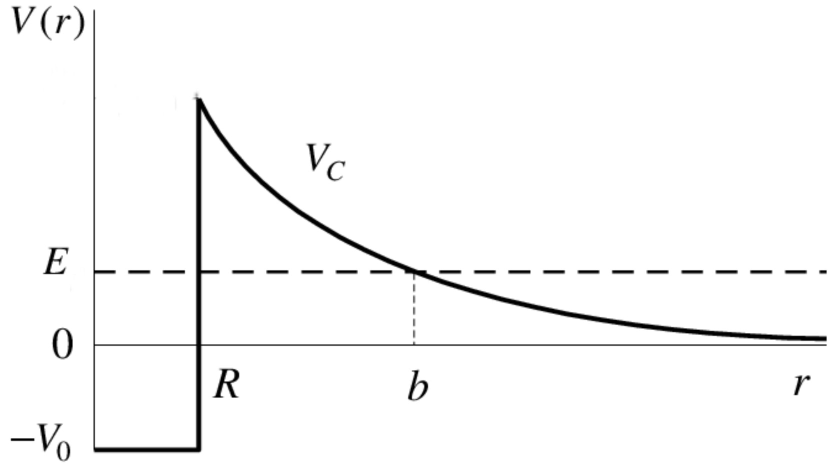

Figure 2.2: Coulomb barrier and nuclear potential combined

Since the nuclei are positively charged, the closer the nuclei are to each other, the bigger the repulsive force would be.

Figure 2.2 shows the nuclear and Coulomb potentials combined where $-V_0$ is the potential of the nuclear well, V_C is the Coulomb potential, R is the nuclear radius, and b is the classical returning point for an incoming particle with energy E.

Classically, a particle cannot penetrate the Coulomb barrier, eq. 2.11, unless it has enough energy to overcome the barrier, $E > E_{Coulomb}$, as shown in figure 2.2. However, Gamow, Condon, and Gurney [42, 40] demonstrated that indeed it exists a probability different from zero that quantum mechanically a particle penetrates the Coulomb barrier.

The probability of finding a particle at a specific position R_n, nuclear radius, is given by the square of its wave function $|\psi(R_n)|^2$. In the same way, to find the particle's probability at the turning point of the Coulomb potential $|\psi(R_C)|^2$. By obtaining the ratio between these two probabilities, equation 2.12, the result is the probability of finding the incoming particle in a position below the Coulomb potential and this is what is known as *Tunnel Effect*.

$$P = \frac{|\psi(R_n)|^2}{|\psi(R_C)|^2} \tag{2.12}$$

Furthermore, when the Coulomb potential is taken into account and Schrodinger's equation is solved, the probability given by eq. 2.12 becomes:

$$P = \exp\left\{-2KR_C\left[\frac{\arctan(R_C/R_n - 1)^{1/2}}{(R_C/R_n - 1)^{1/2}} - \frac{R_n}{R_C}\right]\right\} \tag{2.13}$$

where $K = \left[\frac{2\mu}{\hbar^2}(E_C - E)\right]^{1/2}$.

For energies $E << E_C$, the probability can be simplified to:

$$P = \exp(-2\pi\eta) \tag{2.14}$$

where η is known as the Sommerfeld parameter, $\eta = \frac{Z_1 Z_2 e^2}{\hbar v}$, and this tunneling probability for energies below the Coulomb barrier is known as the Gamow factor.

In terms of the centre of mass energy,

$$2\pi\eta = \frac{\pi Z_1 Z_2 e^2}{\hbar}\left(\frac{2\mu}{E}\right) \tag{2.15}$$

2.2.3 Astrophysical S-Factor and Gamow's Window

The fact that the probability of a particle to penetrate the Coulomb barrier decays exponentially as seen by equation 2.15, makes the cross-section follow this trend, mathematically written

$$\sigma(E) \propto \exp(-2\pi\eta)$$

Additionally, if it is taken into account the de Broglie wavelength equation

$$\lambda = \left(\frac{1}{\mu}\right)^{1/2} \frac{\hbar}{(2E)^{1/2}}$$

then,

$$\sigma(E) \propto \pi\lambda^2 \propto \frac{1}{E}$$

It follows that the cross-section can be expressed as

$$\sigma(E) = \frac{1}{E}\exp(-2\pi\eta)S(E) \tag{2.16}$$

where S(E), known as the *nuclear* or *astrophysical S-factor* is defined by this equation and takes into account only the nuclear effects of the reaction.

Moreover, if the expression for the cross-section, given by equation 2.16, is inserted in the equation for the reaction rate per particle 2.4:

$$\langle \sigma v \rangle = \left(\frac{8}{\pi \mu} \right)^{1/2} \frac{1}{(kT)^{3/2}} \int_0^\infty S(E) \exp\left(-\frac{E}{kT} - \frac{b}{E^{1/2}} \right) dE \tag{2.17}$$

where

$$b = 2\pi\eta E^{1/2} = \frac{\pi Z_1 Z_2 e^2}{\hbar} (1\mu)^{1/2}$$

The quantity b^2 is also known as the Gamow energy E_G.

From equation 2.17, it is possible to observe that the behaviour of the function is mainly determined by the exponential term as $S(E)$ presents a smooth trend for non-resonant reactions and the other terms are constant.
Furthermore, the multiplication of the Maxwell-Boltzmann distribution, $\exp(-E/kT)$, and the probability of penetrating the Coulomb barrier, $\exp(-b/E^{1/2}) = \exp\left[-(E_G/E)^{1/2} \right]$ result in a peak which represents the energy at which nuclear reactions are most probable to occur, represented in figure 2.3. This peak is known as the *Gamow peak*.

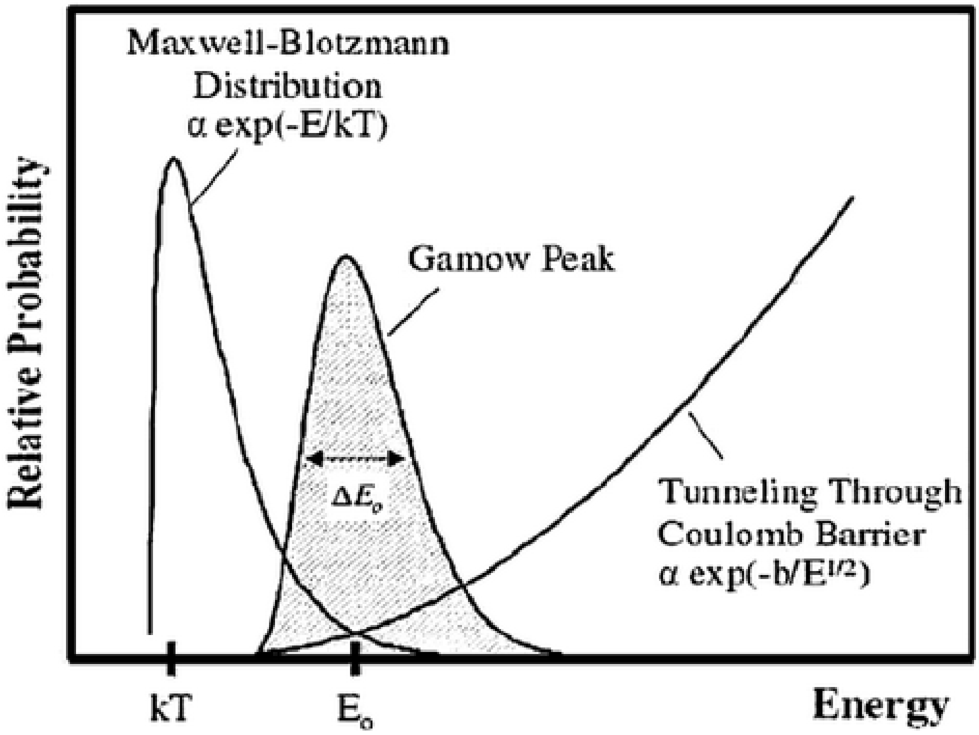

Figure 2.3: The Gamow peak where at E_0 the probability of the fusion to happen is maximum. Plot taken from [103]

A key feature of figure 2.3 is that the Gamow peak is located at an energy above the energy at which the Maxwell-Boltzmann is maximum, $E = kT$. Hence, thanks to the tunnel effect it is possible that nuclear reactions take place below the Coulomb barrier and consequently, a star has energy enough to go through the nucleosynthesis process.

Chapter 3

The ^{12}C+^{12}C Reaction

As mentioned in the previous chapter, hydrogen and helium burning begins with thermonuclear reactions, as a way to avoid the core collapse, at the centre of stars to give birth to new, heavier, and more tightly bound nuclei. Table 3.1 shows the cycle of a star of 25 solar masses [94] where it is shown how via fusion reactions, it is possible to obtain heavy elements such as Fe, Co, and Ni starting from H and He.

Given the importance of Carbon to organic life and also to its role in the nucleosynthesis process, it is vital to understand its fusion process, and particularly, to have an accurate measurement of the cross-section at relevant astrophysical energies. This is the reason why it has been widely studied in the past. Works from Almqvist[2] [3], Becker [15], Erb [32], High [49], Kettner [61], Mazarakis [70], Patterson [82], Spinka [98] are some of the oldest efforts that were made involving the ^{12}C isotope fusion. Figure 3.1 shows the exit channels of the carbon fusion and the properties of the populated states available in each of the fusion exit channels, giving special attention to the ^{20}Ne and ^{23}Na as they correspond to the exit channels measured in this project. It shows the possible particle detection and the energies that can be made to determine the fusion cross-section, where the vast majority of the experimental efforts focused on the detection of either the evaporated charged particles or the characteristic gamma product of the de-excitation of the daughter nucleus. It was not until Jiang and collaborators[58] tried a technique in which the charged particles (as part of the reaction products from the carbon fusion) and gamma rays (from the de-excitation of the daughter nuclei) were measured in coincidence, and served as motivation for the experimental campaigns made for this work.
Particularly, for this work the γ transitions used for the gating were the ones corresponding to the 1634 keV gamma-ray emitted from the $\alpha_1 \rightarrow \alpha_0$ transition in the ^{20}Ne channel, and on the other hand, the 440 keV gamma-ray emitted from the $p_1 \rightarrow p_0$ transition in the ^{23}Na channel, see figure 3.1.

Fuel	Main Product	Secondary Product	T [GK]	Time[years]	Main reaction
H	He	^{14}N	0.02	10^7	$4\text{H} \rightarrow {}^4\text{He}$
He	O, C	^{18}O, ^{20}Ne s process	0.2	10^6	$3\ {}^4\text{He} \rightarrow {}^{12}\text{C}$ $^{12}\text{C}(\alpha,\gamma)\ {}^{16}\text{O}$
C	Ne, Mg	Na	0.8	10^3	$^{12}\text{C}+{}^{12}\text{C}$
Ne	O, Mg	Al, P	1.5	3	$^{20}\text{Ne}(\gamma,\alpha)\ {}^{16}\text{O}$ $^{20}\text{Ne}(\alpha,\gamma)\ {}^{24}\text{Mg}$
O	Si, S	Cl, Ar, K, Ca	2	0.8	$^{16}\text{O}+{}^{16}\text{O}$
Si	Fe	Ti, V, Cr, Mn, Co, Ni	3.5	0.02	$^{28}\text{Si}(\gamma,\alpha)$

Table 3.1: Fuel burning on a star's life cycle for stars of 25 solar masses [94].

Despite the theoretical and experimental efforts, it turns problematic to predict the cross-section of the carbon reaction essentially because of the lack of reliable experimental data. One of the main reasons for this is that the Gamow window ($E_G \approx 1.5$MeV) for the ^{12}C+^{12}C fusion reaction is below the Coulomb barrier, $E_c \approx 6.3$ MeV. Moreover, the presence of resonances at lower energies needs also to be taken into account as shown in figure 3.2.

From figure 3.3, it is shown some of the most relevant experimental and theoretical efforts made to determine the S factor. The lines refer to the theoretical efforts whereas the points were obtained from experimental data. In this plot, it is observed that not only the experimental data points begin to fluctuate and the theoretical lines predict completely different behaviours of the trend as the energy decreases, but also none of the experimental data points obtained lie within the Gamow window and the error bars show an immense increase as lower energies were achieved. Consequently, the theoretical models demand extrapolations at lower energies, i. e. below the ^{12}C Coulomb barrier $E_c \approx 6.3$ MeV.

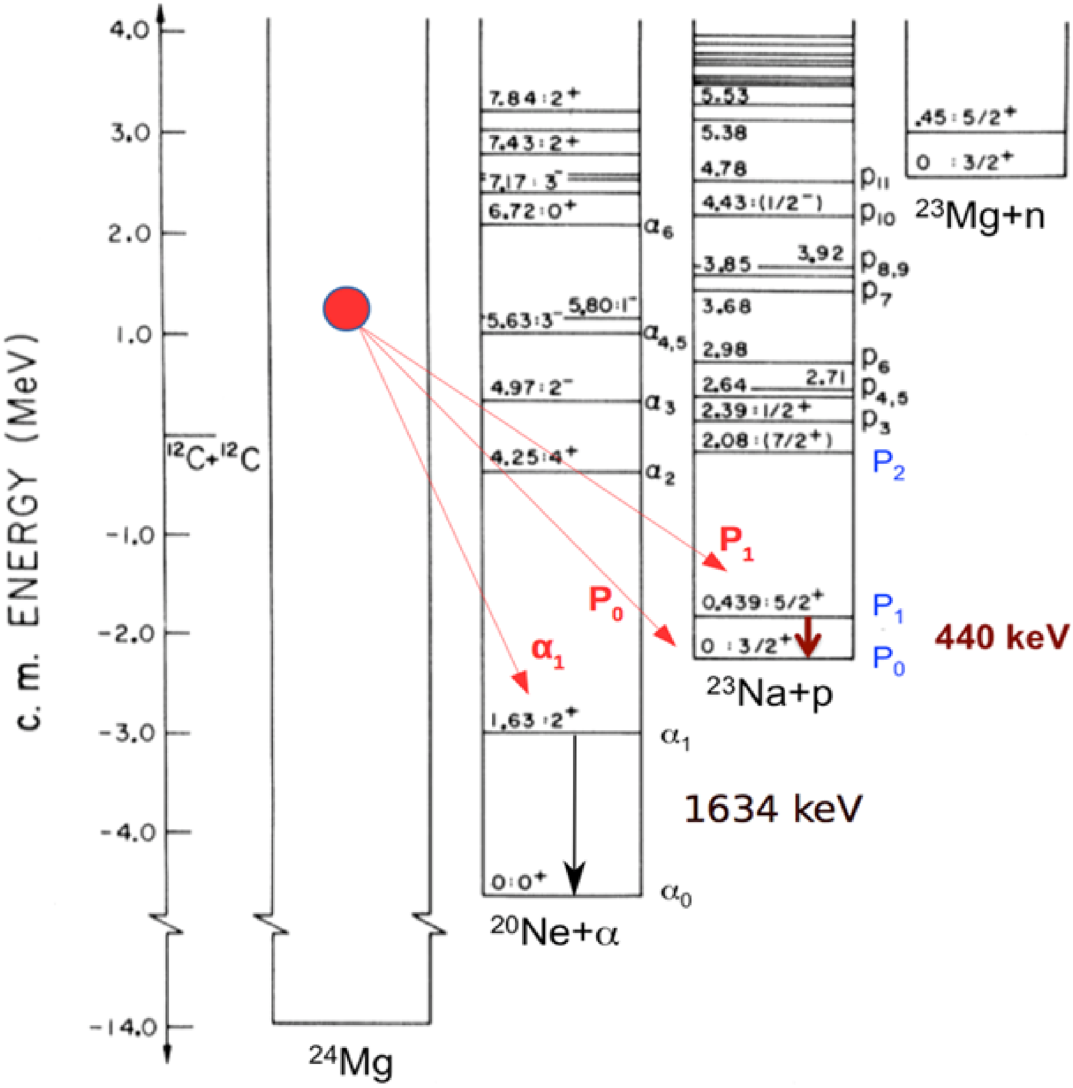

Figure 3.1: Decay scheme of the ^{12}C+^{12}C fusion reaction with its exit channels.Figure adapted from [37]

Further in this chapter, 2 theoretical and 1 experimental approach will be briefly discussed, pointing out their most relevant characteristics and it will be shown the importance of obtaining reliable and accurate data about the carbon fusion reaction.

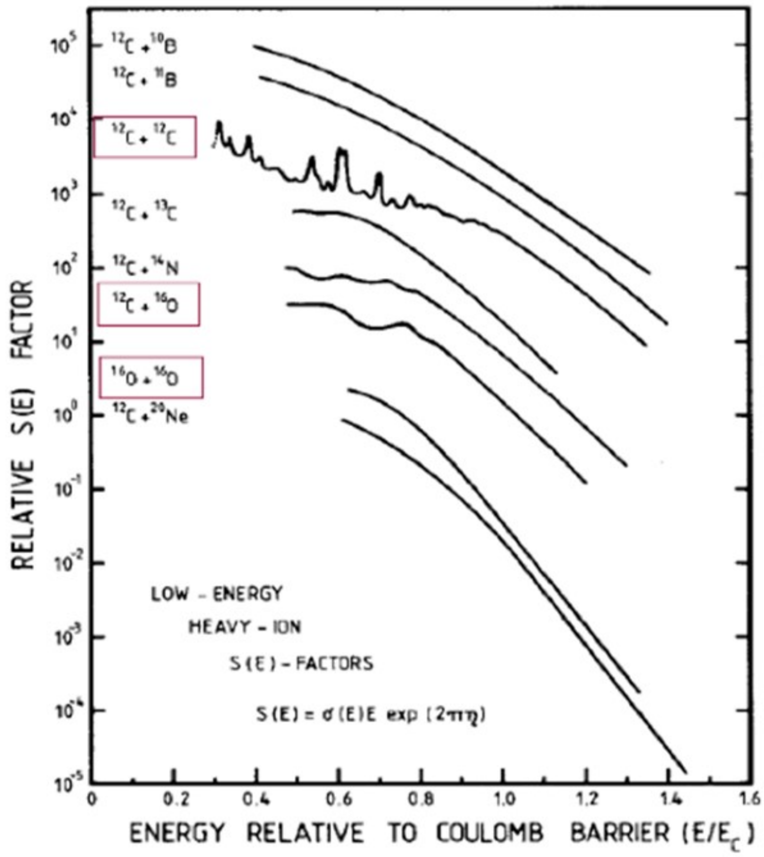

Figure 3.2: S factor of different nuclear reaction. Taken from [12].

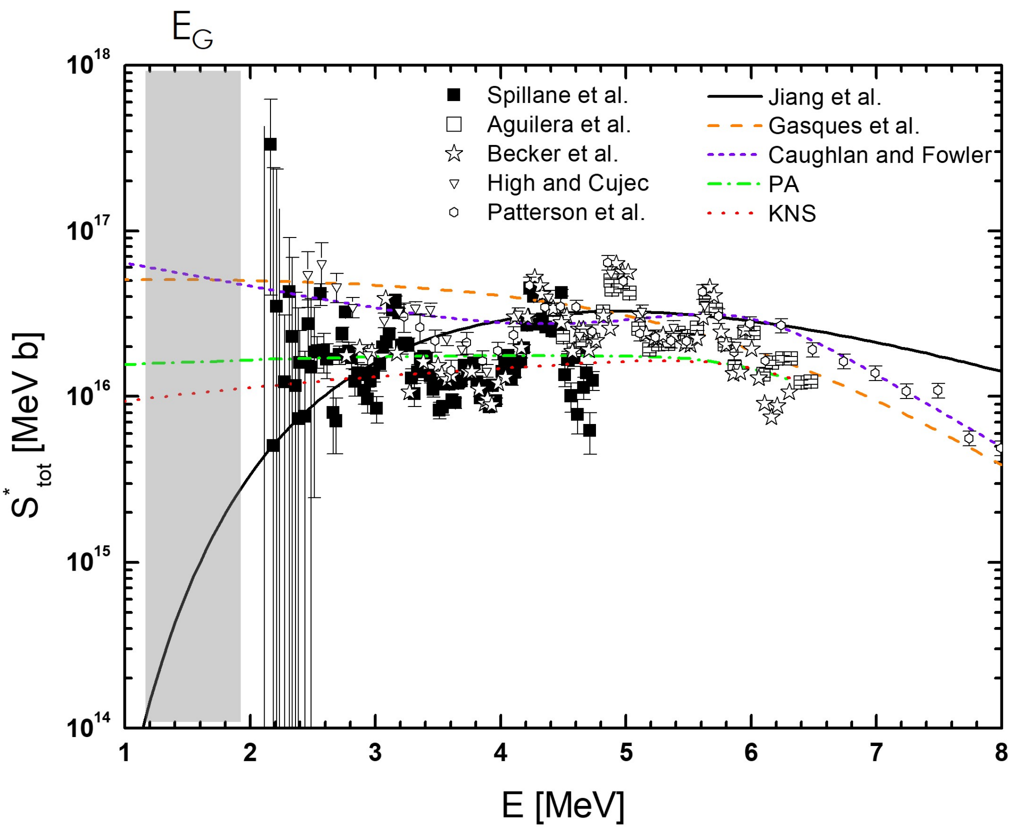

Figure 3.3: Experimental points and theoretical lines representing efforts to determine the astrophysical S factor, where the energy E is in terms of the centre of mass system. Taken from [59]

3.1 Theoretical and Experimental Insights in C Fusion Reaction

3.1.1 Coupled-Channels Approach

The interaction between atomic nuclei comprises different nuclear reactions that can happen as a consequence of a previous nuclear process or as the initial and sole interaction and it is key to make this distinction when it is theoretically required to describe these processes. The C-C approach is a quantum mechanics reaction theory that takes into account internal excitations of the projectile and target nuclei as well as other interactions such as elastic and inelastic scattering, particle transfer, and breakup, extending the 2-body framework described by the Schrödinger equation between colliding particles. If transfer reactions are taken into account, the framework is now known as Coupled-Reaction-Channels (CRC) [43].

CC potentials are based on the phenomenological collective model [19] by using a coupling function $F_{nn'}$, which is defined by a coupling potential V_{coup}, ϕ_n is a particular state, and ξ the intrinsic degree of freedom of a particle. Each n is referred to as a channel, and once this coupling potential is plugged into the Schrödinger equation and projected into a specific ϕ_n state, the *Coupled-Channel equations* are obtained, as shown in equation 3.2.

$$F_{nn'}(x) = \langle \phi_n | V_{coup}(x,\xi) | \phi_{n'} \rangle = \int d\xi \, \phi_n^*(\xi) V_{coup}(x,\xi) \phi_{n'}(\xi) \tag{3.1}$$

$$\langle \phi_n | H - E | \Psi \rangle = \left[\frac{-\hbar^2}{2m} \frac{d^2}{dx^2} + V(x) + \varepsilon_n - E \right] u_n(x) + \sum_{n'} F_{nn'}(x) u_{n'}(x) = 0 \tag{3.2}$$

where the Hamiltonian, H, of the Schrödinger equation and the coupling potential equations have the form of equations 3.3 and 3.1

$$H = -\frac{\hbar^2}{2m} + V(x) + H_0(\xi) + V_{coup}(x,\xi) \tag{3.3}$$

with

$$H_0(\xi)\phi_n(\xi) = \varepsilon_n \phi_n(\xi) \tag{3.4}$$

and the total wave function, $\Psi(x,\xi)$, expanded using the eigenfunctions of H_0, $H_0(\xi)\phi_n(\xi) = \varepsilon_n \phi_n(\xi)$, as basis functions.

$$\Psi(x,\xi) = \sum_n u_n(x) \phi_n(\xi) \tag{3.5}$$

Equations 3.1, 3.2, 3.6, 3.4, and 3.5 are in the case of 1-d particle motion. If a more realistic approach is considered, in 3 dimensions the Hamiltonian and Schrödinger equations take the form of equations 3.6 and 3.7, respectively.

$$H = \frac{-\hbar^2}{2\mu}\nabla^2 + V(R) - iW(R) + H_0(\xi) + V_{coup}(R,\xi) \tag{3.6}$$

where μ is the reduced mass of the system and the imaginary potential term $iW(R)$ is introduced for reaction processes outside the model space defined by ξ. Another example of a process in which an imaginary potential is used is when the optical potential model describes proton scattering by a certain nucleus [71].

$$\left[\frac{-\hbar^2}{2\mu}\frac{d^2}{dR^2} + \frac{L_c(L_c+1)\hbar^2}{2\mu R^2} + V(R) - iW(R) - E + \varepsilon_{nI}\right]\chi^{J_T}_{cc_0}(R) + \sum_{c'} V^{J_T}_{cc'}(R)\chi^{J_T}_{c'c_0}(R) = 0 \tag{3.7}$$

where the index c is a simplified notation for the quantum numbers n, L, I and c_0 represent the quantum number for the entrance channel, ε_{nI} the energy of the intrinsic state $\varphi_{nIm_I}(\xi)$, $\chi^{J_T}_{cc_0}$ is the wave function, $J_T = L + I$ is the total angular momentum, L is the orbital angular momentum, I is the intrinsic angular momentum.

The impact of this theoretical framework in the $^{12}C+^{12}C$ fusion reaction relies on the increment of resonances at energies close to the Coulomb barrier by taking into account the coupling of mutual excitations between the projectile and target, which is explained in terms of a double resonance mechanism, i. e., if the entrance (with energy E and angular momentum J) and excited $(E-\varepsilon_2, J-2)$ channels have resonance states, the number of resonance peaks increases, particularly for the 2^+ state [33].

In figure 3.4, it is shown the modified astrophysical S factor,

$$S^*(E) = \sigma(E)E\exp\left(87.21/\sqrt{E} + 0.46E\right)$$

for the $^{12}C+^{12}C$ reaction where the blue dotted line represents the modified S factor when single channel calculations are considered; the solid line arises when the CC equations are solved for the first 2^+ excited states and the excitations between the target and projectile nuclei; and the dotted red line shows the contribution of J=2 compound nucleus. Here, it is possible to observe that when CC calculations are taken into account, resonance peaks at energies closer to the Coulomb barrier energy

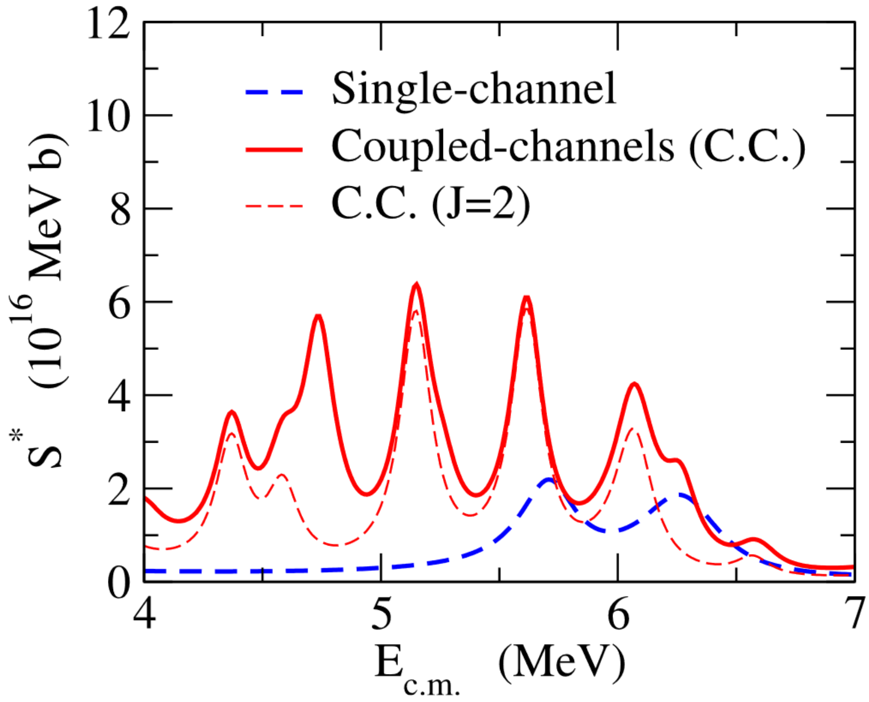

Figure 3.4: Modified Astrophysical S factor, S^{*}, for the $^{12}C+^{12}C$ fusion reaction when single-channel and coupled-channel calculations are taken into account. Figure taken from [43].

arise in comparison with single-channel calculations. The importance of the 2^{+} excited state in the carbon fusion is that it exists a 2^{+} potential resonance in the elastic channel as well as other structures with similar resonance strength [64].

Further discussion of the theoretical framework of the Coupled-Channels approach and its application can be found in reference [43]. Moreover, different computer codes for CC calculations have been developed such as FRESCO [102], CCFULL [44], and ECIS [68].

3.1.2 Fusion Hindrance

Fusion Hindrance refers to the behaviour at low energies, usually below the Coulomb barrier, in which it is observed that the cross sections for different fusion systems exhibit an abrupt decrease, steeper than a simple exponential trend, for instance.

According to [57], the fusion hindrance effect was first observed in [56] where they report this behaviour, particularly on the heavy-ion fusion system $^{60}Ni+^{89}Y$. Nonetheless, it is mentioned that this behaviour was seen in other fusion systems and attempted to be described through Coupled-Channels calculations or using a different type of potential (e.g., Woods-Saxon potential, optical potential).

Furthermore, this effect can be described in terms of the energy at which the S factor has a maximum within low energies. Here, the astrophysical S-factor is defined as

$$S = \sigma E \exp(2\pi\eta) \tag{3.8}$$

where η is the Sommerfeld parameter as in equation 2.15.

For example, for fusion reactions with negative Q-value, the following conditions take place:

$$\sigma(E) \to 0 \Rightarrow S(E) \to 0$$

when

$$E \to -Q$$

This behaviour has as a consequence that when $E > -Q$, the S factor reaches a maximum; and that at energies below that maximum, there's a rapid decrease of the cross-section as smaller energies E are taken into account.

For reactions with positive Q-values,

$$\sigma(E) \to \text{finite}(\geq 0) \Rightarrow S(E) \to \text{finite or } \infty$$

Not only looking at the conditions previously mentioned is how hindrance can be treated, but a function of the energy $L(E)$ is introduced to best also describes the trend at low energies through a logarithmic derivative defined as equation 3.9:

$$L(E) = \frac{d}{dE} \ln(E\sigma) \tag{3.9}$$

The energy-weighted logarithmic derivative of the cross-section, $L(E)$, used in the current fusion models, presumes a constant value or small increase in low energies is reached; whereas the experimental data for $L(E)$ presents an almost linear increase with decreasing energy around the energy at which the S factor reaches its maximum [57].

Misiçu and Esben proposed that the fusion hindrance is due to the saturation properties of nuclear matter, increasing the repulsive part of the nuclear potential inside the barrier to finally result in a hindrance of the quantum tunneling [77].

Particularly, for the ^{12}C+^{12}C fusion reaction, as seen in figure 3.2, due to the strong resonances, present models to describe the complete behaviour are not available and only reproduce its energy averaged behaviour [57].

3.1.3 Trojan Horse Method

The Trojan Horse Method (THM) is an indirect technique to determine the cross sections of low energy nuclear reactions between charged particles that present small cross sections unhindered by the effects of atomic electrons and Coulomb Barrier [105].

Baur proposed the idea of using breakup reactions to extract information of charged particles induced reactions at low relative energies employing a 3-body type reaction to improve the cross-section measurements by reducing the effects of the Coulomb barrier in a two-body interaction [14].

Figure 3.5 shows the Quasi-Free (QF) interaction where in the upper vertex the particle a breaks into x and S; on the other hand, the lower part of the diagram shows the nuclear reaction of main interest.

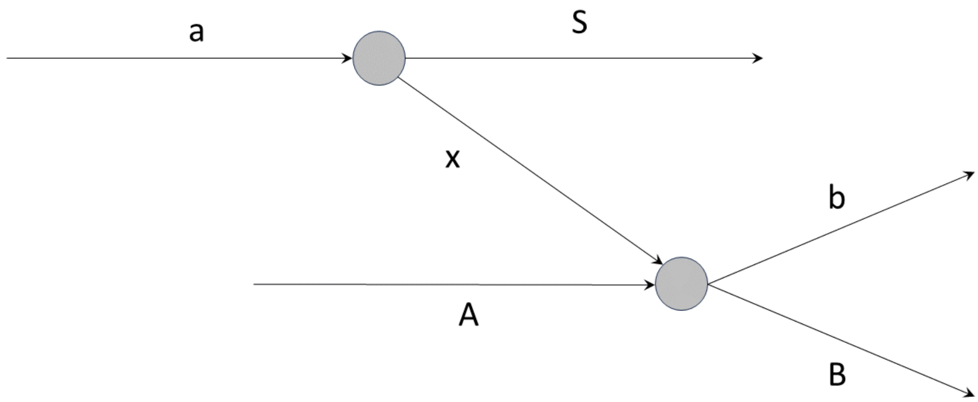

Figure 3.5: Diagram of a quasi-free Trojan Horse reaction A(a,bB)s, where the breakup of a occurs in the upper vertex and the reaction A(x,b)B takes place in the lower vertex.

In this Trojan Horse technique, there are several key aspects to consider. The selection of a suitable A(a,bB)S quasi-free reaction that will prevent Coulomb suppression and electron screening effects to measure the cross-section of a A(x,b)B reaction is essential. The process where the Trojan Horse nucleus a, $a = (xS)$, is involved induces the reaction between x and A and has S as a spectator in the following A(x,b)B reaction. Another key aspect to consider is that x in this latter virtual reaction, does not follow the conventional energy-momentum relation for free particle and has to be substituted by a *half-off-energy-shell (HOES)* treatment. Further details of this method can be found in references [99, 104, 105], as a complete description of this method fall outside the scope of this work.

Additionally, particles a and A are chosen in a way that their movement has relative energy higher than the Coulomb barrier, consequently the transfer of particle x happens within the nuclear field of A, avoiding Coulomb suppression or atomic electron screening effects. Nonetheless, the interaction between A and x takes place at an energy below the Coulomb barrier because the excess of energy due to the motion between a and A is spent in the breakup of the Trojan Horse nucleus a.

The electron screening effect is due to the atomic electron cloud surrounding the interacting nuclei. This has a direct impact on the Coulomb barrier perceived by the projectile, see figure 3.6; it effectively sees a reduced Coulomb barrier in range and intensity, given by equation 3.10 [94]

$$E_{eff} = \frac{Z_1 Z_2 e^2}{R_n} - \frac{Z_1 Z_2 e^2}{R_a} \tag{3.10}$$

where Z_1 is the number of protons of the projectile, Z_2 number of protons of the target, R_n radius of the nucleus of interest and R_a the atomic radius.

So that the cross-section (or equivalently the astrophysical S factor) that takes into account the sole nuclear effect is greater than the one that considers the screening effect, $\sigma_S(E) > \sigma_b(E)$, where the index S and b stand for screened and bare nucleus respectively, as the energy decreases towards the Gamow window. This difference in cross-sections is also because the target nuclei are typically neutral atoms or molecules, and the projectile nuclei come in the form of positively charged ions [10]. Moreover, figure 3.6 shows that the effects of the Coulomb potential on the projectile appear just when it is close to the atomic radius, R_a, contrary to the bare nucleus Coulomb potential where the projectile is affected at greater distances from R_a. Nonetheless, both considerations follow a similar trend as the distance from the projectile approaches the nuclear radius R_n.

The relation between the cross-sections can be described by introducing an enhancement factor f_{lab}, defined as equation 3.11:

$$f_{lab}(E) = \frac{\sigma_S(E)}{\sigma_b(E)} \sim \exp\left(\pi\eta\frac{U_e}{E}\right) \tag{3.11}$$

where U_e is the electron screening potential, and η the Sommerfeld parameter as in equation 2.15.

Particularly, the ^{12}C fusion reaction has no different effects regarding the electron screening. However, according to Rolfs and Rodney [94] this effect is usually negligible given that the energies of this effect oscillate around tenths of keV in comparison, for example, with the beam energy of the projectiles for this experiment, $E_{beam} = 5.07$ MeV. Consequently, it has not been taken into account this effect.

On the other hand, if the experiment had been done directly on the Gamow energy window, an enhancement on the cross-section would have appeared. Firstly, the fact that the reaction happens within this window, by definition, increases the probability of the fusion reaction; and secondly, as previously discussed, the cross-section increases when the effect is taken into account.

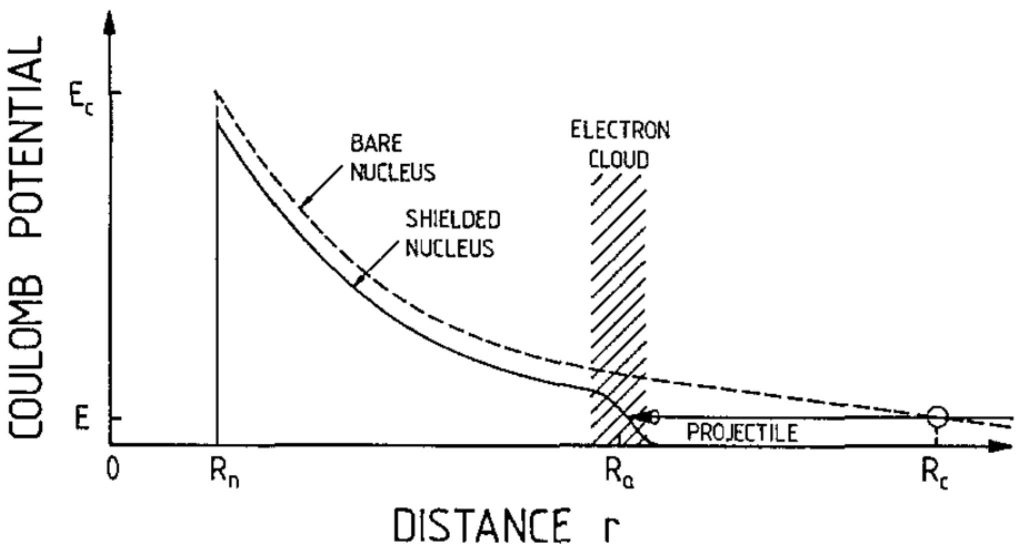

Figure 3.6: Graph showing the effects of the atomic electron cloud on the Coulomb potential Plot taken from [10]

Since experimental data is not available for measurements without the screening effect, it is key to have a good understanding of the electron potential U_e to calculate the cross-sections (or S factors) of the bare nucleus from the experimental data for σ_S [99].

In particular, the Trojan Horse Method has been applied to the $^{12}C+^{12}C$ reaction through $^{12}C(^{14}N,\alpha^{20}Ne)\ ^{2}H$ for the neon exit channel, and $^{12}C(^{14}N,p^{23}Na)\ ^{2}H$ for the sodium exit channel in the works of A. Tumino, et. al., [104]; and it's been reported as well in the work of Spitaleri, et. al., the reaction $^{6}Li(^{12}C,\alpha^{12}C)^{2}H$, [99].

Finally, the Trojan Horse Method is a good alternative to determine cross-sections for low-energy reactions in particular for reactions in which the Gamow window is below the Coulomb barrier given its ability to avoid the Coulomb barrier in the entry channel of the reaction. However, the fact that is still needed experimental data for determining the effects of the bare nuclei (σ_b, e.g.) and an exact theory for three-body reactions including charged particles is not available [78], proves again the need for good reliable data of direct measurements of low energy reactions. The THM uses different theoretical approximations to describe the reactions. In [78], it is discussed how taking into account DWBA (Distorted Wave Born Approximation) or PWA (Plane Wave Approximation) can modify the astrophysical S factor.

In conclusion, both the CC model and Hindrance require the determination of reliable experimental data for calculating the cross-section and generating a precise theory that describes fusion not only for ^{12}C, but for other light heavy-ion systems. Similarly, the Trojan Horse indirect method would be validated once again, allowing, on the other hand, the determination of the cross-section due solely to the atomic nucleus effect. Hence, the goal of this project is precisely to provide an accurate value for the fusion cross-section.

Chapter 4

The Experiment

With the context described in the previous chapter 3, the run plan for the experimental campaign of this experiment was planned as figure 4.1 shows, where the main goal is to determine with as much precision as possible the fusion cross section.

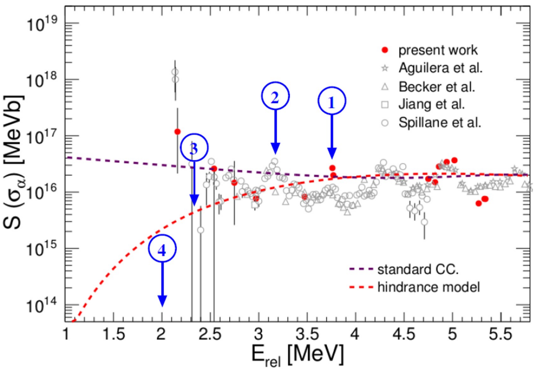

Region	E_{rel} [MeV]	Time [d]	Intensity [pμA]	E_{beam}[1] [MeV]
①	3.8	1/2	10	7.9
②	3.25	1/4	10	6.8
	3.20	1/4	10	6.7
	3.15	1/2	10	6.6
	3.10	1/2	10	6.5
	3.05	1/2	10	6.4
③	2.35	14	10	5.1
④	2.00	21	10	4.38[2]

Figure 4.1: Run plan for the experiment of this work.

The STELLA (STELlar LAboratory) experimental setup used for the determination of fusion cross-sections of light heavy-ion is located within the Andròmede facility at the Institut de Physique Nucléaire (IPN), Orsay, France [5, 30]. Thanks to the UK-FATIMA (FAst TIMing Array) collaboration and the charged particles detectors from STELLA, it was possible to measure the evaporated charged particles of the nuclear reaction products in coincidence with the gamma particles produced by the de-excitation of the final state nuclei.

The methodology used for the gamma-particle coincidence method is based on the one proposed by Jiang, *et al.* [59, 58] and implemented on the first campaign of this collaboration, [46, 37]. In this methodology, alpha particles from the ^{20}Ne and protons from the ^{23}Na exit channels are detected

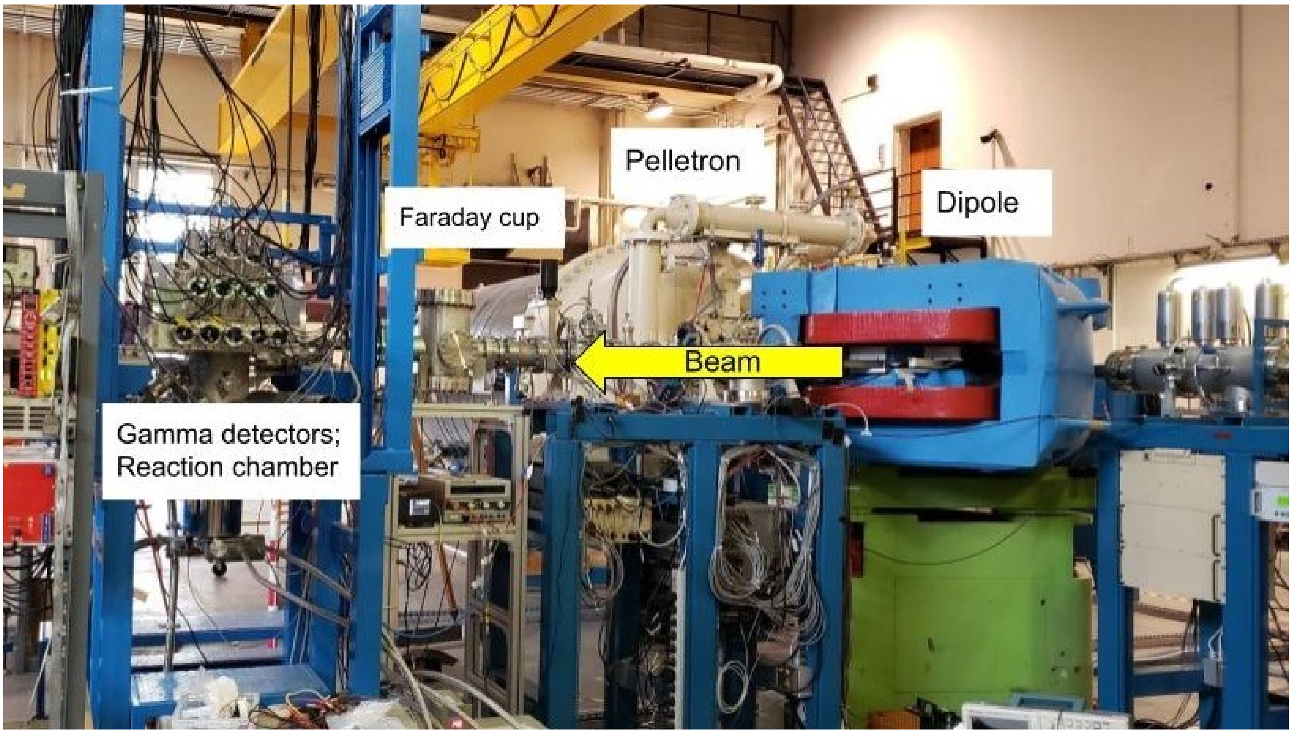

Figure 4.2: A picture of the STELLA facility showing the Pelletron accelerator, dipole for deviation of the beam, gamma-ray detectors, and reaction chamber.

using an array of Silicon detectors whilst a combination of 3 DSSDs is used to detect the gamma rays produced by 20Ne and ^{23}Na excited state residues. This experiment took place at the ATLAS accelerator at Argonne National Laboratory using Gammasphere for γ detection and gating on the evaporation residues to proceed with the charged particle detection via the annular DSSDs. However, for the experiment done within the STELLA collaboration, an array of up to 36 $LaBr_3$(Ce) for the gamma detection and 2 annular DSSDs were used to perform the coincidence measurement.

4.1 Accelerator

The accelerator used in the STELLA collaboration is a 4 MV electrostatic Pelletron accelerator manufactured by the company NEC (National Electrostatic Corporation), see figures 4.2 and 4.3. This Pelletron is capable of producing a range of particles (including the ^{12}C ions used in this thesis), thanks to an ion source that, based on the electron cyclotron resonance (ECR), can get multi-charged ions into the accelerator tube; the ions are selected by a Wien filter and then deflected 90° by a dipole into the reaction chamber.

There are two gases chosen in the accelerator: methane, used for the plasma ionisation to produce the ions that will be accelerated; and sulfur hexafluoride (SF_6), used as an insulating gas inside the

Figure 4.3: Interior of the Pelletron accelerator at Andromede.

Pelletron to reduce the risk of electrical arcing.

With this configuration, it is possible to obtain a stable, intense ($\geq p\mu A$) ^{12}C beam. Additionally, 2 Faraday cups, one before and one after the reaction chamber, were used to monitor the beam as an absolute normalisation of the beam for the fusion cross-section is needed.

4.1.1 Beam

As previously mentioned, a carbon beam was produced using a 4 MV Pelletron accelerator which could deliver a current of carbon ions on a single charge, 2^+ and 3^+ charge state of up to 10 μA [31]. In this experimental campaign the current ranged from 30 pnA to 2pμA. Particularly, the data for this analysis was acquired with an averaged current of $I_{average} = 41.3$ pnA of ^{12}C (2^+) measured at the Faraday cup before the reaction chamber. The selection of this particular range of beam current was made based on two aspects. Firstly, the beam intensity needed to be high enough to achieve sufficient statistics in the low energy region, as well as to decrease the H contamination within the carbon target [97]. Secondly, to avoid target breakage due to energy loss of the beam inside the target, combined with the rise in its temperature while running the experiment. A thermal analysis for heat dissipation was conducted during the first experimental campaign of the STELLA collaboration and was discussed in detail in reference [37].

As previously stated, the experimental run plan, 4.1, was based on the energy of the Coulomb barrier E_C= 6.6 MeV, so that E_{cm} starts above the Coulomb barrier (E_{beam}= 7.9 MeV hence E_{cm}= 3.8 MeV),

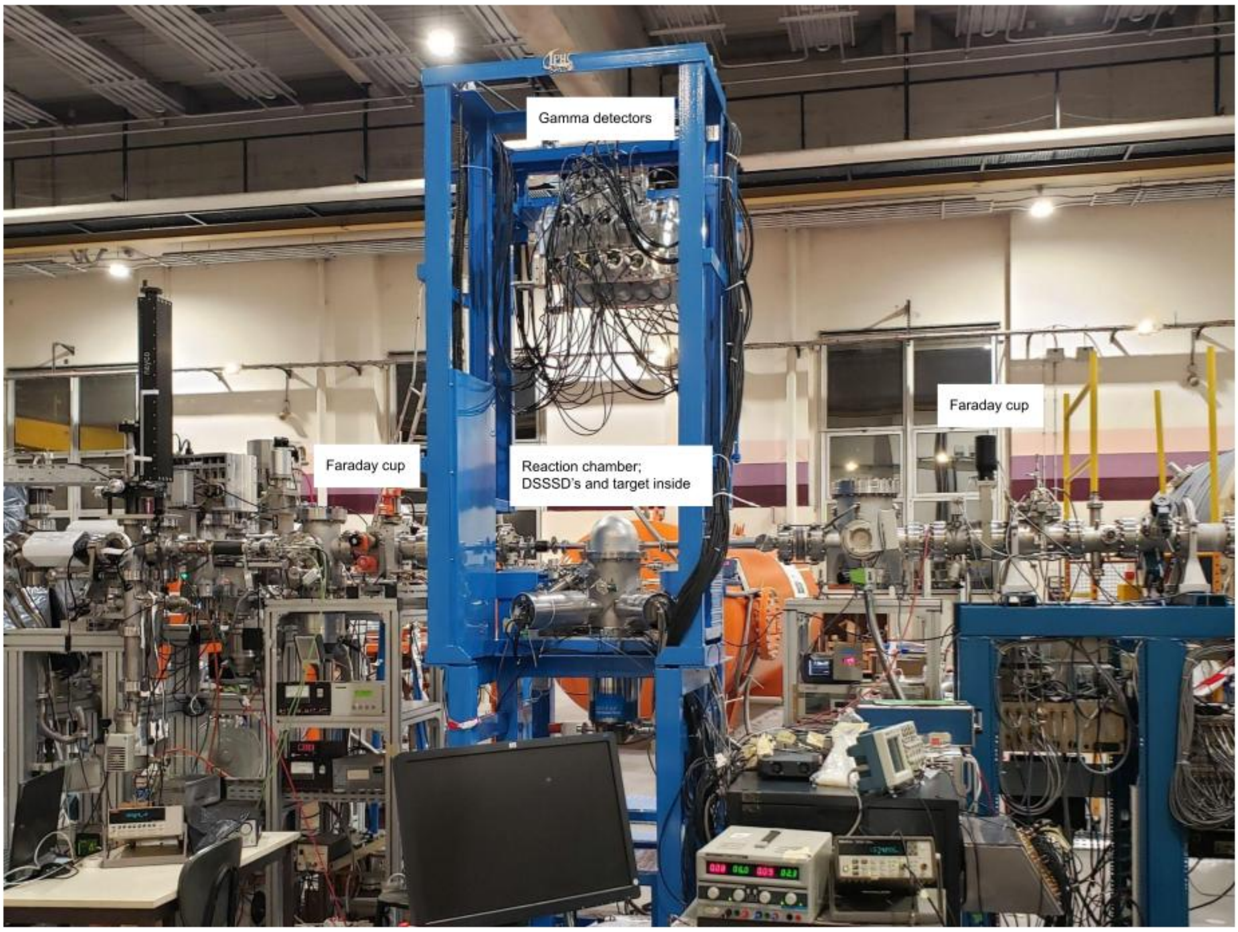

Figure 4.4: Photo of the setup showing the two Faraday cups used as monitors, the reaction chamber and the $LaBr_3(Ce)$ detectors

and explore the region below the Coulomb barrier with a beam energy of E_{beam}= 4.38 MeV hence E_{cm}= 2 MeV [36]. However, the analysis done in this present dissertation was for the beam energy E_{beam} = 5.07 MeV, $E_{cm} \sim 2.5$ MeV, that still fulfills the condition of being energy below the Coulomb barrier energy.

4.1.2 Reaction Chamber

Inside the reaction chamber, the rotating target system was placed. Here, the targets of 20-70 $^{\mu g}/_{cm^2}$ were used, as well as the DSSDs for the detection of the scattered charged particles. This was all enclosed by a 2.5 mm thick aluminium dome-shaped lid and located below the array $LaBr_3(Ce)$ scintillators for the detection of the gamma rays. On the incoming sections 4.2.2,4.2.1, 4.2.3 and 4.3 a more detailed explanation of the detectors and the targets will be done.

An ultra-high vacuum is maintained inside the reaction chamber using a primary dry pump and a cryo

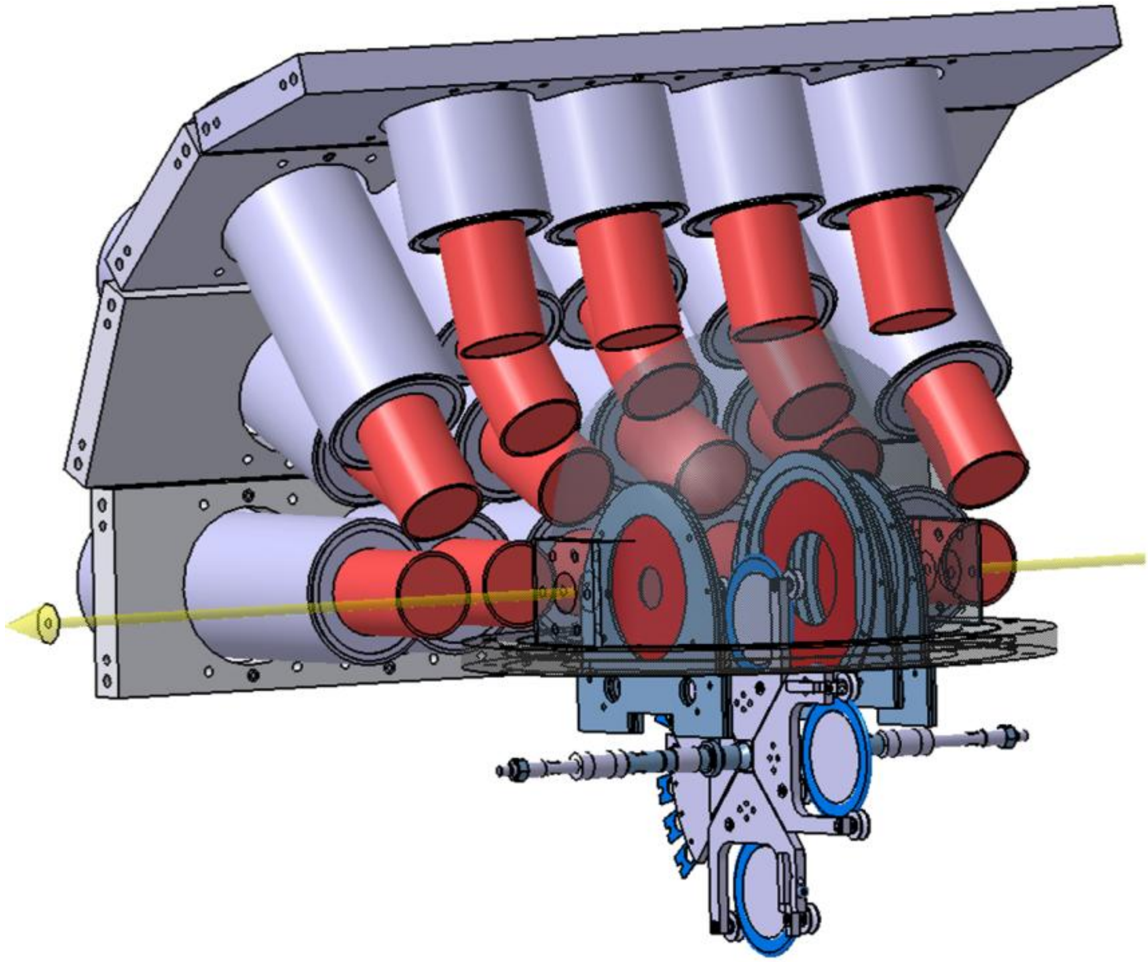

Figure 4.5: Illustration of the lateral view of the scintillator detectors on top of the reaction chamber containing the array of the rotating target system placed in between the Silicon detectors. The yellow arrow indicates the direction of the beam. Sketch taken from [47].

pump, the latter has a working temperature of approximately 15 K, which helps reach pressures of 10^{-8} mbar [38].

This level of vacuum is required to avoid different reactions associated with the charged particles and gamma rays of interest detected as it will be shown further on. This would have an impact on the spectra, complicating the distinction of the fusion events. For instance, ^{13}C along with the presence of ^{1}H and deuterium d, from water molecules, are the most significant sources of background contamination that could be found within the reaction chamber. Different reactions with these contaminants occur, for example, the nuclear reaction ^{12}C+^{16}O could have a small contribution to the energy spectra obtained even though the Coulomb barrier has a higher value; ^{12}C+^{1}H has a cross-section significantly higher than the ^{12}C fusion reaction [15]; the reaction between deuterium and carbon, d(^{12}C,p)^{13}C, has protons of similar energies to the protons produced in the carbon fusion process [109]; the reaction involving the ^{13}C present in the target produce protons and alpha particles with similar energies found on the protons and alpha's produced in the ^{12}C+^{12}C reaction.
On the other hand, the main reactions that take place regarding gamma-rays are: ^{1}H(^{12}C,γ)^{13}N and d(^{12}C,pγ)^{13}C where $E_\gamma = 2.36$ MeV and $E_\gamma = 3.09$ MeV, respectively [62].

This vacuum system is located below the reaction chamber; figure 4.6 shows the inside of the reaction chamber. Nonetheless, the sketches of figures 4.5,4.6 show an extra target hold and DSSSD detector in between the target and the first DSSSD detector. The yellow arrow on both images shows the direction of the beam. The detector being in a more upstream position is the backward detector, and the furthest one along the beam direction, is the forward detector.

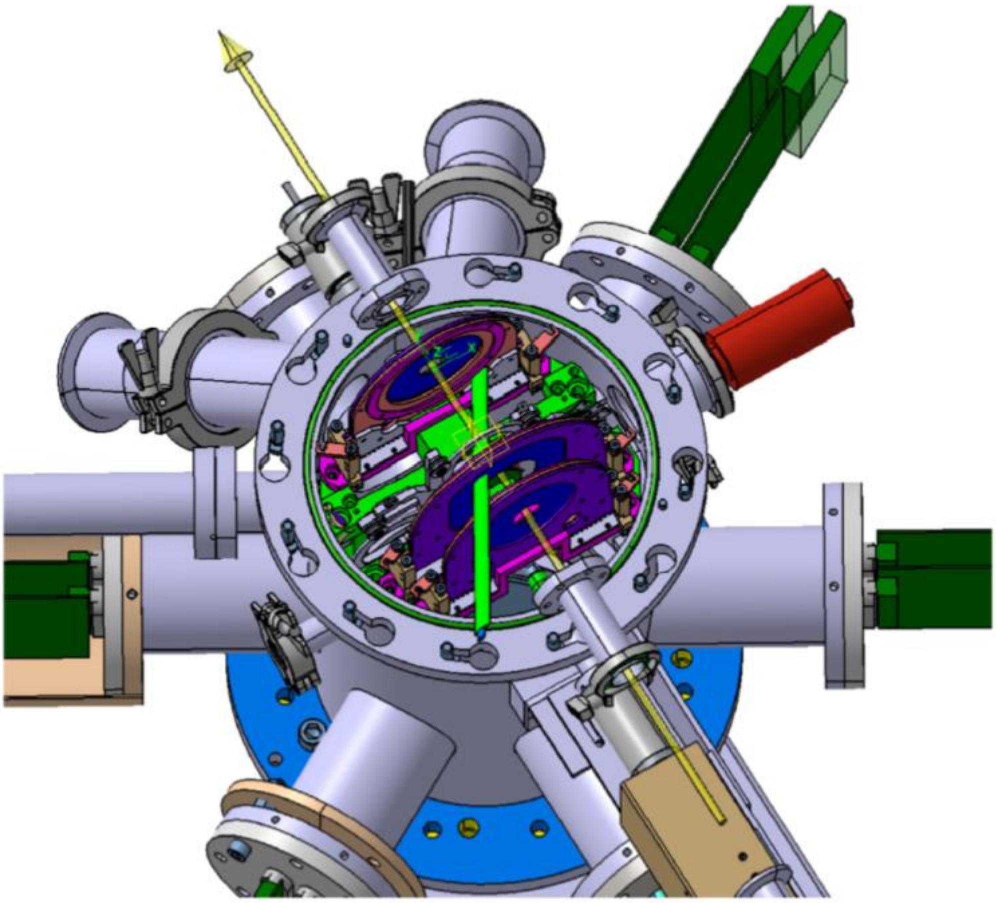

Figure 4.6: Top view of the inside of the reaction chamber, showing the direction of the beam (bottom right to top left. Sketch taken from [39]

4.2 Detectors

The detection system consisted of mainly two parts: the system used for the detection of the evaporated charged particles and the one used for the gamma particles. For the first one, 2 disc-shaped DSSD were located upstream and downstream the target, respectively; and for the latter, an array of 36 $LaBr_3(Ce)$ scintillators with photomultiplier tube readout were located on top of the reaction chamber. These two types of detectors will allow measurement coincidences between the resultant particles of the ^{12}C fusion reaction to reduce the background and, hence, better energy spectra.

4.2.1 Double Sided Silicon Strip Detectors

Semiconductor or solid-state detectors have been widely used for research in the nuclear and high energy physics area, being Silicon (Si) and Germanium (Ge) detectors the most common ones, for example, Jiang and collaborators used this type of detectors to detect the evaporated charged particles of the ^{12}C $+^{12}$C fusion reaction [59]. One of the main advantages of these types of detectors is their exceptional energy resolution given their ability to produce more electron-hole pairs at a lower energy for a given incident radiation in comparison, for example, with gas-filled detectors (~ 3 eV against ~ 30 eV, respectively)[63].

The basic operating principle is the creation of electron-hole pairs when ionising radiation passes through these semiconductor materials, to be then collected using an electric field produced by the detector [67].

In particular, and given the specific type of solid state detectors used for this work, silicon detectors are the ones that will be discussed. These types of detectors are mainly used to detect charged particles and spectroscopy of β particles, amongst other applications such as low-energy photon spectrometry. These applications are possible thanks to the low atomic number that will help the original electrons deposit their full energy without any loss due to back-scattering events. Moreover, Silicon detectors are more frequently used for charged particle detection, and Germanium detectors are generally used for gamma spectroscopy [63].

According to a particular configuration, it exists a variety of semiconductor detectors using silicon, e.g., Single or Double-sided Strip Silicon Detectors (SSD and DSSD, respectively). These two are examples of detectors that can be used for position detection, however, the advantage of the double-sided over the single-sided relies on the fact that the position reconstruction of interaction between the detector and the detected particle is made in two dimensions thanks to the orthogonal strips on the p and n regions of the semiconductor [50].

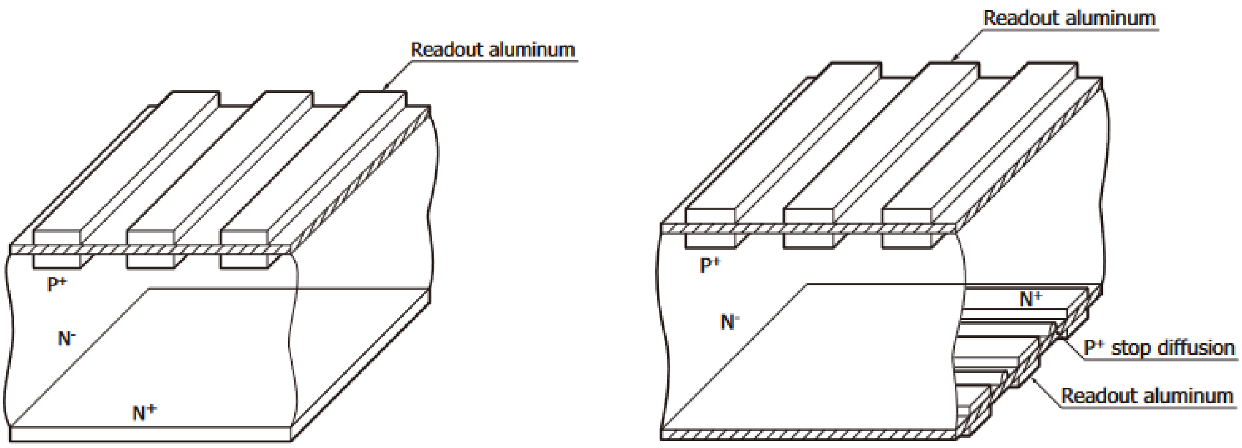

(a) Diagram of a SSD.

(b) Diagram of a DSSD.

Figure 4.7: Diagrams of Silicon detectors used for position detection. Figures taken from [45]

From figure 4.7, it is shown the configurations of a single-sided and a double-sided silicon strip detector. In figure 4.7a, the aluminum readout strips that act as electrodes for the signal transportation, are located on the p^+, p region highly doped, without any other electrode strips on the N^+, n region highly doped. Whereas figure 4.7b shows the main difference with the SSD by having a set of aluminum readout strips on the N^+ region of the detector, allowing to obtain a two-dimensional position detection.

From references [2, 82, 15, 69], it is shown that detection of charged particles, such as protons and alpha particles, can be done using silicon detectors, in addition to a covering foil which protects them from the scattered or delta electrons emitted by the target beam with aluminium or nickel thin foils.

Having the detector's strips positioned at different angles allows to perform an angular distribution measurement and have a better understanding of the characteristics of the reaction.

The DSSDs used for this experiment were a pair of type 3 (S3) detectors built by Micron Semiconductor Ltd. consisting of 24 rings of 886 μm on the junction side and 32 sectors on the ohmic side [74]. The resistive region between rings is of $\sim 10\mu$m. Their active inner diameter is 22 mm and 70 mm for the outer area; with a thickness of 500 μm. These S3 detectors typically have a rise time when a signal is detected of 80-100 ns with a decay time of 15-20 μs.
S3B and S3F detectors stand for type S3 DSSD in the backward and forward position regarding the target and the forward one is the one in the downstream position, respectively.

The silicon detector's system was customised so that a regular PCB (Printed Circuit Board) mount is replaced by a low outgassing ceramic one designed and built by IPHC (Institut Pluridisciplinaire Hubert Curien) Mechanics and Microtechnique Department at Centre National de la Recherche Scientifique (CNRS), Strasbourg, France [47]. Rogers Corporation developed this low-outgassing material used for the new PCB mount and can be found under the name RO4003C, which is a ceramic reinforced with woven glass [93].
With this new ceramic PCB, two key aspects were ensured. On one side, there was no unnecessary and unwanted extra contamination that could affect the measurement thanks to the new ceramic used; on the other hand, the fitting of the detector within the reaction chamber was achieved given that with the original Micron mount, it was not possible using the desired configuration of this silicon and scintillating detectors because the upper part of the original mount did not follow the semi-spherical curvature of the top of the dome, see figure 4.4 for reference of the dome enclosing the reaction chamber.

The signals received from each ring of the detector, red dots of the junction side from figure 4.9, go through 2 differential Mesytec MPR-16D preamplifiers to be polarised with a voltage of -60 V and

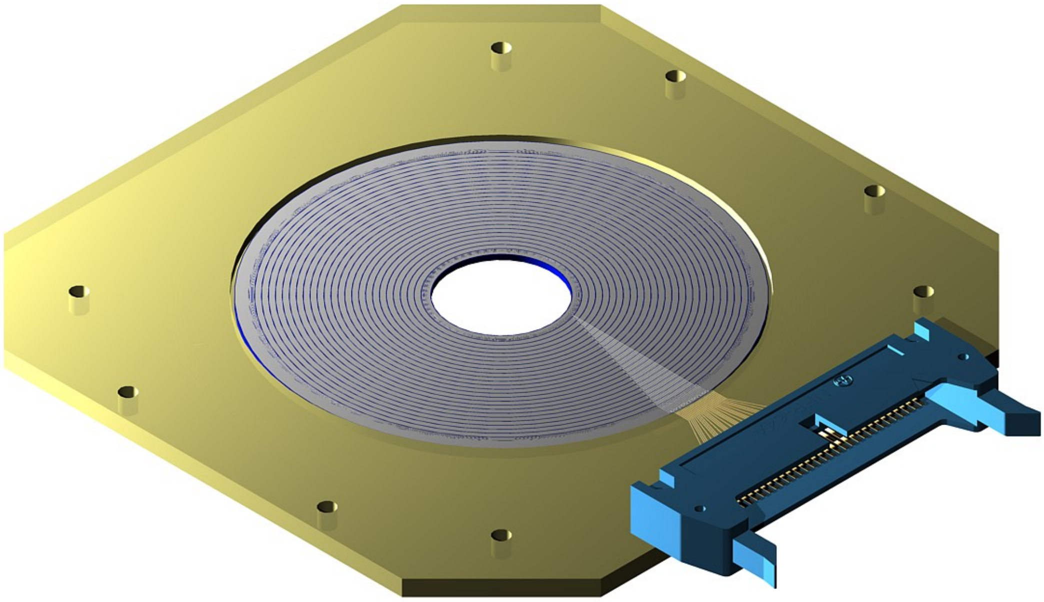

Figure 4.8: Diagram of the Micron S3 type detector showing the junction side with the 24 rings [73].

generate a leakage current of ~ 100 nA [72].

On the lowermost part of the detector's PCB diagrams, figures 4.9, 4.10a and 4.10b, the pin connectors are shown. These jumper-like setups of the pins will then be connected to the preamplifiers via Kapton cables, which are suitable for ultra-high vacuum. Another advantage of this system is that given that the detectors are connected to the preamplifiers straight from the flanges, reducing the amount of electronic noise $\pm 15 - 20$ mV. Furthermore, not only the electronic noise is then filtered in the acquisition system but the preamplifier cards are enclosed within an aluminum cylinder; still, shielded cables were required to send the obtained signals from the preamplifier to the differential and single-ended converters as required for the charged particles DAQ.

Moreover, the two holes of approximately 2 cm, appearing on the bottom part of the PCBs from figures 4.10a and 4.10b serve as a pathway for the scattered beam to reach the monitors placed at an angle of 45°. A more detailed discussion about the monitors will be made in section 4.2.3.

Additional protection to the S3 type DSSDs is used employing an aluminium foil to protect them from the ^{12}C scattered beam and from delta electrons emitted from the target that might appear, as

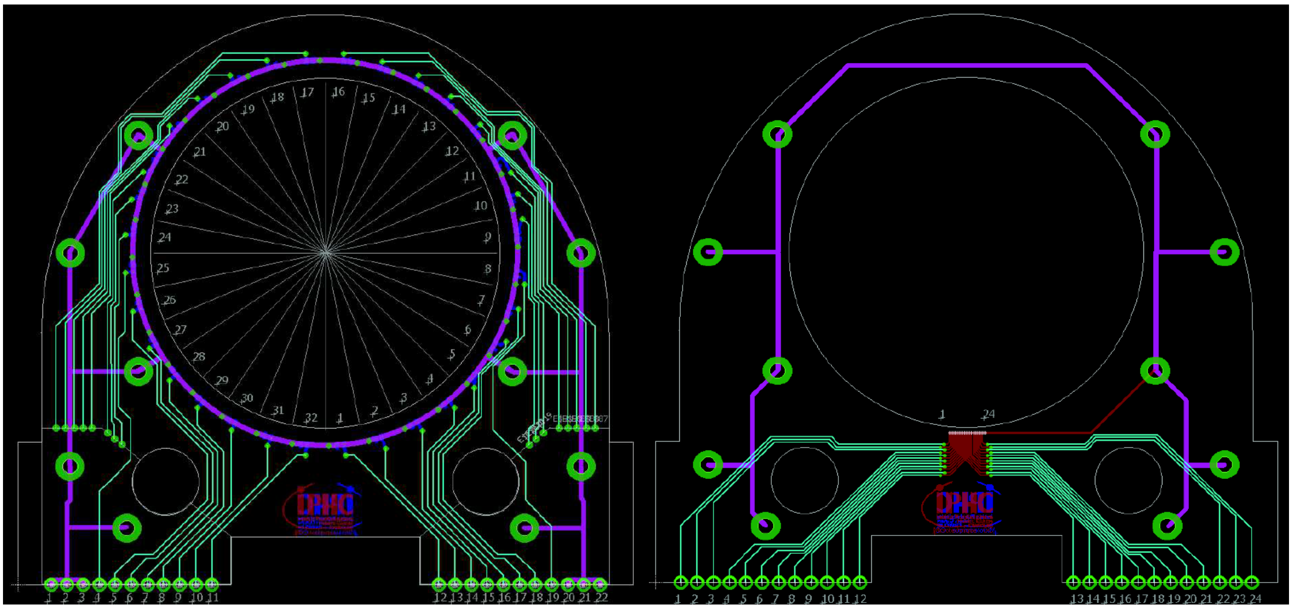

Figure 4.9: Diagram of the customised ceramic PCB built for the S3 detectors with the silicon detectors placed in the middle of it. On the left side, it is shown the ohmic side of the S3 silicon detector with its 32 sectors. On the right side, just one ring of 24 is depicted within the junction sector. The green rings represent the grounding connections in the PCB, the red dots on the ohmic side are the connection points, and the green lines represent the wires that will carry the signal from a detected interaction.

shown in fig. 4.11. The delta electrons that might appear have energies of about tenths of eV, so a thin aluminium foil is enough to stop the electrons as the minimum energy to penetrate the foil is of $\sim$ 500 keV for a foil of a few micrometres [58]. The upstream detector S3F foil's thickness was 10 μm, whereas for the downstream detector S3B, the thickness was 0.8 μm. See 4.11.

Finally, detector S3B is located at a distance of 5.6 cm from the target, along the carbon beam line, and S3F is at 6 cm. Considering that the detectors are annular, the angular coverage range from $148° \leq \theta_{S3B} \leq 169°$ and $10.4° \leq \theta_{S3F} \leq 30.3°$, respectively, as shown in figure 4.12. Hence, the solid angle for detector S3B is 0.84 sr and for detector S3F is 0.75 sr according to formula 4.1

$$\Omega = 2\pi \left[\frac{(r_{outer}^2 + d^2 - d\sqrt{r_{outer}^2 + d^2})}{r_{outer}^2 + d^2} - \frac{(r_{inner}^2 + d^2 - d\sqrt{r_{inner}^2 + d^2})}{r_{inner}^2 + d^2} \right] \tag{4.1}$$

where r_{outer} is the outer radius of the detector, 7 cm; r_{inner} the inner radius of the detector, 2.2 cm; and d is the distance to target, 5.6 cm for S3B and 6 cm, respectively.

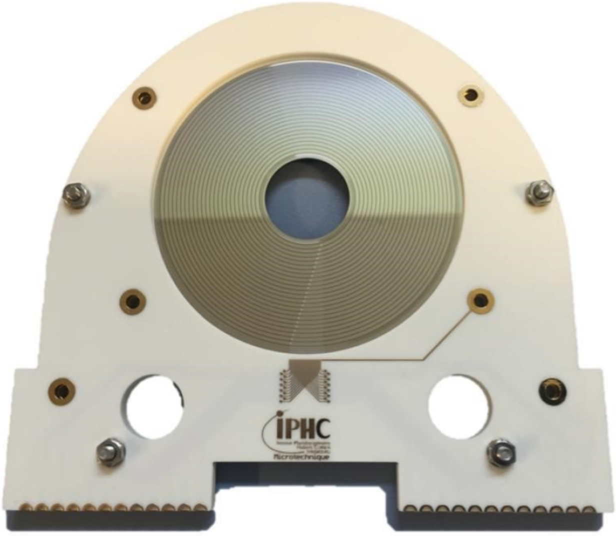

(a) Diagram of the tailored DSSSD.

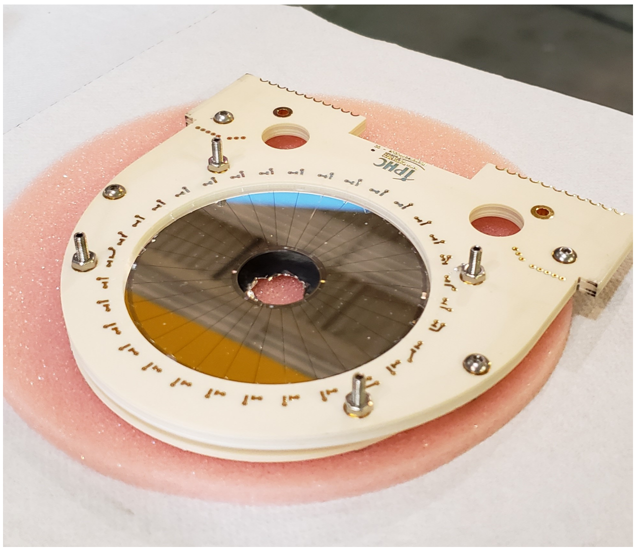

(b) Picture of one of the S3 type DSSSD's tailored for the experiment.

Figure 4.10: Customised Silicon detectors

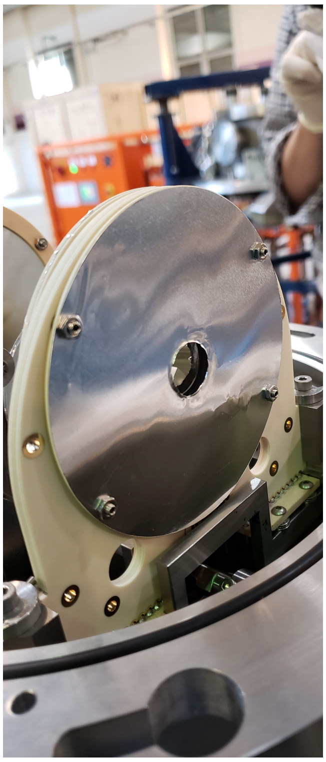

(a) Picture of S3B detector mounted on the reaction chamber and covered with an aluminium foil.

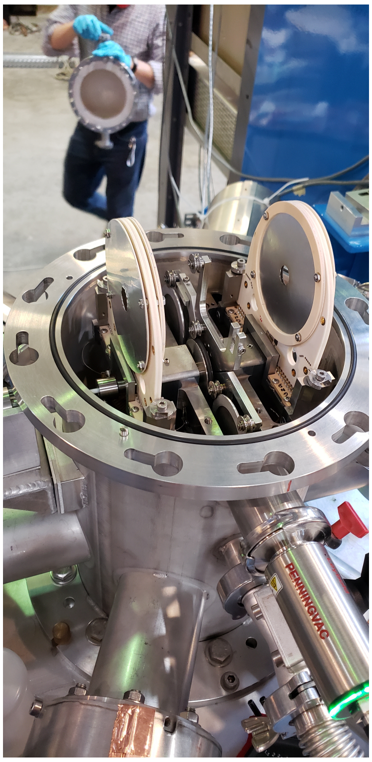

(b) Detectors S3b and S3F mounted on the reaction chamber. In between it is observed the rotating target system without a target.

Figure 4.11: S3 DSSSDs mounted and covered

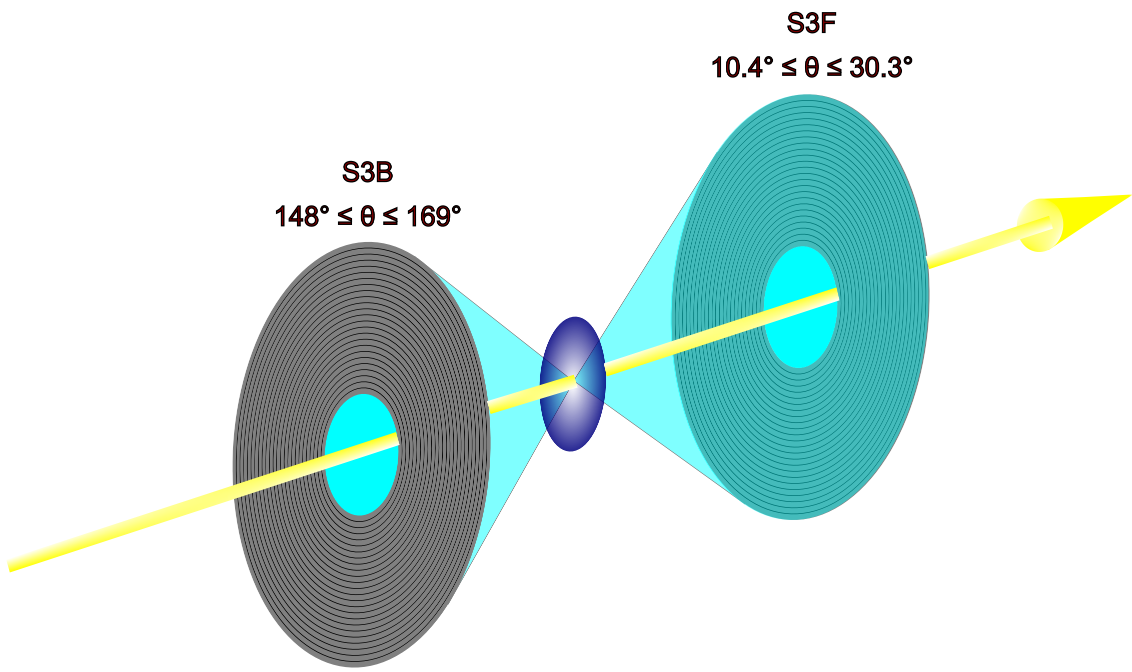

Figure 4.12: Detector geometry showing the S3B and S3F detectors; in between them, the carbon target is located at ~ 6 cm from each detector; the yellow arrow represents the direction of the carbon beam.

4.2.1.1 Calibration

For the calibration of the silicon detectors, a triple α source was used given its well-known and defined energy peaks. The source consists on 3 radioactive elements, ^{239}Pu, ^{241}Am, and ^{244}Cm, which produce the energy peaks, shown in figure 4.13, at 5.15 MeV, 5.49 MeV, and 5.796 MeV, respectively [53]. The resolution for this particular DSSD detector, S3, is in the order of $\sim 0.5\%$ FWHM.

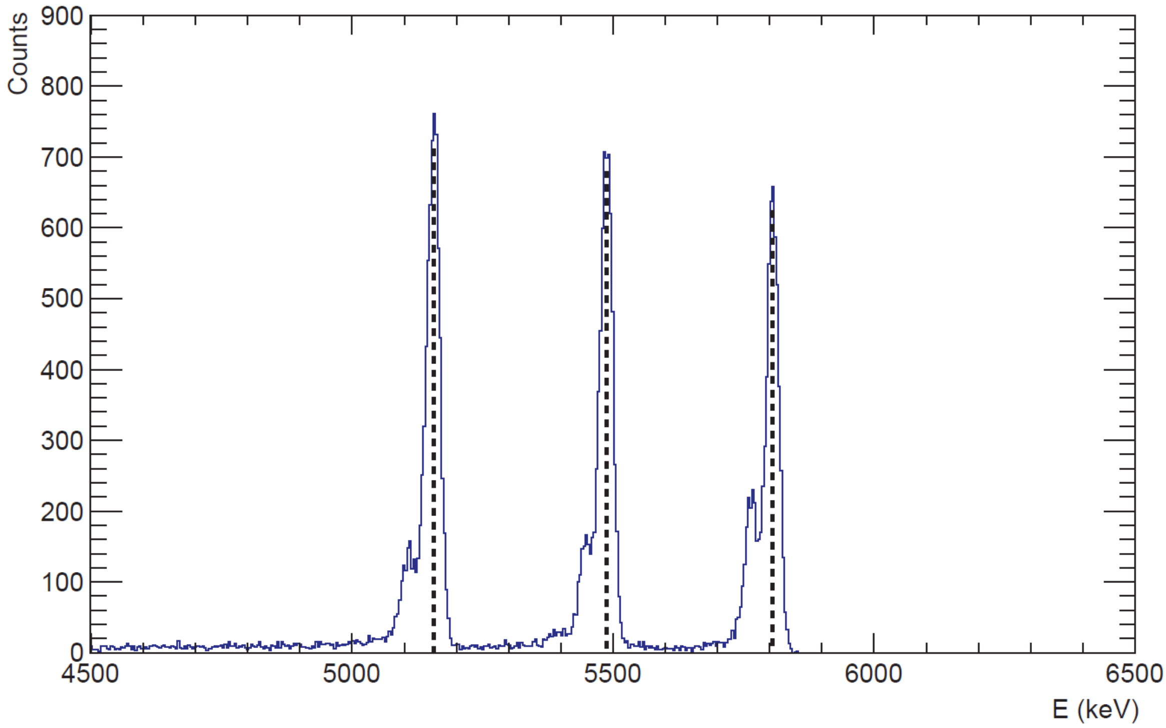

Figure 4.13: Calibrated energy spectrum obtained for a single ring of the S3 detector with a triple α source where each peak corresponds to ^{239}Pu, ^{241}Am, and ^{244}Cm, respectively.

One key aspect of the calibration was the stopping power of the aluminium foils, used as protection for the Silicon detectors, for protons and alpha particles. This was first taken into account within the STELLA collaboration by Fruet [37], and continued for this work, in which a correction factor of 0.986 to the kinematic calculations, particularly the energy at which a charged particle should be detected, was applied.

To obtain this correction factor, the National Institute of Standards and Technology (NIST) program [100] was used to calculate the stopping power in aluminium for protons and alpha particles, respectively, giving as a result the energy loss (ΔE) as a function of the incident energy of the different particles and the density of the material. Additionally, the variation of the detection response of silicon detectors due to particles of different mass for the same energy was also taken into account [63]. The aluminium foil thicknesses were 10μm for the S3F detector and of 0.8μm for the S3B detector.

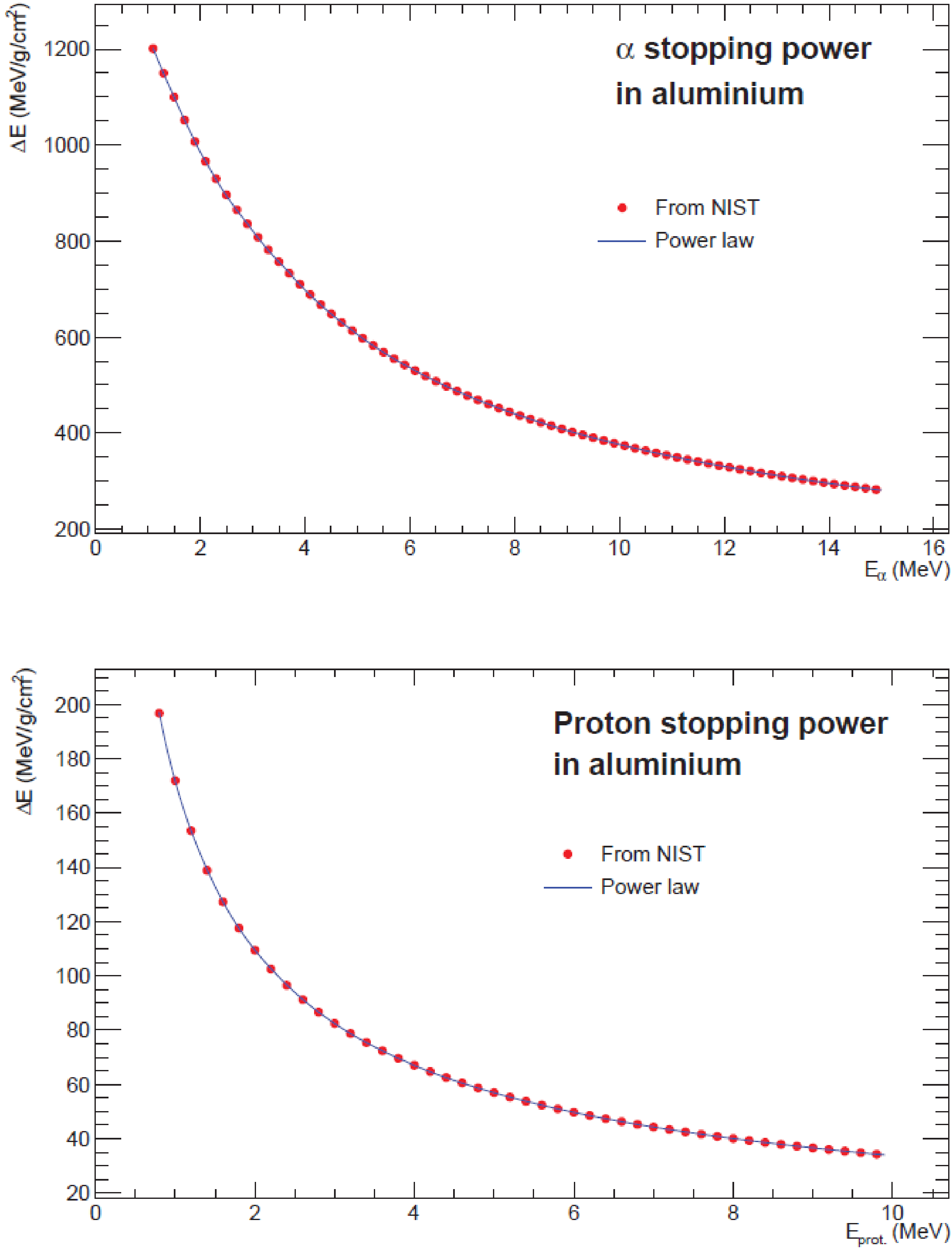

Figure 4.14: Plots of the energy loss of alpha particles (top) and protons (bottom) in aluminium. The dots represent the values obtained from the NIST program and the line is the fitted power law function. Taken from [37].

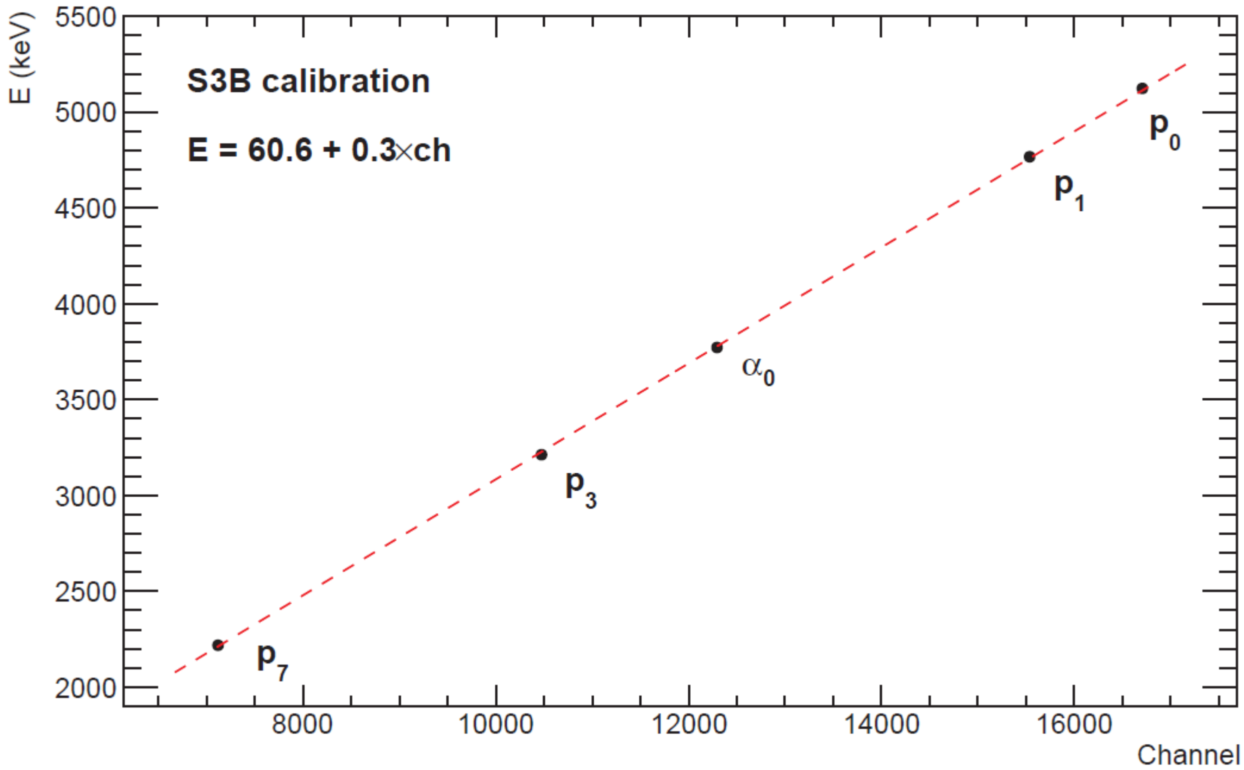

Figure 4.15: Calibration curve for a ring of the S3B detector in which the particles p_0, p_1, α_0, p_3, and p_7 are shown as dots in the plot. The dotted line is the linear function fitted. Taken from [37].

Figure 4.14 shows the loss of energy ΔE for alpha particles and protons, respectively. This was obtained thanks to the NIST program and for a different range of energies where a function of the form

$$\Delta E = a \times E^b \tag{4.2}$$

where E is the incident energy of the particle, and a and b are free parameters.

For example, a calibration curve for a ring of the S3B detector with a beam energy of $E_{lab} = 10.75$ MeV is shown in figure 4.15.

In addition to the triple α source calibration, an additional one was needed as the region energy region covered by this alpha source is in the order of ~ 5 MeV. In contrast, the kinematic calculations for the carbon fusion (see appendix A) show that the energy range for the particles expected is ~ 2 to ~ 6 MeV for the S3B backward detector and ~ 2 to ~ 15 MeV for the S3F forward detector. Therefore, an additional calibration run was made with a beam energy of $E_{beam} = 10.04$ MeV and a target of $30 \frac{\mu g}{cm^2}$, where angular spectra were obtained as shown in figures 4.16 and 4.17. The discussion regarding the targets used for this experiment will be presented further in this chapter.

The red lines correspond to the kinematic calculations for protons and the black lines are associated with α particles. Furthermore, each angle is related to a strip in the S3B and S3F detectors.

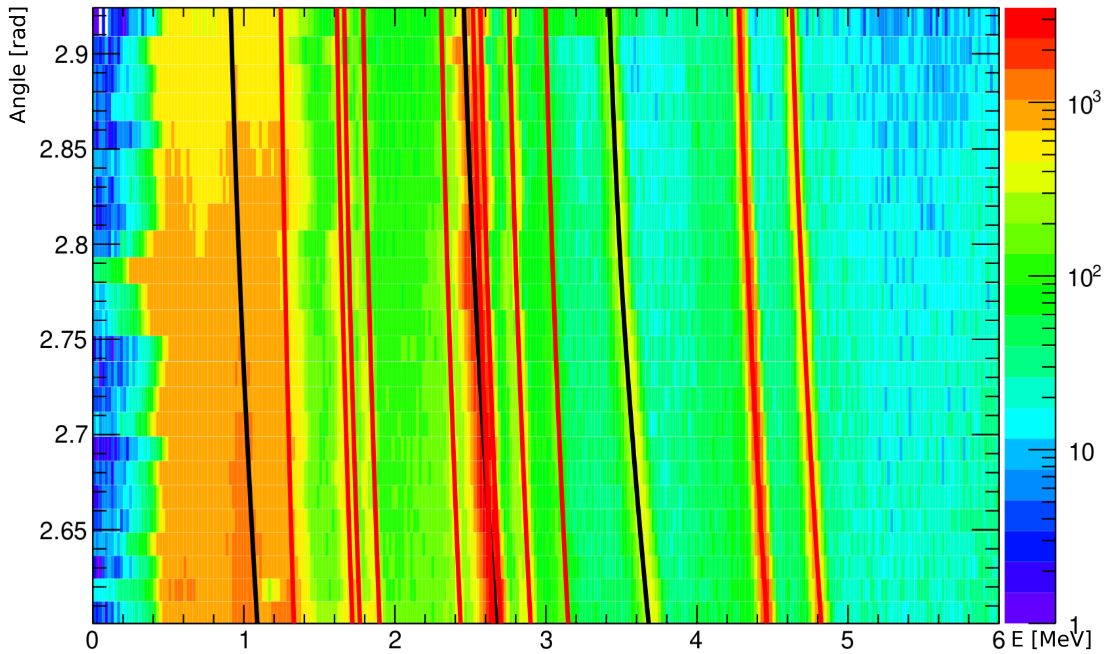

Figure 4.16: 2D angular spectra of the S3B detector for the calibration run. The red lines correspond to the kinematic calculations for protons and the black lines correspond to the ones for alpha particles, taking into account the stopping power of the foil used to protect the detector.

This calibration process was repeated for each ring of the 2 DSSDs, the S3B detector and the S3F detector for the positions backward and forward from the target, respectively.

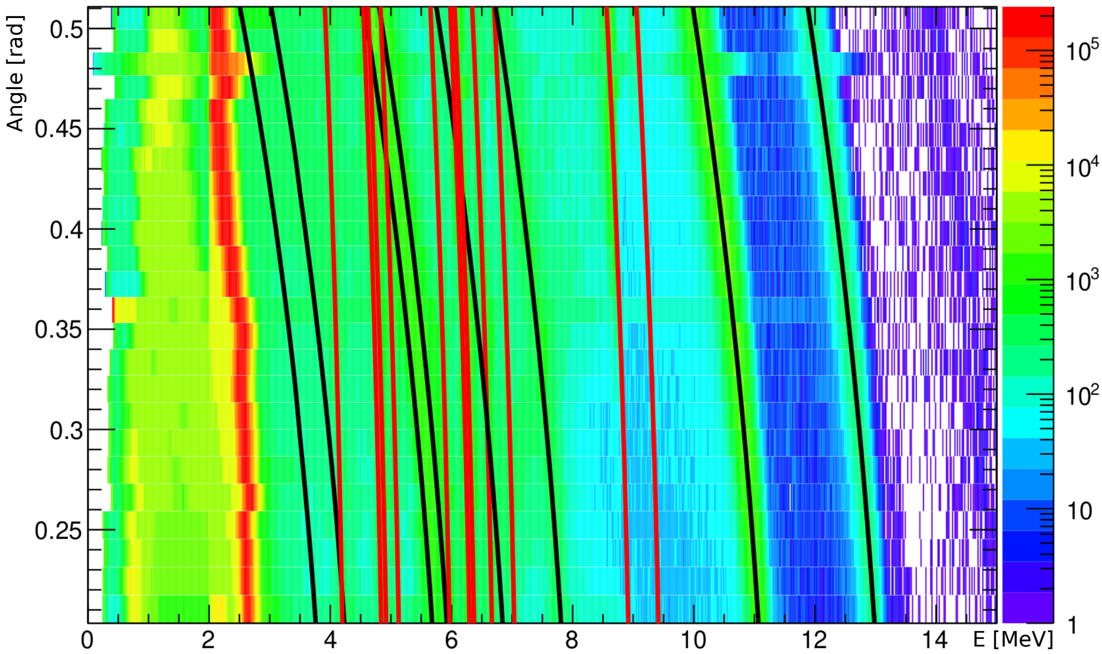

Figure 4.17: 2D angular spectra of the S3F detector for the calibration run. The red lines correspond to the kinematic calculations for protons and the black lines correspond to the ones for alpha particles, taking into account the stopping power of the foil used to protect the detector.

4.2.2 Scintillating Detectors

One of the most used types of detectors for radiation detection is the scintillating detector. Amongst other characteristics, these detectors are chosen given their fast time response with small periods of dead time, particularly, the $LaBr_3(Ce)$ detectors used in this project can work in the sub-nanosecond regime [87]; the possibility to differentiate the type of radiation interaction according to the pulse produced; and the linear behaviour of the pulse produced against the exciting energy [67].

Measuring the decay rates from nuclear excited states via gamma ray detection can shed light on the internal structure of the nucleus which will depend on the conditions before and post-decay of the spin and parity of the nucleus of interest. The mean lifetime of an electromagnetic transition will determine the value of the multipole operator that relates the initial and final quantum state for a particular decay energy [87].

The scintillation process used for the detection of radiation dates back to the early 20^{th} century.

The basic principle of operation of this type of detector is to convert the energy of an incident particle into an electric signal via a scintillating material. The scintillator will convert the energy into a light spark which at the same time will be transformed into an electric pulse thanks to a Photo Multiplier Tube (PMT).

More specifically, the scintillating material of the detector absorbs the energy of the incident radiation to convert it into a light spark of particular characteristics determined by the properties of the material. The creation of this new light spark, known as *fluorescence* or *phosphorescence*, will depend on the type of scintillating material chosen; and the main difference between fluorescence and phosphorescence is the time the material takes to generate the light spark. Fluorescence is the fastest one and consequently, has a shorter wavelength [63].
These newly generated photons will go to the cathode of the photomultiplier tube and, through the photoelectric effect, will be transformed into photo-electrons followed by their collection in the first electrode (dynode) of the PMT. Moreover, an avalanche effect takes place as the electrons pass through each dynode until the final collection of all the secondary electrons in the PMT's anode. Finally, an electric pulse proportional to the original incident radiation's energy is generated [16].

Scintillating materials can be classified as organic or inorganic scintillators and the choice of a particular one depends entirely on the most important characteristics required for the experiment; it could be the need for a fast time response, a detector resistant to radiation, a detector's specific geometry, etc.. particularly, a group of Cerium-activated inorganic scintillating crystal was used for this experiment. A more detailed discussion will be shown further on.

The further development of scintillating detectors led to the usage of *light guides* coupled to the photomultiplier given that, in certain scenarios, it is nonviable to attach the scintillator directly to the photomultiplier. The light guide's performance is based on the internal reflection of light and light losses play a key role on the determination of the ideal material to be used as a light guide. Quartz, polymethyl methacrylate and polyvinyl toluene are some examples of materials used as light guides [16]. Figure 4.18 shows roughly the process of production of an electric pulse when an incident particle interacts with the detector [48].

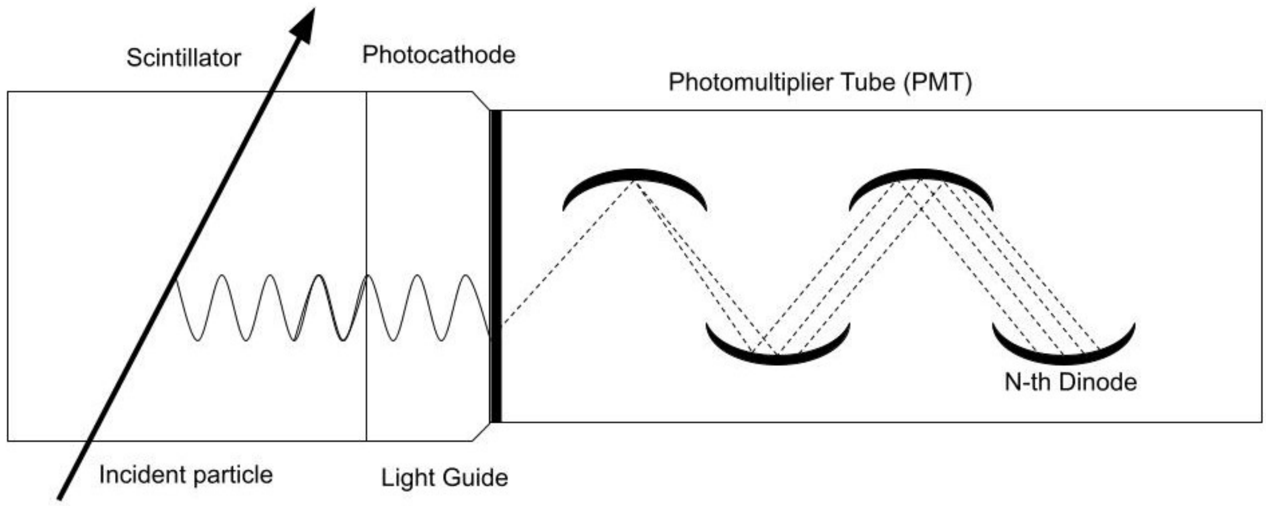

Figure 4.18: Diagram of a scintillating detector. Specifically, a scintillating crystal coupled to a photomultiplier tube using a light guide. Here, an incident particle (black arrow) interacts with the scintillator material producing a light spark (wavy line) that will be guided to the photocathode via a light guide. Then, the photocathode will produce electrons (dashed line), via the photoelectric effect, that will be captured and multiplied in an avalanche effect until the N^{th} dynode, to be finally collected in the anode with a voltage proportional to the energy of the incident particle.

For this experiment, an array of 36 Lanthanum Bromide doped with Cerium, $LaBr_3$(Ce), inorganic scintillating detectors were used. This particular type of detector is commonly used given their exceptional energy resolution, compared with other inorganic crystals, and fast decay time, amongst others[63]. However, the intrinsic self-activity of ^{138}La is one thing to consider when using these detectors [85, 46]. These detectors were used thanks to the UK FATIMA (FAst TIMing Array) collaboration.

Regis and collaborators showed that tenths of picoseconds can be achieved in timing responses with the use of $LaBr_3$(Ce) detectors and if enough statistics are collected, in coincidence mode, also picosecond lifetimes levels can be measured [89, 90, 88].

The emitted light from the lanthanum bromide crystal doped with cerium falls within the blue/UV spectrum with a maximum wavelength of $\lambda_{max} = 380$ nm [95]. Also, their timing response to radiation detection has a huge dependence on the concentration of cerium [96]. Furthermore, O. Roberts, *et al.*, have reported times in the order of hundreds of picoseconds [92] as well as P. Regan reporting sub-nanosecond times when lifetimes of excited nuclear states were measured [87].

The quick response of these detectors will be useful to discriminate between protons and alphas, measured by the DSSDs when they are used in the coincident technique.

Every disc-shaped scintillating crystal, of diameter $d = 1.5''$ and width of $w = 2''$, is coupled to each $3''$ diameter PhotoMultiplier Tube (PMT) to be encapsulated in an aluminium housing, producing a gamma-ray detector. The aluminium housing of the detector is ~ 0.5 mm on the front-facing side and ~ 2 mm. As previously mentioned, 36 of these scintillating detectors were arranged to detect the gammas produced from the carbon fusion events.

One key aspect to consider from these types of detectors is that there is the presence of radioactive isotopes, such as ^{138}La and ^{224}Ac, that will contribute to the measurements as another source of noise if it is not performed an adequate treatment.
The ^{138}La isotope has a natural abundance of 0.08881% and a half-life $T_{\frac{1}{2}} = 1.03 \times 10^{11}$ s, with decaying modes consisting on 65.5% by electron capture to ^{138}Ba and 34.5% by β emission to ^{138}Ce. This two daughter nucleus will then produce γ emissions, $E_{Ba\gamma} = 1435.8$ keV and $E_{Ce\gamma} = 788.74$ keV respectively, as a consequence of the de-excitation of the 2+ first excited state [54, 55].
On the other hand, ^{224}Ac has a half-life of $T_{\frac{1}{2}} = 2.78$ h where 90.9% of its decaying mode is via electron capture to ^{224}Ra and the remaining 9.1% via α emission to ^{220}Fr [53].
In 2005, Milbrath and collaborators showed the background contamination due to the cerium-doped lanthanum crystal detectors self-activity where 3 peaks in the gamma-energy spectra are observed within 1600 and 3000 keV [76].

The background contamination due to the $LaBr_3$(Ce) self-activity is significantly reduced thanks to the coincidence technique. Moreover, a Geant4 simulation was fulfilled by Fruet *et al.,* [37] to obtain a detector calibration that takes into account the temperature changes and their effect on the PMT's gain.

The photomultiplier tubes' signals were acquired and sorted using 1 GHz VME-based Caen V1751 cards. Further processing was made thanks to the software MIDAS (Multi Instance Data Acquisition System) and will be further discussed in section 4.4.
Regarding the detector's power supply, a CAEN multi-channel power supply module delivered $\sim$ 1000 V to the detectors.

Figure 4.19: Picture of the scintillating detectors ready to be placed on top of the reaction chamber.

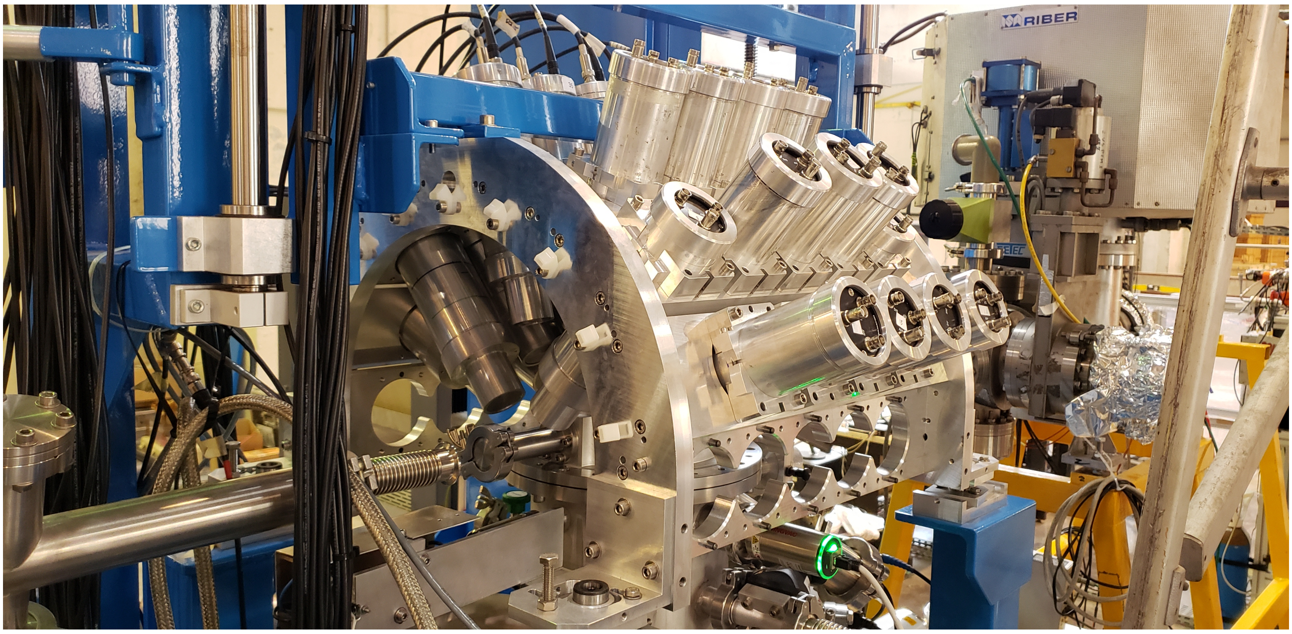

Figure 4.20: Picture of the $LaBr_3(Ce)$ scintillator detectors mounted on top of the reaction chamber.

4.2.2.1 Calibration

An ^{152}Eu radioactive source was used for the calibration of the $LaBr_3(Ce)$ detectors. This source type produces well-known gamma-ray spectra with energy peaks ranging from 120-1408 keV [53]. The source used particularly for the calibration had an activity of 330 kBq, intense enough to collect enough statistics fast enough to calibrate all the scintillating detectors.

Although the self-activity of the scintillating detectors is present in the calibrated energy spectrum of figure 4.21, it is barely distinguishable given the intense activity of the source compared to one of the detectors. Particularly, the gamma-rays related to the internal activity of these detectors have an energy of $E_\gamma = 1435.8$ keV from the decay of ^{138}La to ^{138}Ba by electron capture (branching ratio of 65.6%), and $E_\gamma = 788.7$ keV from the β^- decay of ^{138}La to ^{138}Ba (branching ratio of 34.4%) [87].

The calibrated energy spectrum, shown in figure 4.21, is the one of a single $LaBr_3(Ce)$ scintillating detector where the most prominent energy peaks are labelled with their corresponding energy. Knowing the gamma rays' energy emitted from this radioactive source, it is possible to calibrate the detectors using the correlation between channel and energy experimentally obtained from equation 4.3.

$$E = 0.04 + (1.7 \times 10^{-3} ch) + (2.2 \times 10^{-10} ch^2) \tag{4.3}$$

where ch is the channel from the uncalibrated spectrum.

From equation 4.3, the dominance of the linear term by several orders of magnitude is noteworthy

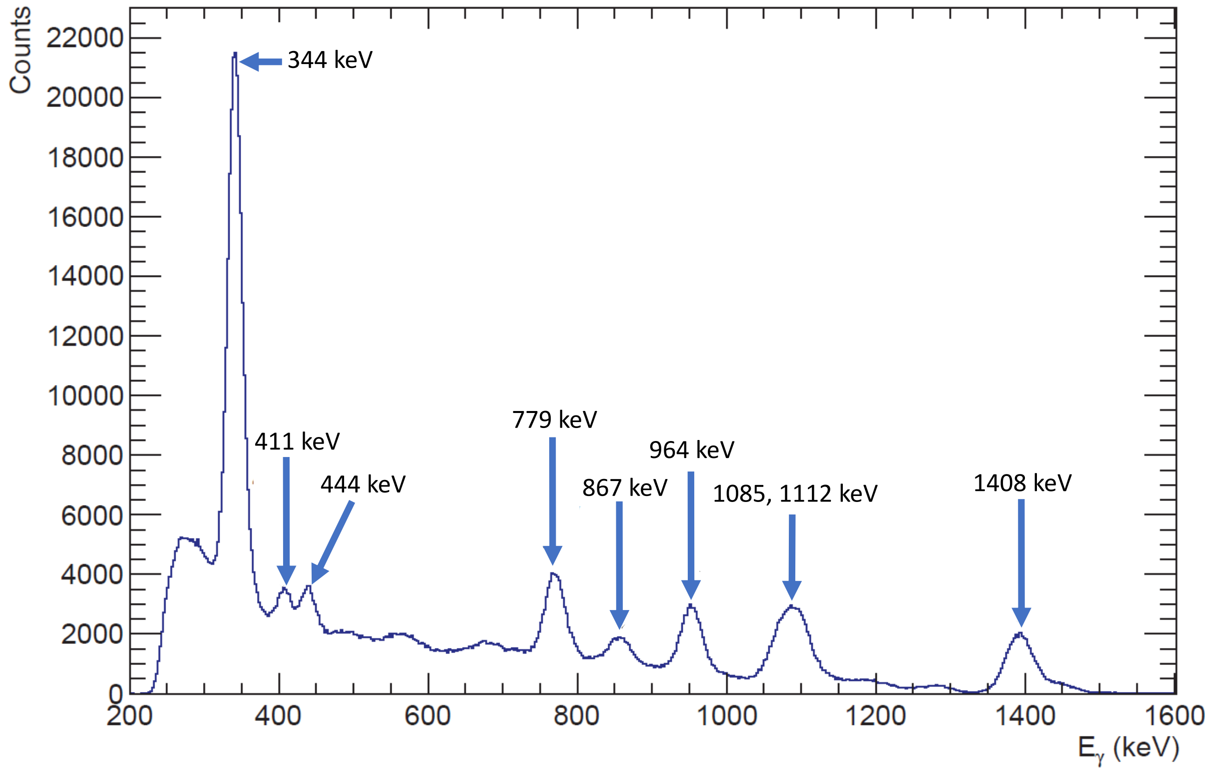

Figure 4.21: Calibrated energy spectrum for a $LaBr_3(Ce)$ scintillating detector using an ^{152}Eu radioactive source, performed by the FATIMA collaboration. This spectrum corresponds to one of the scintillating detectors and the process was analogous for the remaining detectors.

against the quadratic term. Despite of this dominance, the calibration using the non-linear calibration was performed.

In addition to the experimental calibration, a simulation for the self-activity of the $LaBr_3(Ce)$ was done using the Geant4 software and for a scintillating detector, performed by the FATIMA collaboration team. Moreover, a calibrated histogram of the simulated ^{138}La decay is shown in figure 4.22, where the peaks of 0.789 MeV and 1.436 MeV were used as key points for the calibration.

Finally, this procedure was repeated analogously for all the remaining $LaBr_3(Ce)$ scintillating detectors as part of the FATIMA collaboration.

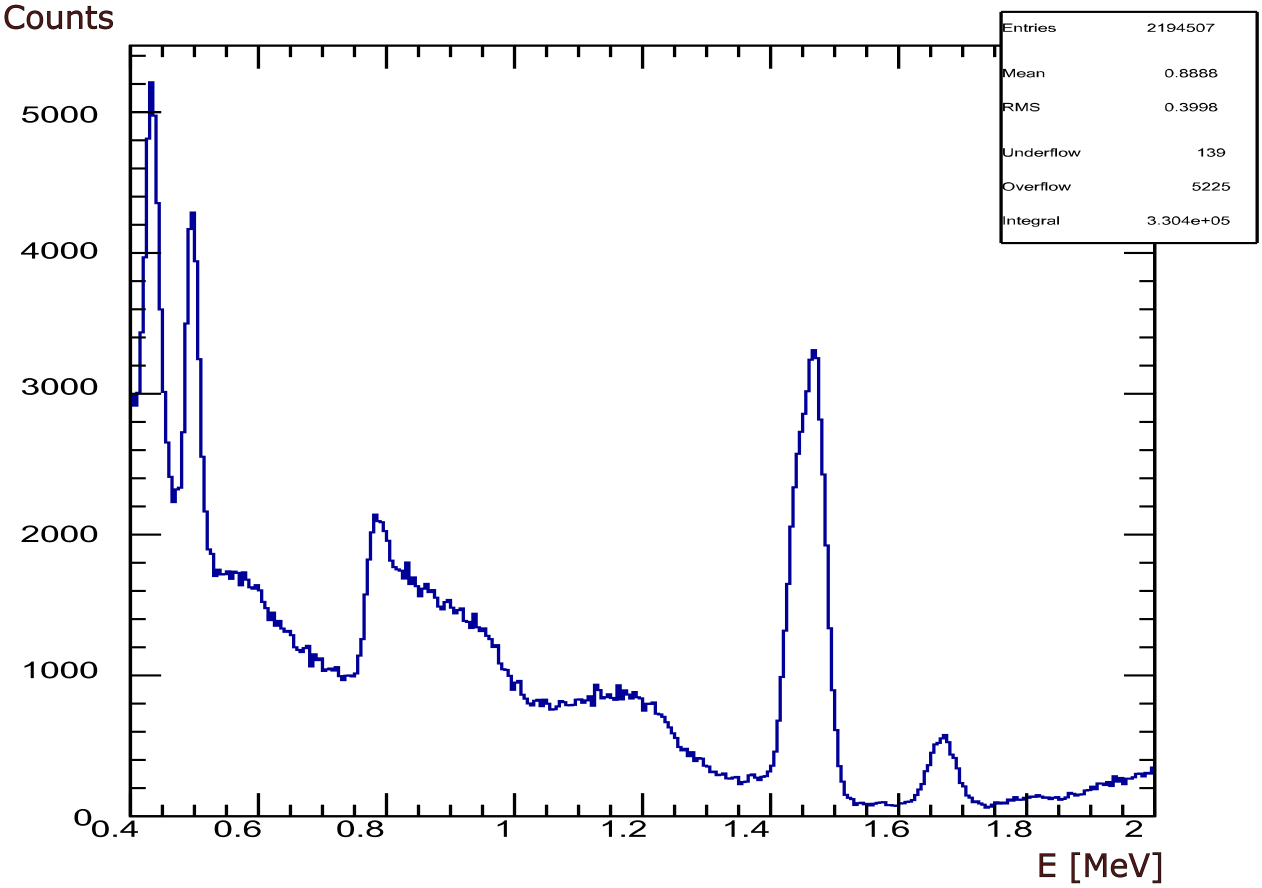

Figure 4.22: Spectrum for the simulated ^{138}La decay for one of the scintillating detectors. Taken from [37].

4.2.3 Monitors

The importance of obtaining a measurement of the scattered beam is because an absolute normalisation of the fusion cross section is needed given by equation 4.4.

$$\left(\frac{d\sigma}{d\Omega}\right)^{fus}_{lab} = \frac{N_{fus}}{N_{mon}} \left(\frac{d\sigma}{d\Omega}\right)^{diff}_{lab} \frac{\Delta\Omega_{mon}}{\varepsilon\Delta\Omega} \left[\frac{b}{sr}\right] \tag{4.4}$$

where N_{fus} is the number of fusion events, $\Delta\Omega$ is the solid angle of the detectors measuring the fusion events with efficiency ε; N_{mon} are the number of scattered nuclei by the target, $\Delta\Omega_{mon}$ the solid angle of the monitors that measured the scattered particles.

To acquire this information, two surface barrier detectors were placed at a distance of $\sim$ 23 cm from the target and forming an angle with respect to the beam axis $\theta_{mon} = 45°$ (see figure 4.6). As previously mentioned in chapter 3, this angle between the monitors and the beam axis was chosen given that at 45° the Mott differential cross-section has a local maximum regardless of the beam energy. Additionally, the surface barrier monitors were protected from the scattered ^{12}C with an aluminium collimator which has a diameter $d = 1$ mm and its aperture is placed off-centre of the monitor as to reduce as much as possible the damage received by the high counting rates and extend its life.

Taking into account the previous, the solid angle for each monitor is $\Delta\Omega = 1.38 \times 10^{-5} sr$.

To keep track of the beam intensity and beam focusing, two Faraday Cups were used along the beam-line in addition to the surface barrier monitors. One was located just before the reaction chamber and the other one was located after the reaction chamber. Alongside the Faraday cups, an Ortec current integrator [4] was used to know the number of events registered at each Faraday cup, given that the number of events is proportional to the current measured.

4.3 Targets

Carbon foil targets of densities ranging from 30 to 70 μg and diameter of 4.6 centimetres were put in a rotating target system that could hold up to 3 targets at the same time. The rotation speed of the system could reach up to 1000 rpm. However, this frequency was never achieved to prevent the carbon target from breaking. Given the fragility of the carbon foil, the beam was set to hit the target off-centre so when the target rotated, it was not hit on the same spot during the duration of each run.

A rotating target system was developed for the STELLA project in collaboration with Grand Accélérateur National d'Ions Lourds (GANIL) to avoid carbon target breakage. This is achieved by increasing the irradiation area on the target.

From the previous STELLA campaign, it was shown that thin carbon targets from around $\sim 20-75\mu g/cm^2$ which were irradiated with a carbon beam of microamperes, lasted a few tenths of minutes. For example, a fixed target of $50\mu g/cm^2$ irradiated by a 5 MeV ^{12}C with a current of $5p\mu A$ would have absorbed 1.75 W within it and the beam would have a 350 keV energy loss [37]. Hence, if the target rotates, the area of irradiation is increased and, thus, the irradiation time can be extended according to the requirements of the experiment.

As shown in figure 4.23, the target rotating system is capable of holding 3 rotating targets in addition to a 4^{th} section that can hold another 6 smaller fixed targets. However, the fixed targets were not used in the campaign related to this work.

The carbon targets used were manufactured at GANIL and were made of graphite. The final thin

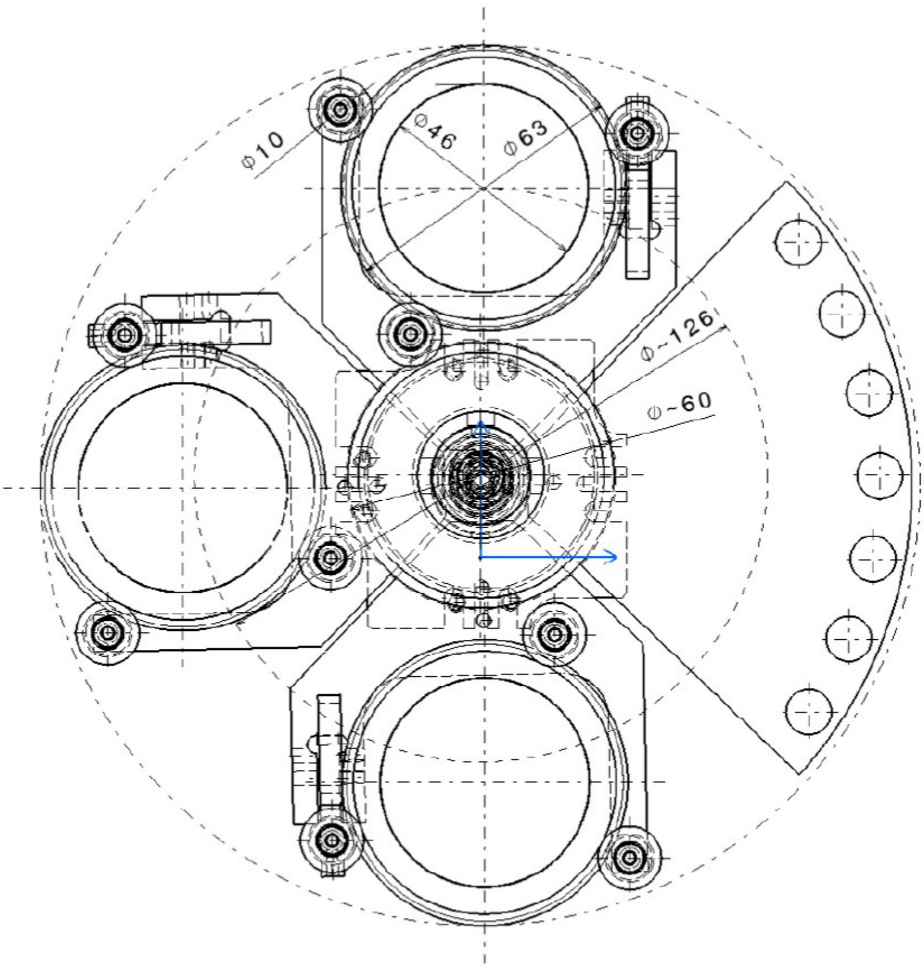

Figure 4.23: Sketch of the rotating target system. At the centre of the sketch, it is possible to observe the central bearing that, coupled to the motor, will rotate and, consequently provide motion to the targets. The upper, lower, and left side of the sketch shows the carbon target frames placed within the 3 smaller bearings connected to the central bearing. The frame for the 6 fixed targets is shown on the right side of the sketch; it has 6 openings to place small targets on it, in addition to a central opening which is left empty for beam focusing purposes. Measures are in millimetres.

circular carbon foils have densities from 30 $\mu g/cm^2$ to 75 $\mu g/cm^2$ and were placed in the 46 mm diameter circular frames. As well as with the monitors, the carbon targets were placed in a position such that the carbon beam does not hit the centre of the target but $\sim$ 5 mm apart from the edge of it. Then, the targets were placed on the three metal bearings from the rotating system that will rotate the carbon frames thanks to the central bearing. The central bearing external side has an elastomer seal that will produce the rotation of the smaller bearings thanks to the friction between them. Moreover, the central bearing is magnetically coupled (UHV Design Ltd. [106]) to a motor outside the reaction chamber capable of reaching rotation speeds of $\geq 1000 rpm$. In addition to the energy loss of the beam on a fixed target, its rotation will reduce the carbon thickening effect [17].

The rotating system was designed as a technique to avoid the breakage of the target, and at the same time, it avoids carbon build-up securing the original carbon target properties for as long as possible. Previous studies of the temperature and energy dissipation in the target were performed by solving the Stefan-Boltzmann equation for net heat loss by radiation as a function of time [37], given by equation 4.5.

$$P_{rad} = \varepsilon \sigma S (T^4 - T_t^4) \tag{4.5}$$

where $\varepsilon = 0.8$ is the emissivity, σ the Stefan-Boltzmann constant, S the irradiated surface during one rotation, $T = 20°$ C the temperature of the environment, and T_t the target temperature.

It was found that the most important factors in the temperature increase and dissipation were the beam size in the target and the rotation speed, respectively. The study fixed values for P, such as 1, 2, and 3 W, varied the beam diameter, and calculated the target temperature T_t, having as a result that for rotation speeds of 1000 rpm and beam diameter of $\sim$ 2mm the target temperature will not rise above 1000° C. This will prevent the target from breaking and avoid carbon build-up.

In conclusion, this off-centre positioning of the target combined with the target rotation increases the target's useful life because the carbon beam takes one target's rotation to hit the same spot twice, allowing it to have an increased impact surface and prevent its rupture and carbon build-up.

Figures 4.24a, 4.24b, 4.24c, show different stages of the carbon mounting process. Fig. 4.24a, shows the targets mounted in the frames ready to be placed within the small bearings, protected with plastic envelopes; in fig. 4.24b, the target is mounted; and in fig. 4.24c, the target is placed and ready with the S3F detector.

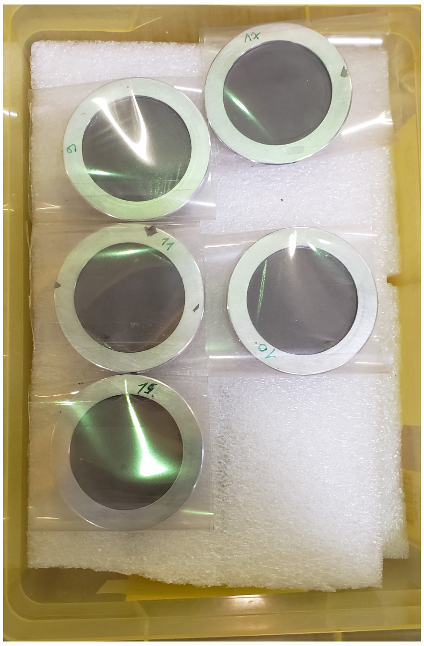

(a) Samples of the carbon foils used as targets.

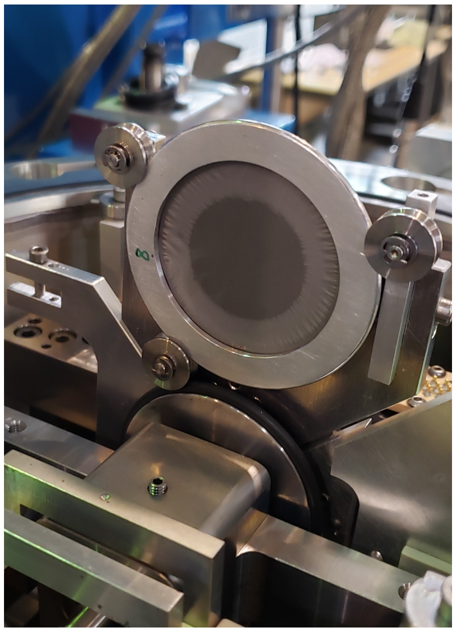

(b) Carbon target mounted on the rotating frame inside the reaction chamber.

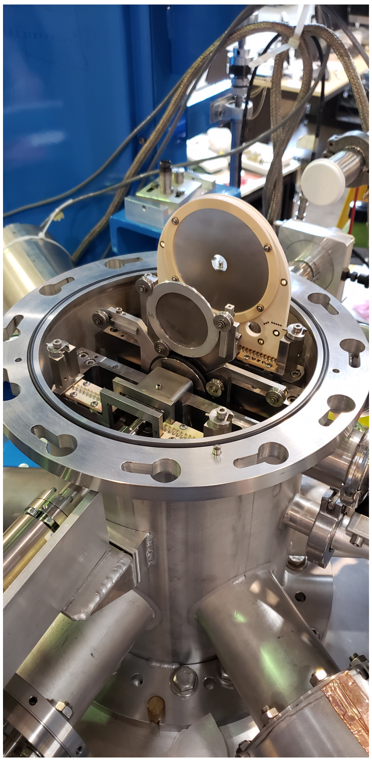

(c) Carbon target alongside the S3F detector inside the reaction chamber.

Figure 4.24: Targets

4.4 Acquisition System

The Digital AcQuisition (DAQ) system used for this experiment was developed in collaboration with the "Measurements and Acquisition Systems" at IPHC, and consisted of two parts: firstly, the STELLA DAQ, regarding the acquisition of the α particles and proton signals using DSSD detectors; and on the other hand, the FATIMA DAQ for the gamma-rays detected employing the $LaBr_3$(Ce) scintillating detectors. Coincidences between the evaporated charged particles and gamma-rays were obtained to reduce the background noise on the energy spectra.

The photomultiplier tubes' signals were acquired and sorted using 1 GHz VME-based Caen V1751 cards. Further processing was made thanks to the software MIDAS (Multi Instance Data Acquisition System) [75].

The charged particle detection system consists of 96 channels connected to 8 FMC112 cards and grouped into 4 FC7 AMCs (Advanced Mezzanine Card) [83] having 12 channels per card. The communication between this and the control room computer was made using a TNT (Tracking Numerical Treatment) corpus based interface [9]. This interface grants single signal analysis as well as time-stamped signal acquisition. Not only these FC7 cards were connected to the DSSDs, but also to the monitors and the Faraday cups.

This system is controlled via an Ethernet connection to a μTCA (micro Telecommunications Computing Architecture) module containing all the acquisition cards, having a graphic interface in which energy and oscilloscope mode can be displayed.

Both VME-based and μTCA accept external clocks and triggers to synchronize.

Furthermore, GLIB (Gbit Link Interface) card from the STELLA crate provides a reference synchronization signal between the clocks of STELLA and FATIMA with nanosecond precision [107]. A 125 MHz signal is generated on the STELLA DAQ and then sent to the FATIMA DAQ for clock synchronization. The sampling rate per channel of the FATIMA DAQ of 1GHz/10 bits; the one for STELLA DAQ was 125 MHz/14bits [47].

A more detailed explanation of the triggering system and synchronisation between the STELLA and FATIMA DAQs will be done in the upcoming sections.

4.4.1 Trigger System

For the DSSD's signal, a trigger system for recording their signals once a gamma particle is detected in the scintillating detectors was employed and, consequently, a fast coincidence detection method was implemented.

Typically, triggering systems are designed by setting a threshold for the output signal of the preamplifier, and if it's reached, start the recording of the silicon detector's signals. However, to avoid baseline signal fluctuations in addition to the long decay time of the preamplifier output, a method developed by Jordanov and Knoll was implemented [60].

In the first place, the signal is differentiated by getting the received signal delayed and obtaining the difference with the original one; followed by an integration over a defined number of samples. Thus, the triggering process now would be done using the integrated and differentiated signal rather than with the amplitude of the raw signal, see figure 4.25. This method was developed for the processing of signals with exponential decay, such as the ones of this semiconductor detectors, and transforming them into trapezoidal-shaped signals as shown in figure 4.26. The parameters of the trapezoid such as the plateau height, width, and rise time can be manipulated through the graphic interface of the system.

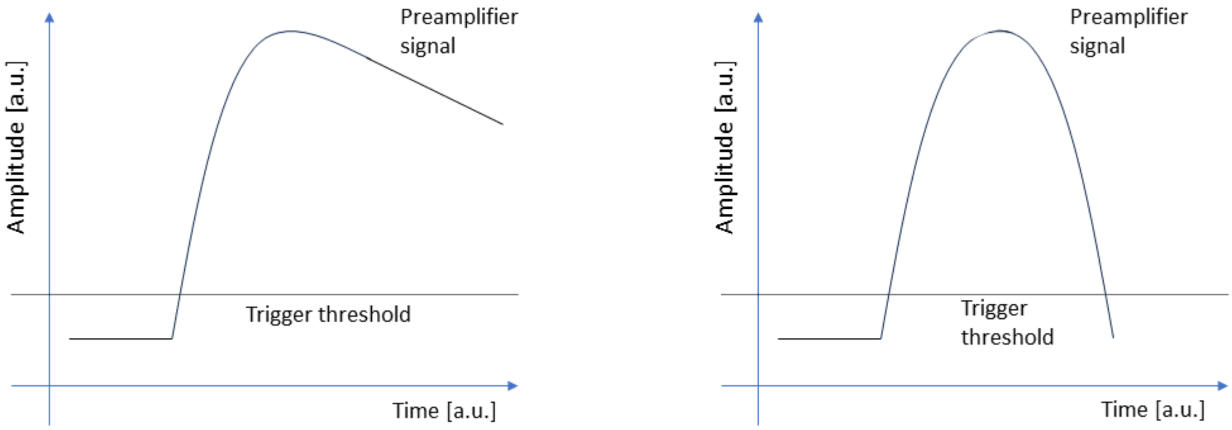

Figure 4.25: On the left side, it is shown a signal obtained from the preamplifier that passed the trigger threshold. On the right side, the modified signal which is first differentiated and then integrated, before comparing it to the triggering threshold.

Another advantage of this method is that the acquisition dead time is reduced given the trapezoidal shape, allowing sampling rates of tenths of nanoseconds.

4.4.2 Synchronising FATIMA and STELLA

The μTCA module is connected to the GLIB (Gigabit Link Interface Board) [107] which will synchronise the 4FC7 cards from the STELLA DAQ with a 10 MHz clock. Then, the FC7 cards send a sinusoidal signal of 125 MHz to the 8 FC112 cards. Each one of the FC112 will transmit this 125

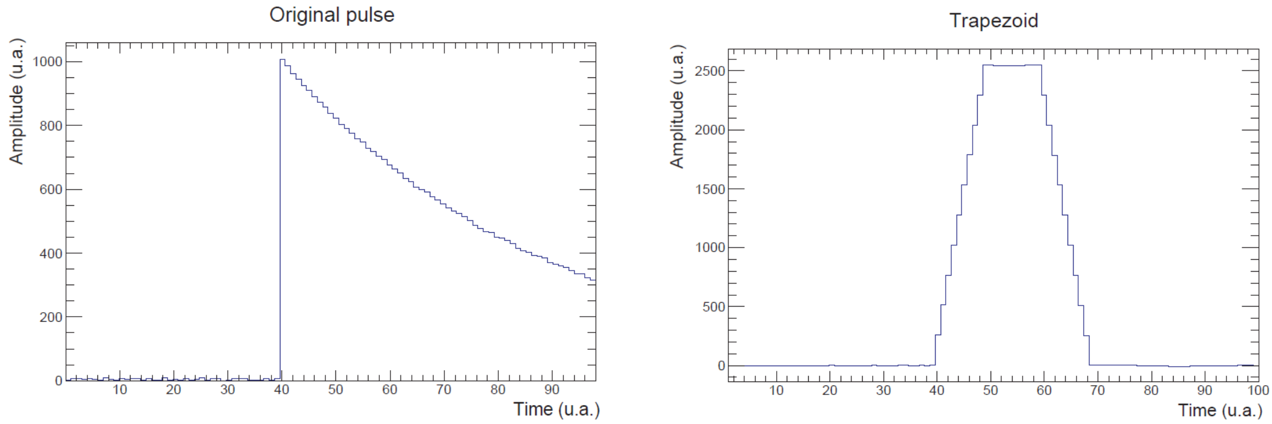

Figure 4.26: Example of an exponential raw signal (left) and the same signal after applying the Jordanov and Knoll method. Image taken from [37].

MHz signal to the 5 V1751 cards from the FATIMA DAQ that are connected in way in which the V1751 share the same clock. Thus, both acquisition systems would share the same clock, see figure 4.27.

In the event of a time delay between STELLA and FATIMA internal clocks, a synchronisation signal would be generated to re-synchronise both clocks (a more detailed discussion will be done in chapter 5. Moreover, this process was repeated every 30 minutes to check if there was a time delay in addition to the fact that the synchronisation signal could be generated manually through the graphic interface.

From previous experiences with this system, information regarding the channel number that triggered the acquisition, amplitude, and a time stamp from the said signal, as well as having a special section within the data recording disks for events that are not in the established range of $\pm$2V or that accumulate too fast (pile-up), is possible to obtain and it proved to be reliable and stable throughout the experimental campaign.

In conclusion, for the STELLA DAQ 4 FC7 were available, and 5 V1751 modules for FATIMA's signal processing resulting in 96 channels for the evaporated charged particles and 38 channels for the gamma detection. However, not all the channels were used since they were not needed. The experiment just required 24 signals for each DSSD and 36 for the $LaBr_3$(Ce) detectors.

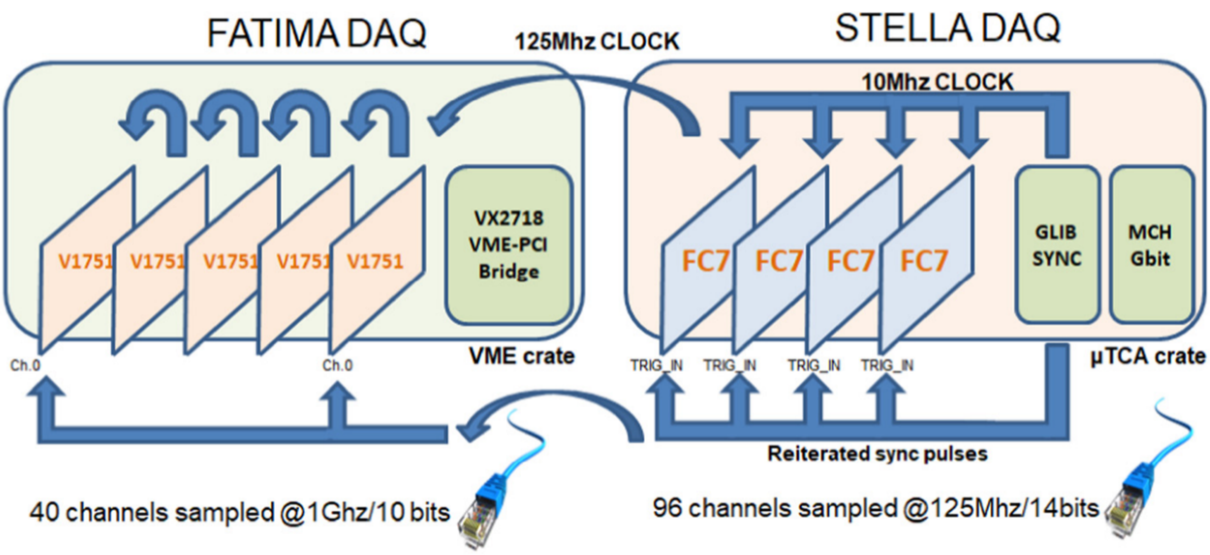

Figure 4.27: Representation of the synchronisation between the STELLA DAQ and the FATIMA DAQ. The GLIB sync is also responsible for the distribution of the synchronisation signal when a time delay occurs. Figure taken from [47].

Chapter 5

Results and Discussion

5.1 Energy Spectra

To illustrate the difference between using and not using the coincidence method, an angular distribution plot regarding the reaction d(^{12}C,p)^{13}C is shown in figure 5.1, where a cleaner plot is produced using coincidence method (top) compared with the one without it (bottom). This also affects the energy spectra plots as it will be shown further in this chapter.

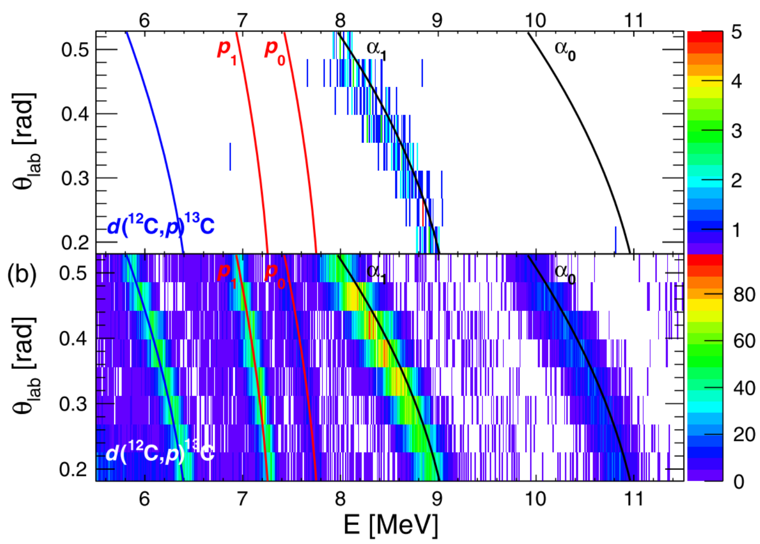

Figure 5.1: Angular charged particle spectra for the ^{12}C fusion at an energy of E_{rel} = 3.77 MeV. The spectrum on top is for coincident events with a 1634 keV gamma ray and the one at the bottom corresponds to a spectra taken without a coincident event. Taken from [36].

As mentioned in chapter 4, the data obtained from the gamma-particle coincidence technique for this experiment was using a beam energy of E_{beam}=5.07 MeV, and the Carbon ions were in a 3+ charge state.

The first plots shown are the charged particle spectra from each one of the 24 rings of the backward and forward silicon detectors, respectively. The plots shown of figures 5.2, 5.3, 5.4, 5.5, 5.6, and 5.7 correspond to the backward detector; figures 5.8, 5.9, 5.10, 5.11, 5.12, and 5.13 show the plots of the forward detector. All of the plots previously referenced have arbitrary units on the x-axis and counts on the y-axis, as well as a peak finder mark in very early stages and that would be further corrected. This peak marker can also make the distinction between the evaporated charged particles, alphas or protons, and works based on the kinematics calculations. See Appendix A for more details. The black markers correspond to the alpha particles and the red ones correspond to the protons, both products of the carbon fusion. Alpha particles are related to the Neon exit channel and the protons to the Sodium one.

It is important to mention that “det 1” corresponds to the outermost ring of the annular DSSD, “det 2” is the second outermost ring, and so on until “det 24” that is the ring closest to the centre of the detector. From this point forward, the number of the detector will correspond to the ring following the convention previously stated.

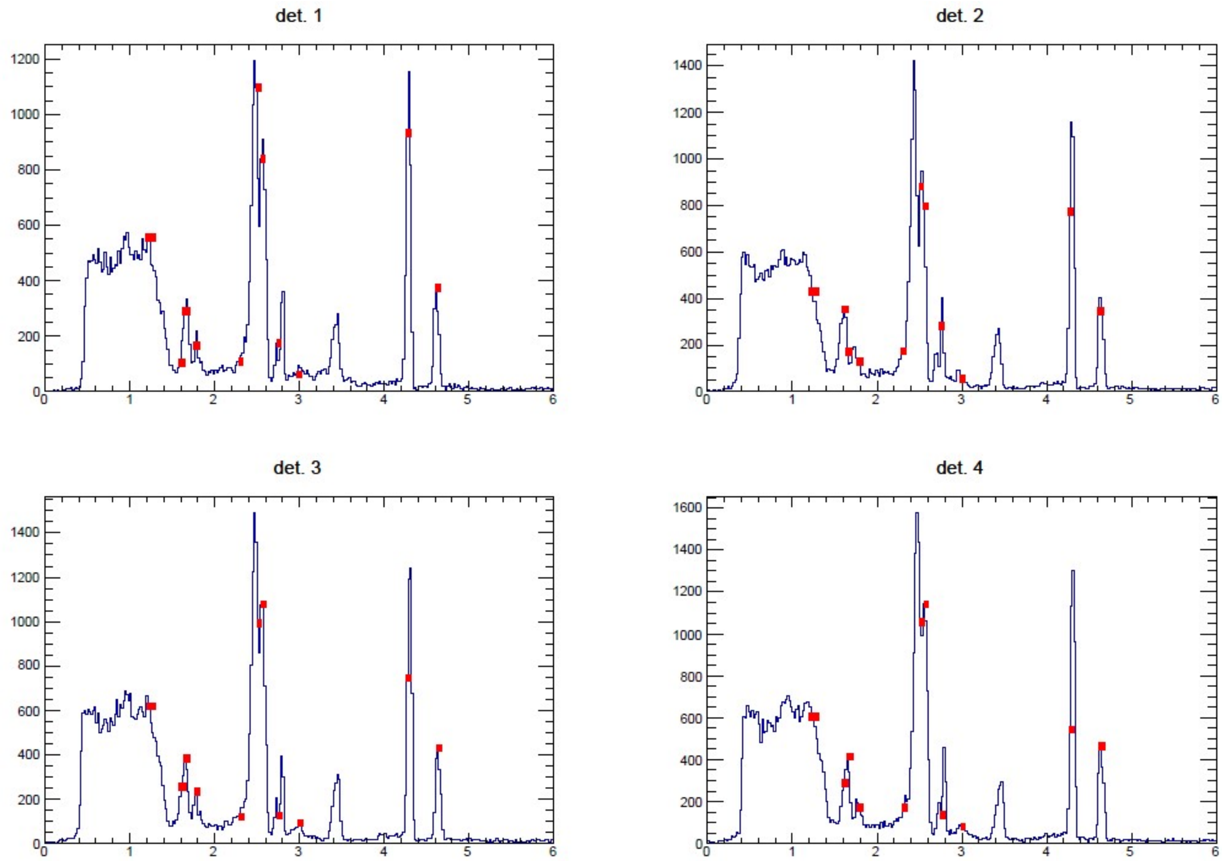

Figure 5.2: Charged particle single spectra taken for rings 1-4 of the backward detector with a rudimentary peak finder marker. The black markers correspond to alpha particles whereas the red ones to protons.

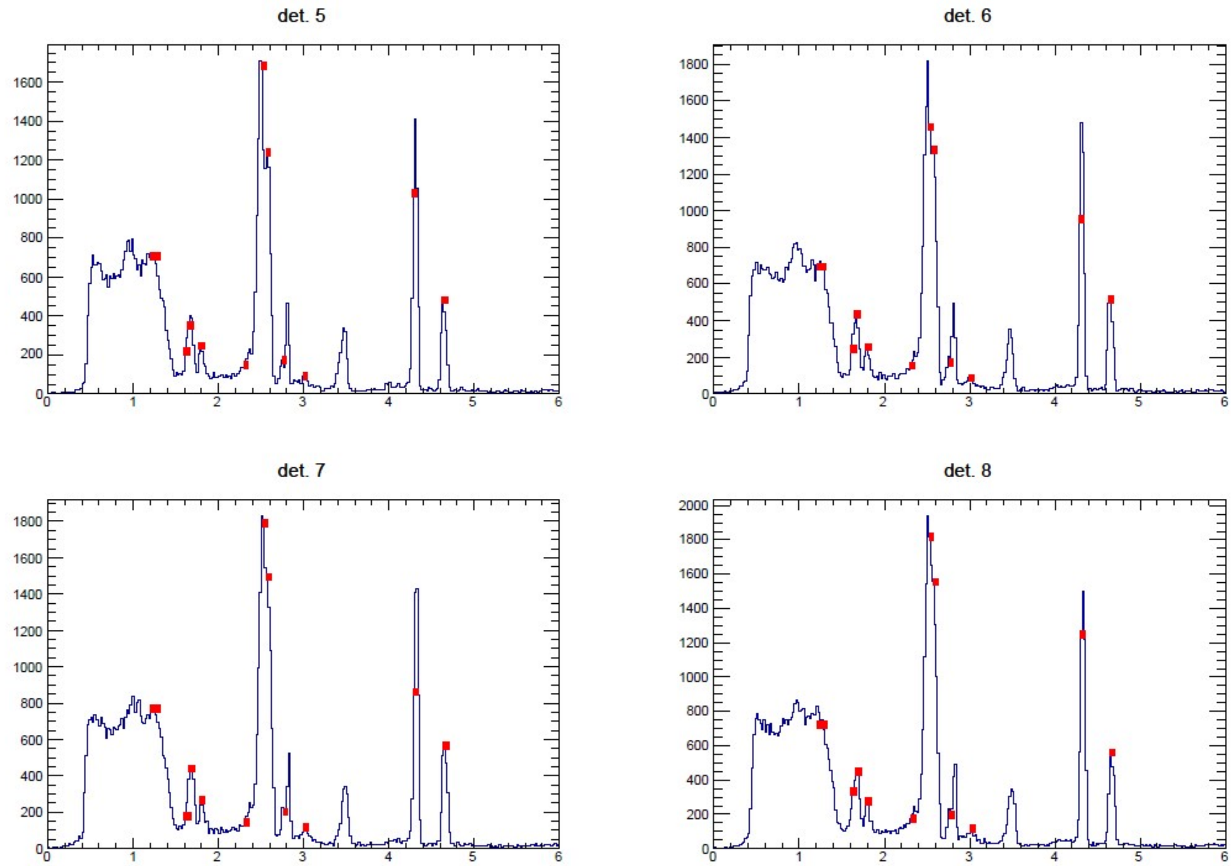

Figure 5.3: Charged particle single spectra taken for rings 5-8 of the backward detector with a rudimentary peak finder marker. The black markers correspond to alpha particles whereas the red ones to protons.

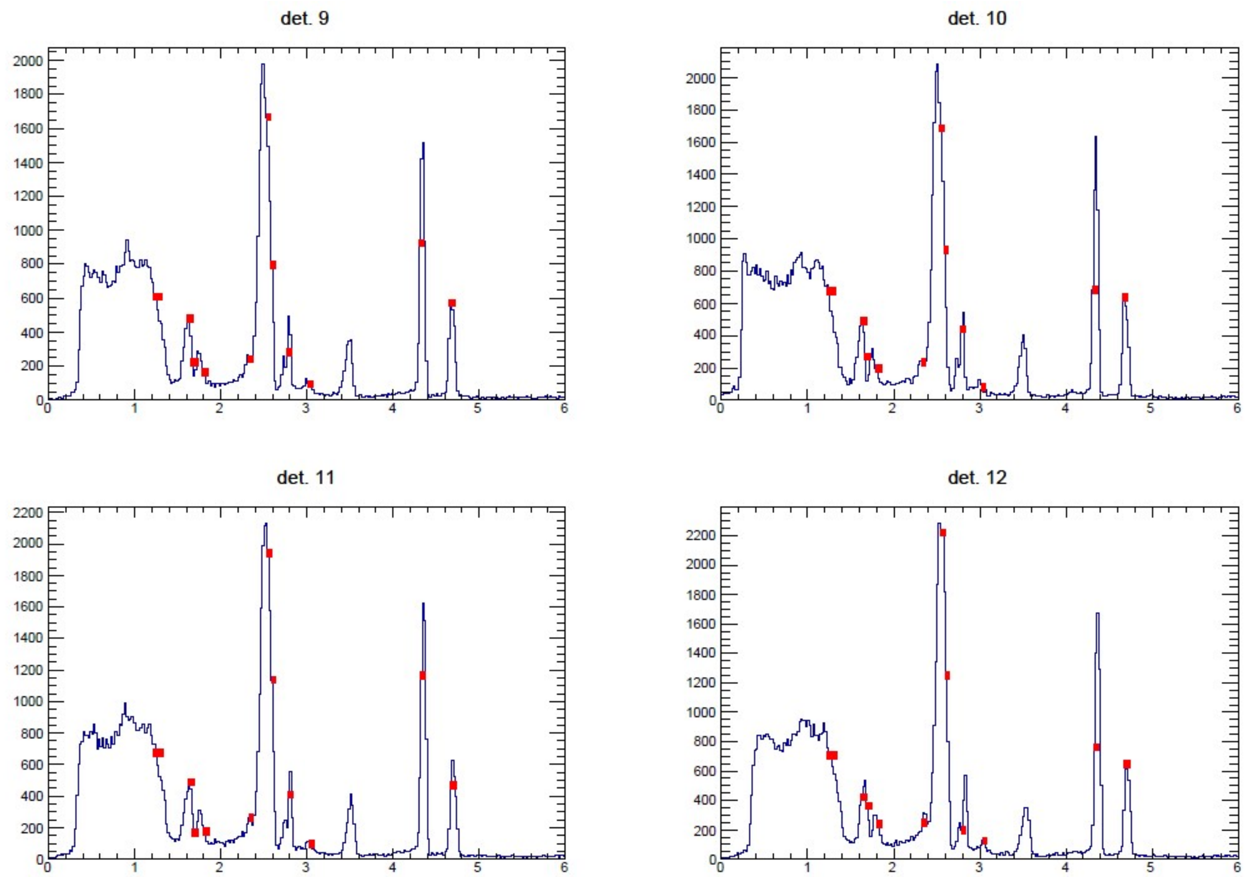

Figure 5.4: Charged particle single spectra taken for rings 9-12 of the backward detector with a rudimentary peak finder marker. The black markers correspond to alpha particles whereas the red ones to protons.

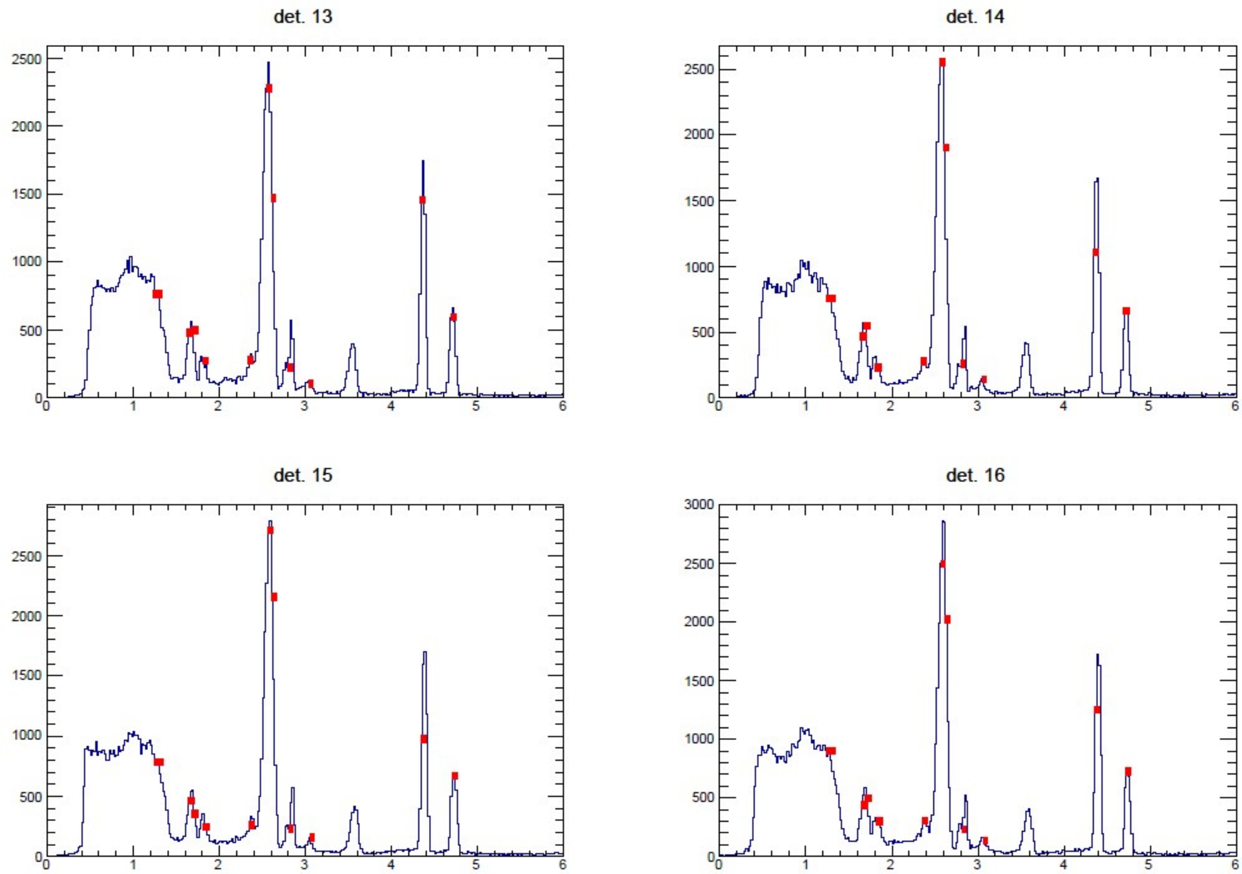

Figure 5.5: Charged particle single spectra taken for rings 13-16 of the backward detector with a rudimentary peak finder marker. The black markers correspond to alpha particles whereas the red ones to protons.

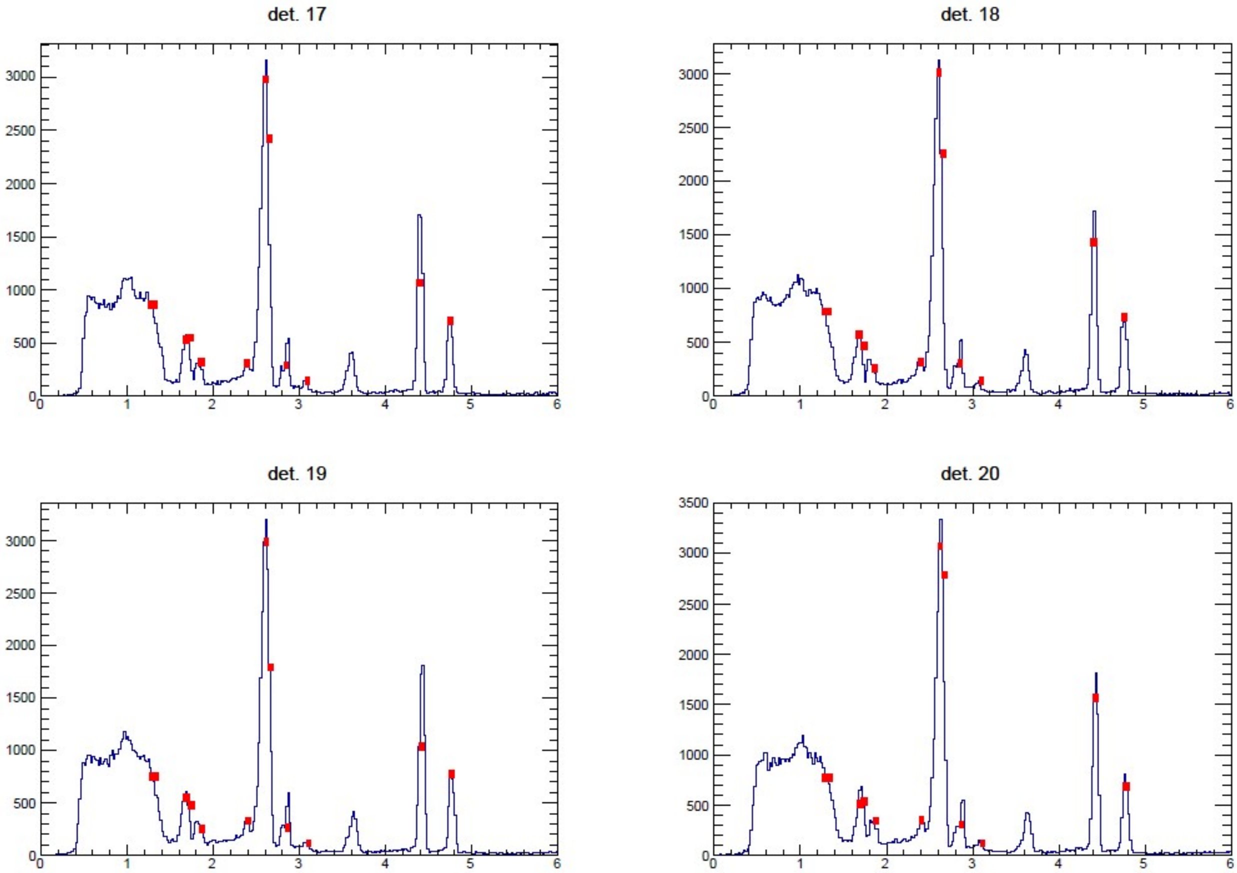

Figure 5.6: Charged particle single spectra taken for rings 17-20 of the backward detector with a rudimentary peak finder marker. The black markers correspond to alpha particles whereas the red ones to protons.

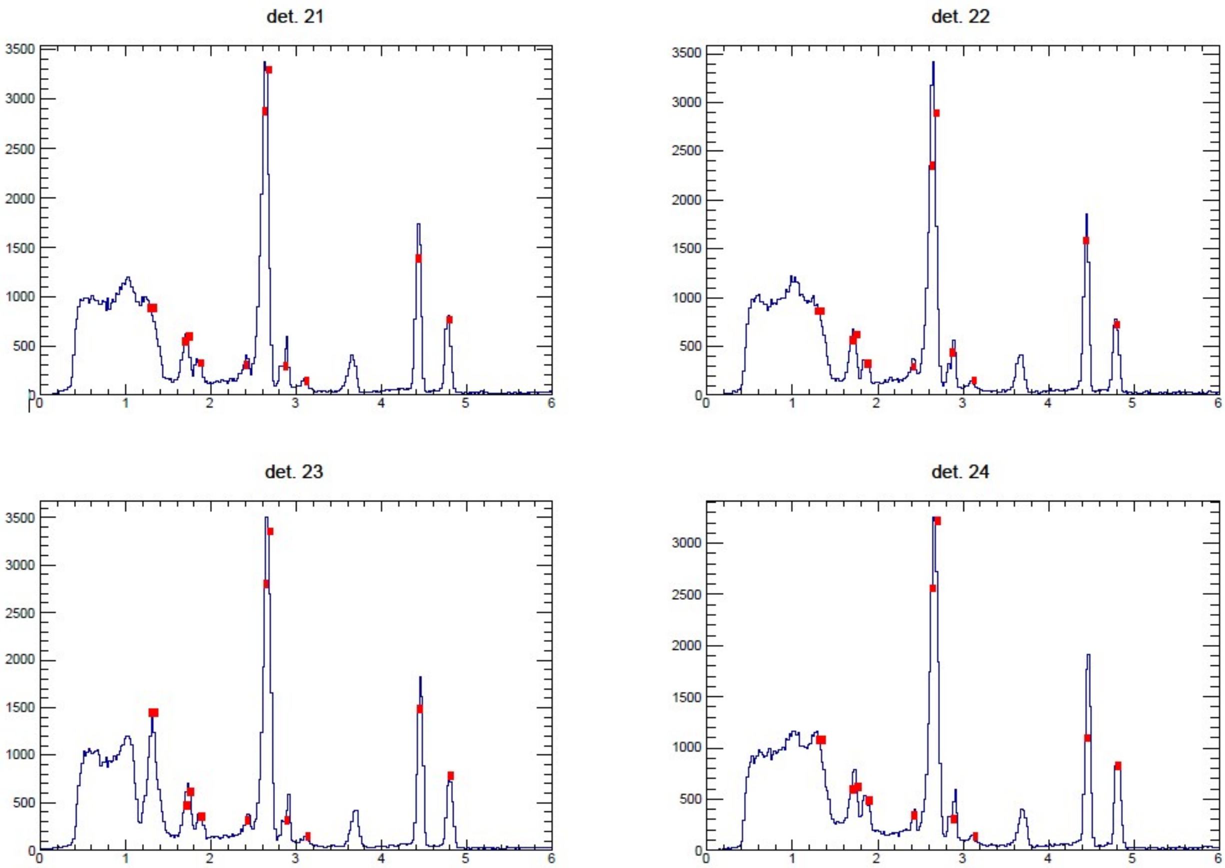

Figure 5.7: Charged particle single spectra taken for rings 21-24 of the backward detector with a rudimentary peak finder marker. The black markers correspond to alpha particles whereas the red ones to protons.

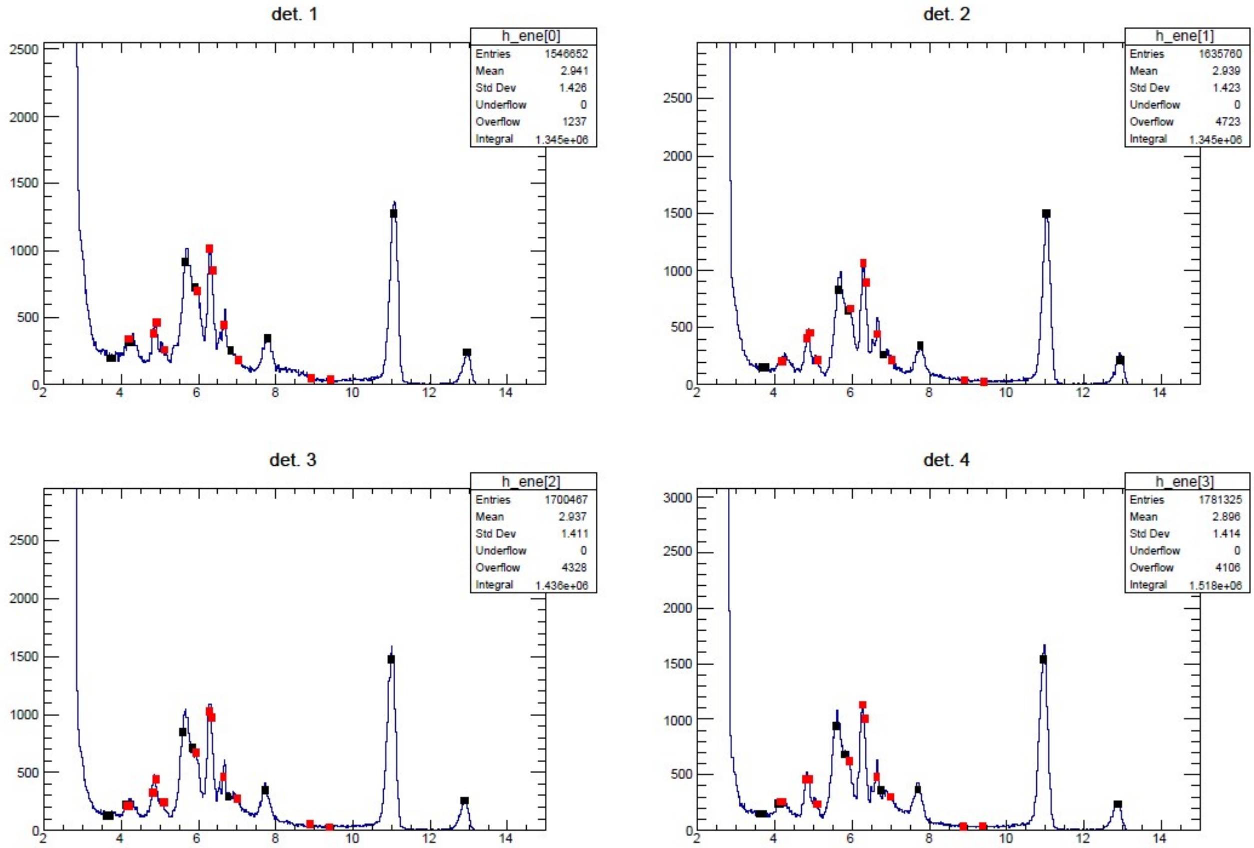

Figure 5.8: Charged particle single spectra taken for rings 1-4 of the forward detector with a rudimentary peak finder marker. The black markers correspond to alpha particles whereas the red ones to protons.

From the spectra obtained from the forward detector, it is noticeable that the highest energy ones are the cleanest ones in terms of background contamination, almost negligible and there is not an overlapping of peaks of the charged particles. There are several things worth mentioning from the spectra of figures 5.8, 5.9, 5.10, 5.11, 5.12, and 5.13. The 2 highest energy peaks correspond to α particles, before these peaks, protons start to appear on the spectrum and a collection of peaks is notorious when the background becomes perceptible. Some peak markers of protons and alphas appear on what is plotted as a single peak. However, further on the analysis and thanks to a linear combination of the functions that will be used to make the peak fitting, the distinction of the particles is possible and the mean of the peak, integral, and sigma of the fittings are obtained.

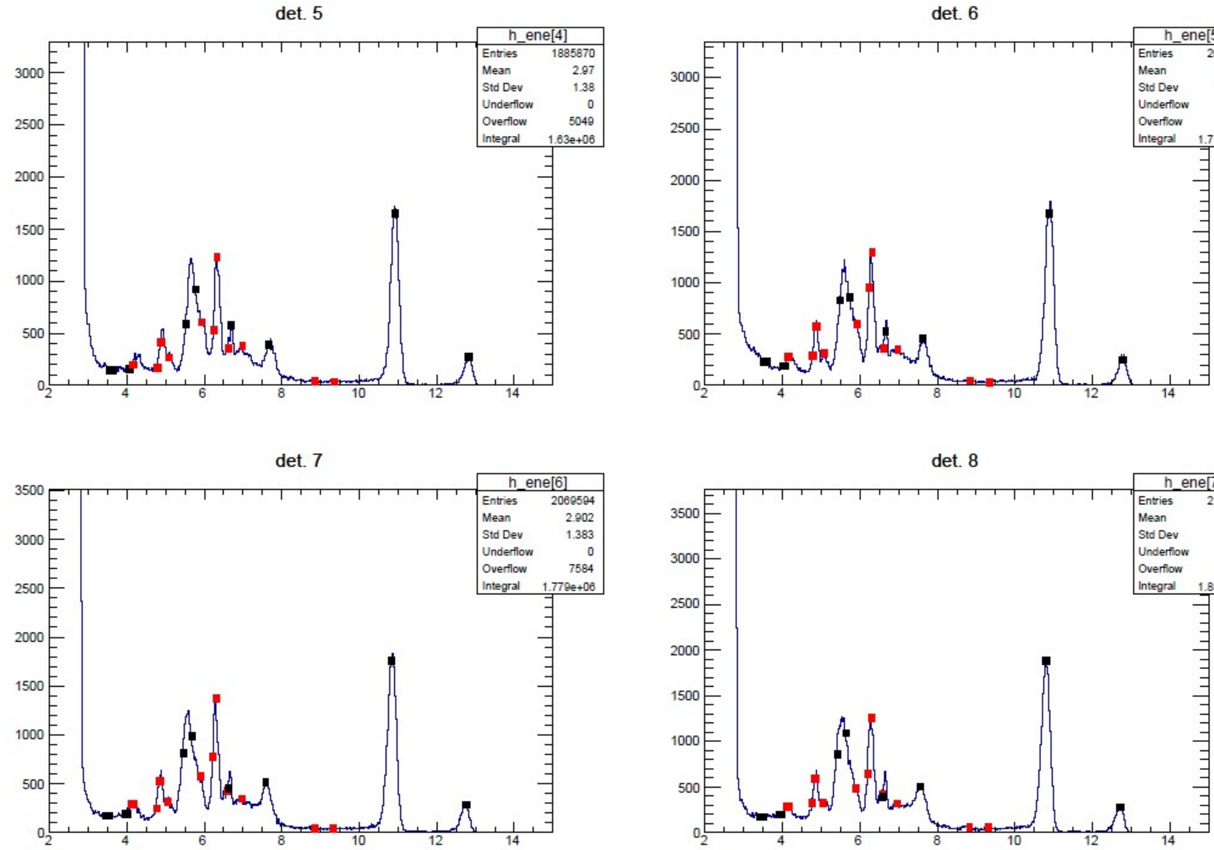

Figure 5.9: Charged particle single spectra taken for rings 5-8 of the forward detector with a rudimentary peak finder marker. The black markers correspond to alpha particles whereas the red ones to protons.

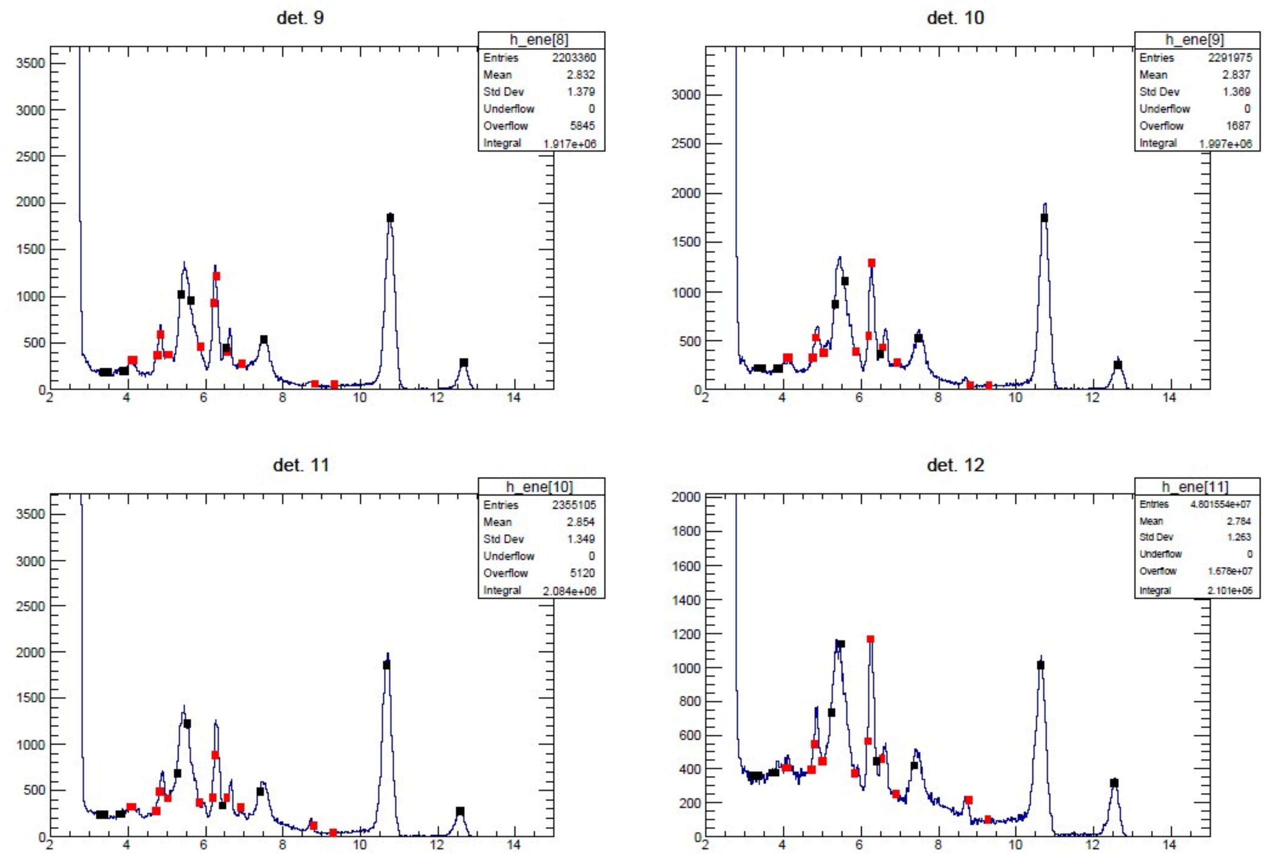

Figure 5.10: Charged particle single spectra taken for rings 9-12 of the forward detector with a rudimentary peak finder marker. The black markers correspond to alpha particles whereas the red ones to protons.

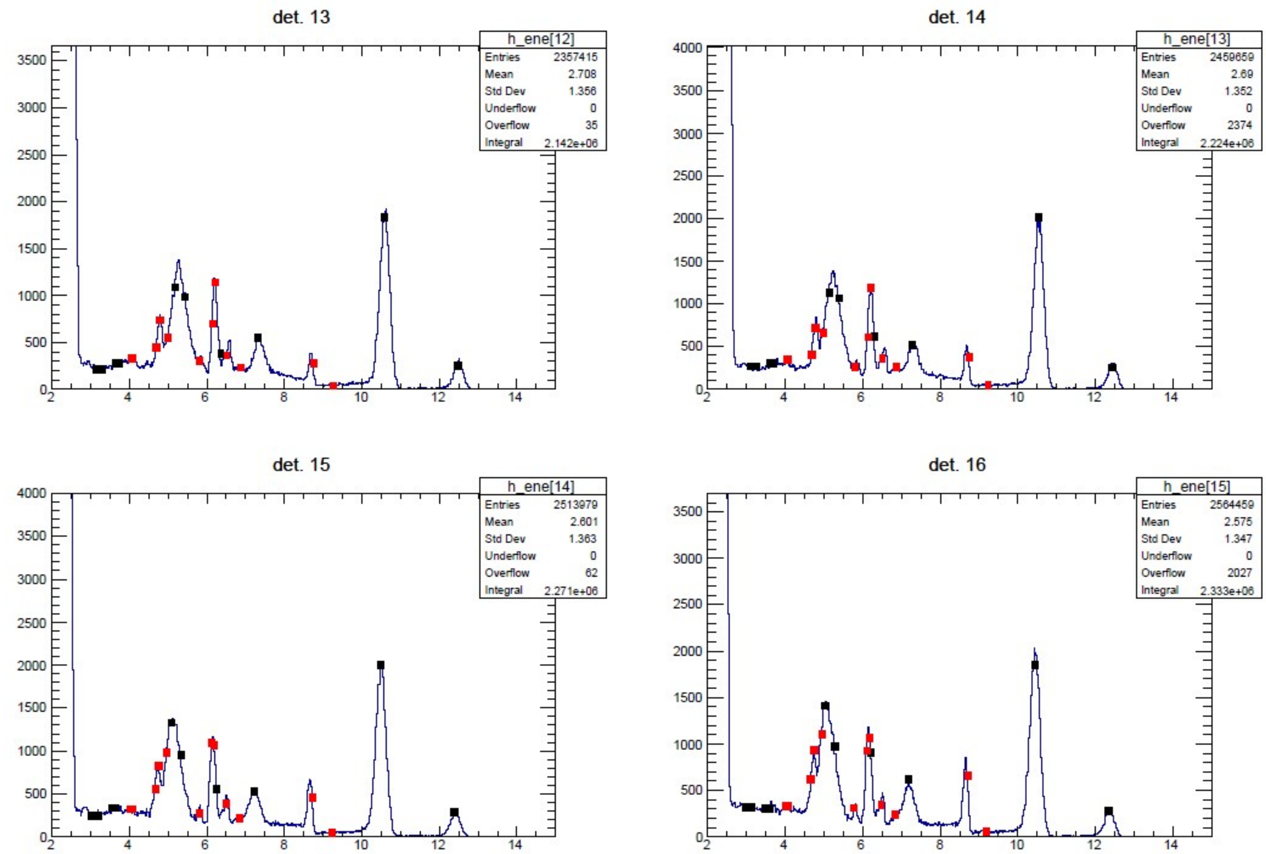

Figure 5.11: Charged particle single spectra taken for rings 13-16 of the forward detector with a rudimentary peak finder marker. The black markers correspond to alpha particles whereas the red ones to protons.

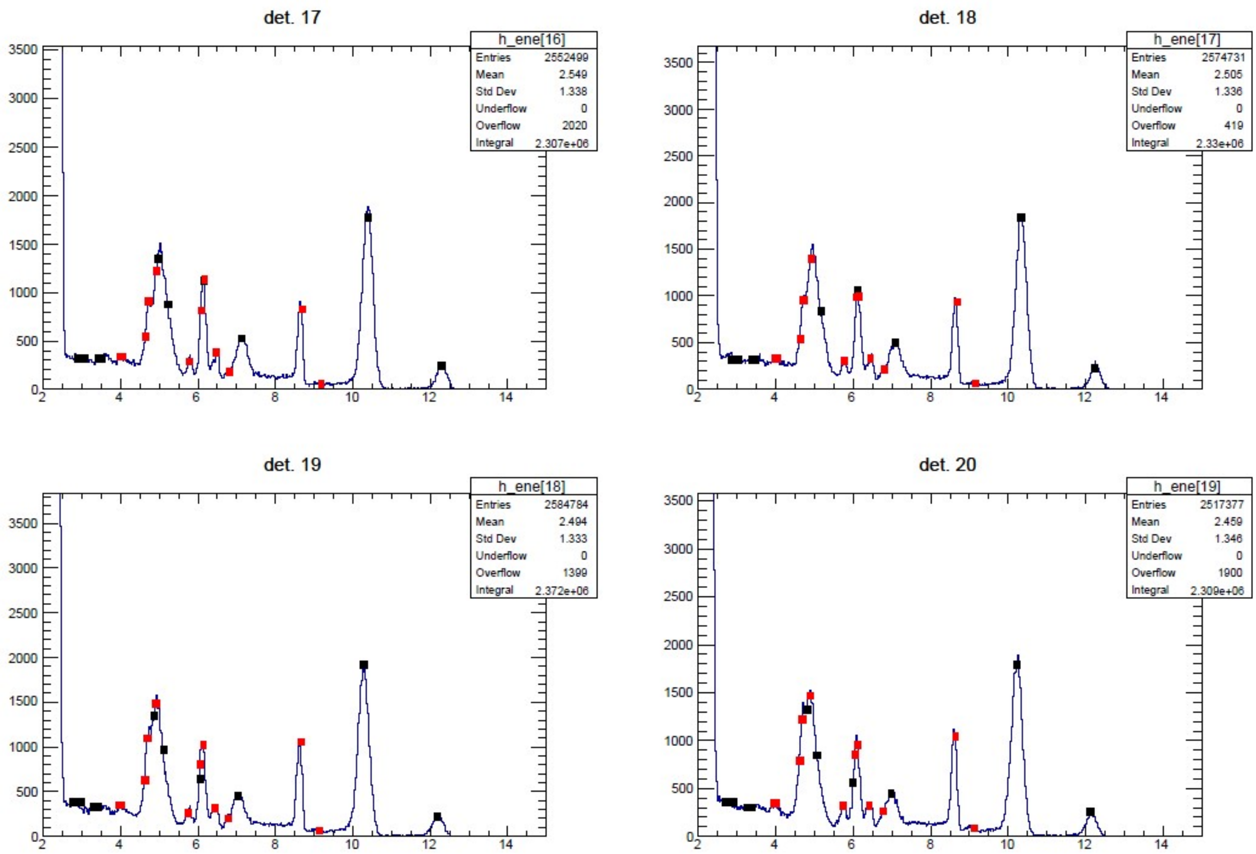

Figure 5.12: Charged particle single spectra taken for rings 17-20 of the forward detector with a rudimentary peak finder marker. The black markers correspond to alpha particles whereas the red ones to protons.

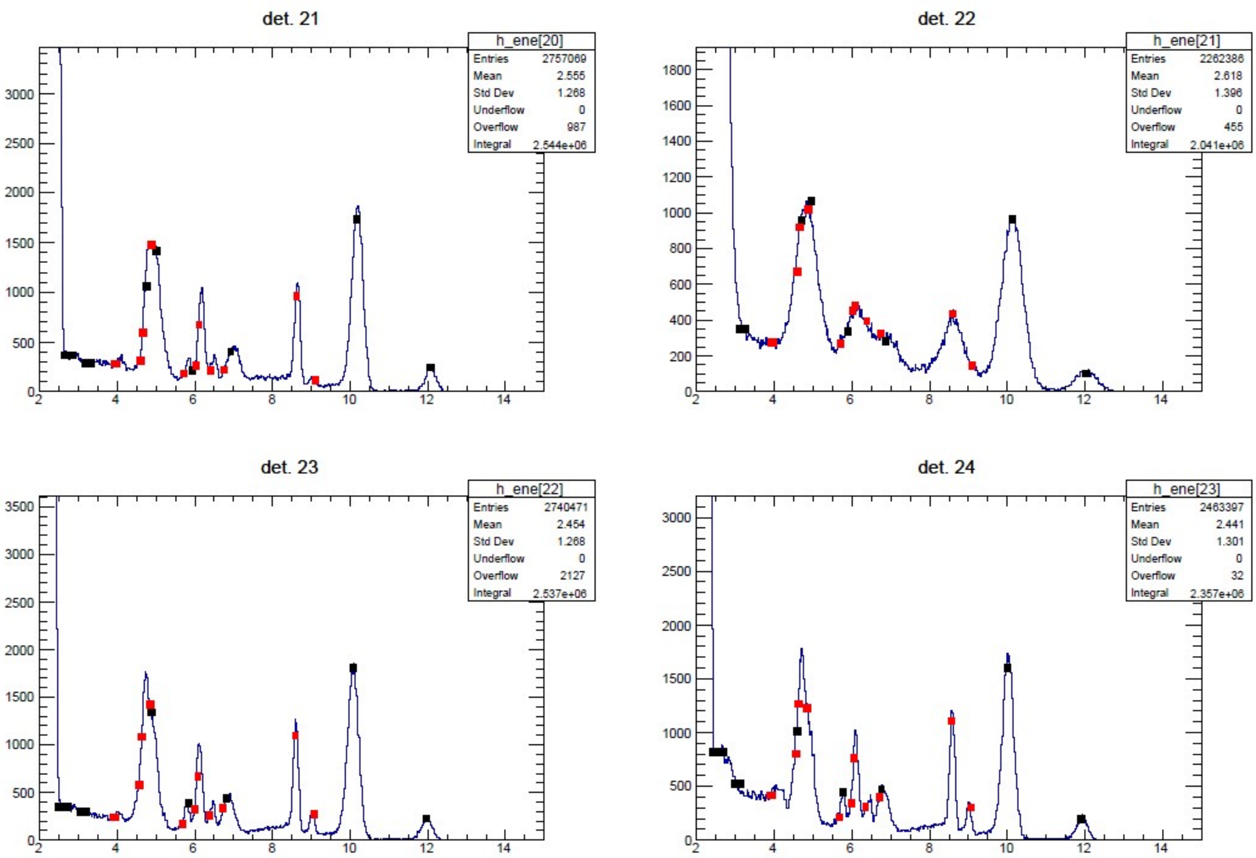

Figure 5.13: Charged particle single spectra taken for rings 21-24 of the forward detector with a rudimentary peak finder marker. The black markers correspond to alpha particles whereas the red ones to protons.

With the histograms previously shown for each ring of the detector, energy plots were obtained and information about each charged particle peak was extracted, as shown in figures 5.14, 5.15, 5.16, 5.17, 5.18, 5.19, 5.20, 5.21, 5.22, 5.23, 5.24, and 5.25, where a fitting routine was employed and will be explained further on this chapter. Additionally, these plots correspond to charged particle spectra using gamma-ray coincidences.

A first comparison between the spectra obtained using the coincidence method and not using this method shows a reduction in the number of counts registered. For example, for the α_1 energy peak, the highest energy peak located at $\sim$ 11 MeV, the number of counts registered with the coincidence method corresponds to $\sim 6\%$ of the counts of the charged particle single spectra without coincidences, figures 5.14 and 5.8 respectively.

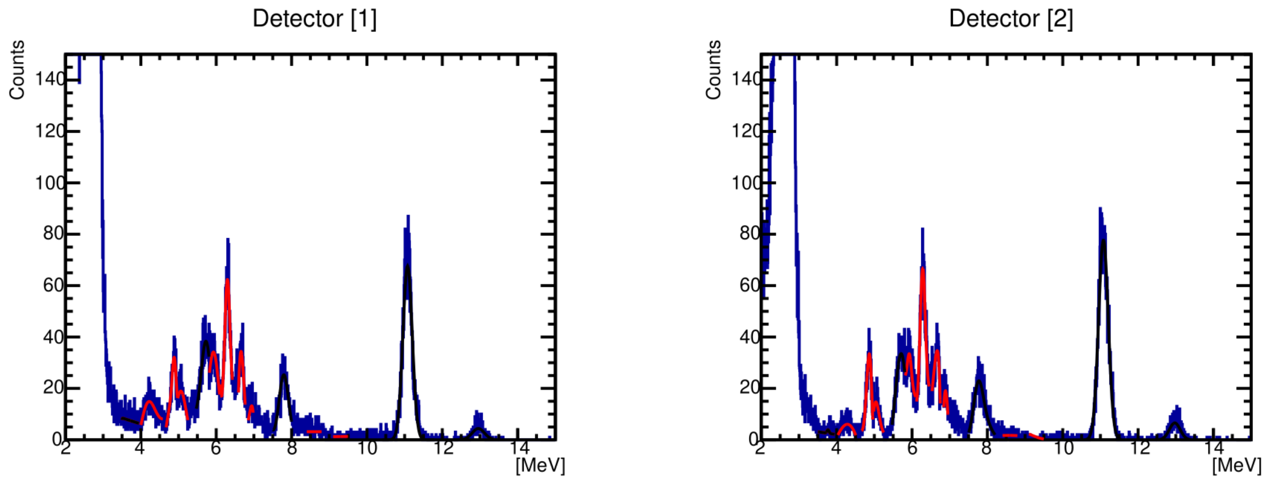

Figure 5.14: Gamma-ray coincidence energy plots with the fitting of the proton (red) and alpha (black) peaks for detectors 1 and 2 of the forward detector.

As shown in figures 5.14, 5.15, 5.16, 5.17, 5.18, 5.19, 5.20, 5.21, 5.22, 5.23, 5.24, and 5.25, the Gaussian fit, that follows equation 5.1, provides an accurate description of the two most energetic alpha peaks. Nonetheless, at lower energies, the overlapping of the peaks proves complicated to have an accurate fit, consequently, linear combinations of a Gaussian function with an exponential (equation 5.2), and a Gaussian function with a linear polynomial (5.3) were made as a way to describe the background. Furthermore, for the overlapping of the peaks and considering the efficiency of the detectors, a 5% of the peak's energy was set to distinguish between peaks.

$$f(x) = p_0 \exp\left[-0.5\left(\frac{x-p_1}{p_2}\right)^2\right] \tag{5.1}$$

where p_1 is the mean and p_2 is the σ of the distribution.

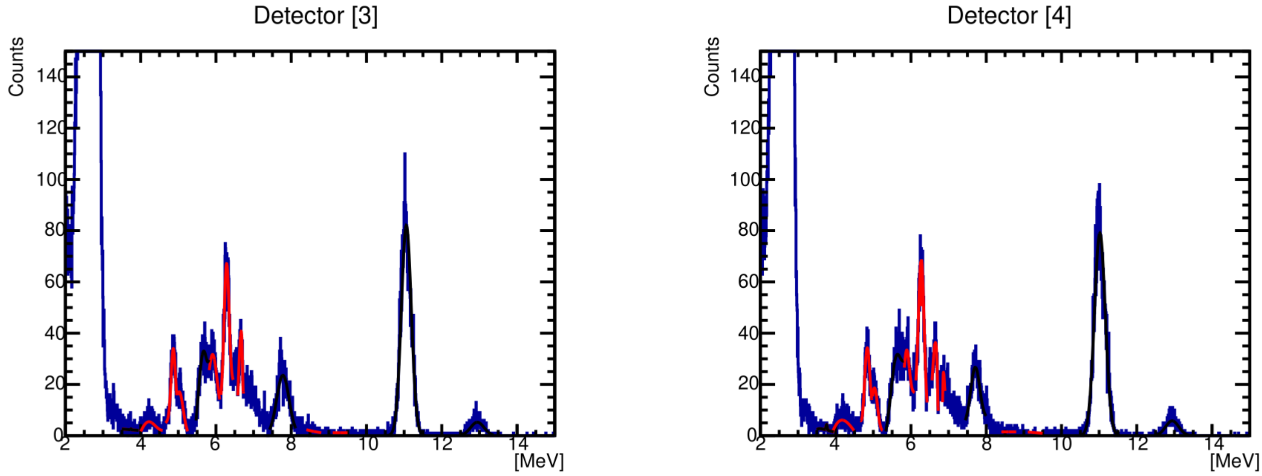

Figure 5.15: Gamma-ray coincidence energy plots with the fitting of the proton (red) and alpha (black) peaks for detectors 3 and 4 of the forward detector.

$$f(x) = p_0 \exp\left[-0.5\left(\frac{x-p_1}{p_2}\right)^2\right] + p_3 \exp\left[-0.5\left(\frac{x-p_4}{p_5}\right)^2\right] + \exp(p_6 + p_7 x) \tag{5.2}$$

$$f(x) = p_0 \exp\left[-0.5\left(\frac{x-p_1}{p_2}\right)^2\right] + p_3 \exp\left[-0.5\left(\frac{x-p_4}{p_5}\right)^2\right] + p_6 + p_7 x \tag{5.3}$$

where p_i are parameters of the function.

Specifically, peaks 1 to 4 fitting followed the form of equation 5.1; peaks 5, 6, and 7 followed the form of equation 5.2; and peaks 8 to 14 followed equation 5.3. The parameters were varied according to each peak to get a good fit and can be found in the appendix B.

This fitting routine was done for 14 peaks for each strip of the S3F detector, resulting in peaks 1, 2, 5, 10, and 14 being the ones for α particles and peaks 3, 4, 6, 7, 8, 9, 11, 12, and 13 corresponding to protons, where the sorting of the peaks is the highest energy peak corresponds to the first peak, peak number 2 is the second highest energy peak, etc.

Once the fitting routine for the S3F detector is finished, the S3B fitting routine was made with the difference that it was only applied for 3 highest energy peaks corresponding to 2 protons and an α particle, as shown in figures 5.26, 5.27, 5.28, 5.29, 5.30, 5.31, 5.32, 5.33, 5.34, 5.35, 5.36, and 5.37. These plots also correspond to the energy spectra using gamma-ray coincidences.

Conversely to the S3F fittings, for the S3B fitted peaks a gaussian function (eq. 5.1) was the only one required.

The mean, amplitude, and sigma of the fitting will be then extracted so that this information can be

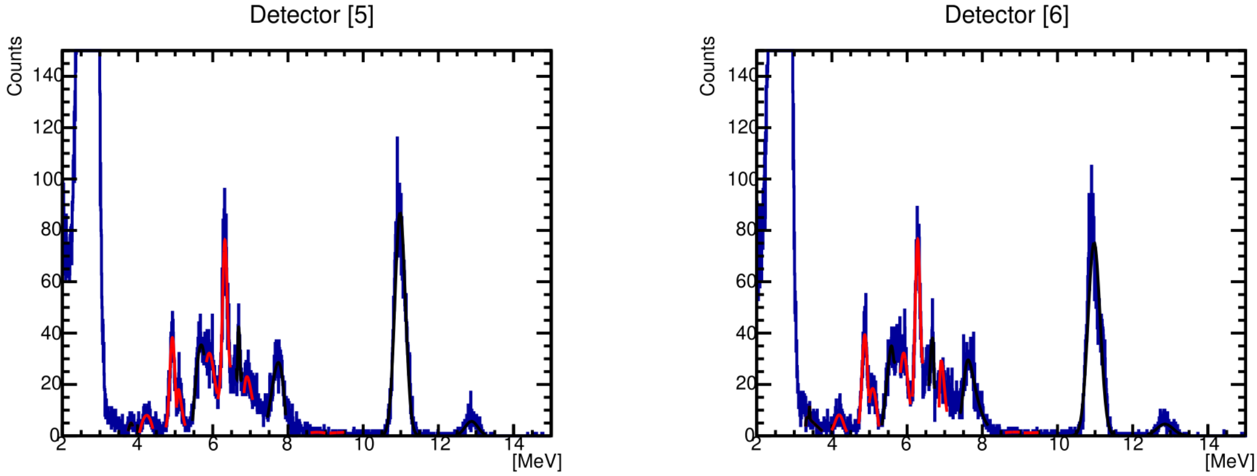

Figure 5.16: Gamma-ray coincidence energy plots with the fitting of the proton (red) and alpha (black) peaks for detectors 5 and 6 of the forward detector.

used to calculate the angular distribution for each charged particle.

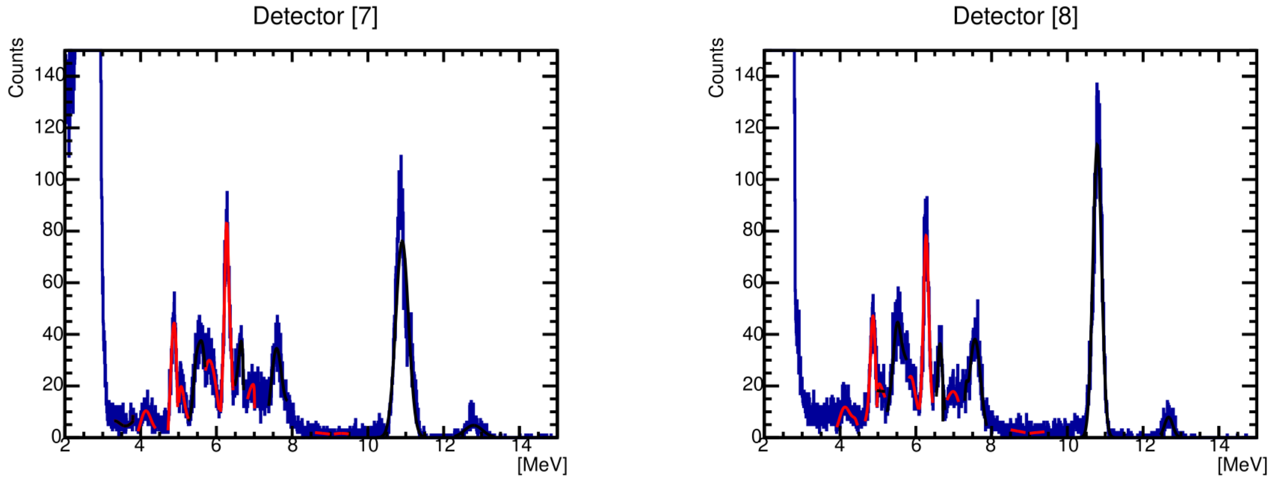

Figure 5.17: Gamma-ray coincidence energy plots with the fitting of the proton (red) and alpha (black) peaks for detectors 7 and 8 of the forward detector.

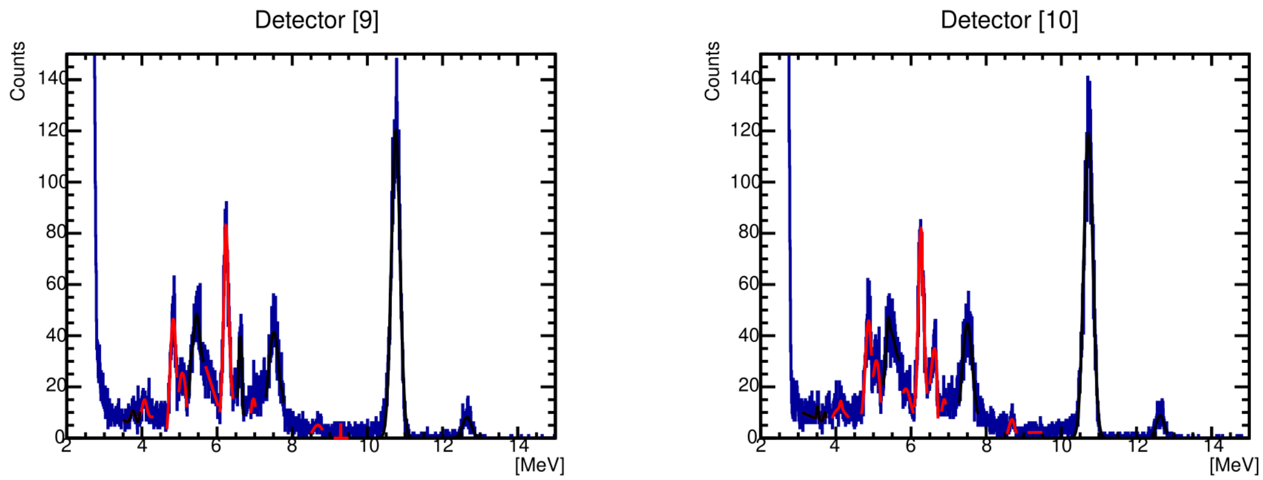

Figure 5.18: Gamma-ray coincidence energy plots with the fitting of the proton (red) and alpha (black) peaks for detectors 9 and 10 of the forward detector.

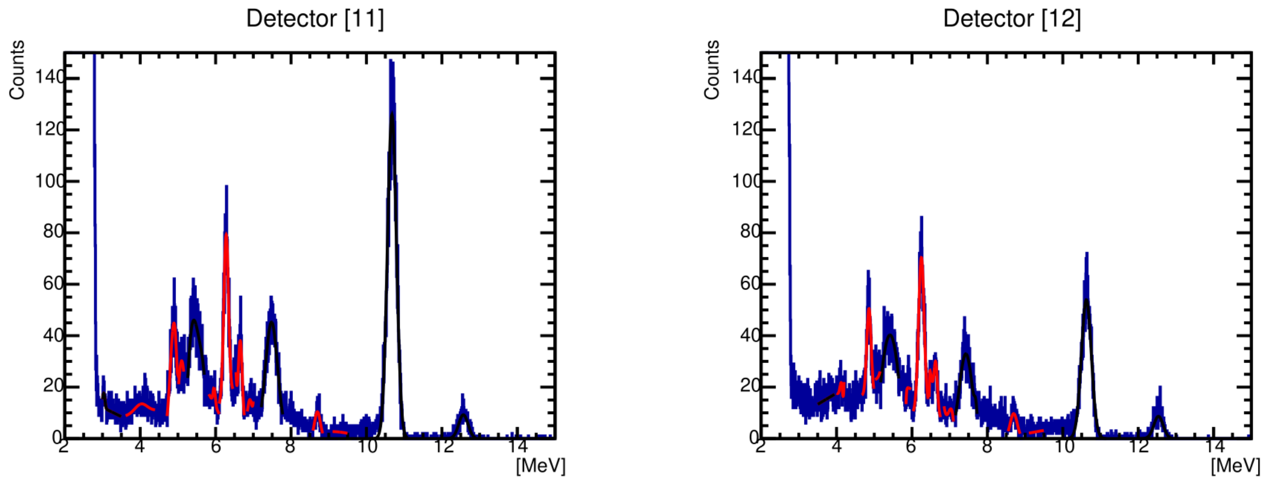

Figure 5.19: Gamma-ray coincidence energy plots with the fitting of the proton (red) and alpha (black) peaks for detectors 11 and 12 of the forward detector.

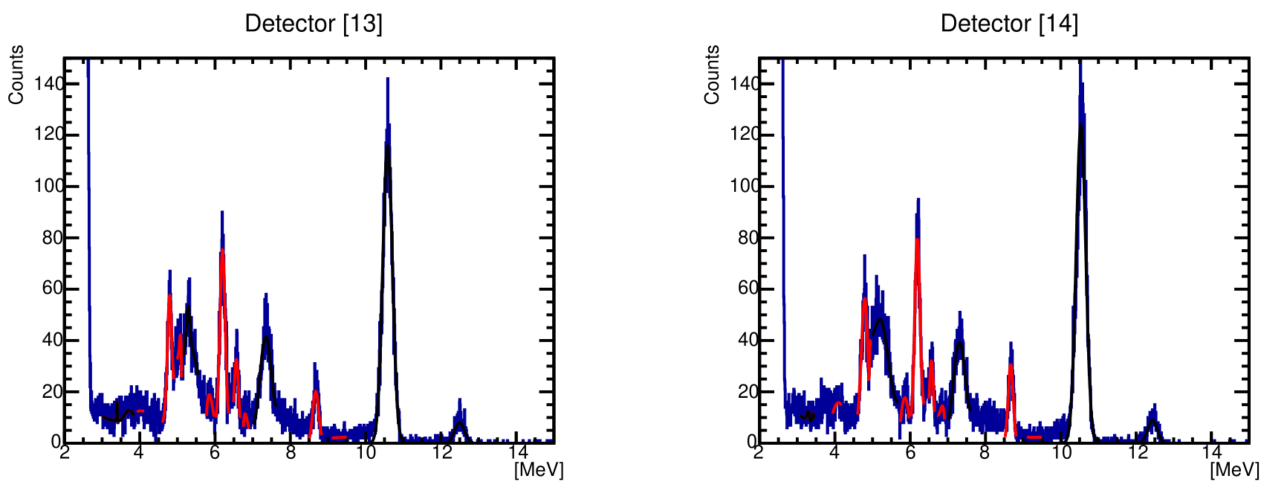

Figure 5.20: Gamma-ray coincidence energy plots with the fitting of the proton (red) and alpha (black) peaks for detectors 13 and 14 of the forward detector.

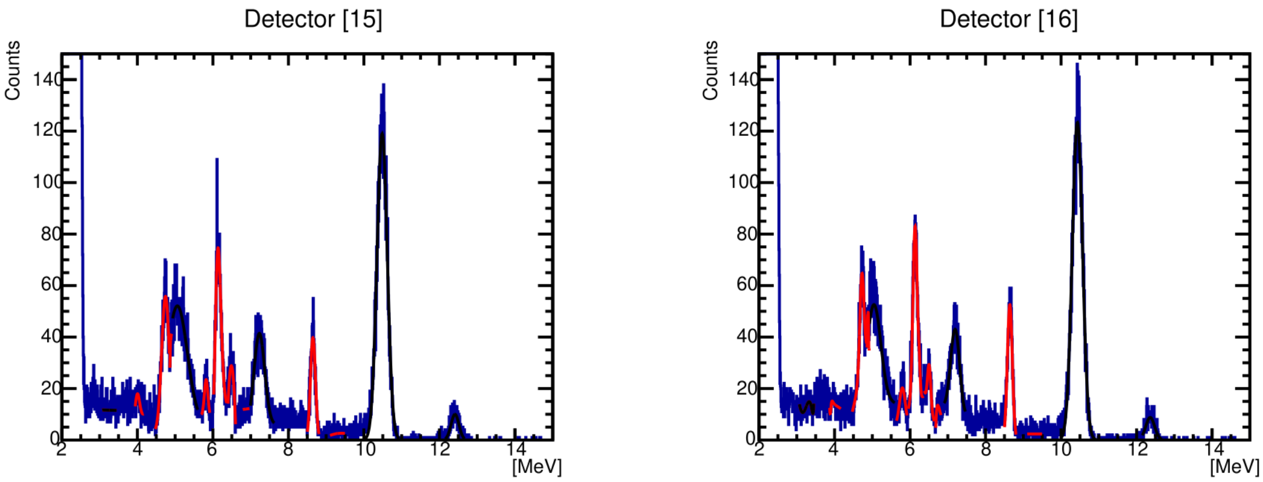

Figure 5.21: Gamma-ray coincidence energy plots with the fitting of the proton (red) and alpha (black) peaks for detectors 15 and 16 of the forward detector.

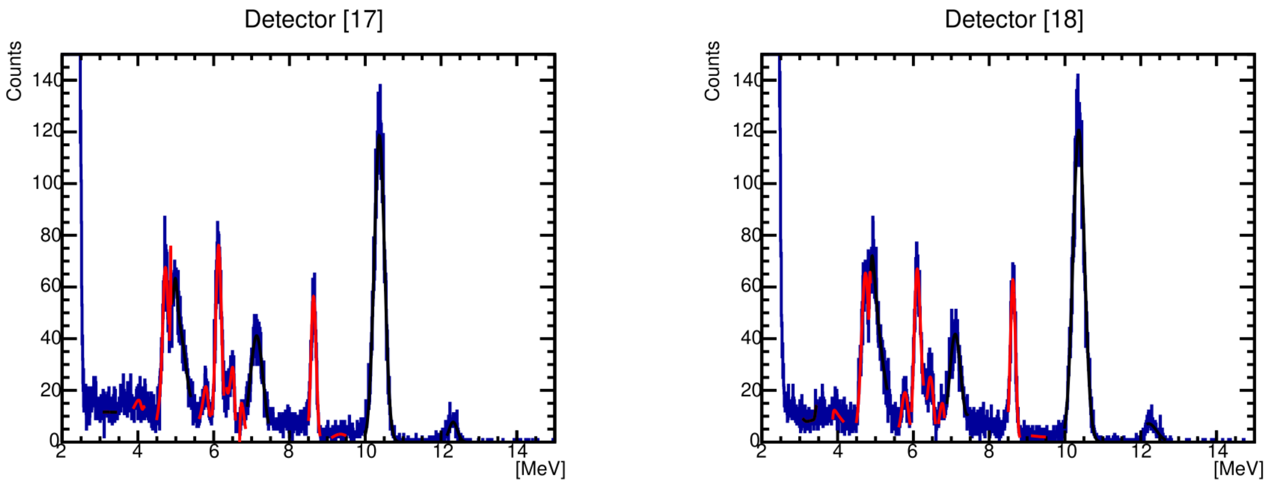

Figure 5.22: Gamma-ray coincidence energy plots with the fitting of the proton (red) and alpha (black) peaks for detectors 17 and 18 of the forward detector.

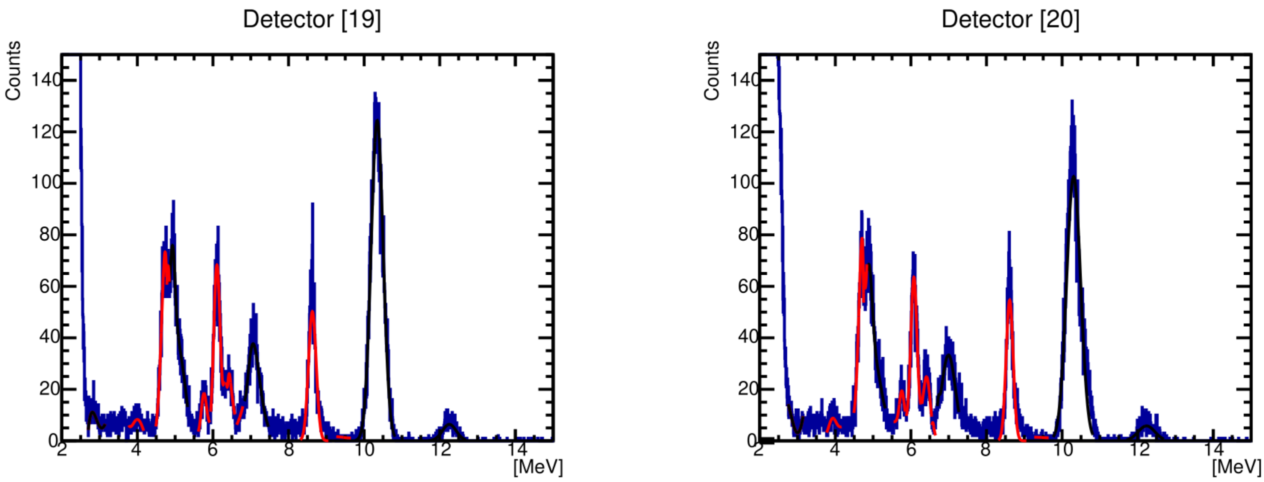

Figure 5.23: Gamma-ray coincidence energy plots with the fitting of the proton (red) and alpha (black) peaks for detectors 19 and 20 of the forward detector.

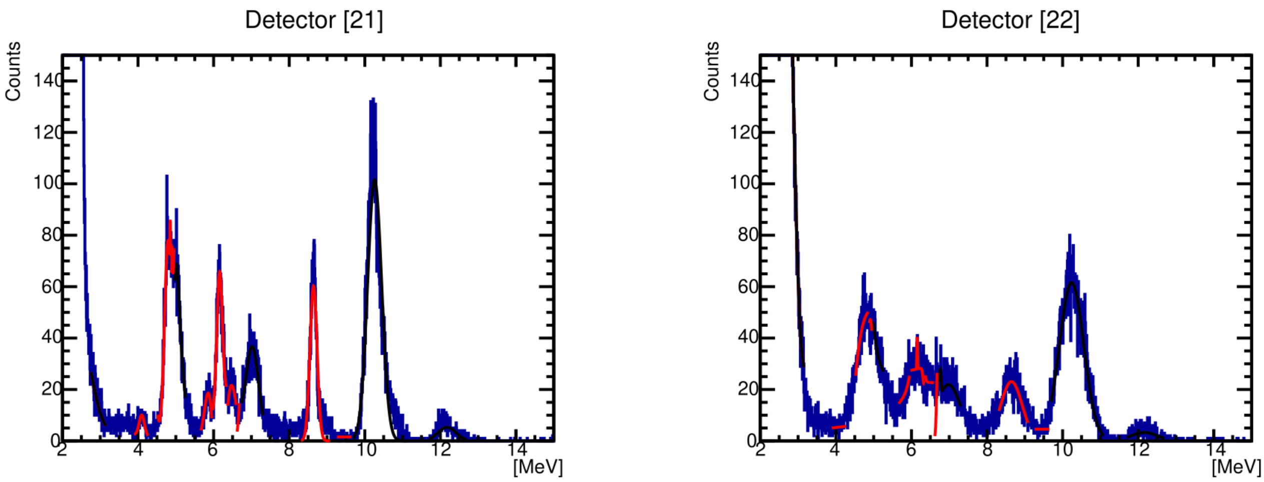

Figure 5.24: Gamma-ray coincidence energy plots with the fitting of the proton (red) and alpha (black) peaks for detectors 21 and 22 of the forward detector.

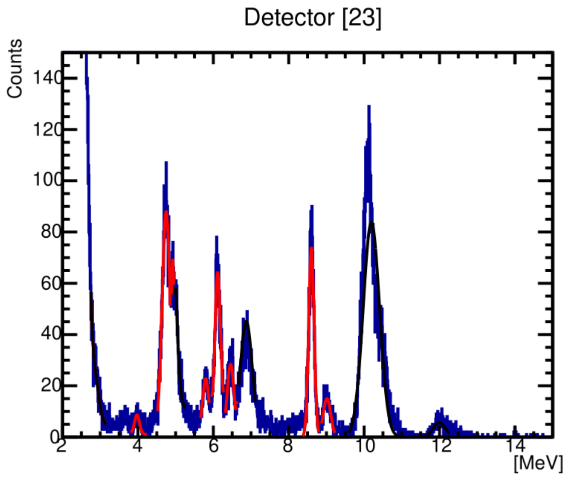

Figure 5.25: Gamma-ray coincidence energy plots with the fitting of the proton (red) and alpha (black) peaks for detectors 23 and 24 of the forward detector.

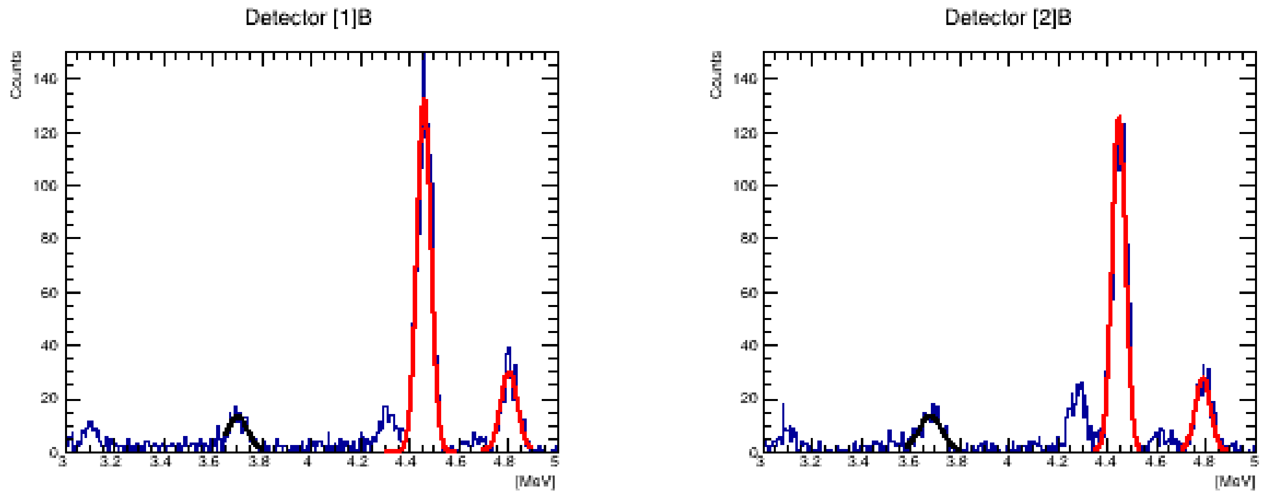

Figure 5.26: Gamma-ray coincidence energy plots with the fitting of the proton (red) and alpha (black) peaks for detectors 1 and 2 of the backward detector.

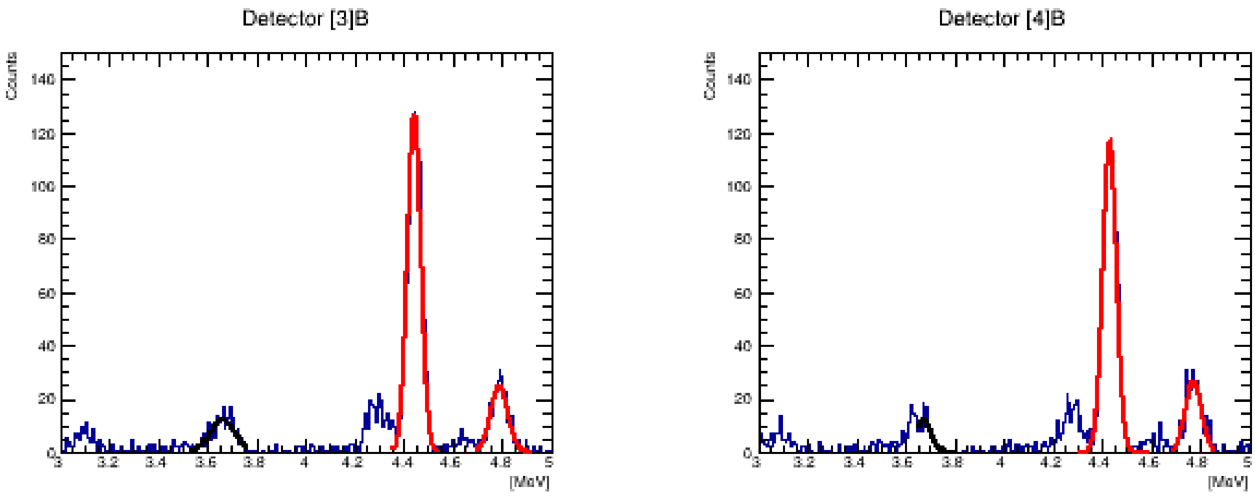

Figure 5.27: Gamma-ray coincidence energy plots with the fitting of the proton (red) and alpha (black) peaks for detectors 3 and 4 of the backward detector.

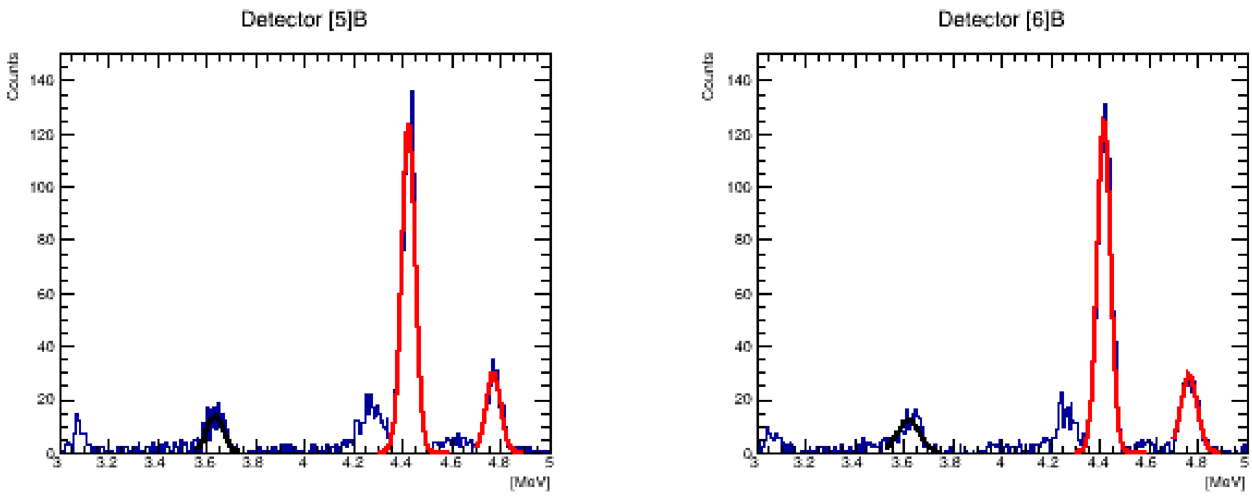

Figure 5.28: Gamma-ray coincidence energy plots with the fitting of the proton (red) and alpha (black) peaks for detectors 5 and 6 of the backward detector.

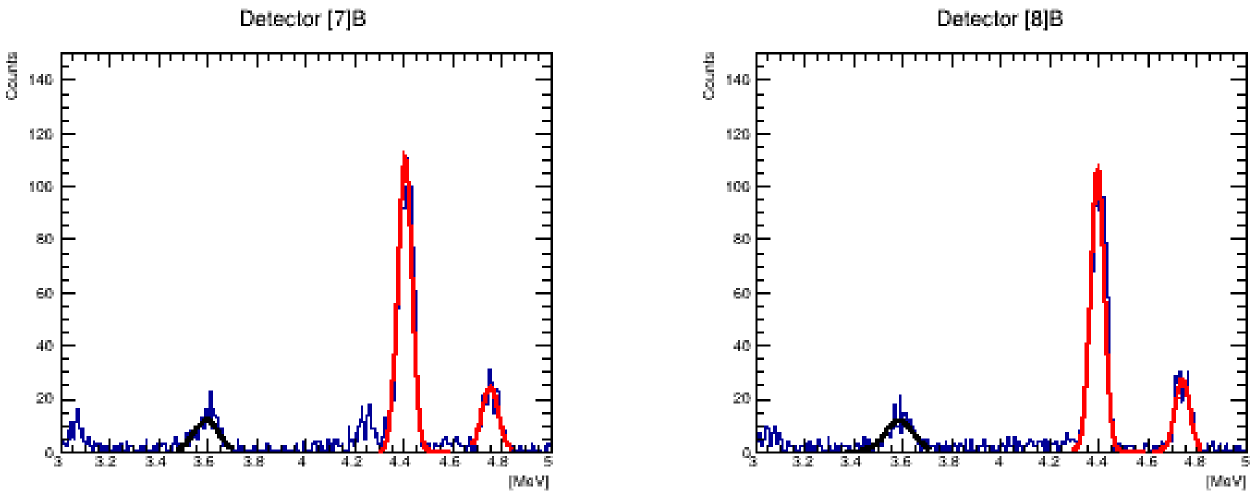

Figure 5.29: Gamma-ray coincidence energy plots with the fitting of the proton (red) and alpha (black) peaks for detectors 7 and 8 of the backward detector.

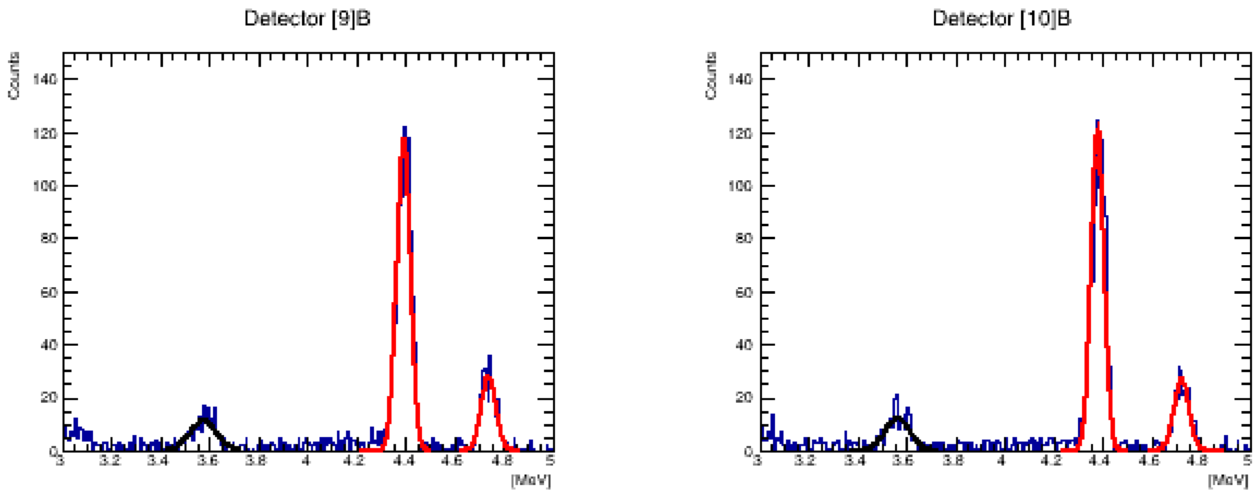

Figure 5.30: Gamma-ray coincidence energy plots with the fitting of the proton (red) and alpha (black) peaks for detectors 9 and 10 of the backward detector.

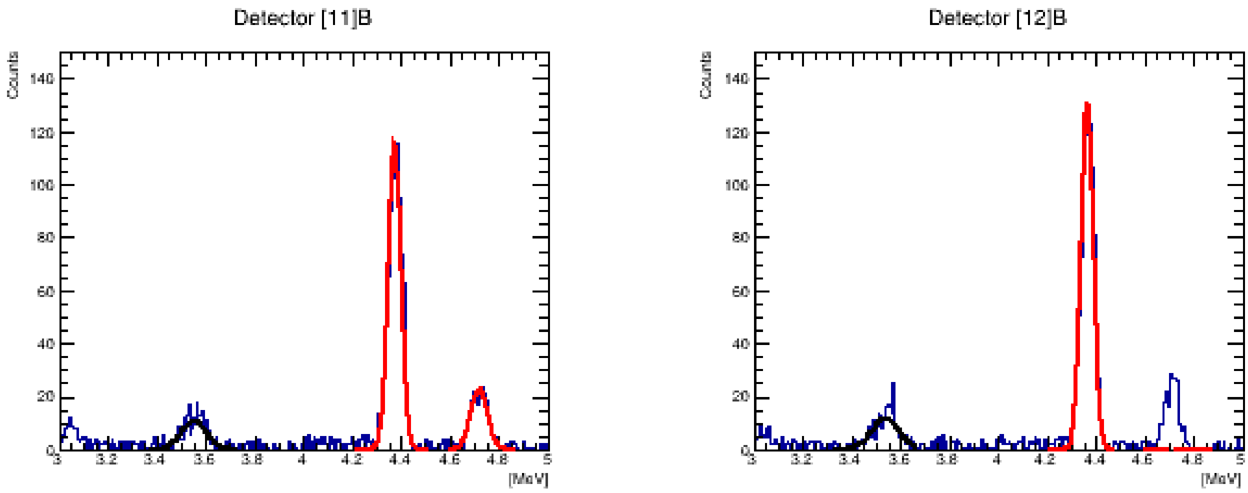

Figure 5.31: Gamma-ray coincidence energy plots with the fitting of the proton (red) and alpha (black) peaks for detectors 11 and 12 of the backward detector.

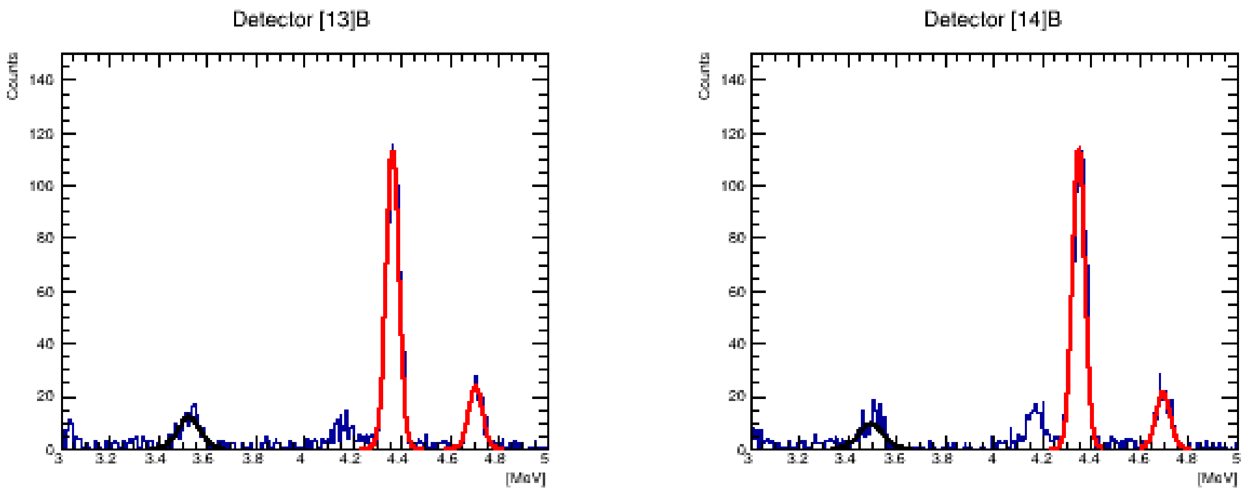

Figure 5.32: Gamma-ray coincidence energy plots with the fitting of the proton (red) and alpha (black) peaks for detectors 13 and 14 of the backward detector.

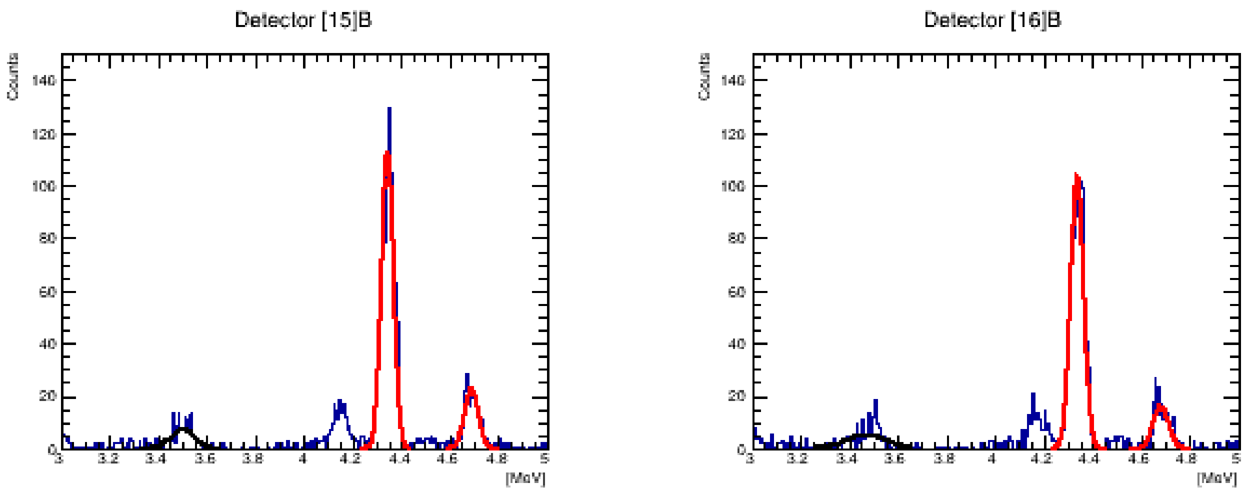

Figure 5.33: Gamma-ray coincidence energy plots with the fitting of the proton (red) and alpha (black) peaks for detectors 15 and 16 of the backward detector.

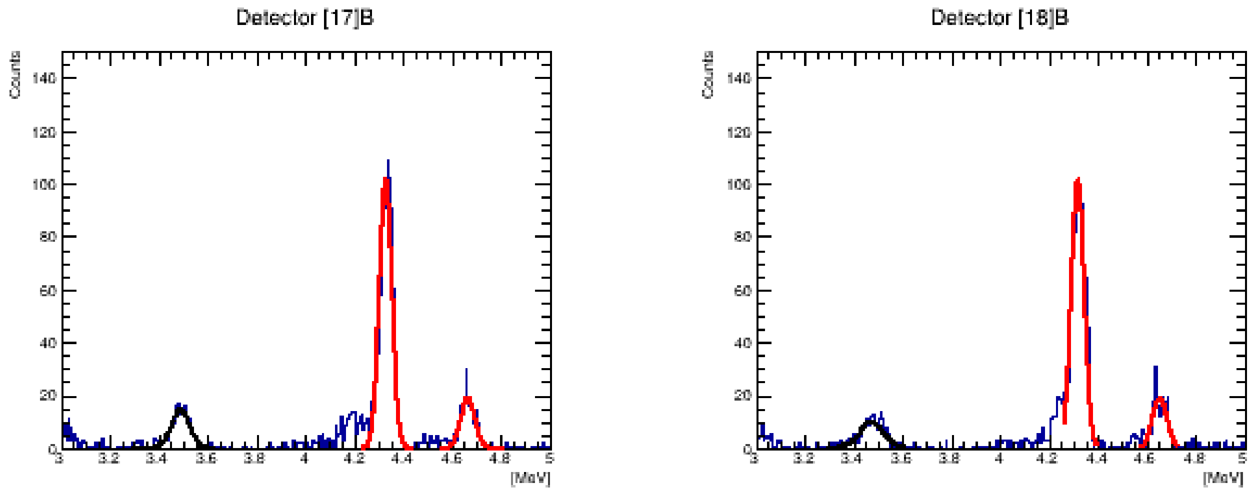

Figure 5.34: Gamma-ray coincidence energy plots with the fitting of the proton (red) and alpha (black) peaks for detectors 17 and 18 of the backward detector.

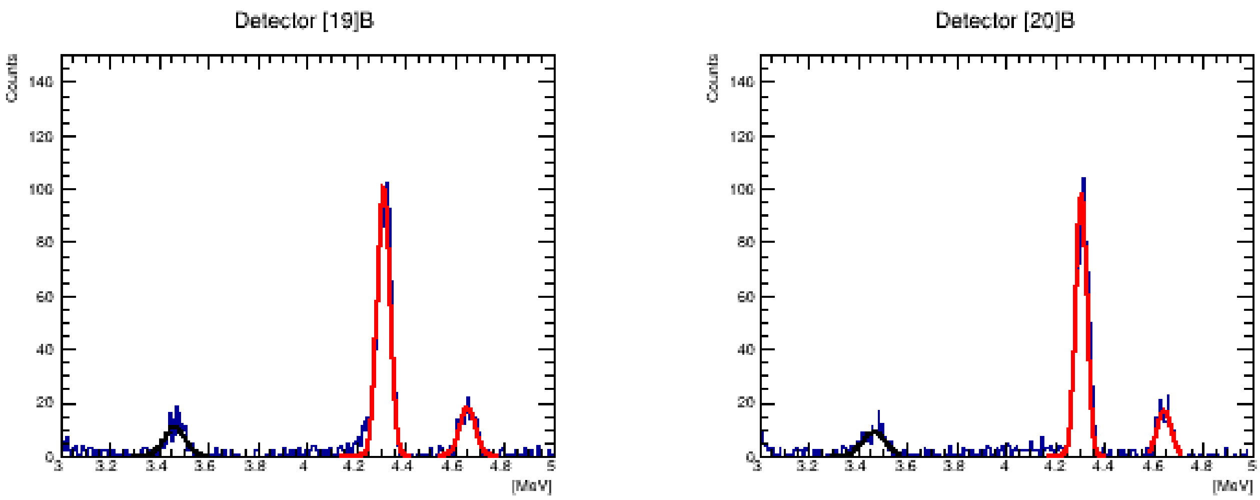

Figure 5.35: Gamma-ray coincidence energy plots with the fitting of the proton (red) and alpha (black) peaks for detectors 19 and 20 of the backward detector.

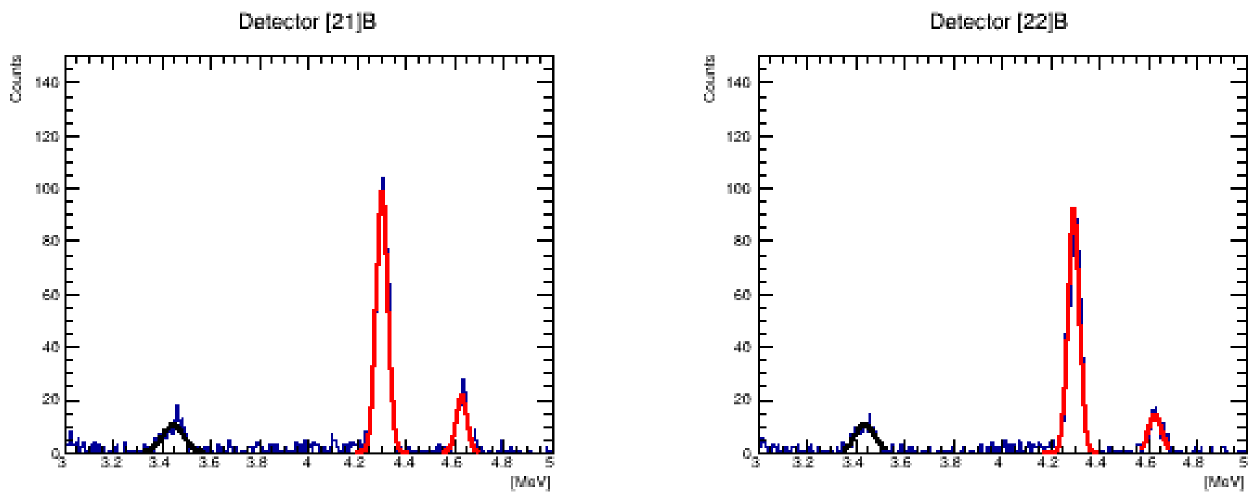

Figure 5.36: Gamma-ray coincidence energy plots with the fitting of the proton (red) and alpha (black) peaks for detectors 21 and 22 of the backward detector.

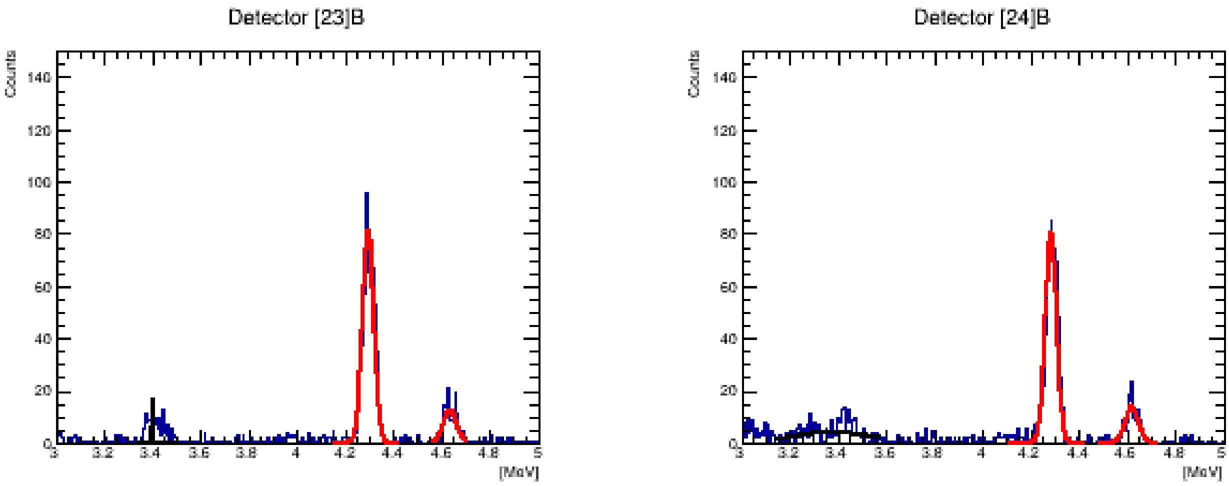

Figure 5.37: Gamma-ray coincidence energy plots with the fitting of the proton (red) and alpha (black) peaks for detectors 23 and 24 of the backward detector.

5.2 Angular Distributions and Cross-sections

For the further stages of the analysis regarding the differential cross-section, the determination of the solid angle of each strip of the DSSD detectors is needed apart from the fitting parameters.

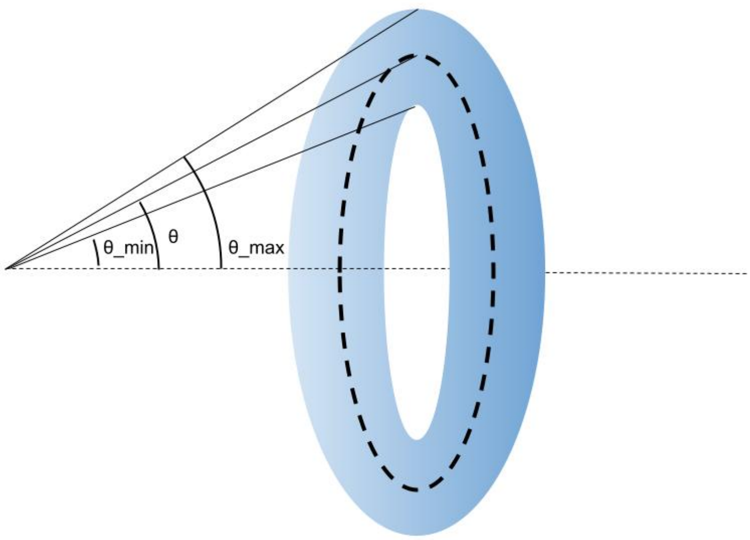

Figure 5.38: Diagram of the angle calculated for each strip of the DSSD.

Figure 5.38 shows schematically how the determination of the angle was made using equation 5.4, where the distance to the target and radii of the detector were known. The distance from the detector to the target was 6 ± 0.05 cm; to determine the radius of each strip, the outermost strip radius of the detector was 3.5 ± 0.05 cm, and the innermost 1.1 ± 0.05 cm; the strip pitch was 0.0886 ± 0.00005 cm; and it were 24 rings [74].

$$\Omega = \left[\frac{(r_a^2 + d^2 - d\sqrt{r_a^2 + d^2})}{r_a^2 + d^2} - \frac{(r_b^2 + d^2 - d\sqrt{r_b^2 + d^2})}{r_b^2 + d^2} \right] \tag{5.4}$$

Where r_a is the inner radius of the silicon detector's strip, r_b is the outer radius, and d is the distance between the target and the DSSD.

So the solid angle for the S3B and S3F detectors, shown in table 5.1, results as the sum of the angular acceptance of each detector's strip.

$\Delta\Omega(S3B)[sr]$	$\Delta\Omega(S3F)[sr]$
0.84	0.75

Table 5.1: Solid angle for the S3B and S3F detectors

On the other hand, ROOT's Gaussian function was used to obtain the number of events N corresponding either to alpha particles or protons.

Once a satisfactory peak fitting was done, and with the information of the fitting function, it is possible now to calculate the differential cross section using equation 5.5, to then produce the angular distribution plots. Afterwards, a Legendre polynomial fitting was made to obtain information about the spin and parity, J^{π}, of the evaporated charged particle being studied.

$$\left(\frac{d\sigma}{d\Omega}\right)_{lab} = \frac{N}{I \cdot \varepsilon_{\gamma} \cdot \Delta\Omega \cdot \Delta t \cdot N_t} \tag{5.5}$$

Where N is the number of coincident events, I beam intensity, ε_{γ} is the γ efficiency, $\Delta\Omega$ is the solid angle of the DSSD, Δt is the acquisition time and N_t is the number of atoms in the target [39].

Equation 5.5 can be rearranged as equation 5.6.

$$\left(\frac{d\sigma}{d\Omega}\right)_{lab} = \frac{N \cdot m_{mol} \cdot e \cdot q}{\Delta\Omega \cdot z \cdot N_A \cdot I\Delta t} \tag{5.6}$$

Where m_{mol} is the molar mass, e the electron charge, q the charge state, z the target thickness, N_A Avogadro's number, I the intensity of the beam, and Δt the acquisition time.

All of these parameters are known to the experiment. In particular, table 5.2 shows the parameter values taken into account to calculate the differential cross section.

Cross section parameters	
m_{mol}	12 g/mol
Electron charge	$1.602C \times 10^{-19}$
Charge state	3
Target density	30×10^{-6} g/cm^2
Avogadro's number	6.022×10^{23} mol^{-1}
Beam intensity	93×10^{-9}e
Acquisition time	5040 s
$\Delta\Omega$ S3F	0.75 sr
$\Delta\Omega$ S3B	0.84 sr

Table 5.2: Differential cross-section parameters

The angular distribution plots obtained with the parameters of the fittings are shown in figures 5.39, 5.40, 5.41, and 5.42 for α_0, α_1, p_0, and p_1, respectively. Also, the plots shown correspond to the centre of mass system. The transformation from the *Lab* system to the *CMS* system is made thanks to the γ conversion factor, see Appendix A.

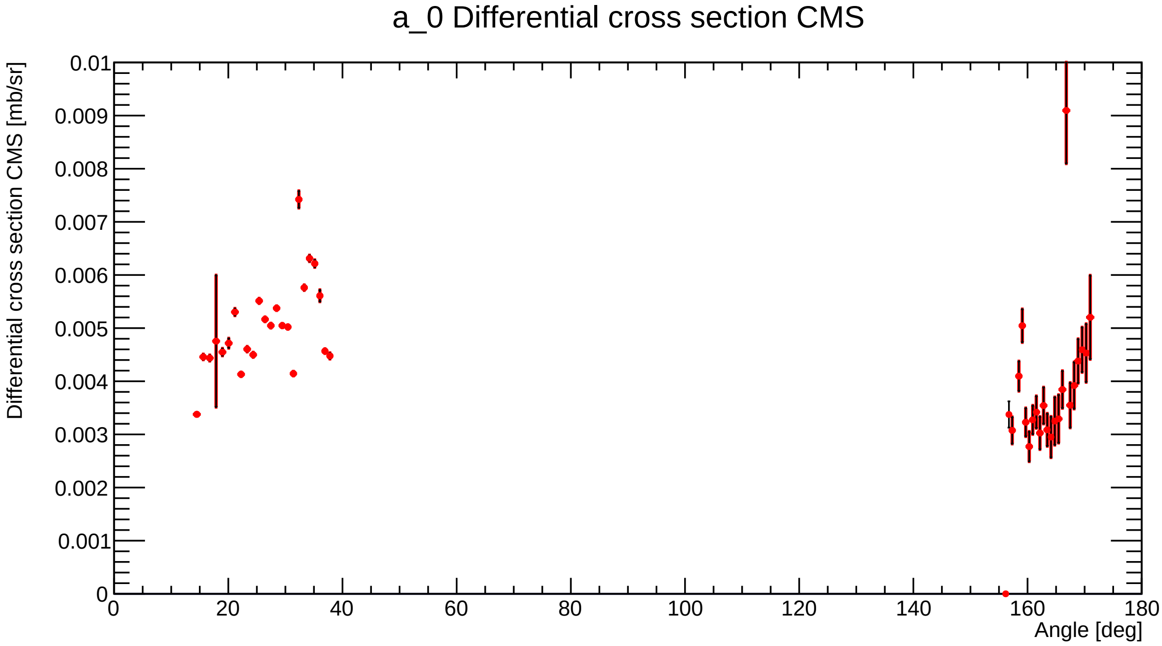

Figure 5.39: Angular distribution of the α_0 exit channel in the forward (S3F) and backward (S3B) detectors.

Each data point from the angular distribution plots corresponds to a strip of either the S3B backward detector ($\sim 150° < \theta <\sim 170°$) or to the S3F forward detector ($\sim 15° < \theta <\sim 40°$).

A trend from the proton exit channels can be observed in the graphs for the angular distributions concerning the S3B backward detector, $\theta > 150°$, in which they appear to be flatter than the α exit channels, as expected from ref. [15] or even the same proton channel but compared to S3F forward detector.

Nevertheless, some anomalies in the figures where angular distribution was plotted for both detectors. In the first place, the error bars concerning the calculations of the differential cross-section of the S3B detector are larger than the ones of the S3F detector. This is possibly due to the fitting process and its associated error despite the fittings shown in the section 5.1 being satisfactory. The associated error takes into account how the gaussian function fits the peak without considering the linear or exponential background, and it is possible to see a tail in the second proton peak for the S3B detector, for example. Secondly, it was expected that the distribution would be symmetrical with respect to $\theta = 90°$ as the entrance channel of the ^{12}C involves even-even nuclei. However, the trends of the

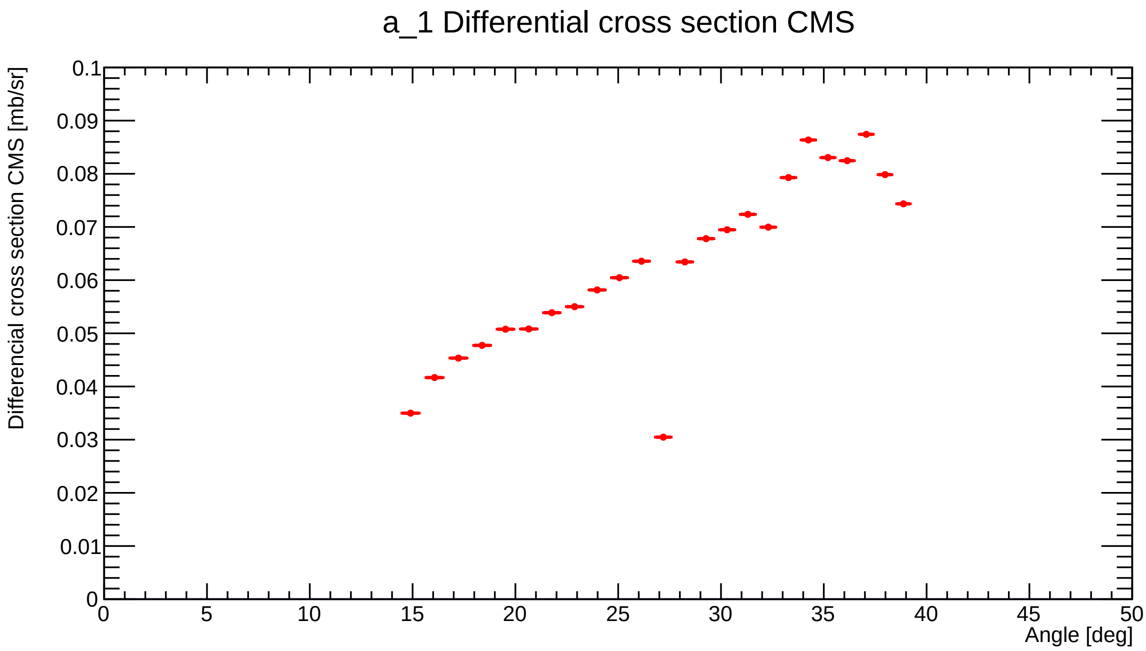

Figure 5.40: Angular distribution of the α_1 exit channel in the forward (S3F) detector.

distribution of the charged particles in the S3B detector are in agreement with the one shown in refs. [37, 15].

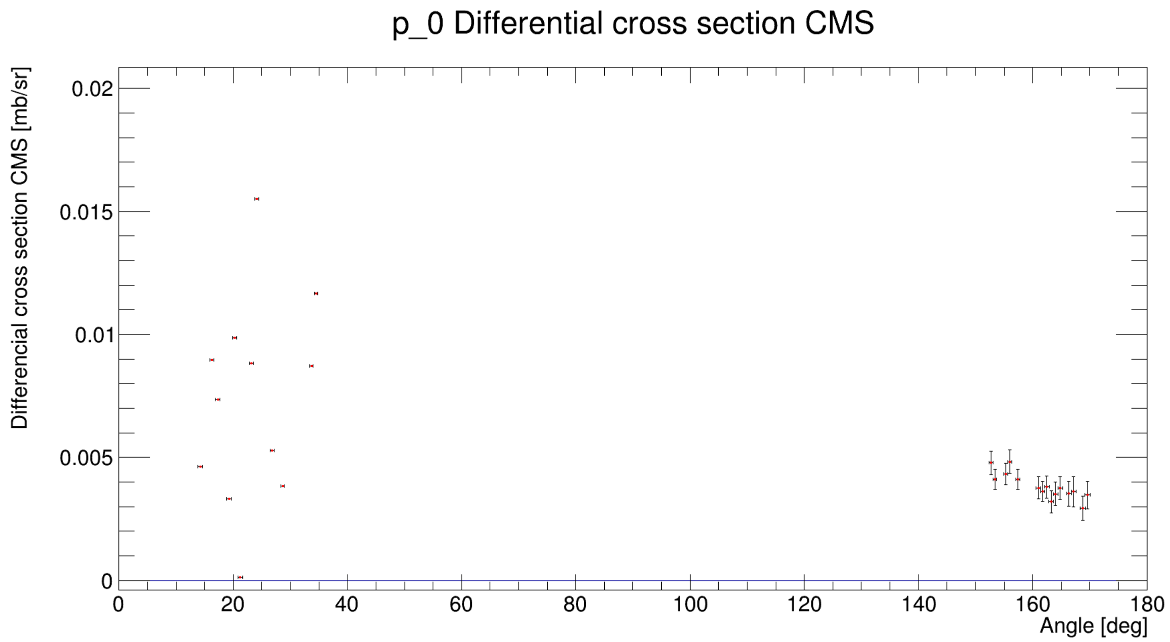

Figure 5.41: Angular distribution of the p_0 exit channel in the forward (S3F) and backward (S3B) detectors.

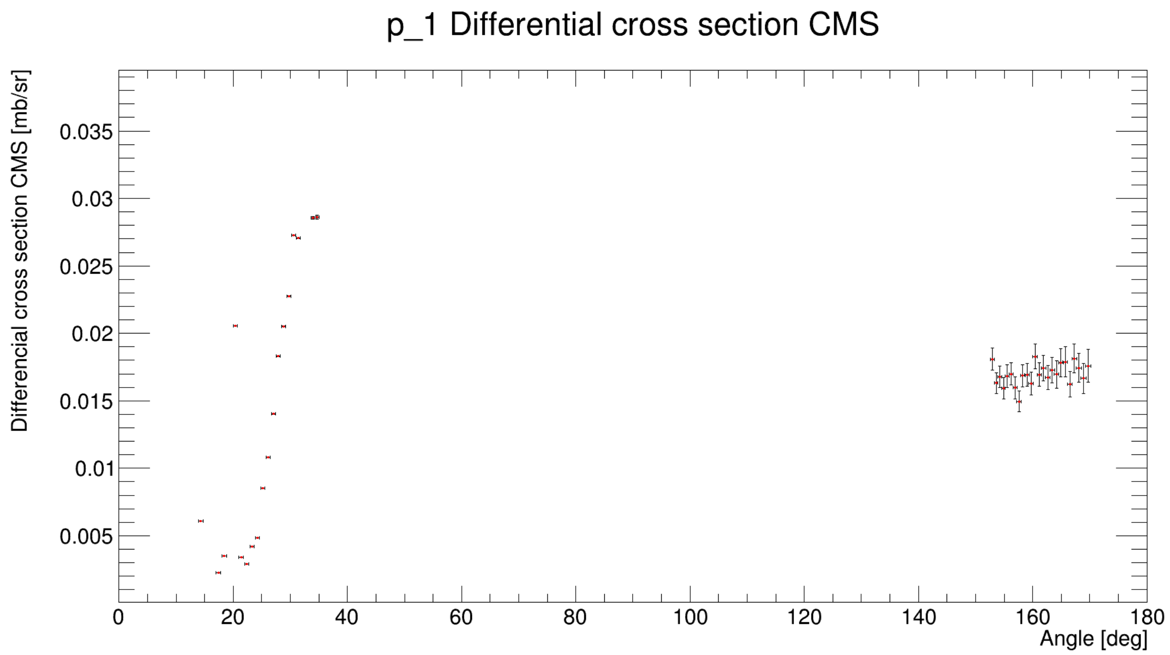

Figure 5.42: Angular distribution of the p_1 exit channel in the forward (S3F) and backward (S3B) detectors.

Once the angular distributions for each exit channel are obtained, the next step to obtain the cross-section would be to fit a Legendre polynomial to the angular distributions as a way to obtain the spin and parity of a specific reaction product, followed by the integration over 4π. Despite having the two Silicon detectors covering 0.75 sr and 0.84 sr each, the angular coverage that was achieved is not enough to fully cover this total solid angle and the Legendre polynomial fit would lack accuracy. Additionally, the fact that the angular distributions for the S3F detector, the small angle region, have an unexpected behaviour, would make the fitting less accurate. Thus, averaging over the differential cross-section for each exit channel followed by the integration over 4π is done. Preliminary results for the α_0, α_1, p_0, and p_1 are shown in table 5.3.

	Cross-section [mb]	Error[mb]
α_0	0.0584	0.00024
α_1	4.2173	0.00024
p_0	0.2024	0.00015
p_1	4.3254	0.00015

Table 5.3: Preliminary cross-sections for the different exit channels of the fusion reaction with a beam energy of $E_{beam} = 5.07$ MeV.

The statistical error associated with each measurement to obtain the differential cross-section is given by equation 5.7

$$\Delta\sigma_{stat} = \sqrt{\sum_i \Delta S_i^2} \tag{5.7}$$

where ΔS_i^2 is the uncertainty associated with each data point in the angular distribution plots.

Particularly, the integrated cross-section comes from integrating the differential cross-section described by equation 5.5. This equation has different factors, such as N, I, $\Delta\Omega$, that come with its own uncertainty. For example, the gamma-ray efficiency detection has an uncertainty of 10%, the beam intensity and target thickness come with a $\sim 12\%$ uncertainty, an uncertainty of 5% for the measurements for distances inside the reaction chamber given the precision of 0.5 mm. These uncertainties are carried onto the uncertainty of the integrated cross-section.

5.3 Discussion

The preliminary cross-sections obtained based on the angular distribution plots for some exit channels of the carbon fusion reaction need to consider some key factors to be reliable.

In the first place, as previously mentioned, an ideal scenario would be to be able to produce angular distribution plots covering a wider angle range regarding the silicon detectors, particularly around $\theta_{cm} = 90°$, followed by the Legendre polynomial fitting that follows equation 5.8 and the behaviour is represented in figure 5.43

$$P_l(x) = \frac{1}{2^l l!} \frac{d^l}{dx^l} \left(x^2 - 1\right)^l \tag{5.8}$$

for $l \geq 0$, $|x| \leq 1$, in the Rodrigues representation [66].

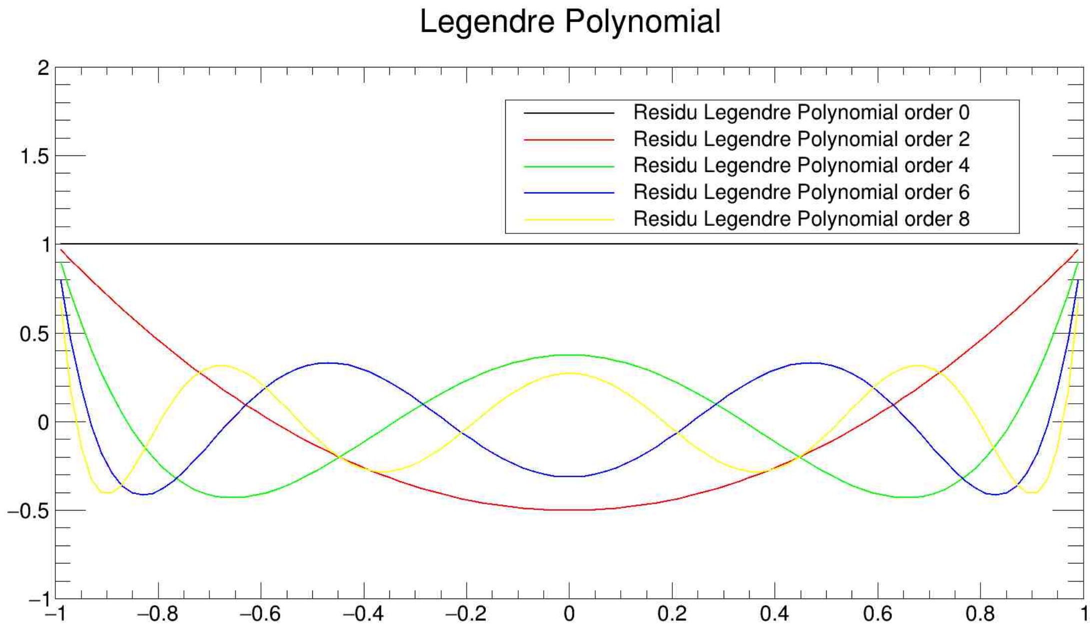

Figure 5.43: Legendre polynomial plots from order 0 to 8.

However, the procedure of averaging the partial cross-sections for each channel and integrating over the total solid angle, which translates into a multiplication by 4π, was implemented. Additionally, it is possible to obtain the total cross-section by comparing the averaged cross-sections obtained in this work with the total ones obtained by gamma-spectroscopy in the works of Becker, *et al.*, [15], as done previously in the first campaign of the STELLA project for a beam energy of $E_{lab} = 10.75$ MeV [37]. Here, it was found that the fraction of the total cross-section for the particles of interest varies according to the exit channel as shown in table 5.4.

Particle	Fraction of the total cross-section [%]
α_0 α_1	48
α_1	31.9
p_0 p_1	28.4
p_1	15.6

Table 5.4: Average fraction of the total cross-section in comparison with the Becker *et al.* data [15]. Taken from [37].

Based on the plots of the angular distributions, the data sets that follow more the trend seen in references [15, 37] are the ones for the proton channel of the S3B backward detector. Nonetheless, a correction factor F_γ can be applied to the differential cross-section formula, equation 5.5, for the different γ transitions in the ^{23}Na nucleus used for making the gating in the coincidence method, based on the data obtained by Firestone [34] for the proton channel. The alpha exit channel is more complex and needs more study. The final equation for the differential cross-section with the correction factor is as equation 5.9 shows, and some correction factors F_γ are shown in table 5.5.

$$\left(\frac{d\sigma}{d\Omega}\right)_{lab} = F_\gamma \frac{N}{I\varepsilon_\gamma \Delta\Omega \Delta t N_t} \tag{5.9}$$

where the parameters are the same as in equation 5.5 with the addition of the correction factor.

Transition	F_γ
$p_2 \rightarrow p_1$	1.903
$p_3 \rightarrow p_0$	1.521
$p_3 \rightarrow p_1$	2.919
$p_5 \rightarrow p_1$	1.029

Table 5.5: F_γ for the γ transitions regarding different populated states of the sodium nuclei.

Once the total cross-section for a certain exit channel, either α or proton, is obtained, the astrophysical

S factor can be calculated. However, a modified version of the S factor, defined as equation 5.10,

$$S* = \sigma E \exp(2\pi\eta + gE) \tag{5.10}$$

where η is the Sommerfeld parameter, eq. 2.15, and $g = 0.122\sqrt{\mu R^3/Z_1 Z_2}$ is the form factor for the ^{12}C fusion reaction derived for $l = 0$ states in a square model potential [36].

Additionally, once it is calculated the S-factor for the proton exit channel, the trend supports the Standard Hindrance model; whereas for the alpha exit channel, the trend is in agreement also with the hindrance model except for the data points below the barrier [36].

Also, the fact that angular distributions follow the trend established by Fruet *et al.* suggests that hindrance behaviour in the carbon fusion is more likely to happen [36] and that a resonance reported by Spillane *et al.* at $E_{rel} = 2.14$ MeV takes place [97].

In conclusion, the path to follow to obtain reliable determination of the S-factor based on the differential cross-sections previously is shown. Despite the anomalies in the trends of the S3F forward detector, the proton exit channel using the S3B detector looks promising especially taking into account the low-energy regime at which this project was done.

Chapter 6

Conclusions

Even though the ^{12}C+^{12}C fusion reaction has been widely studied in the past making use of very meticulous experimental and theoretical tools, there is still the need to make improvements experimentally to accurately determine the cross-section of this reaction. Once precise experimental data points are provided, it is due that the theoretical models adjust to model more accurately, thus, getting a better understanding of the nucleosynthesis process as well as of the internal structure of the carbon 12 isotope.

In this PhD project, the novel technique of using coincident measurements between the evaporated charged particles and gamma-rays was implemented to try to determine more precisely the cross-section of the reaction.

After providing information on the astrophysical scenarios in which carbon takes place as well as the background theory to understand the fusion process in chapter 2, it is discussed in chapter 3 the importance of the ^{12}C+^{12}C fusion and the theoretical and experimental efforts to determine the astrophysical S factor as well as the challenges they face.

In chapter 4, a description of the methodology and experimental setup used for the campaign at IPN to measure coincidences between the evaporated charged particles and the gamma rays related to the de-excitation of the daughter nucleus is made. The setup used proved to be very efficient for background reduction and avoiding target contamination, which were some of the most relevant issues for obtaining a more precise measurement, as previous studies reported.

The angular distributions obtained from the fitting of the peaks in the energy histograms, shown in chapter 5, take into account the α_0, α_1, p_0, and p_1 exit channels. The distributions obtained allowed the calculation of a preliminary cross-section, and even though further analysis is required, the trend of the angular distributions for the backward detector is in agreement with the work of Fruet *et al.* [37], considering that this work was for an energy of interaction well below the Coulomb barrier. Hence, an optimistic attitude towards the remaining analysis is held. Furthermore, it also discusses the path to follow for the calculation of the astrophysical S-factor. The implications of having a reliable cross-section, consequently an S factor, calculation below the Coulomb barrier are essential to get a better understanding of the nucleosynthesis process as well as the outcomes that the carbon fusion will provoke in the life of a star in a particular scenario.

Since the first STELLA collaboration, it has been possible to improve the measurements of the cross-section by reducing the uncertainty of the measurement in the region above the Coulomb barrier [39]. This will be useful not only in the discrimination of theoretical models, such as Hindrance or CC, regarding the description of light heavy-ion fusion but also in the validation of the S-factor proposed by the Trojan Horse Method [104].

Furthermore, the STELLA collaboration and its experimental setup allowed the exploration of carbon fusion at an energy well below the Coulomb barrier thanks to some key features. The coincidence method involving the fast timing $LaBr_3$(Ce) detectors and the DSSDs, alongside the rotating target system, are the principal elements that allowed the good results in the previous campaign [36] as well as the preliminary determination of cross-sections that look promising in an intricate energy region. This methodology is not exclusive to the carbon fusion reaction, it can also be applied to other nuclear reactions key to stellar nucleosynthesis such as ^{12}C+^{16}O or ^{16}O+^{16}O where particular conditions of energy and background noise reduction are involved.
Thus, by continuing with the exploration of the ^{12}C fusion at energies below the Coulomb barrier using the methodology followed in this project, it would shed light on the evolution of, for example, stars with an initial mass of $M_{\odot} = 25$ solar masses and temperatures of $T = 0.9$ GK corresponding to the low energy region in which this project worked.

Appendix A

Kinematics in Nonrelativistic Scenarios

This section refers to the equations used in chapter 5 for two body kinematics used for the calculations of the differential cross sections, as well as for the transformation between the laboratory reference frame and the centre of mass frame taken from [13].

Given a certain nuclear reaction

$$A_1 + A_2 \rightarrow A_3 + A_4$$

where A_3 is the particle being observed.

For the laboratory reference frame, the following quantities are used: E_1, E_3, θ_3, $d\omega_3$. For the centre of mass reference frame, the following quantities were used: E_i, $E_f = E_i + Q$, Θ, $d\Omega$, where Q is the Q-value of the reaction.

For transformations from the CM system to the laboratory frame:

$$\gamma_3 = \left(\frac{A_1 A_3}{A_2 A_4} \frac{E_i}{E_i + Q} \right)^2 \tag{A.1}$$

$$\tan \theta_3 = \frac{\sin \Theta}{\cos \Theta + \gamma_3} \tag{A.2}$$

$$E_3 = \frac{A_1 A_3 E_i}{A_2 (A_1 + A_2)} \left(\frac{1 + \gamma_3^2 + 2\gamma_3 \cos \Theta}{\gamma_3^2} \right) \tag{A.3}$$

$$\frac{d\sigma}{d\omega_3} = \frac{d\sigma}{d\Omega} \frac{(1 + \gamma_3^2 + 2\gamma_3 \cos \Theta)^{\frac{3}{2}}}{|1 + \gamma_3 \cos \Theta|} \tag{A.4}$$

To obtain the angle and differential cross section in the CM reference frame given a laboratory angle:

$$\sin\Theta = \sin\theta_3[\gamma_3\cos\theta_3 \pm \left(1-\gamma_3^2\sin^2\theta_3\right)^{\frac{1}{2}}] \tag{A.5}$$

$$E_3 = \frac{A_1A_3E_i}{A_2(A_1+A_2)}\frac{[\gamma_3\cos\theta_3 \pm (1-\gamma_3^2\sin^2\theta_3)^{\frac{1}{2}}]^2}{\gamma_3^2} \tag{A.6}$$

$$\frac{d\sigma}{d\omega_3} = \frac{d\sigma}{d\Omega}\frac{[\gamma_3\cos\theta_3 \pm (1-\gamma_3^2\sin^2\theta_3)^{\frac{1}{2}}]^2}{\left(1-\gamma_3^2\sin^2\theta_3\right)^{\frac{1}{2}}} \tag{A.7}$$

Figure A.1 shows the kinematic calculations for the p_0 and p_1 particles of the ^{23}Na exit channel of the ^{12}C fusion reaction which has a Q value of $Q = 2.24$ MeV. This simulation was done for a beam energy of $E_{beam} = 9.74$ MeV and in the laboratory reference system [37].

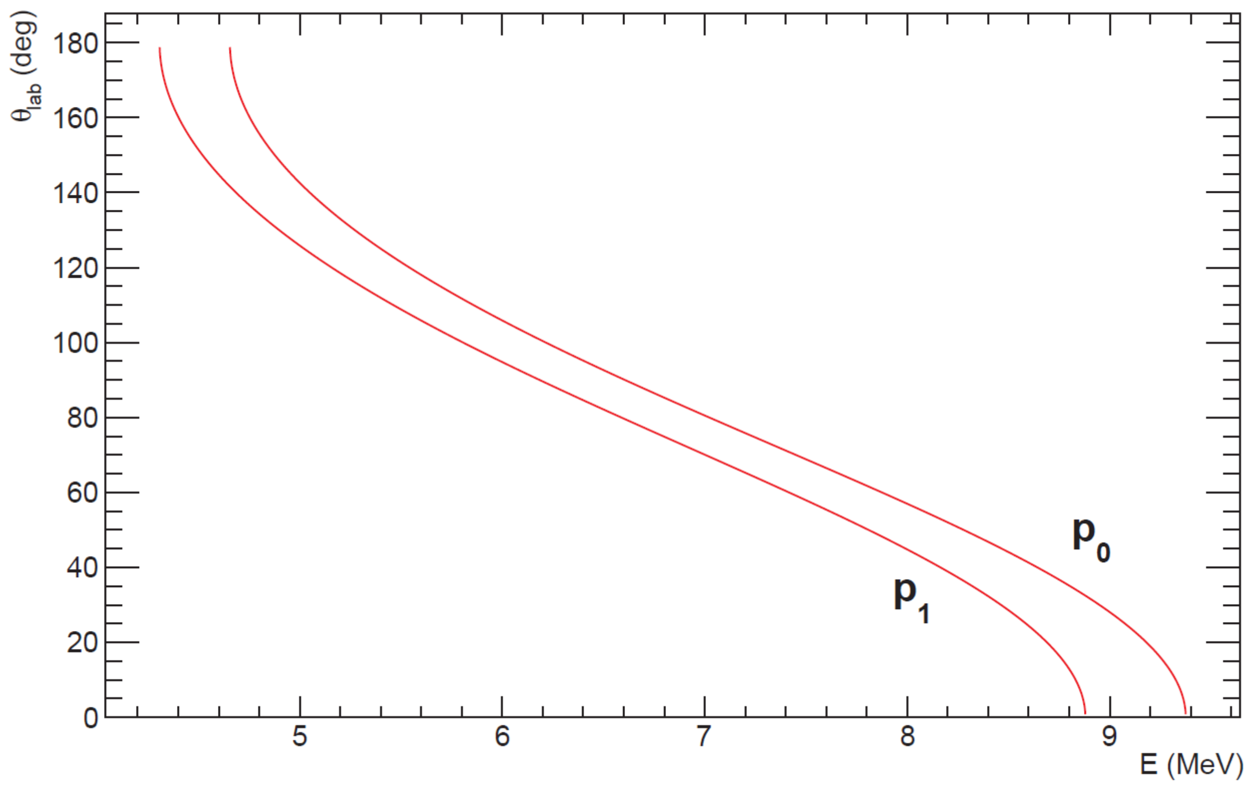

Figure A.1: p_0 and p_1 kinematic calculations for the ^{23}Na exit channel of the ^{12}C fusion reaction with $E_{beam} = 9.74$ MeV. Taken from [37].

Appendix B

Parameters of the fitting routine

The peak parameters for each peak of the 24 detectors of S3F are shown in the tables below along with their associated error. The peak fitting routine was done using "CERN ROOT" software through the chi-square method. The plots of the energy histograms with their respective fittings are shown in chapter 5.

Detector 1		Value	Error
Peak 1	p0	4.393	0.457609
	p1	12.9563	0.0126767
	p2	0.162805	0.0187265
Peak 2	p0	67.6394	1.65789
	p1	11.0786	0.0026934
	p2	0.124043	0.0010809

Table B.1 continued from previous page

Detector 1		Value	Error
Peak 3	p0	2.4719	40.6977
	p1	17.3379	49.0185
	p2	6.95437	166.4
Peak 4	p0	6.87861	23.5515
	p1	-1239.88	2817.58
	p2	999.975	854.052
Peak 5	p0	26.0322	7.09E-16
	p1	7.2665	2.06E-17
	p2	0.105348	0
	p3	25.2985	3.35E-16
	p4	7.79465	2.36E-18
	p5	0.126695	0
	p6	-20.4939	1.59E-14

Table B.1 continued from previous page

Detector 1		Value	Error
	p7	-5.0552	1.18E-23
Peak 6	p0	-1.40E+03	2.54E+00
	p1	7.41E+00	1.00E+00
	p2	1.46E-01	6.10E+02
	p3	6.63E+01	2.51E+00
	p4	7.19E+00	1.00E+00
	p5	1.69E-01	6.09E+02
	p6	8.76E+00	2.53E+00
	p7	-4.90E+00	1.00E+00
Peak 7	p0	-9.62E+02	1.15E+00
	p1	6.25E+00	1.00E+00
	p2	1.14E-01	6.10E+02
	p3	3.62E+01	2.58E+00

Table B.1 continued from previous page

Detector 1		Value	Error
	p4	6.65E+00	1.00E+00
	p5	8.72E-02	6.11E+02
	p6	5.10E+01	1.15E+00
	p7	-1.25E+01	1.00E+00
Peak 8	p0	6.59E+05	3.96E+06
	p1	5.98E+00	4.27E-02
	p2	3.09E-02	8.52E-03
	p3	4.75E+01	3.88E+00
	p4	6.30E+00	2.97E-03
	p5	6.66E-02	7.68E-03
	p6	-7.35E+01	9.02E+00
	p7	1.40E+01	1.46E+00
Peak 9	p0	2.98E+04	6.36E+01

Table B.1 continued from previous page

Detector 1		Value	Error
	p1	4.57E+00	1.73E+00
	p2	2.32E-04	6.15E+02
	p3	3.96E+01	1.38E+00
	p4	5.93E+00	1.00E+00
	p5	1.57E-01	6.10E+02
	p6	1.23E+01	1.30E+00
	p7	-2.99E+00	1.01E+00
Peak 10	p0	3.93E+05	6.36E+01
	p1	6.68E+00	1.55E-05
	p2	5.97E-02	1.29E-03
	p3	3.03E+01	3.61E+00
	p4	5.73E+00	1.22E-02
	p5	1.24E-01	2.22E-02
	p6	1.80E+01	2.09E+00

Table B.1 continued from previous page

Detector 1		Value	Error
	p7	-1.75E+00	3.40E-01
Peak 11	p0	-1.94E+02	1.41E+00
	p1	4.70E+00	1.00E+00
	p2	1.71E-02	6.13E+02
	p3	1.72E+01	1.44E+00
	p4	5.06E+00	1.00E+00
	p5	1.32E-01	6.10E+02
	p6	1.59E+01	1.40E+00
	p7	-2.80E+00	1.05E+00
Peak 12	p0	-3.38E+01	8.31E+00
	p1	5.05E+00	1.62E-01
	p2	1.34E-01	5.20E-02
	p3	1.87E+01	8.06E+00

Table B.1 continued from previous page

Detector 1		Value	Error
	p4	4.89E+00	1.68E-02
	p5	5.28E-02	1.60E-02
	p6	-5.17E+02	2.05E+02
	p7	1.12E+02	4.37E+01
Peak 13	p0	5.69E+01	1.41E+00
	p1	4.78E+00	1.41E+00
	p2	2.93E-02	7.08E+02
	p3	1.66E+01	1.11E+00
	p4	4.17E+00	1.14E-02
	p5	1.97E-01	2.39E-02
	p6	-8.77E+01	1.37E+00
	p7	2.05E+01	4.39E-01
Peak 14	p0	-4.39E+11	7.52E+12

Table B.1 continued from previous page

Detector 1		Value	Error
	p1	3.18E+00	1.68E-01
	p2	4.32E-02	1.24E-01
	p3	1.65E+02	8.50E+01
	p4	3.29E+00	4.15E-03
	p5	5.10E-03	4.51E-04
	p6	2.51E+01	3.30E-01
	p7	-4.75E+00	8.83E-02

Table B.1: Peak parameters for S3F 1st detector.

Detector 2

	Parameter	Value	Error
Peak 1	p0	6.57E+00	5.29E-01
	p1	1.30E+01	8.59E-03
	p2	1.44E-01	1.08E-02

Table B.2 continued from previous page

Detector 2

Peak 2	p0	7.77E+01	1.60E+00
	p1	1.11E+01	2.18E-03
	p2	1.28E-01	1.65E-03
Peak 3	p0	2.88E+00	1.00E+00
	p1	8.90E+00	1.99E+00
	p2	2.83E-01	8.46E+02
Peak 4	p0	1.72E+00	2.71E-01
	p1	8.56E+00	5.66E-01
	p2	6.78E-01	3.40E+00
Peak 5	p0	2.02E+01	1.03E+00
	p1	7.76E+00	1.54E-02
	p2	1.27E-01	1.02E-02

Table B.2 continued from previous page

Detector 2

	p3	5.69E+00	2.25E+00
	p4	7.96E+00	2.02E-02
	p5	1.63E-01	3.19E-02
	p6	-4.46E+10	3.50E+04
	p7	-8.72E+00	3.22E-20
Peak 6	p0	-3.68E+02	1.49E+02
	p1	6.55E+00	2.24E-01
	p2	2.88E-01	4.41E-01
	p3	2.49E+02	2.31E+02
	p4	6.79E+00	4.40E-02
	p5	1.62E-01	1.55E-01
	p6	-7.24E+00	2.15E-16
	p7	-9.57E+15	2.21E+03

Table B.2 continued from previous page

Detector 2

Peak 7	p0	-9.47E+06	7.39E+06
	p1	8.63E+00	2.29E-01
	p2	3.93E-01	6.53E-02
	p3	2.02E+02	4.01E+01
	p4	7.01E+00	4.21E-02
	p5	2.34E-01	2.30E-02
	p6	4.86E+00	7.99E+00
	p7	-1.38E+00	8.80E-01
Peak 8	p0	1.22E+01	8.52E+00
	p1	6.67E+00	6.23E-02
	p2	3.02E-01	4.83E-01
	p3	5.17E+01	5.31E+00
	p4	6.28E+00	4.10E-03
	p5	6.72E-02	6.27E-03

Table B.2 continued from previous page

Detector 2

	p6	1.33E+01	2.27E+01
	p7	-5.85E-01	1.90E+00
Peak 9	p0	8.15E+02	6.36E+01
	p1	5.18E+00	1.41E+00
	p2	2.02E-03	2.91E-06
	p3	1.27E+01	3.33E+00
	p4	5.93E+00	9.19E-03
	p5	5.40E-02	2.23E-02
	p6	1.67E+02	4.91E+01
	p7	-2.47E+01	7.87E+00
Peak 10	p0	1.47E+02	4.30E+05
	p1	-2.44E+02	1.68E+01
	p2	1.35E+00	4.94E-03

Table B.2 continued from previous page

Detector 2

	p3	4.16E+01	8.54E+00
	p4	5.71E+00	9.48E-03
	p5	1.59E-01	3.07E-02
	p6	8.28E+00	5.14E+00
	p7	-2.86E+00	6.74E-01
Peak 11	p0	-1.33E+04	1.11E+00
	p1	3.31E+00	2.32E+00
	p2	4.42E-01	5.57E-01
	p3	1.81E+01	1.63E+01
	p4	5.01E+00	9.73E-02
	p5	1.02E-01	5.10E-02
	p6	3.21E+01	4.64E+01
	p7	-5.62E+00	9.25E+00

Table B.2 continued from previous page

Detector 2

Peak 12	p0	-1.98E+01	3.26E+01
	p1	5.05E+00	2.75E-01
	p2	1.25E-01	1.24E-01
	p3	4.15E+01	7.33E+00
	p4	4.88E+00	1.11E-02
	p5	7.86E-02	9.58E-03
	p6	8.67E+01	4.99E+00
	p7	-1.80E+01	1.06E+00
Peak 13	p0	-2.01E+03	8.05E-01
	p1	3.97E+00	8.11E-01
	p2	7.72E-03	7.12E+02
	p3	4.28E+01	7.86E-01
	p4	4.41E+00	2.08E-02
	p5	4.91E-01	3.70E-02

Table B.2 continued from previous page

Detector 2

	p6	5.45E+01	7.86E-01
	p7	-2.10E+01	2.55E-01
Peak 14	p0	1.46E+04	6.36E+01
	p1	4.84E+00	1.73E+00
	p2	5.26E-04	6.15E+02
	p3	1.37E+00	1.16E+00
	p4	3.77E+00	1.00E+00
	p5	2.82E-02	6.13E+02
	p6	1.10E+01	1.02E+00
	p7	-2.24E+00	1.00E+00

Table B.2: Peak parameters for S3F 2nd detector.

Detector 3

	Parameter	Value	Error

Table B.3 continued from previous page

Detector 3

Peak 1	p0	5.25E+00	4.04E-01
	p1	1.29E+01	1.17E-02
	p2	1.78E-01	1.33E-02
Peak 2	p0	8.20E+01	1.60E+00
	p1	1.11E+01	2.16E-03
	p2	1.32E-01	1.56E-03
Peak 3	p0	1.15E+00	1.25E+00
	p1	8.89E+01	1.52E+04
	p2	7.01E+02	5.38E+02
Peak 4	p0	3.62E+02	1.68E+03
	p1	2.47E+00	7.66E+00
	p2	1.87E+00	1.69E+00

Table B.3 continued from previous page

Detector 3

Peak 5	p0	2.36E+01	6.27E-01
	p1	7.78E+00	4.86E-03
	p2	1.65E-01	3.45E-03
	p3	-3.43E+04	3.20E+01
	p4	2.09E+01	1.41E+00
	p5	5.68E-03	7.10E+02
	p6	-1.76E+20	1.41E+00
	p7	-7.17E+00	1.41E+00
Peak 6	p0	-1.13E+07	4.04E-09
	p1	7.37E+00	1.84E-11
	p2	9.26E-02	3.30E-12
	p3	-8.55E+00	4.04E-09
	p4	7.03E+00	1.01E-10

Table B.3 continued from previous page

Detector 3

	p5	6.16E-02	3.46E-11
	p6	5.11E+00	9.05E-08
	p7	-5.74E+00	1.09E-18
Peak 7	p0	-5.53E+01	8.48E-01
	p1	6.64E+00	7.52E-04
	p2	3.68E-02	6.25E-04
	p3	9.23E+01	7.68E-01
	p4	6.65E+00	5.02E-04
	p5	4.52E-02	4.41E-04
	p6	2.65E+01	6.73E+05
	p7	-6.65E+00	1.29E+05
Peak 8	p0	5.20E+01	4.45E+00
	p1	6.28E+00	3.88E-03

Table B.3 continued from previous page

Detector 3

	p2	6.68E-02	6.25E-03
	p3	-5.00E+01	4.78E+01
	p4	6.11E+00	2.26E-01
	p5	1.07E+00	3.26E+00
	p6	-4.58E+01	2.30E+02
	p7	1.76E+01	4.20E+01
Peak 9	p0	8.54E+02	6.36E+01
	p1	5.23E+00	1.41E+00
	p2	6.27E-03	1.09E-06
	p3	2.36E+01	1.07E+00
	p4	5.91E+00	8.58E-03
	p5	1.15E-01	1.10E-02
	p6	1.93E+01	7.52E-01
	p7	-1.89E+00	1.26E-01

Table B.3 continued from previous page

Detector 3

Peak 10	p0	-9.42E+01	1.18E+01
	p1	5.87E+00	1.98E-02
	p2	1.28E-01	1.23E-02
	p3	1.97E+02	1.69E+01
	p4	6.06E+00	2.25E-02
	p5	3.05E-01	1.51E-02
	p6	-3.94E+00	6.07E+00
	p7	-3.55E+00	1.11E+00
Peak 11	p0	-1.55E+04	6.36E+01
	p1	3.11E+00	1.42E+00
	p2	3.07E-01	9.26E-05
	p3	1.66E+01	2.48E+00
	p4	5.03E+00	2.42E-02

Table B.3 continued from previous page

Detector 3

	p5	1.05E-01	3.39E-02
	p6	1.39E+01	1.34E+00
	p7	-2.65E+00	2.61E-01
Peak 12	p0	-5.08E+06	1.77E+06
	p1	-5.55E+01	8.33E-01
	p2	1.20E+01	1.64E-01
	p3	2.62E+01	1.89E+00
	p4	4.87E+00	4.00E-03
	p5	5.63E-02	4.40E-03
	p6	-9.85E+00	5.98E+00
	p7	6.96E+00	1.26E+00
Peak 13	p0	-1.37E+01	2.34E+01
	p1	5.15E+00	2.75E+00

Table B.3 continued from previous page

Detector 3

	p2	8.65E-01	1.62E+00
	p3	8.01E+00	4.63E+00
	p4	4.17E+00	4.39E-02
	p5	2.15E-01	7.18E-02
	p6	-7.01E+01	2.25E+01
	p7	1.79E+01	3.56E+00
Peak 14	p0	1.78E+03	1.00E+00
	p1	3.03E+00	1.00E+00
	p2	4.57E-02	2.46E-01
	p3	3.59E-01	1.00E+00
	p4	3.74E+00	1.00E+00
	p5	9.32E-03	2.30E+02
	p6	7.07E+00	1.00E+00
	p7	-1.28E+00	1.00E+00

Table B.3 continued from previous page

Detector 3

Table B.3: Peak parameters for S3F 3rd detector.

Detector 4

	Parameter	Value	Error
Peak 1	p0	5.78E+00	4.63E-01
	p1	1.29E+01	1.09E-02
	p2	1.73E-01	1.40E-02
Peak 2	p0	7.91E+01	1.52E+00
	p1	1.10E+01	2.26E-03
	p2	1.44E-01	1.71E-03
Peak 3	p0	1.81E+00	6.05E+00
	p1	8.49E+00	5.54E+00
	p2	8.69E-01	2.84E+00

Table B.4 continued from previous page

Detector 4

Peak 4	p0	1.55E+00	9.76E+00
	p1	-2.01E+02	1.11E+04
	p2	7.09E+02	5.85E+02
Peak 5	p0	2.14E+01	1.45E-92
	p1	7.71E+00	9.68E-95
	p2	1.19E-01	0.00E+00
	p3	9.39E+00	1.23E-92
	p4	9.11E+00	1.66E-93
	p5	1.31E+00	0.00E+00
	p6	-3.80E+01	5.00E-137
	p7	-1.19E+01	2.13E-114
Peak 6	p0	-3.12E+02	2.96E+01

Table B.4 continued from previous page

Detector 4

	p1	6.77E+00	7.37E-03
	p2	1.22E-01	7.46E-03
	p3	6.52E+01	1.09E+01
	p4	6.85E+00	6.25E-03
	p5	3.89E-02	6.97E-03
	p6	3.83E+01	8.72E-02
	p7	-4.82E+00	1.95E-02
Peak 7	p0	3.37E+02	8.87E+00
	p1	6.85E+00	7.22E-03
	p2	1.60E-01	6.48E-03
	p3	-2.04E+03	5.79E+01
	p4	7.21E+00	2.13E-03
	p5	2.32E-01	8.47E-04
	p6	1.63E+01	3.29E+02

Table B.4 continued from previous page

Detector 4

	p7	-2.63E+00	4.81E+01
Peak 8	p0	-1.95E+01	8.62E+02
	p1	6.27E+00	1.71E-02
	p2	1.89E-03	1.01E-01
	p3	6.03E+01	5.34E+00
	p4	6.27E+00	5.08E-03
	p5	7.58E-02	8.89E-03
	p6	1.41E+02	1.13E+02
	p7	-2.11E+01	1.76E+01
Peak 9	p0	-8.86E+02	6.37E+01
	p1	5.34E+00	1.64E+00
	p2	1.73E-02	7.65E+02
	p3	1.66E+01	1.00E+00

Table B.4 continued from previous page

Detector 4

	p4	5.89E+00	1.64E+00
	p5	6.54E-02	7.63E+02
	p6	2.04E+01	1.79E+00
	p7	-6.05E-01	1.64E+00
Peak 10	p0	1.71E+01	3.02E+00
	p1	5.59E+00	1.94E-02
	p2	1.23E-01	2.54E-02
	p3	1.14E+02	3.67E+01
	p4	6.99E+00	3.89E-01
	p5	1.16E+00	5.08E-01
	p6	-3.11E+01	2.28E+01
	p7	-1.92E+00	1.27E+00
Peak 11	p0	-5.82E+01	6.47E+01

Table B.4 continued from previous page

Detector 4

	p1	1.51E+01	1.65E+01
	p2	1.29E+01	2.32E+01
	p3	2.23E+01	1.60E+00
	p4	5.02E+00	1.29E-02
	p5	8.88E-02	1.28E-02
	p6	-8.49E+01	1.10E+01
	p7	2.47E+01	1.06E+01
Peak 12	p0	-4.29E+02	1.37E+02
	p1	4.81E+00	9.95E-02
	p2	7.81E-02	2.02E-02
	p3	4.51E+02	1.20E+02
	p4	4.81E+00	9.53E-02
	p5	7.76E-02	1.55E-02
	p6	2.05E+01	3.34E+00

Table B.4 continued from previous page

Detector 4

	p7	-2.54E+00	1.39E+00
Peak 13	p0	-2.90E+01	3.28E+01
	p1	3.55E+00	4.39E-01
	p2	2.94E-01	1.48E-01
	p3	2.43E+03	1.18E+04
	p4	4.18E+00	3.22E-03
	p5	2.35E-04	7.58E-04
	p6	1.02E+02	3.96E-01
	p7	-2.23E+01	1.74E-01
Peak 14	p0	-1.67E+05	1.68E+06
	p1	2.30E+00	7.47E-01
	p2	2.44E-01	1.38E-01
	p3	2.06E+00	1.16E+00

Table B.4 continued from previous page

Detector 4

	p4	3.76E+00	1.06E-02
	p5	1.56E-02	8.88E-03
	p6	1.67E+01	1.19E+00
	p7	-3.86E+00	3.12E-01

Table B.4: Peak parameters for S3F 4th detector.

Detector 5

	Parameter	Value	Error
Peak 1	p0	5.63E+00	4.27E-01
	p1	1.29E+01	1.10E-02
	p2	1.70E-01	1.21E-02
Peak 2	p0	8.70E+01	1.59E+00
	p1	1.10E+01	2.14E-03
	p2	1.39E-01	1.52E-03

Table B.5 continued from previous page

Detector 5

Peak 3	p0	1.44E+00	7.73E+00
	p1	9.80E+00	1.80E+01
	p2	8.95E-01	7.03E+01
Peak 4	p0	1.37E+00	2.77E-01
	p1	8.78E+00	1.24E-01
	p2	3.16E-01	3.97E-01
Peak 5	p0	6.28E+01	8.20E+01
	p1	7.83E+00	1.55E-01
	p2	2.46E-01	1.53E-01
	p3	-1.27E+02	2.38E+02
	p4	8.77E+00	4.69E-01
	p5	6.06E-01	3.90E-01

Table B.5 continued from previous page

Detector 5

	p6	-5.85E+14	3.91E+04
	p7	-8.14E+00	1.21E-11
Peak 6	p0	-5.52E+03	3.35E+02
	p1	5.82E+00	5.58E-03
	p2	3.11E-01	1.64E-03
	p3	4.86E+01	1.19E+00
	p4	6.72E+00	6.23E-03
	p5	2.24E-01	5.85E-03
	p6	-1.57E+05	2.92E+00
	p7	-2.96E+22	1.41E+00
Peak 7	p0	-2.54E+02	4.55E+01
	p1	6.66E+00	5.24E-03
	p2	6.67E-02	6.95E-03

Table B.5 continued from previous page

Detector 5

	p3	1.52E+02	4.92E+01
	p4	6.68E+00	4.37E-03
	p5	4.30E-02	3.12E-03
	p6	5.40E+01	4.11E+00
	p7	-7.36E+00	6.20E-01
Peak 8	p0	-7.92E+01	1.72E-02
	p1	7.81E+00	2.98E+01
	p2	2.91E+02	8.45E+02
	p3	5.70E+01	4.24E-02
	p4	6.32E+00	5.47E-05
	p5	6.08E-02	4.04E-05
	p6	-8.39E+01	1.72E-02
	p7	2.89E+01	2.74E-03

Table B.5 continued from previous page

Detector 5

Peak 9	p0	-7.16E+02	6.36E+01
	p1	5.14E+00	1.03E+00
	p2	3.37E-03	6.14E+02
	p3	2.03E+01	1.45E+00
	p4	5.91E+00	1.00E+00
	p5	1.23E-01	6.10E+02
	p6	2.15E+01	1.26E+00
	p7	-1.62E+00	1.01E+00
Peak 10	p0	-4.32E+02	2.19E+02
	p1	6.00E+00	2.19E+02
	p2	2.36E-02	6.73E+02
	p3	6.71E+01	4.76E+00
	p4	5.70E+00	2.19E+02
	p5	2.13E-01	6.78E+02

Table B.5 continued from previous page

Detector 5

	p6	-1.46E+01	1.97E+02
	p7	-3.00E+00	2.18E+02
Peak 11	p0	-2.30E+04	2.22E+04
	p1	4.45E+00	9.97E-02
	p2	1.66E-01	2.83E-02
	p3	2.30E+02	3.83E+01
	p4	4.71E+00	9.75E-02
	p5	1.87E-01	4.65E-02
	p6	4.34E+01	1.41E+01
	p7	-8.00E+00	2.60E+00
Peak 12	p0	1.82E+04	6.36E+01
	p1	6.78E+00	1.41E+00
	p2	1.13E-02	5.04E-09

Table B.5 continued from previous page

Detector 5

	p3	3.69E+01	1.73E+00
	p4	4.93E+00	2.85E-03
	p5	6.93E-02	6.79E-03
	p6	1.31E+01	1.44E+00
	p7	-2.38E+00	2.78E-01
Peak 13	p0	-2.98E+01	1.00E+01
	p1	3.75E+00	4.92E-03
	p2	7.11E-02	1.61E-03
	p3	8.12E+01	2.26E+00
	p4	4.27E+00	8.14E-03
	p5	4.50E-01	2.55E-02
	p6	-2.53E+01	7.58E-01
	p7	-1.12E+01	2.90E-01

Table B.5 continued from previous page

Detector 5

Peak 14	p0	-4.16E+04	7.66E+04
	p1	5.05E+00	5.15E-01
	p2	2.87E-01	1.74E-01
	p3	4.22E+01	3.91E+01
	p4	3.98E+00	1.71E-02
	p5	2.56E-01	3.13E-02
	p6	-4.53E+00	1.34E+01
	p7	-5.48E+00	3.61E+00

Table B.5: Parameters for S3F 5th detector.

Detector 6

	Parameter	Value	Error
Peak 1	p0	4.56E+00	3.67E-01
	p1	1.29E+01	1.49E-02
	p2	2.17E-01	1.89E-02

Table B.6 continued from previous page

Detector 6

Peak 2	p0	7.52E+01	1.40E+00
	p1	1.10E+01	2.69E-03
	p2	1.60E-01	1.84E-03
Peak 3	p0	1.83E+00	4.18E+00
	p1	1.31E+01	1.21E+01
	p2	4.17E+00	1.10E+01
Peak 4	p0	1.45E+00	2.85E-01
	p1	8.87E+00	4.19E-01
	p2	4.58E-01	1.07E+00
Peak 5	p0	1.72E+02	8.83E+01
	p1	6.69E+00	2.99E-01

Table B.6 continued from previous page

Detector 6

	p2	5.34E-01	7.84E-02
	p3	-6.63E+01	4.47E+00
	p4	7.35E+00	2.33E-02
	p5	1.30E-01	1.32E-02
	p6	-3.82E+10	1.17E-03
	p7	-8.34E+00	1.31E-14
Peak 6	p0	-6.01E+02	1.21E-54
	p1	6.62E+00	7.82E-59
	p2	9.65E-02	0.00E+00
	p3	5.56E+01	4.65E-56
	p4	6.77E+00	1.33E-58
	p5	1.54E-01	0.00E+00
	p6	6.85E+00	3.13E-70
	p7	-1.00E+01	6.45E-93

Table B.6 continued from previous page

Detector 6

Peak 7	p0	-1.66E+03	8.37E-15
	p1	6.99E+00	1.34E-17
	p2	9.81E-02	0.00E+00
	p3	7.00E+01	6.67E-15
	p4	6.80E+00	2.43E-17
	p5	1.38E-01	0.00E+00
	p6	2.83E+01	1.87E-13
	p7	-9.66E+00	3.67E-30
Peak 8	p0	2.68E+04	9.17E+04
	p1	7.14E+00	1.50E-01
	p2	1.82E-01	3.98E-02
	p3	6.65E+01	5.22E+00
	p4	6.28E+00	3.22E-03

Table B.6 continued from previous page

Detector 6

	p5	6.58E-02	6.24E-03
	p6	-7.16E+01	9.37E+00
	p7	1.30E+01	1.53E+00
Peak 9	p0	-4.29E+04	6.36E+01
	p1	4.77E+00	1.73E+00
	p2	2.08E-04	6.15E+02
	p3	2.52E+01	1.43E+00
	p4	5.91E+00	1.00E+00
	p5	1.03E-01	6.11E+02
	p6	1.82E+01	1.25E+00
	p7	-1.89E+00	1.01E+00
Peak 10	p0	1.09E+02	4.16E+01
	p1	5.96E+00	3.37E-01

Table B.6 continued from previous page

Detector 6

	p2	4.42E-01	5.02E-02
	p3	-2.24E+01	1.83E+01
	p4	5.68E+00	4.92E-02
	p5	5.23E-02	3.86E-02
	p6	-5.85E+00	1.08E+01
	p7	-5.57E+00	2.68E+00
Peak 11	p0	-1.58E+03	6.37E+01
	p1	4.35E+00	1.66E+00
	p2	2.00E-03	6.14E+02
	p3	2.92E+01	6.08E+00
	p4	5.09E+00	1.00E+00
	p5	1.41E-01	6.10E+02
	p6	1.27E+01	1.79E+00
	p7	-4.62E+00	1.60E+00

Table B.6 continued from previous page

Detector 6

Peak 12	p0	-7.62E+05	6.36E+01
	p1	1.14E+01	1.11E+01
	p2	1.04E-01	6.19E+02
	p3	3.89E+01	2.28E+00
	p4	4.87E+00	1.00E+00
	p5	7.59E-02	6.11E+02
	p6	1.34E+01	1.21E+00
	p7	-2.65E+00	1.01E+00
Peak 13	p0	1.23E+04	1.01E+02
	p1	2.50E+00	1.07E+01
	p2	3.75E-03	8.88E+02
	p3	8.01E+00	1.58E+00
	p4	4.20E+00	1.04E+01

Table B.6 continued from previous page

Detector 6

	p5	1.15E-01	8.92E+02
	p6	7.22E+00	9.77E+00
	p7	-1.69E+00	1.04E+01
Peak 14	p0	-2.11E+06	8.98E+06
	p1	2.90E+00	9.12E-02
	p2	7.86E-02	1.67E-02
	p3	5.04E+00	3.61E+00
	p4	3.41E+00	1.11E-02
	p5	9.76E-03	9.88E-03
	p6	5.42E+01	1.91E+00
	p7	-1.40E+01	5.30E-01

Table B.6: Peak parameters for S3F 6th detector.

Detector 7

	Parameter	Value	Error
Peak 1	p0	4.75E+00	3.55E-01
	p1	1.28E+01	1.54E-02
	p2	2.34E-01	1.84E-02
Peak 2	p0	7.61E+01	1.48E+00
	p1	1.09E+01	2.88E-03
	p2	1.68E-01	2.20E-03
Peak 3	p0	1.62E+00	2.87E-01
	p1	9.31E+00	1.37E-01
	p2	3.59E-01	4.95E-01
Peak 4	p0	4.42E+01	4.20E+02
	p1	1.43E+00	2.58E+01
	p2	2.87E+00	6.25E+00

Table B.7 continued from previous page

Detector 7

Peak 5	p0	3.42E+01	2.96E-45
	p1	7.59E+00	1.89E-47
	p2	1.42E-01	0.00E+00
	p3	1.38E+01	4.37E-45
	p4	8.00E+00	6.60E-47
	p5	1.50E-01	0.00E+00
	p6	-3.44E+01	1.27E-43
	p7	-2.01E-01	1.34E-110
Peak 6	p0	-1.35E+03	2.02E+03
	p1	7.10E+00	8.08E-02
	p2	2.94E-02	2.36E-02
	p3	2.07E+01	2.60E+00
	p4	6.98E+00	1.43E-01

Table B.7 continued from previous page

Detector 7

	p5	2.01E-01	1.71E-01
	p6	3.19E+01	3.39E+00
	p7	-5.65E+00	4.95E-01
Peak 7	p0	-7.58E+03	4.82E+03
	p1	7.40E+00	1.20E-01
	p2	2.42E-01	8.24E-03
	p3	2.38E+02	1.13E+02
	p4	6.86E+00	4.75E-02
	p5	1.44E-01	2.87E-02
	p6	6.65E+00	4.69E+01
	p7	-5.81E-01	7.30E+00
Peak 8	p0	7.71E+01	4.38E+01
	p1	6.29E+00	5.17E-03

Table B.7 continued from previous page

Detector 7

	p2	1.41E-01	7.51E-02
	p3	3.24E+01	9.68E+00
	p4	6.27E+00	6.20E-03
	p5	4.09E-02	8.52E-03
	p6	1.02E+01	3.51E+01
	p7	-5.66E+00	2.39E+00
Peak 9	p0	-1.59E+02	5.10E+01
	p1	5.48E+00	3.27E-01
	p2	4.85E-01	1.26E-01
	p3	1.98E+02	2.46E+01
	p4	5.67E+00	1.04E-01
	p5	3.91E-01	2.56E-02
	p6	3.26E+00	1.51E+01
	p7	-5.63E+00	4.23E+00

Table B.7 continued from previous page

Detector 7

Peak 10	p0	1.86E+01	1.10E+01
	p1	5.46E+00	3.17E-02
	p2	7.64E-02	1.75E-02
	p3	3.07E+01	4.15E+00
	p4	5.62E+00	3.20E-02
	p5	9.75E-02	3.15E-02
	p6	3.03E+01	5.24E+00
	p7	-4.63E+00	9.98E-01
Peak 11	p0	-1.52E+02	2.72E+02
	p1	4.74E+00	3.22E-01
	p2	1.57E-01	9.19E-02
	p3	4.21E+01	6.72E+00
	p4	4.97E+00	3.22E-02

Table B.7 continued from previous page

Detector 7

	p5	1.17E-01	2.79E-02
	p6	6.22E+01	1.71E+01
	p7	-1.07E+01	3.38E+00
Peak 12	p0	-9.09E+01	9.47E+01
	p1	5.19E+00	1.78E-01
	p2	1.85E-01	1.42E-01
	p3	9.54E+01	6.70E+01
	p4	4.92E+00	5.38E-03
	p5	1.22E-01	1.48E-02
	p6	1.54E+02	2.10E+02
	p7	-3.65E+01	4.35E+01
Peak 13	p0	-4.84E+00	1.14E+01
	p1	3.53E+00	1.60E-01

Table B.7 continued from previous page

Detector 7

	p2	4.08E-01	5.00E-01
	p3	9.90E+00	3.65E+00
	p4	4.13E+00	2.17E-02
	p5	1.38E-01	3.86E-02
	p6	-6.30E+00	4.93E+01
	p7	2.03E+00	1.13E+01
Peak 14	p0	1.04E+01	1.08E+01
	p1	3.23E+00	1.89E-01
	p2	2.11E-01	1.31E-01
	p3	3.47E+02	7.18E+02
	p4	3.83E+00	5.59E-02
	p5	1.00E-02	1.93E-02
	p6	-6.54E+01	5.59E+01
	p7	1.88E+01	1.45E+01

Table B.7 continued from previous page

Detector 7

Table B.7: Peak parameters for S3F 7th detector

Detector 8

	Parameter	Value	Error
Peak 1	p0	7.91E+00	6.30E-01
	p1	1.27E+01	7.06E-03
	p2	1.09E-01	7.76E-03
Peak 2	p0	1.13E+02	2.13E+00
	p1	1.08E+01	1.77E-03
	p2	1.15E-01	1.41E-03
Peak 3	p0	2.32E+00	3.79E+00
	p1	9.63E+00	4.44E+00
	p2	7.44E-01	4.96E+00

Table B.8 continued from previous page

Detector 8

Peak 4	p0	4.24E+00	3.13E+00
	p1	7.75E+00	1.15E+00
	p2	9.19E-01	6.25E-01
Peak 5	p0	3.81E+01	1.19E+00
	p1	7.56E+00	6.23E-03
	p2	1.48E-01	6.15E-03
	p3	9.98E+00	2.29E+00
	p4	7.33E+00	1.00E-02
	p5	3.78E-02	1.11E-02
	p6	-1.57E+14	6.95E+04
	p7	-7.83E+00	5.89E-11
Peak 6	p0	-3.58E+01	9.15E-01

Table B.8 continued from previous page

Detector 8

	p1	7.40E+00	3.61E-03
	p2	2.15E-01	2.22E-03
	p3	3.47E+01	3.05E-01
	p4	7.37E+00	4.41E-03
	p5	4.28E-01	4.61E-03
	p6	4.01E+01	1.30E+05
	p7	-8.49E+00	1.99E+04
Peak 7	p0	2.86E+01	3.00E+00
	p1	6.64E+00	4.14E-03
	p2	6.10E-02	6.28E-03
	p3	-1.59E+01	4.25E+00
	p4	6.72E+00	9.86E-04
	p5	4.79E-04	9.79E-04
	p6	2.91E+00	2.36E-01

Table B.8 continued from previous page

Detector 8

	p7	-1.29E-01	6.14E-02
Peak 8	p0	2.71E+01	9.84E-03
	p1	8.19E+00	4.80E+01
	p2	4.02E+02	5.19E+02
	p3	6.80E+01	2.56E-02
	p4	6.27E+00	2.96E-05
	p5	6.85E-02	2.09E-05
	p6	-4.65E+01	9.84E-03
	p7	4.72E+00	1.57E-03
Peak 9	p0	2.07E+03	6.36E+01
	p1	5.28E+00	1.41E+00
	p2	1.35E-02	5.17E-08
	p3	1.58E+01	9.94E-01

Table B.8 continued from previous page

Detector 8

	p4	5.86E+00	1.13E-02
	p5	1.17E-01	9.46E-03
	p6	1.90E+01	6.88E-01
	p7	-1.88E+00	1.15E-01
Peak 10	p0	7.39E+01	7.14E+00
	p1	5.67E+00	7.27E-02
	p2	4.88E-01	1.04E-01
	p3	1.65E+01	3.93E+00
	p4	5.50E+00	1.14E-02
	p5	8.64E-02	1.61E-02
	p6	-1.25E+01	6.56E+00
	p7	-5.30E+00	1.18E+00
Peak 11	p0	-6.63E+04	3.79E+04

Table B.8 continued from previous page

Detector 8

	p1	4.49E+00	2.48E-01
	p2	1.16E-01	5.87E-02
	p3	2.38E+02	8.49E+01
	p4	4.88E+00	2.87E+03
	p5	5.70E-05	1.91E-08
	p6	2.33E+02	1.16E+02
	p7	-4.19E+01	2.25E+01
Peak 12	p0	-1.83E+02	2.09E+01
	p1	4.92E+00	2.71E-02
	p2	1.09E-01	3.06E-02
	p3	1.75E+02	3.82E+01
	p4	4.89E+00	1.32E-02
	p5	8.80E-02	1.23E-02
	p6	-7.11E+02	5.56E+02

Table B.8 continued from previous page

Detector 8

	p7	1.55E+02	1.21E+02
Peak 13	p0	-3.81E+00	4.07E+00
	p1	4.48E+00	9.02E-02
	p2	4.23E-02	5.29E-02
	p3	7.86E+00	4.02E+00
	p4	4.11E+00	3.59E-02
	p5	1.27E-01	6.67E-02
	p6	-4.56E+01	3.70E+01
	p7	1.20E+01	8.15E+00
Peak 14	p0	-1.72E+05	6.36E+01
	p1	3.46E+00	1.41E+00
	p2	1.00E-01	7.06E+02
	p3	2.00E+02	1.41E+00

Table B.8 continued from previous page

Detector 8

	p4	3.46E+00	1.41E+00
	p5	7.50E-02	7.07E+02
	p6	2.60E+01	7.27E-01
	p7	-1.57E+00	1.43E-01

Table B.8: Peak parameters for S3F 8th detector.

Detector 9

	Parameter	Value	Error
Peak 1	p0	8.14E+00	6.35E-01
	p1	1.26E+01	7.06E-03
	p2	1.18E-01	8.02E-03
Peak 2	p0	1.20E+02	2.16E+00
	p1	1.08E+01	1.70E-03
	p2	1.14E-01	1.32E-03

Table B.9 continued from previous page

Detector 9

Peak 3	p0	5.91E+00	2.79E+00
	p1	9.29E+00	1.40E-03
	p2	4.10E-03	1.39E-03
Peak 4	p0	5.13E+00	4.86E-01
	p1	8.68E+00	1.48E-02
	p2	1.26E-01	1.86E-02
Peak 5	p0	4.14E+01	1.32E+00
	p1	7.51E+00	5.31E-03
	p2	1.50E-01	7.72E-03
	p3	5.72E+00	2.46E+00
	p4	7.75E+00	3.48E-02
	p5	2.91E-02	2.11E-02

Table B.9 continued from previous page

Detector 9

	p6	-2.78E+05	5.69E+01
	p7	-7.25E+00	3.53E-05
Peak 6	p0	-2.70E+02	1.02E+02
	p1	7.46E+00	1.52E-01
	p2	8.93E-01	6.10E-01
	p3	2.52E+02	1.10E+02
	p4	7.02E+00	3.41E-02
	p5	2.97E-01	1.28E-01
	p6	2.08E+00	3.46E+06
	p7	-1.38E+01	6.24E-58
Peak 7	p0	1.26E+01	6.77E+00
	p1	6.58E+00	9.35E-02
	p2	9.50E-02	1.01E-01

Table B.9 continued from previous page

Detector 9

	p3	2.80E+01	8.94E+00
	p4	6.62E+00	4.85E-03
	p5	4.20E-02	5.83E-03
	p6	1.08E+01	5.75E+01
	p7	-1.84E+00	8.73E+00
Peak 8	p0	5.77E+01	8.48E+00
	p1	6.24E+00	5.64E-03
	p2	7.93E-02	1.16E-02
	p3	1.82E+01	1.12E+01
	p4	6.23E+00	9.45E-03
	p5	3.36E-02	8.53E-03
	p6	-1.19E+02	6.06E+01
	p7	2.03E+01	9.73E+00

Table B.9 continued from previous page

Detector 9

Peak 9	p0	-3.08E+03	1.41E+00
	p1	4.05E+00	1.41E+00
	p2	2.41E-01	7.19E+02
	p3	-2.06E+05	8.49E+01
	p4	5.50E+00	1.41E+00
	p5	1.77E-03	7.10E+02
	p6	2.93E+02	6.05E-01
	p7	-4.66E+01	1.03E-01
Peak 10	p0	-1.45E+01	7.18E+00
	p1	5.24E+00	8.83E-03
	p2	2.85E-02	1.26E-02
	p3	1.84E+01	4.26E+00
	p4	5.46E+00	1.42E-02
	p5	7.25E-02	2.12E-02

Table B.9 continued from previous page

Detector 9

	p6	5.45E+01	9.64E+01
	p7	-4.50E+00	1.71E+01
Peak 11	p0	2.95E+02	2.98E+01
	p1	5.05E+00	9.56E-02
	p2	4.02E-01	5.60E-02
	p3	-3.44E+01	2.31E+01
	p4	4.81E+00	2.28E-02
	p5	3.03E-01	4.33E-01
	p6	-9.12E+01	5.87E+00
	p7	-3.06E+01	5.05E+00
Peak 12	p0	-6.11E+05	6.36E+01
	p1	4.46E+00	6.71E-06
	p2	4.31E-04	8.65E-10

Table B.9 continued from previous page

Detector 9

	p3	5.06E+01	1.33E+00
	p4	4.83E+00	3.56E-03
	p5	8.73E-02	2.31E-03
	p6	1.09E+01	7.34E-01
	p7	-3.12E+00	1.54E-01
Peak 13	p0	1.84E+01	9.89E+06
	p1	4.67E+00	1.00E+00
	p2	4.50E-02	6.12E+02
	p3	6.94E+00	1.00E+00
	p4	4.07E+00	1.00E+00
	p5	5.87E-02	6.12E+02
	p6	3.46E+00	1.00E+00
	p7	1.12E+00	1.00E+00

Table B.9 continued from previous page

Detector 9

Peak 14	p0	2.87E+02	1.20E+03
	p1	4.28E+00	4.95E-01
	p2	1.26E-01	1.20E-01
	p3	6.79E+00	1.11E+00
	p4	3.78E+00	1.72E-02
	p5	7.13E-02	1.93E-02
	p6	5.24E+01	3.87E+00
	p7	-1.29E+01	1.09E+00

Table B.9: Peak parameters for S3F 9th detector.

Detector 10

	Parameter	Value	Error
Peak 1	p0	8.83E+00	6.73E-01
	p1	1.26E+01	6.54E-03
	p2	1.06E-01	7.18E-03

Table B.10 continued from previous page

Detector 10

Peak 2	p0	1.19E+02	2.09E+00
	p1	1.07E+01	1.73E-03
	p2	1.20E-01	1.35E-03
Peak 3	p0	4.65E+00	5.92E+00
	p1	2.26E+01	1.18E+01
	p2	1.08E+01	9.78E+00
Peak 4	p0	7.33E+00	7.38E-01
	p1	8.68E+00	6.87E-03
	p2	7.52E-02	7.86E-03
Peak 5	p0	4.47E+01	1.16E-54
	p1	7.50E+00	5.76E-57

Table B.10 continued from previous page

Detector 10

	p2	1.41E-01	0.00E+00
	p3	8.70E+00	1.88E-54
	p4	7.95E+00	5.16E-56
	p5	1.24E-01	0.00E+00
	p6	-2.51E+01	4.60E-53
	p7	-5.40E+00	2.11E-132
Peak 6	p0	-3.09E+02	3.42E+01
	p1	7.29E+00	2.46E-02
	p2	2.55E-01	3.92E-02
	p3	1.52E+02	3.57E+01
	p4	7.04E+00	7.00E-02
	p5	1.70E-01	4.15E-02
	p6	8.36E+00	4.63E+00
	p7	-1.40E+00	1.48E-05

Table B.10 continued from previous page

Detector 10

Peak 7	p0	-3.20E+02	1.16E+02
	p1	6.93E+00	1.82E-02
	p2	1.20E-01	1.25E-02
	p3	1.29E+02	3.74E+01
	p4	6.99E+00	1.46E-01
	p5	2.60E-01	7.98E-02
	p6	-1.92E+01	7.23E-32
	p7	-8.16E+00	1.89E-24
Peak 8	p0	-1.59E+01	7.43E+00
	p1	6.30E+00	3.54E-03
	p2	6.13E-03	3.58E-03
	p3	6.94E+01	2.99E+00
	p4	6.26E+00	3.23E-03

Table B.10 continued from previous page

Detector 10

	p5	6.86E-02	3.97E-03
	p6	-6.45E+01	5.46E+01
	p7	1.23E+01	8.82E+00
Peak 9	p0	9.78E+03	6.36E+01
	p1	5.12E+00	1.41E+00
	p2	1.80E-05	1.23E-09
	p3	1.19E+01	4.90E+00
	p4	5.86E+00	2.47E-02
	p5	1.20E-01	5.68E-02
	p6	1.91E+01	2.48E+00
	p7	-2.00E+00	4.62E-01
Peak 10	p0	3.10E+01	3.65E+01
	p1	5.41E+00	8.50E-02

Table B.10 continued from previous page

Detector 10

	p2	1.56E-01	1.10E-01
	p3	7.88E+00	4.30E+00
	p4	5.39E+00	1.56E-02
	p5	3.22E-02	1.46E-02
	p6	-2.74E+02	4.32E+02
	p7	5.24E+01	7.34E+01
Peak 11	p0	2.39E+01	2.14E+02
	p1	4.92E+00	1.85E-01
	p2	3.05E-02	6.08E-02
	p3	2.09E+02	7.21E+00
	p4	5.09E+00	9.63E-03
	p5	3.05E-01	4.40E-02
	p6	-5.99E+01	7.12E+00
	p7	-2.34E+01	1.40E+00

Table B.10 continued from previous page

Detector 10

Peak 12	p0	3.27E+04	2.19E+05
	p1	1.10E+01	6.29E-01
	p2	9.34E-01	1.74E-01
	p3	4.07E+01	3.72E+00
	p4	4.87E+00	5.94E-03
	p5	8.70E-02	1.26E-02
	p6	1.54E+01	2.63E+00
	p7	-2.12E+00	3.70E-01
Peak 13	p0	-1.20E+02	9.66E+01
	p1	4.77E+00	1.49E-01
	p2	4.87E-01	1.57E-01
	p3	3.14E+00	1.47E+00
	p4	4.13E+00	1.83E-02

Table B.10 continued from previous page

Detector 10

	p5	2.69E-02	9.71E-03
	p6	-4.76E+02	2.70E+02
	p7	1.30E+02	7.69E+01
Peak 14	p0	4.04E+00	1.55E+00
	p1	3.71E+00	1.99E-02
	p2	3.17E-02	1.22E-02
	p3	4.92E+00	1.57E+00
	p4	3.51E+00	9.47E-03
	p5	2.68E-02	9.38E-03
	p6	3.07E+01	7.35E+00
	p7	-6.66E+00	2.19E+00

Table B.10: Peak parameters for S3F 10th detector

Detector 11

	Parameter	Value	Error
Peak 1	p0	9.24E+00	6.92E-01
	p1	1.26E+01	6.69E-03
	p2	1.24E-01	8.20E-03
Peak 2	p0	1.26E+02	2.18E+00
	p1	1.07E+01	1.63E-03
	p2	1.18E-01	1.30E-03
Peak 3	p0	2.70E+00	6.75E-01
	p1	9.09E+00	8.11E-01
	p2	5.70E-01	1.04E+00
Peak 4	p0	1.04E+01	8.91E-01
	p1	8.70E+00	6.23E-03
	p2	7.63E-02	7.36E-03

Table B.11 continued from previous page

Detector 11

Peak 5	p0	8.78E+00	7.50E-01
	p1	7.47E+00	2.56E-02
	p2	2.20E-01	2.55E-02
	p3	3.65E+01	9.31E-01
	p4	7.48E+00	4.79E-03
	p5	1.55E-01	3.80E-03
	p6	-2.66E+25	3.05E+00
	p7	-5.70E+00	1.41E+00
Peak 6	p0	-2.78E+01	2.83E+01
	p1	7.01E+00	3.65E-02
	p2	5.83E-02	2.53E-02
	p3	8.82E+01	9.04E+01
	p4	7.24E+00	4.45E-02

Table B.11 continued from previous page

Detector 11

	p5	1.93E-01	2.82E-02
	p6	9.33E+01	4.47E+01
	p7	-1.50E+01	8.04E+00
Peak 7	p0	1.64E+04	3.95E+03
	p1	6.10E+00	4.27E-03
	p2	1.19E-01	3.12E-03
	p3	3.36E+01	5.83E+00
	p4	6.65E+00	3.92E-03
	p5	5.25E-02	1.03E-02
	p6	-5.35E+00	1.38E+01
	p7	1.02E+00	1.84E+00
Peak 8	p0	6.46E+01	5.34E+00
	p1	6.29E+00	6.98E-04

Table B.11 continued from previous page

Detector 11

	p2	8.56E-05	6.13E-04
	p3	6.35E+01	2.57E+00
	p4	6.28E+00	2.61E-03
	p5	6.14E-02	3.27E-03
	p6	-7.63E+01	4.08E+01
	p7	1.47E+01	6.58E+00
Peak 9	p0	-3.05E+03	6.36E+01
	p1	4.88E+00	1.41E+00
	p2	1.36E-04	1.18E-08
	p3	6.40E+00	2.35E+00
	p4	5.96E+00	1.10E-02
	p5	2.96E-02	1.31E-02
	p6	1.80E+02	1.81E+00
	p7	-2.79E+01	3.00E-01

Table B.11 continued from previous page

Detector 11

Peak 10	p0	7.45E+01	1.33E+01
	p1	5.75E+00	3.40E-02
	p2	1.57E-01	2.57E-02
	p3	1.29E+02	8.78E+00
	p4	5.38E+00	1.81E-02
	p5	2.20E-01	2.02E-02
	p6	-3.25E+01	7.82E+00
	p7	-1.05E+01	1.43E+00
Peak 11	p0	-7.22E+01	4.81E+01
	p1	5.27E+00	5.50E-04
	p2	1.03E-01	1.24E-02
	p3	1.70E+02	2.31E+01
	p4	5.36E+00	1.14E-01

Table B.11 continued from previous page

Detector 11

	p5	3.25E-01	1.60E-01
	p6	-2.60E+01	5.01E+01
	p7	-9.40E+00	9.53E+00
Peak 12	p0	2.98E+02	8.11E+02
	p1	5.11E+00	1.02E-01
	p2	4.60E-02	2.74E-02
	p3	1.73E+02	2.87E+02
	p4	4.96E+00	9.79E-02
	p5	1.62E-01	1.08E-01
	p6	1.75E+03	3.04E+03
	p7	-3.82E+02	6.72E+02
Peak 13	p0	1.50E+02	6.36E+01
	p1	-2.80E+00	1.73E+00

Table B.11 continued from previous page

Detector 11

	p2	1.36E-01	6.10E+02
	p3	3.58E+00	1.12E+00
	p4	4.02E+00	1.00E+00
	p5	1.65E-01	6.09E+02
	p6	-1.36E+00	1.05E+00
	p7	2.79E+00	1.00E+00
Peak 14	p0	5.75E+00	1.49E+00
	p1	3.03E+00	1.16E-02
	p2	2.96E-02	7.45E-03
	p3	-2.41E+05	8.49E+01
	p4	4.06E+00	1.41E+00
	p5	2.45E-03	7.10E+02
	p6	3.34E+01	3.76E-01
	p7	-7.12E+00	1.15E-01

Table B.11 continued from previous page

Detector 11

Table B.11: Peak parameters for S3F 11th detector.

Detector 12

	Parameter	Value	Error
Peak 1	p0	8.64E+00	6.19E-01
	p1	1.25E+01	6.76E-03
	p2	1.24E-01	7.16E-03
Peak 2	p0	5.40E+01	1.39E+00
	p1	1.06E+01	2.69E-03
	p2	1.32E-01	2.34E-03
Peak 3	p0	3.53E+00	2.14E+00
	p1	9.88E+00	1.21E+00
	p2	7.65E-01	8.45E-01

Table B.12 continued from previous page

Detector 12

Peak 4	p0	9.72E+00	7.94E-01
	p1	8.70E+00	6.96E-03
	p2	9.35E-02	8.52E-03
Peak 5	p0	3.30E+01	7.56E-01
	p1	7.43E+00	5.00E-03
	p2	1.72E-01	4.28E-03
	p3	4.91E+00	1.32E+00
	p4	7.69E+00	1.27E-02
	p5	3.17E-02	9.24E-03
	p6	-1.67E+07	3.01E+00
	p7	-8.11E+00	1.41E+00
Peak 6	p0	-1.27E+03	1.46E+02

Table B.12 continued from previous page

Detector 12

	p1	8.41E+00	7.38E-02
	p2	8.37E-01	7.58E-02
	p3	2.75E+02	3.59E+01
	p4	7.24E+00	2.02E-02
	p5	2.29E-01	1.93E-02
	p6	8.69E+00	1.13E+00
	p7	-5.18E-01	1.43E-01
Peak 7	p0	-1.42E+01	3.95E+00
	p1	6.45E+00	4.80E-03
	p2	1.13E-02	7.33E-03
	p3	1.59E+01	2.13E+00
	p4	6.63E+00	5.83E-03
	p5	4.20E-02	7.55E-03
	p6	3.10E+01	5.60E+00

Table B.12 continued from previous page

Detector 12

	p7	-4.28E+00	8.57E-01
Peak 8	p0	4.54E+01	1.97E+00
	p1	6.28E+00	9.22E-04
	p2	5.95E-04	3.70E-04
	p3	5.91E+01	2.48E+00
	p4	6.25E+00	3.35E-03
	p5	7.30E-02	4.38E-03
	p6	-2.76E+01	4.33E+01
	p7	6.21E+00	7.12E+00
Peak 9	p0	2.13E+03	6.36E+01
	p1	5.58E+00	1.00E+00
	p2	1.74E-02	6.13E+02
	p3	-2.34E+02	1.01E+02

Table B.12 continued from previous page

Detector 12

	p4	5.73E+00	1.00E+00
	p5	4.28E-02	6.12E+02
	p6	6.79E+01	1.31E+00
	p7	-8.14E+00	1.01E+00
Peak 10	p0	-5.76E+01	3.03E+01
	p1	5.17E+00	5.89E-03
	p2	7.54E-04	2.94E-03
	p3	2.12E+02	5.65E+01
	p4	5.45E+00	1.01E-02
	p5	5.68E-01	8.77E-02
	p6	-5.56E+01	4.02E+01
	p7	-2.15E+01	3.03E+00
Peak 11	p0	4.37E+03	1.41E+00

Table B.12 continued from previous page

Detector 12

	p1	5.54E+00	1.36E+00
	p2	5.25E-02	6.42E-03
	p3	1.00E+02	1.41E+00
	p4	5.47E+00	5.98E-01
	p5	1.20E-01	2.30E-01
	p6	7.55E+00	1.39E+00
	p7	3.05E+00	5.18E-01
Peak 12	p0	-1.12E+05	1.65E+00
	p1	5.63E+00	1.00E+00
	p2	7.03E-02	6.11E+02
	p3	3.39E+01	1.49E+00
	p4	4.86E+00	1.00E+00
	p5	5.76E-02	6.12E+02
	p6	1.90E+01	1.49E+00

Table B.12 continued from previous page

Detector 12

	p7	-4.97E-01	1.08E+00
Peak 13	p0	-2.55E+02	4.51E+00
	p1	4.21E+00	7.60E-03
	p2	4.87E-02	6.47E-03
	p3	2.78E+02	4.81E+00
	p4	4.22E+00	8.29E-03
	p5	5.44E-02	7.69E-03
	p6	7.02E+01	4.70E+00
	p7	-1.31E+01	1.16E+00
Peak 14	p0	-2.68E+05	9.00E+01
	p1	4.28E+00	1.41E+00
	p2	2.38E-04	7.11E+02
	p3	2.85E+03	4.61E+03

Table B.12 continued from previous page

Detector 12

	p4	3.95E+00	8.16E-05
	p5	1.88E-04	2.19E-05
	p6	-1.72E+01	4.73E-01
	p7	8.73E+00	1.27E-01

Table B.12: Peak parameters for S3F 12th detector.

Detector 13

	Parameter	Value	Error
Peak 1	p0	8.10E+00	6.13E-01
	p1	1.25E+01	7.27E-03
	p2	1.29E-01	8.47E-03
Peak 2	p0	1.16E+02	1.99E+00
	p1	1.06E+01	1.78E-03
	p2	1.28E-01	1.38E-03

Table B.13 continued from previous page

Detector 13

Peak 3	p0	6.30E+00	7.31E+01
	p1	1.38E+01	3.23E+00
	p2	3.14E+00	8.12E+02
Peak 4	p0	2.02E+01	1.21E+00
	p1	8.67E+00	3.91E-03
	p2	7.91E-02	4.23E-03
Peak 5	p0	4.15E+01	8.52E-01
	p1	7.35E+00	4.04E-03
	p2	1.64E-01	3.29E-03
	p3	6.52E+00	1.80E+00
	p4	7.66E+00	1.53E-02
	p5	4.40E-02	1.16E-02

Table B.13 continued from previous page

Detector 13

	p6	-2.77E+05	2.99E+00
	p7	-9.57E+04	1.41E+00
Peak 6	p0	-2.10E+03	6.66E-13
	p1	6.31E+00	1.82E-15
	p2	1.42E-01	0.00E+00
	p3	3.31E+01	4.68E-13
	p4	6.64E+00	2.62E-15
	p5	1.42E-01	2.78E-14
	p6	-5.26E+00	1.49E-11
	p7	-5.40E+00	1.75E-16
Peak 7	p0	-4.72E+05	1.41E+00
	p1	5.90E+00	1.82E+00
	p2	8.10E-02	4.38E+01

Table B.13 continued from previous page

Detector 13

	p3	3.26E+01	1.09E+00
	p4	6.57E+00	3.66E-03
	p5	6.27E-02	3.82E-03
	p6	2.46E+01	1.41E+00
	p7	-5.29E+00	1.41E+00
Peak 8	p0	-2.54E+05	6.36E+01
	p1	6.20E+00	1.41E+00
	p2	5.66E-05	7.11E+02
	p3	6.78E+01	1.79E+00
	p4	6.20E+00	2.05E-03
	p5	6.83E-02	1.43E-03
	p6	1.98E+01	7.36E-01
	p7	-2.00E+00	1.19E-01

Table B.13 continued from previous page

Detector 13

Peak 9	p0	-4.22E+05	2.53E+04
	p1	4.47E+00	3.96E-03
	p2	2.96E-01	8.83E-04
	p3	-2.02E+05	1.20E+02
	p4	5.23E+00	1.41E+00
	p5	4.10E-03	7.10E+02
	p6	7.79E+02	7.00E-01
	p7	-1.29E+02	1.19E-01
Peak 10	p0	-1.36E+03	4.93E+02
	p1	2.92E+00	3.80E-01
	p2	1.09E+00	1.60E-01
	p3	1.45E+01	2.72E+00
	p4	5.29E+00	8.72E-03
	p5	4.13E-02	7.96E-03

Table B.13 continued from previous page

Detector 13

	p6	1.50E+03	2.36E+02
	p7	-2.53E+02	3.76E+01
Peak 11	p0	-1.39E+08	5.48E+07
	p1	5.78E+00	1.16E-01
	p2	1.24E-01	2.40E-02
	p3	1.71E+02	7.89E+01
	p4	5.20E+00	5.60E-02
	p5	6.11E-02	2.03E-02
	p6	2.53E+01	1.40E+01
	p7	1.45E+00	2.50E+00
Peak 12	p0	-9.94E+06	6.36E+01
	p1	4.95E+00	4.26E-04
	p2	1.88E-05	6.05E-09

Table B.13 continued from previous page

Detector 13

	p3	4.12E+01	2.25E+00
	p4	4.79E+00	2.89E-03
	p5	5.36E-02	3.89E-03
	p6	-1.94E+02	1.07E+01
	p7	4.38E+01	2.35E+00
Peak 13	p0	-3.07E+00	1.89E+00
	p1	3.82E+00	1.01E+00
	p2	6.76E-02	6.11E+02
	p3	2.19E+02	8.49E+01
	p4	4.31E+00	1.01E+00
	p5	6.99E-05	6.15E+02
	p6	2.08E+01	1.20E+00
	p7	-2.04E+00	1.01E+00

Table B.13 continued from previous page

Detector 13

Peak 14	p0	6.27E+00	4.18E+00
	p1	3.74E+00	5.53E-02
	p2	1.39E-01	9.57E-02
	p3	7.83E+00	3.54E+00
	p4	3.39E+00	3.76E-03
	p5	9.03E-03	4.50E-03
	p6	2.58E+01	2.27E+01
	p7	-5.16E+00	7.27E+00

Table B.13: Peak parameters for S3F 13th detector.

Detector 14

	Parameter	Value	Error
Peak 1	p0	8.86E+00	5.98E-01
	p1	1.24E+01	6.82E-03
	p2	1.25E-01	6.77E-03

Table B.14 continued from previous page

Detector 14

Peak 2	p0	1.24E+02	2.07E+00
	p1	1.05E+01	1.74E-03
	p2	1.27E-01	1.35E-03
Peak 3	p0	2.28E+00	1.96E-01
	p1	9.39E+00	1.41E+00
	p2	5.40E+01	5.77E+02
Peak 4	p0	3.06E+01	1.50E+00
	p1	8.67E+00	2.68E-03
	p2	6.62E-02	2.49E-03
Peak 5	p0	3.92E+01	4.72E+00
	p1	7.31E+00	1.64E-02

Table B.14 continued from previous page

Detector 14

	p2	1.67E-01	1.45E-02
	p3	1.66E+01	3.40E+01
	p4	7.76E+00	7.06E-02
	p5	9.35E-02	7.24E-02
	p6	-2.74E+01	8.91E-24
	p7	3.42E+00	6.21E+00
Peak 6	p0	-2.65E+03	8.62E+02
	p1	7.57E+00	2.54E-01
	p2	2.46E-01	1.09E-01
	p3	1.41E+02	7.87E+01
	p4	7.07E+00	1.86E-02
	p5	1.47E-01	2.15E-02
	p6	3.59E+01	4.40E-01
	p7	-5.02E+00	2.74E-02

Table B.14 continued from previous page

Detector 14

Peak 7	p0	4.25E+06	5.09E+01
	p1	7.60E+00	1.73E+00
	p2	1.00E-02	6.14E+02
	p3	3.21E+01	2.00E+00
	p4	6.57E+00	1.00E+00
	p5	5.97E-02	6.12E+02
	p6	-1.28E+01	1.73E+00
	p7	-1.08E+01	1.00E+00
Peak 8	p0	7.04E+01	6.36E+01
	p1	6.16E+00	1.41E+00
	p2	7.06E-06	1.03E-07
	p3	6.98E+01	1.86E+00
	p4	6.19E+00	3.07E-03

Table B.14 continued from previous page

Detector 14

	p5	6.74E-02	1.69E-03
	p6	-8.62E+01	7.67E-01
	p7	1.55E+01	1.24E-01
Peak 9	p0	-2.91E+04	6.36E+01
	p1	6.92E+00	5.29E-05
	p2	3.50E-03	8.80E-12
	p3	1.27E+02	6.47E-01
	p4	5.87E+00	6.79E-03
	p5	3.00E-01	4.13E-02
	p6	-3.92E+01	7.12E-01
	p7	-1.19E+01	1.04E-01
Peak 10	p0	-1.31E+02	1.19E+02
	p1	5.55E+00	1.87E-01

Table B.14 continued from previous page

Detector 14

	p2	9.75E-01	2.77E-01
	p3	3.10E+01	1.50E+01
	p4	5.24E+00	3.31E-02
	p5	1.92E-01	5.26E-02
	p6	1.16E+02	6.97E+01
	p7	4.81E+00	7.42E+00
Peak 11	p0	-1.23E+07	1.59E+07
	p1	6.54E+00	1.06E-01
	p2	3.45E-01	2.38E-02
	p3	3.06E+02	4.89E+02
	p4	4.99E+00	4.69E-02
	p5	4.83E-02	2.72E-02
	p6	8.57E+01	6.27E+01
	p7	7.85E+00	5.11E+00

Table B.14 continued from previous page

Detector 14

Peak 12	p0	-1.93E+06	2.89E+06
	p1	7.61E+00	3.51E+00
	p2	5.64E-01	7.13E-01
	p3	5.80E+01	1.73E+01
	p4	4.81E+00	2.21E-02
	p5	9.58E-02	2.18E-02
	p6	1.40E+01	5.24E+00
	p7	-1.63E+00	1.75E+00
Peak 13	p0	1.50E+02	8.85E+01
	p1	7.69E+00	2.61E+00
	p2	3.94E-02	6.12E+02
	p3	9.82E+01	1.87E+00
	p4	4.10E+00	1.00E+00

Table B.14 continued from previous page

Detector 14

	p5	5.12E-01	6.24E+02
	p6	-6.97E+01	1.87E+00
	p7	-3.09E+00	1.14E+00
Peak 14	p0	3.85E+00	3.20E+00
	p1	3.42E+00	1.56E-02
	p2	2.55E-02	1.70E-02
	p3	3.57E+00	1.95E+00
	p4	3.29E+00	1.76E-02
	p5	3.39E-02	2.19E-02
	p6	3.93E+01	2.99E+01
	p7	-9.28E+00	9.50E+00

Table B.14: Peak parameters for S3F 14th detector.

Detector 15

	Parameter	Value	Error
Peak 1	p0	9.99E+00	6.82E-01
	p1	1.24E+01	5.68E-03
	p2	1.04E-01	5.21E-03
Peak 2	p0	9.99E+00	6.82E-01
	p1	1.24E+01	5.68E-03
	p2	1.04E-01	5.21E-03
Peak 3	p0	2.63E+00	3.00E-01
	p1	9.41E+00	2.19E-01
	p2	3.48E-01	3.39E-01
Peak 4	p0	3.98E+01	1.67E+00
	p1	8.65E+00	2.27E-03
	p2	6.61E-02	2.04E-03

Table B.15 continued from previous page

Detector 15

Peak 5	p0	3.68E+01	5.59E+00
	p1	7.23E+00	1.39E-02
	p2	1.43E-01	1.95E-02
	p3	8.07E+00	2.54E+01
	p4	8.89E+00	7.03E+00
	p5	1.57E+00	3.66E+00
	p6	-1.68E+03	4.14E-151
	p7	-6.80E+00	6.00E-152
Peak 6	p0	-4.85E+04	7.40E+01
	p1	7.27E+06	1.41E+00
	p2	2.09E+02	5.78E+02
	p3	-5.62E+01	1.41E+00
	p4	7.46E+00	1.41E+00

Table B.15 continued from previous page

Detector 15

	p5	1.22E-04	7.11E+02
	p6	1.33E+00	5.44E-02
	p7	1.68E-01	7.91E-03
Peak 7	p0	-1.16E+03	2.19E+02
	p1	1.79E+00	8.42E-01
	p2	8.59E+00	3.01E+00
	p3	1.03E+03	2.40E+02
	p4	6.47E+00	7.47E-03
	p5	5.18E-01	6.48E-02
	p6	-5.25E+15	7.92E+04
	p7	-1.89E+10	2.85E-01
Peak 8	p0	-1.56E+02	7.40E+01
	p1	6.01E+00	2.78E-02

Table B.15 continued from previous page

Detector 15

	p2	8.02E-02	8.96E-03
	p3	1.64E+02	5.55E+01
	p4	6.04E+00	5.14E-02
	p5	1.07E-01	2.02E-02
	p6	-1.27E+00	1.82E+01
	p7	2.18E+00	2.58E+00
Peak 9	p0	6.09E+03	6.36E+01
	p1	6.62E+00	1.41E+00
	p2	7.54E-02	1.58E-07
	p3	1.42E+01	1.29E+00
	p4	5.82E+00	5.39E-03
	p5	4.61E-02	4.07E-03
	p6	2.19E+01	6.52E-01
	p7	-2.17E+00	1.12E-01

Table B.15 continued from previous page

Detector 15

Peak 10	p0	-4.78E+06	8.09E+01
	p1	3.69E+00	3.42E+00
	p2	2.23E-03	9.90E+02
	p3	4.50E+01	1.27E+00
	p4	5.06E+00	3.42E+00
	p5	2.63E-01	9.88E+02
	p6	1.71E+01	3.00E+00
	p7	-1.98E+00	3.41E+00
Peak 11	p0	-4.47E+03	1.00E+00
	p1	4.62E+00	2.47E-02
	p2	2.82E-02	2.70E-02
	p3	-3.36E+01	1.01E+00
	p4	4.82E+00	2.45E-02

Table B.15 continued from previous page

Detector 15

	p5	3.05E-02	1.89E-02
	p6	3.70E+01	1.00E+00
	p7	9.28E-01	1.10E+00
Peak 12	p0	-2.55E+05	6.36E+01
	p1	6.18E+00	2.04E-03
	p2	1.25E-01	9.74E-06
	p3	5.35E+01	1.59E+00
	p4	4.74E+00	4.13E-03
	p5	1.00E-01	5.84E-03
	p6	1.28E+01	6.92E-01
	p7	-2.20E+00	1.81E-01
Peak 13	p0	-1.05E+01	2.47E+01
	p1	3.96E+00	6.42E-02

Table B.15 continued from previous page

Detector 15

	p2	6.02E-02	1.90E-02
	p3	2.01E+01	1.97E+01
	p4	3.98E+00	5.34E-02
	p5	6.33E-02	2.01E-02
	p6	-5.41E+01	1.15E+01
	p7	1.54E+01	2.92E+00
Peak 14	p0	-1.94E+06	6.36E+01
	p1	3.64E+00	1.86E-06
	p2	6.44E-04	1.20E-08
	p3	-2.48E+06	2.39E+07
	p4	3.03E+00	1.14E+00
	p5	6.98E-03	1.39E+00
	p6	1.30E+01	4.47E-01
	p7	-4.19E-01	1.37E-01

Table B.15 continued from previous page

Detector 15

Table B.15: Peak parameters for S3F 15th detector.

Detector 16

	Parameter	Value	Error
Peak 1	p0	8.77E+00	6.33E-01
	p1	1.24E+01	7.03E-03
	p2	1.18E-01	7.65E-03
Peak 2	p0	1.23E+02	1.98E+00
	p1	1.04E+01	1.76E-03
	p2	1.36E-01	1.37E-03
Peak 3	p0	2.46E+00	6.19E-01
	p1	-2.58E+02	3.70E+03
	p2	1.00E+03	5.66E+02

Table B.16 continued from previous page

Detector 16

Peak 4	p0	5.26E+01	1.90E+00
	p1	8.64E+00	2.05E-03
	p2	6.52E-02	1.68E-03
Peak 5	p0	3.70E+01	5.73E+00
	p1	7.20E+00	1.44E-02
	p2	1.26E-01	1.68E-02
	p3	2.24E+01	1.37E+02
	p4	6.31E+00	4.82E+00
	p5	5.24E-01	1.73E+00
	p6	-5.56E+01	1.36E+02
	p7	7.67E+00	1.81E+01
Peak 6	p0	-1.62E+03	7.67E+02

Table B.16 continued from previous page

Detector 16

	p1	6.40E+00	1.71E-02
	p2	1.01E-01	6.16E-03
	p3	7.03E+01	7.08E+01
	p4	6.54E+00	3.63E-02
	p5	8.56E-02	1.77E-02
	p6	3.76E+01	3.54E-01
	p7	-5.18E+00	5.21E-02
Peak 7	p0	2.20E+02	4.72E+02
	p1	5.59E+00	6.27E-01
	p2	3.28E-01	1.94E-01
	p3	1.84E+01	2.53E+00
	p4	6.50E+00	3.48E-03
	p5	4.53E-02	7.23E-03
	p6	4.33E+00	3.89E+01

Table B.16 continued from previous page

Detector 16

	p7	-3.82E-01	5.80E+00
Peak 8	p0	8.30E+00	3.99E+00
	p1	6.24E+00	1.28E-02
	p2	2.50E-02	9.18E-03
	p3	6.90E+01	2.73E+00
	p4	6.13E+00	3.39E-03
	p5	5.79E-02	3.59E-03
	p6	-6.56E+01	3.42E+01
	p7	1.30E+01	5.52E+00
Peak 9	p0	-9.00E+02	6.36E+01
	p1	6.80E+00	1.73E+00
	p2	1.95E-04	6.15E+02
	p3	1.52E+01	1.34E+00

Table B.16 continued from previous page

Detector 16

	p4	5.80E+00	1.00E+00
	p5	7.88E-02	6.11E+02
	p6	1.80E+01	1.14E+00
	p7	-2.23E+00	1.00E+00
Peak 10	p0	-9.53E+05	6.36E+01
	p1	3.96E+00	1.00E+00
	p2	7.66E-03	6.14E+02
	p3	3.75E+01	1.84E+00
	p4	5.05E+00	1.00E+00
	p5	1.80E-01	6.09E+02
	p6	2.45E+01	1.10E+00
	p7	-1.85E+00	1.00E+00
Peak 11	p0	8.19E+02	8.49E+02

Table B.16 continued from previous page

Detector 16

	p1	4.72E+00	7.08E-02
	p2	8.87E-02	3.28E-02
	p3	5.58E+02	7.46E+02
	p4	4.92E+00	1.04E-02
	p5	6.88E-02	3.80E-02
	p6	-2.72E+02	3.83E+02
	p7	-6.70E+01	9.06E+01
Peak 12	p0	-1.24E+05	9.00E+01
	p1	6.05E+00	1.41E+00
	p2	1.04E-02	7.09E+02
	p3	3.77E+01	1.98E+00
	p4	4.72E+00	3.59E-03
	p5	5.41E-02	2.78E-03
	p6	-2.72E+02	6.68E-01

Table B.16 continued from previous page

Detector 16

	p7	6.33E+01	1.45E-01
Peak 13	p0	-2.28E+01	4.97E+00
	p1	3.86E+00	5.81E+01
	p2	3.01E-02	7.39E+02
	p3	2.69E+02	7.03E+02
	p4	3.70E+00	5.81E+01
	p5	7.52E-02	7.37E+02
	p6	5.29E+01	6.02E+01
	p7	-9.78E+00	5.82E+01
Peak 14	p0	1.23E+03	4.54E+02
	p1	3.60E+00	8.48E-02
	p2	4.89E-02	2.84E-02
	p3	1.45E+02	1.62E+02

Table B.16 continued from previous page

Detector 16

	p4	3.50E+00	8.77E-02
	p5	2.52E-01	9.15E-02
	p6	9.32E+02	7.85E+02
	p7	-3.10E+02	2.72E+02

Table B.16: Peak parameters for S3F 16th detector

Detector 17

	Parameter	Value	Error
Peak 1	p0	7.72E+00	6.74E-01
	p1	1.23E+01	7.60E-03
	p2	1.10E-01	9.80E-03
Peak 2	p0	1.19E+02	1.95E+00
	p1	1.04E+01	1.81E-03
	p2	1.36E-01	1.43E-03

Table B.17 continued from previous page

Detector 17

Peak 3	p0	3.06E+00	3.64E-01
	p1	9.35E+00	4.21E-02
	p2	2.16E-01	7.82E-02
Peak 4	p0	5.63E+01	1.97E+00
	p1	8.64E+00	2.11E-03
	p2	6.81E-02	1.84E-03
Peak 5	p0	4.11E+01	9.90E-01
	p1	7.13E+00	5.40E-03
	p2	1.68E-01	3.62E-03
	p3	-3.52E+02	2.26E+01
	p4	7.96E+00	1.41E+00
	p5	1.15E-03	1.95E-04

Table B.17 continued from previous page

Detector 17

	p6	-3.29E+01	9.03E+05
	p7	-1.14E+01	2.42E-51
Peak 6	p0	-6.65E+03	nan
	p1	6.24E+00	nan
	p2	1.42E-01	nan
	p3	7.71E+01	nan
	p4	6.55E+00	nan
	p5	1.30E-01	nan
	p6	1.08E+01	nan
	p7	-6.26E+00	nan
Peak 7	p0	-3.04E+01	2.67E+01
	p1	6.59E+00	4.58E-02
	p2	4.04E-02	3.06E-02

Table B.17 continued from previous page

Detector 17

	p3	-3.58E+02	9.37E+01
	p4	6.12E+00	5.22E-02
	p5	2.23E-01	1.81E-02
	p6	3.48E+01	1.80E-01
	p7	-4.62E+00	3.02E-02
Peak 8	p0	-2.09E+05	6.36E+01
	p1	6.10E+00	1.41E+00
	p2	5.19E-05	7.11E+02
	p3	7.08E+01	1.71E+00
	p4	6.13E+00	2.14E-03
	p5	7.58E-02	1.58E-03
	p6	1.90E+01	8.23E-01
	p7	-2.24E+00	1.35E-01

Table B.17 continued from previous page

Detector 17

Peak 9	p0	-1.68E+01	4.21E+01
	p1	5.90E+00	6.87E-02
	p2	5.40E-02	4.07E-02
	p3	2.29E+01	3.87E+01
	p4	5.87E+00	2.52E-01
	p5	1.18E-01	1.41E-01
	p6	4.29E+01	1.53E+02
	p7	-6.42E+00	2.85E+01
Peak 10	p0	-3.90E+01	7.06E+00
	p1	5.45E+00	6.05E-02
	p2	1.99E-01	4.56E-02
	p3	1.22E+01	3.92E+00
	p4	4.99E+00	1.36E-02
	p5	4.51E-02	1.93E-02

Table B.17 continued from previous page

Detector 17

	p6	3.92E+01	7.31E+00
	p7	2.91E+00	1.46E+00
Peak 11	p0	-1.69E+04	1.44E+03
	p1	4.88E+00	2.08E-02
	p2	3.69E-03	6.11E-03
	p3	2.46E+02	3.83E+01
	p4	4.94E+00	6.92E-02
	p5	3.97E-02	3.95E-02
	p6	2.08E+01	1.82E+01
	p7	2.77E+00	1.02E+00
Peak 12	p0	-3.41E+05	6.36E+01
	p1	5.67E+00	1.41E+00
	p2	1.79E-02	7.09E+02

Table B.17 continued from previous page

Detector 17

	p3	4.02E+01	1.88E+00
	p4	4.72E+00	3.76E-03
	p5	6.24E-02	2.76E-03
	p6	-3.59E+02	7.08E-01
	p7	8.18E+01	1.54E-01
Peak 13	p0	-3.39E+03	7.07E+02
	p1	4.46E+00	8.38E-03
	p2	1.10E-01	2.84E-03
	p3	2.64E+02	5.05E+01
	p4	4.26E+00	8.41E-03
	p5	6.08E-02	3.30E-03
	p6	-9.80E+01	4.67E+00
	p7	2.86E+01	1.18E+00

Table B.17 continued from previous page

Detector 17

Peak 14	p0	1.03E+02	6.36E+01
	p1	4.17E+00	1.41E+00
	p2	2.44E-02	2.01E-03
	p3	7.68E-02	9.47E-01
	p4	3.18E+00	1.18E-01
	p5	5.31E-02	7.07E+02
	p6	1.20E+01	4.42E-01
	p7	-1.27E-01	1.36E-01

Table B.17: Peak parameters for S3F 17th detector.

Detector 18

	Parameter	Value	Error
Peak 1	p0	7.10E+00	5.53E-01
	p1	1.22E+01	4.85E-02
	p2	2.13E-01	3.35E-02

Table B.18 continued from previous page

Detector 18

Peak 2	p0	1.21E+02	1.87E+00
	p1	1.04E+01	1.87E-03
	p2	1.51E-01	1.53E-03
Peak 3	p0	3.29E+01	2.63E+02
	p1	1.35E+00	2.38E+01
	p2	3.40E+00	5.82E+00
Peak 4	p0	6.27E+01	2.13E+00
	p1	8.63E+00	1.97E-03
	p2	6.77E-02	1.83E-03
Peak 5	p0	4.17E+01	nan
	p1	7.10E+00	nan

Table B.18 continued from previous page

Detector 18

	p2	1.53E-01	nan
	p3	1.65E+01	nan
	p4	7.60E+00	nan
	p5	1.23E-01	nan
	p6	-2.66E+01	nan
	p7	-5.82E+00	0.00E+00
Peak 6	p0	-1.52E+03	3.14E+00
	p1	7.44E+00	6.20E-02
	p2	3.37E-01	6.56E-02
	p3	5.07E+02	1.47E+02
	p4	7.06E+00	3.14E-02
	p5	2.34E-01	4.28E-02
	p6	-3.73E+01	5.66E+01
	p7	3.57E+00	7.38E+00

Table B.18 continued from previous page

Detector 18

Peak 7	p0	-2.93E+01	1.20E+01
	p1	6.68E+00	3.76E-02
	p2	4.25E-01	8.27E-02
	p3	-1.07E+02	5.90E+01
	p4	6.27E+00	5.74E-02
	p5	9.58E-02	2.83E-02
	p6	3.69E+01	8.13E-01
	p7	-5.06E+00	1.43E-01
Peak 8	p0	2.06E+02	1.15E+02
	p1	6.80E+00	2.13E-02
	p2	9.91E-02	1.19E-02
	p3	6.25E+01	6.69E+00
	p4	6.10E+00	5.84E-03

Table B.18 continued from previous page

Detector 18

	p5	8.56E-02	1.09E-02
	p6	-3.27E+02	1.14E+02
	p7	5.44E+01	1.83E+01
Peak 9	p0	7.13E+02	1.00E+00
	p1	5.17E+00	1.00E+00
	p2	3.27E-03	6.14E+02
	p3	1.61E+01	1.00E+00
	p4	5.78E+00	1.00E+00
	p5	8.34E-02	6.11E+02
	p6	1.69E+01	1.00E+00
	p7	-2.39E+00	1.00E+00
Peak 10	p0	-1.79E+03	8.77E+02
	p1	4.63E+00	1.07E-01

Table B.18 continued from previous page

Detector 18

	p2	8.23E-02	3.81E-02
	p3	6.04E+02	2.24E+02
	p4	3.49E+00	4.64E-01
	p5	6.93E-01	1.70E-01
	p6	4.28E+01	6.38E+00
	p7	-7.89E+00	2.31E+00
Peak 11	p0	-7.11E+03	5.19E+03
	p1	5.33E+00	3.25E-01
	p2	1.48E-01	1.20E-01
	p3	3.44E+02	1.62E+02
	p4	4.89E+00	4.78E-02
	p5	1.10E-01	3.48E-02
	p6	-9.66E+01	8.77E+01
	p7	-2.42E+01	1.73E+01

Table B.18 continued from previous page

Detector 18

Peak 12	p0	-1.05E+05	6.36E+01
	p1	5.66E+00	1.41E+00
	p2	7.66E-03	3.28E-10
	p3	6.23E+01	2.78E+00
	p4	4.73E+00	3.17E-03
	p5	1.02E-01	2.53E-03
	p6	1.38E+01	8.53E-01
	p7	-2.27E+00	1.78E-01
Peak 13	p0	3.34E+01	6.95E+01
	p1	2.66E+00	1.86E+00
	p2	6.10E-01	6.26E-01
	p3	-7.69E+02	5.81E+03
	p4	3.68E+00	3.34E-01

Table B.18 continued from previous page

Detector 18

	p5	6.05E-02	7.14E-02
	p6	4.95E+01	2.43E+01
	p7	-1.04E+01	6.10E+00
Peak 14	p0	1.93E+00	4.10E+00
	p1	3.04E+00	1.96E-01
	p2	6.16E-02	9.16E-02
	p3	5.35E+00	2.73E+00
	p4	3.44E+00	3.44E-02
	p5	2.79E-02	1.88E-02
	p6	-3.69E+00	3.46E+01
	p7	3.64E+00	1.05E+01

Table B.18: Peak parameters for S3F 18th detector.

Detector 19

	Parameter	Value	Error
Peak 1	p0	6.38E+00	4.48E-01
	p1	1.23E+01	9.89E-03
	p2	1.84E-01	1.12E-02
Peak 2	p0	1.24E+02	1.78E+00
	p1	1.03E+01	1.88E-03
	p2	1.59E-01	1.35E-03
Peak 3	p0	1.13E+02	6.89E+02
	p1	2.40E+00	1.34E+01
	p2	2.36E+00	3.41E+00
Peak 4	p0	5.02E+01	2.05E+00
	p1	8.63E+00	2.66E-03
	p2	1.01E-01	3.45E-03

Table B.19 continued from previous page

Detector 19

Peak 5	p0	7.36E+01	8.96E+00
	p1	6.80E+00	4.41E-02
	p2	2.91E-01	1.99E-02
	p3	-5.82E+01	8.85E+00
	p4	6.82E+00	2.01E-02
	p5	1.37E-01	1.68E-02
	p6	-2.63E+01	3.05E-150
	p7	-8.92E+01	3.05E-151
Peak 6	p0	-5.43E+04	3.60E+01
	p1	8.57E+00	3.59E+01
	p2	2.11E-01	7.91E+02
	p3	-4.54E+00	3.60E+01
	p4	9.04E+00	3.59E+01

Table B.19 continued from previous page

Detector 19

	p5	2.91E-01	7.90E+02
	p6	-2.93E+01	1.80E+00
	p7	4.70E+00	3.55E+01
Peak 7	p0	-1.93E+01	1.10E+01
	p1	6.36E+00	2.73E-02
	p2	3.40E-02	2.31E-02
	p3	4.59E+01	2.06E+01
	p4	6.17E+00	9.59E-02
	p5	2.00E-01	7.77E-02
	p6	3.37E+01	6.31E+00
	p7	-4.90E+00	1.12E+00
Peak 8	p0	1.69E+03	6.35E+02
	p1	6.71E+00	1.99E-01

Table B.19 continued from previous page

Detector 19

	p2	1.37E-01	6.99E-02
	p3	6.65E+01	4.43E+00
	p4	6.11E+00	4.08E-03
	p5	8.47E-02	5.66E-03
	p6	-2.06E+01	1.21E+01
	p7	3.64E+00	2.26E+00
Peak 9	p0	-1.65E+05	1.00E+00
	p1	4.97E+00	1.20E+07
	p2	1.03E-01	9.37E+02
	p3	1.41E+01	1.20E+07
	p4	5.76E+00	1.20E+07
	p5	6.57E-02	9.37E+02
	p6	-6.76E+01	1.20E+07
	p7	1.25E+01	1.20E+07

Table B.19 continued from previous page

Detector 19

Peak 10	p0	-7.55E+01	1.40E+01
	p1	5.71E+00	7.91E-02
	p2	3.35E-01	5.08E-02
	p3	2.92E+01	4.86E+00
	p4	4.93E+00	7.78E-03
	p5	6.37E-02	1.16E-02
	p6	4.06E+01	7.95E+00
	p7	2.29E+00	1.57E+00
Peak 11	p0	1.19E+03	2.45E+03
	p1	5.30E+00	1.85E-01
	p2	2.14E-01	9.73E-02
	p3	4.95E+02	1.46E+02
	p4	4.77E+00	7.20E-02

Table B.19 continued from previous page

Detector 19

	p5	1.41E-01	6.33E-02
	p6	-2.45E+02	1.42E+02
	p7	-5.31E+01	2.80E+01
Peak 12	p0	-1.12E+04	6.65E+03
	p1	5.70E+00	1.98E-01
	p2	3.00E-01	9.00E-02
	p3	1.55E+02	1.26E+01
	p4	4.82E+00	3.01E-02
	p5	1.30E-01	1.76E-02
	p6	-1.26E+02	2.51E+02
	p7	2.86E+01	5.72E+01
Peak 13	p0	-2.01E+01	1.01E+00
	p1	3.74E+00	1.29E-02

Table B.19 continued from previous page

Detector 19

	p2	1.58E-01	7.88E-03
	p3	1.09E+02	6.74E+02
	p4	4.03E+00	1.27E-04
	p5	4.08E-05	2.43E-05
	p6	2.29E+02	5.18E-01
	p7	-5.39E+01	1.29E-01
Peak 14	p0	-2.89E+02	1.24E+01
	p1	2.04E+00	1.55E-02
	p2	5.13E-01	9.66E-03
	p3	1.30E+02	5.51E+00
	p4	2.59E+00	1.09E-02
	p5	2.60E-01	7.86E-03
	p6	-5.11E+01	3.01E+00
	p7	2.30E+01	9.57E-01

Table B.19 continued from previous page

Detector 19

Table B.19: Peak parameters for S3F 19th detector.

Detector 20

	Parameter	Value	Error
Peak 1	p0	5.78E+00	3.73E-01
	p1	1.22E+01	1.25E-02
	p2	2.21E-01	1.28E-02
Peak 2	p0	1.03E+02	1.62E+00
	p1	1.03E+01	2.68E-03
	p2	1.85E-01	2.02E-03
Peak 3	p0	3.48E+01	3.06E+02
	p1	-9.49E-01	4.65E+01
	p2	4.04E+00	1.35E+01

Table B.20 continued from previous page

Detector 20

Peak 4	p0	5.47E+01	2.13E+00
	p1	8.61E+00	2.30E-03
	p2	9.20E-02	2.91E-03
Peak 5	p0	5.29E+00	2.24E+00
	p1	6.73E+00	1.52E-02
	p2	3.07E-02	1.77E-02
	p3	3.33E+01	1.11E+00
	p4	6.99E+00	7.31E-03
	p5	1.85E-01	1.07E-02
	p6	-1.25E+02	3.37E-94
	p7	-2.36E+01	1.32E-57
Peak 6	p0	-2.75E+04	5.43E-10

Table B.20 continued from previous page

Detector 20

	p1	6.18E+00	1.40E-12
	p2	9.74E-02	3.33E-13
	p3	6.56E+01	5.19E-10
	p4	6.43E+00	1.27E-12
	p5	8.47E-02	6.66E-13
	p6	1.87E+00	1.21E-08
	p7	-5.06E+00	2.12E-15
Peak 7	p0	1.44E+01	2.04E+01
	p1	6.12E+00	3.20E-03
	p2	1.15E-01	6.39E-03
	p3	2.44E+01	1.27E+00
	p4	6.42E+00	1.32E-02
	p5	9.45E-02	1.25E-02
	p6	-2.96E+04	3.36E+05

Table B.20 continued from previous page

Detector 20

	p7	-1.10E+01	5.11E-14
Peak 8	p0	7.00E+01	6.36E+01
	p1	5.17E+00	1.41E+00
	p2	5.06E-03	3.14E-06
	p3	5.45E+01	1.58E+00
	p4	6.08E+00	5.44E-03
	p5	7.74E-02	3.33E-03
	p6	-3.62E+01	7.72E-01
	p7	7.45E+00	1.25E-01
Peak 9	p0	1.07E+03	6.36E+01
	p1	6.52E+00	1.41E+00
	p2	1.41E-03	5.03E-07
	p3	1.25E+01	1.06E+00

Table B.20 continued from previous page

Detector 20

	p4	5.76E+00	6.76E-03
	p5	6.22E-02	5.92E-03
	p6	1.89E+01	5.36E-01
	p7	-2.08E+00	9.46E-02
Peak 10	p0	-1.87E+01	7.90E+00
	p1	5.36E+00	7.60E-02
	p2	1.35E-01	6.69E-02
	p3	3.83E+01	6.66E+00
	p4	4.89E+00	1.62E-02
	p5	9.32E-02	1.84E-02
	p6	2.56E+01	7.05E+00
	p7	9.65E-01	1.37E+00
Peak 11	p0	2.21E+04	2.56E+03

Table B.20 continued from previous page

Detector 20

	p1	7.50E+00	1.35E-01
	p2	1.15E+00	5.85E-02
	p3	-3.27E+03	3.09E+02
	p4	5.06E+00	1.21E-02
	p5	5.06E-01	1.24E-02
	p6	8.32E+02	6.63E+01
	p7	1.54E+02	1.26E+01
Peak 12	p0	-1.34E+03	1.88E+03
	p1	4.92E+00	1.12E-01
	p2	6.45E-02	2.88E-02
	p3	1.32E+02	3.61E+01
	p4	4.76E+00	4.95E-02
	p5	1.29E-01	3.40E-02
	p6	7.07E+02	2.95E+02

Table B.20 continued from previous page

Detector 20

	p7	-1.59E+02	6.58E+01
Peak 13	p0	-2.52E+05	6.36E+01
	p1	3.40E+00	1.41E+00
	p2	2.93E-02	7.08E+02
	p3	5.76E+00	5.50E-01
	p4	3.92E+00	1.17E-02
	p5	9.36E-02	9.71E-03
	p6	-3.36E+01	3.18E-01
	p7	9.32E+00	8.02E-02
Peak 14	p0	5.19E+01	1.50E+01
	p1	2.40E+00	7.69E-02
	p2	4.72E-01	2.15E-01
	p3	9.98E+01	7.14E+01

Table B.20 continued from previous page

Detector 20

	p4	2.53E+00	1.10E-01
	p5	2.91E-01	7.48E-02
	p6	-6.84E+02	3.05E+02
	p7	2.12E+02	8.83E+01

Table B.20: Peak parameters for S3F 20th detector.

Detector 21

	Parameter	Value	Error
Peak 1	p0	5.27E+00	3.59E-01
	p1	1.22E+01	1.37E-02
	p2	2.39E-01	1.57E-02
Peak 2	p0	1.02E+02	1.68E+00
	p1	1.03E+01	2.75E-03
	p2	1.85E-01	2.14E-03

Table B.21 continued from previous page

Detector 21

Peak 3	p0	1.52E+00	2.08E+00
	p1	2.47E+01	8.05E+04
	p2	8.85E+02	5.46E+02
Peak 4	p0	6.03E+01	2.16E+00
	p1	8.64E+00	2.04E-03
	p2	9.30E-02	2.66E-03
Peak 5	p0	3.13E+01	5.28E+00
	p1	7.03E+00	1.12E-02
	p2	1.61E-01	2.62E-02
	p3	1.19E+01	1.92E+01
	p4	6.13E+00	2.37E+00
	p5	7.15E-01	1.20E+00

Table B.21 continued from previous page

Detector 21

	p6	-6.15E+38	9.13E-05
	p7	-6.00E+00	6.41E-08
Peak 6	p0	6.32E+01	1.38E+00
	p1	6.95E+00	2.92E-01
	p2	9.74E-02	2.10E-01
	p3	9.13E+01	1.38E+00
	p4	6.87E+00	2.10E-02
	p5	9.84E-02	1.48E-02
	p6	4.85E+00	1.38E+00
	p7	-5.18E+00	1.38E+00
Peak 7	p0	-2.17E+01	5.85E+01
	p1	6.12E+00	2.32E-02
	p2	1.57E-01	1.26E-02

Table B.21 continued from previous page

Detector 21

	p3	2.34E+01	3.54E+00
	p4	6.46E+00	8.68E-02
	p5	1.41E-01	6.05E-02
	p6	7.61E+02	1.62E+02
	p7	-1.21E+02	2.57E+01
Peak 8	p0	-2.05E+04	9.00E+01
	p1	6.49E+00	1.41E+00
	p2	7.47E-04	7.11E+02
	p3	5.11E+01	1.68E+00
	p4	6.16E+00	2.80E-03
	p5	7.11E-02	2.03E-03
	p6	-1.29E+02	7.33E-01
	p7	2.33E+01	1.20E-01

Table B.21 continued from previous page

Detector 21

Peak 9	p0	-1.24E+04	1.37E+03
	p1	6.58E+00	1.70E-03
	p2	2.31E-02	7.11E-07
	p3	7.29E+01	1.89E+01
	p4	5.92E+00	2.41E-02
	p5	1.70E-01	2.32E-02
	p6	8.70E+02	2.56E+02
	p7	-1.57E+02	4.64E+01
Peak 10	p0	-1.62E+03	8.69E+02
	p1	4.58E+00	5.55E-02
	p2	1.67E-01	6.07E-02
	p3	3.92E+02	2.32E+02
	p4	4.69E+00	2.93E-01
	p5	2.05E-01	9.71E-02

Table B.21 continued from previous page

Detector 21

	p6	4.12E+01	2.41E+01
	p7	-6.14E+00	4.97E+00
Peak 11	p0	-9.01E+02	4.18E+02
	p1	4.84E+00	7.07E-02
	p2	1.76E-02	3.22E-02
	p3	-2.55E+02	1.36E+02
	p4	4.93E+00	1.07E-02
	p5	7.87E-02	7.95E-02
	p6	2.62E+02	1.13E+02
	p7	1.17E+01	5.68E+00
Peak 12	p0	2.43E+01	9.46E+00
	p1	4.85E+00	4.71E-03
	p2	8.86E-03	7.44E-03

Table B.21 continued from previous page

Detector 21

	p3	1.44E+02	5.31E+00
	p4	4.82E+00	9.41E-03
	p5	1.18E-01	7.02E-03
	p6	1.12E+03	6.87E+00
	p7	-2.48E+02	1.52E+00
Peak 13	p0	8.98E+01	6.36E+01
	p1	2.12E+00	1.41E+00
	p2	9.14E-02	1.86E-04
	p3	8.12E+00	7.15E-01
	p4	4.10E+00	7.78E-03
	p5	6.99E-02	5.04E-03
	p6	1.18E+01	2.79E-01
	p7	-2.41E+00	6.86E-02

Table B.21 continued from previous page

Detector 21

Peak 14	p0	-8.67E+06	6.36E+01
	p1	2.42E+00	1.41E+00
	p2	4.66E-04	3.61E-13
	p3	1.81E+01	8.43E-01
	p4	2.63E+00	1.94E-02
	p5	2.00E-01	1.53E-02
	p6	5.76E+01	4.19E-01
	p7	-1.66E+01	1.39E-01

Table B.21: Peak parameters for S3F 21st detector.

Detector 22

	Parameter	Value	Error
Peak 1	p0	3.25E+00	2.46E-01
	p1	1.22E+01	2.69E-02
	p2	3.48E-01	3.71E-02

Table B.22 continued from previous page

Detector 22

Peak 2	p0	6.16E+01	9.12E-01
	p1	1.02E+01	4.51E-03
	p2	3.23E-01	3.74E-03
Peak 3	p0	4.55E+00	3.23E-01
	p1	-1.60E+00	1.26E+04
	p2	1.00E+03	6.95E+02
Peak 4	p0	2.31E+01	7.15E-01
	p1	8.65E+00	9.42E-03
	p2	2.84E-01	1.29E-02
Peak 5	p0	1.02E+01	3.24E+00
	p1	6.76E+00	8.81E-03

Table B.22 continued from previous page

Detector 22

	p2	2.00E-02	7.99E-03
	p3	2.19E+01	8.00E-01
	p4	6.98E+00	2.96E-02
	p5	3.29E-01	5.22E-02
	p6	-4.51E+11	2.86E+00
	p7	-8.92E+00	1.41E+00
Peak 6	p0	-2.98E+05	1.84E-01
	p1	7.12E+00	1.26E-02
	p2	9.69E-02	2.61E-03
	p3	7.23E+01	1.84E-01
	p4	6.73E+00	1.58E-02
	p5	4.09E-02	1.09E-02
	p6	3.26E+01	1.85E+00
	p7	-5.24E+00	1.56E+01

Table B.22 continued from previous page

Detector 22

Peak 7	p0	2.63E+06	8.50E+06
	p1	5.88E+00	1.00E+00
	p2	9.38E-02	6.29E+02
	p3	-2.00E+02	4.25E+01
	p4	5.89E+00	2.08E+00
	p5	1.09E-02	7.70E-04
	p6	3.48E+00	2.06E+00
	p7	-5.47E-02	1.12E+00
Peak 8	p0	-6.31E+00	4.19E+00
	p1	6.33E+00	6.13E-02
	p2	2.73E-02	7.86E-02
	p3	1.25E+01	4.77E+00
	p4	6.15E+00	3.97E-03

Table B.22 continued from previous page

Detector 22

	p5	8.87E-03	2.97E-03
	p6	1.00E+01	9.15E+01
	p7	2.91E+00	1.51E+01
Peak 9	p0	5.06E+03	3.23E+04
	p1	7.14E+00	1.91E+00
	p2	3.28E-01	4.61E-01
	p3	1.72E+01	1.22E+02
	p4	6.14E+00	2.31E-01
	p5	1.02E+00	8.78E+00
	p6	-4.85E+01	2.62E+02
	p7	8.38E+00	2.71E+01
Peak 10	p0	-4.72E+05	2.66E+05
	p1	4.36E+00	2.71E-01

Table B.22 continued from previous page

Detector 22

	p2	1.34E-01	7.16E-02
	p3	2.77E+02	3.88E+02
	p4	4.65E+00	2.10E-01
	p5	1.47E-01	5.55E-02
	p6	1.92E+02	1.47E+02
	p7	-3.14E+01	2.82E+01
Peak 11	p0	-1.37E+04	2.30E+04
	p1	3.76E+00	1.15E+00
	p2	3.40E-01	4.15E-01
	p3	4.55E+02	3.39E+02
	p4	4.75E+00	1.40E-01
	p5	3.97E-01	4.42E-01
	p6	-1.40E+02	1.36E+02
	p7	-3.75E+01	3.21E+01

Table B.22 continued from previous page

Detector 22

Peak 12	p0	-1.32E+07	6.36E+01
	p1	5.61E+00	1.41E+00
	p2	3.79E-02	7.08E+02
	p3	-5.89E+01	4.08E+00
	p4	4.22E+00	1.00E-02
	p5	2.26E-01	6.09E-03
	p6	3.33E+01	8.87E-01
	p7	3.70E+00	1.90E-01
Peak 13	p0	-4.84E+05	1.41E+00
	p1	2.49E+01	2.00E+00
	p2	3.54E+00	1.43E+00
	p3	-1.60E+02	8.49E+01
	p4	4.55E+00	1.41E+00

Table B.22 continued from previous page

Detector 22

	p5	3.72E-04	2.97E-06
	p6	-1.70E+00	1.66E+00
	p7	1.74E+00	4.02E-01
Peak 14	p0	4.27E+02	8.13E+02
	p1	2.66E+00	1.00E-01
	p2	4.54E-02	3.25E-02
	p3	2.57E+02	8.96E+01
	p4	2.63E+00	1.00E-01
	p5	1.99E-01	4.11E-02
	p6	-1.74E+01	5.69E+01
	p7	1.20E+01	1.75E+01

Table B.22: Peak parameters for S3F 22nd detector.

Detector 23

	Parameter	Value	Error
Peak 1	p0	5.67E+00	4.61E-01
	p1	1.20E+01	1.11E-02
	p2	1.62E-01	1.37E-02
Peak 2	p0	8.37E+01	1.47E+00
	p1	1.02E+01	3.63E-03
	p2	2.16E-01	2.77E-03
Peak 3	p0	1.50E+01	8.64E-01
	p1	9.01E+00	5.43E-03
	p2	9.94E-02	5.39E-03
Peak 4	p0	7.38E+01	2.28E+00
	p1	8.60E+00	1.64E-03
	p2	7.16E-02	1.57E-03

Table B.23 continued from previous page

Detector 23

Peak 5	p0	4.51E+01	1.66E+00
	p1	6.87E+00	1.00E+00
	p2	1.58E-01	6.10E+02
	p3	1.19E+02	6.58E+00
	p4	-3.24E+03	1.73E+00
	p5	1.14E+02	8.81E+02
	p6	-4.06E+01	1.00E+00
	p7	-7.42E+00	1.00E+00
Peak 6	p0	-6.77E+01	1.70E+01
	p1	7.05E+00	6.53E+00
	p2	2.19E+02	6.14E+02
	p3	8.12E+01	1.68E+01
	p4	2.48E+00	3.80E+00

Table B.23 continued from previous page

Detector 23

	p5	9.34E+02	5.24E+02
	p6	5.00E+00	7.23E+04
	p7	-1.83E+26	8.90E-02
Peak 7	p0	1.25E+06	1.76E+04
	p1	7.23E+00	1.00E+00
	p2	4.97E-02	6.12E+02
	p3	2.84E+01	1.99E+00
	p4	6.46E+00	1.00E+00
	p5	9.24E-02	6.11E+02
	p6	-2.07E+01	1.00E+00
	p7	-3.26E+17	3.34E+05
Peak 8	p0	5.44E+01	3.04E+01
	p1	5.92E+00	5.61E-02

Table B.23 continued from previous page

Detector 23

	p2	5.50E-02	2.95E-02
	p3	8.77E+01	7.78E+00
	p4	6.10E+00	6.02E-03
	p5	8.80E-02	9.37E-03
	p6	-1.06E+03	8.74E+00
	p7	1.69E+02	1.45E+00
Peak 9	p0	3.70E+03	8.14E+01
	p1	6.42E+00	4.31E-03
	p2	2.83E-02	2.04E-07
	p3	2.04E+01	2.68E+00
	p4	5.80E+00	1.11E-03
	p5	8.14E-02	8.97E-04
	p6	1.63E+01	8.87E-01
	p7	-2.40E+00	2.16E-01

Table B.23 continued from previous page

Detector 23

Peak 10	p0	-4.45E+01	2.40E+01
	p1	4.95E+00	2.48E-02
	p2	2.84E-02	1.09E-02
	p3	4.78E+02	3.54E+02
	p4	4.65E+00	1.60E-01
	p5	1.71E-01	4.70E-02
	p6	2.90E+01	1.30E+01
	p7	-3.55E+00	2.67E+00
Peak 11	p0	7.51E+02	1.13E+03
	p1	5.63E+00	2.17E-01
	p2	3.23E-01	1.23E-01
	p3	2.76E+02	6.87E+01
	p4	4.91E+00	2.29E-02

Table B.23 continued from previous page

Detector 23

	p5	9.57E-02	4.33E-02
	p6	-1.28E+02	3.09E+01
	p7	-2.95E+01	5.68E+00
Peak 12	p0	-1.04E+04	5.33E+02
	p1	5.27E+00	1.56E-02
	p2	6.66E-02	4.04E-03
	p3	8.75E+01	4.22E+00
	p4	4.75E+00	3.34E-03
	p5	1.06E-01	8.09E-03
	p6	1.26E+01	2.63E+00
	p7	-2.57E+00	5.02E-01
Peak 13	p0	-5.71E+02	1.51E-02
	p1	3.50E+00	1.07E-05

Table B.23 continued from previous page

Detector 23

	p2	3.90E-02	5.05E-03
	p3	7.28E+00	2.79E-04
	p4	3.98E+00	3.09E-06
	p5	6.44E-02	1.84E-06
	p6	6.83E+00	9.30E-05
	p7	-1.37E+00	2.31E-05
Peak 14	p0	1.74E+03	1.11E+03
	p1	2.03E+00	2.00E-01
	p2	3.04E-01	5.69E-02
	p3	-5.63E+01	2.92E+01
	p4	2.70E+00	3.49E-02
	p5	1.02E-01	2.24E-02
	p6	-5.13E+00	9.39E+00
	p7	2.50E+00	3.20E+00

Table B.23 continued from previous page

Detector 23

Table B.23: Peak parameters for S3F 23rd detector.

Detector 24

	Parameter	Value	Error
Peak 1	p0	4.19E+00	3.53E-01
	p1	1.19E+01	1.56E-02
	p2	2.14E-01	2.04E-02
Peak 2	p0	9.26E+01	1.55E+00
	p1	1.01E+01	2.49E-03
	p2	1.81E-01	2.05E-03
Peak 3	p0	1.52E+01	8.55E-01
	p1	8.92E+00	7.84E-03
	p2	1.31E-01	1.10E-02

Table B.24 continued from previous page

Detector 24

Peak 4	p0	6.87E+01	2.17E+00
	p1	8.57E+00	1.87E-03
	p2	7.69E-02	1.87E-03
Peak 5	p0	3.65E+01	nan
	p1	6.84E+00	nan
	p2	1.50E-01	nan
	p3	1.49E+01	nan
	p4	6.49E+00	nan
	p5	1.49E-01	nan
	p6	-2.63E+01	nan
	p7	-4.88E+00	nan
Peak 6	p0	-1.98E+03	1.36E+00

Table B.24 continued from previous page

Detector 24

	p1	6.94E+00	1.32E-01
	p2	9.54E-02	1.78E-02
	p3	7.59E+01	1.39E+00
	p4	6.75E+00	3.96E-02
	p5	8.81E-02	1.25E-02
	p6	5.29E+00	1.36E+00
	p7	-5.24E+00	1.36E+00
Peak 7	p0	-9.54E+01	2.22E+01
	p1	7.28E+00	2.86E-02
	p2	3.08E-01	1.13E-02
	p3	2.90E+01	9.02E-01
	p4	6.43E+00	5.22E-03
	p5	1.09E-01	5.77E-03
	p6	-4.23E+30	3.77E+00

Table B.24 continued from previous page

Detector 24

	p7	-9.64E+24	1.41E+00
Peak 8	p0	-1.77E+01	3.81E+01
	p1	6.25E+00	2.65E-02
	p2	1.14E-02	4.56E-03
	p3	5.09E+01	3.46E+00
	p4	6.08E+00	3.09E-03
	p5	5.75E-02	5.90E-03
	p6	-1.43E+02	4.62E+01
	p7	2.65E+01	7.87E+00
Peak 9	p0	-2.25E+05	7.62E+04
	p1	6.00E+00	1.21E-01
	p2	2.95E-02	2.75E-02
	p3	2.47E+01	5.65E+00

Table B.24 continued from previous page

Detector 24

	p4	5.77E+00	8.35E-03
	p5	8.98E-02	2.47E-02
	p6	1.66E+01	4.16E+00
	p7	-2.36E+00	3.93E-01
Peak 10	p0	-1.62E+06	7.08E+05
	p1	4.61E+00	8.36E+00
	p2	4.20E-02	9.08E+00
	p3	4.99E+01	3.29E+00
	p4	4.93E+00	7.69E-03
	p5	8.73E-02	1.04E-02
	p6	1.73E+01	1.87E+00
	p7	-1.54E+00	3.59E-01
Peak 11	p0	-5.57E+02	1.27E+03

Table B.24 continued from previous page

Detector 24

	p1	4.68E+00	3.27E-02
	p2	3.98E-02	1.28E-02
	p3	1.06E+01	6.45E+00
	p4	4.82E+00	5.37E-03
	p5	5.06E-03	4.89E-03
	p6	2.96E+01	2.16E+01
	p7	6.56E+00	4.36E+00
Peak 12	p0	-2.12E+04	1.78E+05
	p1	4.94E+00	6.84E-02
	p2	3.70E-02	2.68E-02
	p3	4.99E+01	2.60E+00
	p4	4.70E+00	7.74E-03
	p5	8.19E-02	7.53E-03
	p6	-3.62E+02	7.19E+00

Table B.24 continued from previous page

Detector 24

	p7	8.57E+01	1.62E+00
Peak 13	p0	-3.78E+02	2.77E+02
	p1	3.69E+00	4.72E-02
	p2	9.59E-01	1.97E-01
	p3	3.05E+02	1.97E+02
	p4	3.87E+00	7.50E-02
	p5	6.12E-01	1.52E-01
	p6	3.43E+01	2.50E+01
	p7	1.25E+01	1.27E+01
Peak 14	p0	3.08E+05	1.00E+00
	p1	2.34E+00	1.84E+07
	p2	6.34E-02	8.11E+02
	p3	2.59E+01	1.84E+07

Table B.24 continued from previous page

Detector 24

	p4	2.83E+00	1.84E+07
	p5	1.18E-01	8.10E+02
	p6	1.70E+01	1.84E+07
	p7	-2.63E-01	1.84E+07

Table B.24: Peak parameters for S3F 24th detector.

Bibliography

[1] E. F. Aguilera et al. "New γ-ray measurements for C12+C12 sub-Coulomb fusion: Toward data unification". In: *Physical Review C - Nuclear Physics* 73.6 (2006). DOI: 10.1103/PhysRevC.73.064601.

[2] E. Almqvist, D. A. Bromley, and J. A. Kuehner. "Resonances in C-12 on Carbon Reactions". In: *Phys.Rev.Lett.* 4.10 (1960), pp. 515–517. DOI: 10.1103/PHYSREVLETT.4.515.

[3] E. Almqvist et al. "Effects of Sample Size and Statistical Weights on Fluctuations in the C12(C12, alpha)Ne20 Reactions". In: *PhRv* 136.1B (1964), pp. 84–98. DOI: 10.1103/PHYSREV.136.B84. URL: https://ui.adsabs.harvard.edu/abs/1964PhRv..136...84A/abstract.

[4] AMETEK ORTEC. *439 Digital Current Integrator | Pulse Processing Electronics | AMETEK ORTEC*. URL: https://www.ortec-online.com/products/electronics/digital-current-integrator/439.

[5] Andromede. *IPN Orsay - ANDROMEDE*. 2022. URL: http://ipnwww.in2p3.fr/ANDROMEDE.

[6] W. David Arnett. "A possible model of supernovae: Detonation of 12C". In: *Astrophysics and Space Science 1969 5:2* 5.2 (Oct. 1969), pp. 180–212. DOI: 10.1007/BF00650291. URL: https://link.springer.com/article/10.1007/BF00650291.

[7] W. David Arnett. "Explosive Nucleosynthesis in Stars". In: *The Astrophysical Journal* 157 (1969).

[8] W. David Arnett. "Pulsars and Neutron Star Formation". In: *Nature 1969 222:5191* 222.5191 (1969), pp. 359–361. DOI: 10.1038/222359b0. URL: https://www.nature.com/articles/222359b0.

[9] L. Arnold et al. "TNT digital pulse processor". In: *IEEE Transactions on Nuclear Science* 53.3 (June 2006), pp. 723–728. DOI: 10.1109/TNS.2006.873712.

[10] H. J. Assenbaum, K. Langanke, and C. Rolfs. “Effects of electron screening on low-energy fusion cross sections”. In: *Zeitschrift für Physik A Atomic Nuclei* 327.4 (Dec. 1987), pp. 461–468. DOI: 10.1007/BF01289572/METRICS. URL: https://link.springer.com/article/10.1007/BF01289572.

[11] W. Baade and F. Zwicky. “Remarks on Super-Novae and Cosmic Rays”. In: *Physical Review* 46.1 (July 1934), p. 76. DOI: 10.1103/PhysRev.46.76.2. URL: https://journals.aps.org/pr/abstract/10.1103/PhysRev.46.76.2.

[12] C. A. Barnes et al. *Essays in nuclear astrophysics : presented to William A. Fowler, on the occasion of his seventieth birthday*. Cambridge University Press, 1982, p. 193.

[13] Reiner Bass. *Nuclear Reactions with Heavy Ions*. 1st ed. Berlin, etc., Springer, 1980, p. 410.

[14] G. Baur. “Breakup reactions as an indirect method to investigate low-energy charged-particle reactions relevant for nuclear astrophysics”. In: *Physics Letters B* 178.2-3 (Oct. 1986), pp. 135–138. DOI: 10.1016/0370-2693(86)91483-8.

[15] H W Becker et al. *The 12C+ 12C Reaction at Subcoulomb Energies (II)**. Tech. rep. 1981, pp. 305–312.

[16] J. B. Birks. *The Theory and Practice of Scintillation Counting*. Elsevier, 1964. DOI: 10.1016/C2013-0-01791-4.

[17] G. Blondiaux et al. “Study of the growth of carbon on targets during ion bombardment”. In: *Nuclear Instruments and Methods in Physics Research Section A: Accelerators, Spectrometers, Detectors and Associated Equipment* 227.1 (Nov. 1984), pp. 19–23. DOI: 10.1016/0168-9002(84)90095-0.

[18] Giuseppe Bono et al. “Intermediate-Mass Star Models with Different Helium and Metal Contents”. In: *The Astrophysical Journal* 543.2 (Nov. 2000), pp. 955–971. DOI: 10.1086/317156/FULLTEXT/. URL: https://iopscience.iop.org/article/10.1086/317156%20https://iopscience.iop.org/article/10.1086/317156/meta.

[19] Ricardo A. Broglia and Aage Winther. “Heavy ion reactions: The elementary processes, parts I&II”. In: *Heavy Ion Reactions: The Elementary Processes, Parts I and II* (Jan. 2018), pp. 1–504. DOI: 10.4324/9780429500039/HEAVY-ION-REACTIONS-RICARDO-BROGLIA. URL: https://www.taylorfrancis.com/books/mono/10.4324/9780429500039/heavy-ion-reactions-ricardo-broglia.

[20] E. Margaret Burbidge et al. “Synthesis of the Elements in Stars”. In: *Reviews of Modern Physics* 29.4 (Oct. 1957), p. 547. DOI: 10.1103/RevModPhys.29.547. URL: https://journals.aps.org/rmp/abstract/10.1103/RevModPhys.29.547.

[21] E. Margaret Burbidge et al. "Synthesis of the Elements in Stars". In: *Reviews of Modern Physics* 29.4 (Oct. 1957), p. 547. DOI: 10.1103/RevModPhys.29.547. URL: https://journals.aps.org/rmp/abstract/10.1103/RevModPhys.29.547.

[22] A. G. W. Cameron. *Stellar evolution, nuclear astrophysics, and nucleogenesis. Second edition (Technical Report) | OSTI.GOV*. 1957. URL: https://www.osti.gov/biblio/4709881.

[23] S. Chandrasekhar, Chandrasekhar, and S. "Some Remarks on the State of Matter in the Interior of Stars. Mit 3 Abbildungen." In: *ZA* 5 (1932), p. 321. URL: https://ui.adsabs.harvard.edu/abs/1932ZA......5..321C/abstract.

[24] S. Chandrasekhar, Chandrasekhar, and S. "The highly collapsed configurations of a stellar mass". In: *MNRAS* 91.5 (Mar. 1931), pp. 456–466. DOI: 10.1093/MNRAS/91.5.456. URL: https://ui.adsabs.harvard.edu/abs/1931MNRAS..91..456C/abstract.

[25] S. Chandrasekhar, Chandrasekhar, and S. "The highly collapsed configurations of a stellar mass (Second paper)". In: *MNRAS* 95.3 (Jan. 1935), pp. 207–225. DOI: 10.1093/MNRAS/95.3.207. URL: https://ui.adsabs.harvard.edu/abs/1935MNRAS..95..207C/abstract.

[26] S. Chandrasekhar and E. A. Milne. "The Highly Collapsed Configurations of a Stellar Mass". In: *Monthly Notices of the Royal Astronomical Society* 91.5 (Mar. 1931), pp. 456–466. DOI: 10.1093/MNRAS/91.5.456. URL: https://academic.oup.com/mnras/article/91/5/456/985147.

[27] Chandrasekhar and Subrahmanyan. *An introduction to the study of stellar structure*. Chicago: The University of Chicago press, 1939. URL: https://ui.adsabs.harvard.edu/abs/1939isss.book.....C/abstract.

[28] Alessandro Chieffi, Marco Limongi, and Oscar Straniero. "The Evolution of a 25 M Star from the Main Sequence up to the Onset of the Iron Core Collapse". In: *The Astrophysical Journal* 502.2 (Aug. 1998), p. 737. DOI: 10.1086/305921. URL: https://iopscience.iop.org/article/10.1086/305921%20https://iopscience.iop.org/article/10.1086/305921/meta.

[29] Andrew Cumming et al. "Long Type I X-Ray Bursts and Neutron Star Interior Physics". In: *The Astrophysical Journal* 646.1 (July 2006), pp. 429–451. DOI: 10.1086/504698/FULLTEXT/. URL: https://iopscience.iop.org/article/10.1086/504698%20https://iopscience.iop.org/article/10.1086/504698/meta.

[30] Serge Della Negra. "Andromeda unique tool to produce and analyze nanoobjects". In: *Innovation Review* 93 (2016), pp. 38–40. URL: http://ipnwww.in2p3.fr/ANDROMEDE,384.

[31] Michael J. Eller et al. "Andromede project: Surface analysis and modification with probes from hydrogen to nano-particles in the MeV energy range". In: *Nuclear Instruments and Methods in Physics Research, Section B: Beam Interactions with Materials and Atoms* 365 (Dec. 2015), pp. 367–370. DOI: 10.1016/J.NIMB.2015.07.090.

[32] K. A. Erb et al. "Resonant and average behavior of the C-12+ C-12 total reaction cross section: 5.6 <= Ec.m. <= 10.0 MeV". In: *Phys.Rev.C* 22.2 (1980), pp. 507–514. DOI: 10.1103/PHYSREVC.22.507.

[33] H. J. Fink, W. Scheid, and W. Greiner. "Nuclear molecular structure in 12C-12C scattering". In: *Nuclear Physics A* 188.2 (June 1972), pp. 259–288. DOI: 10.1016/0375-9474(72)90059-0.

[34] R. B. Firestone. "Nuclear Data Sheets for A = 24". In: *Nuclear Data Sheets* 108.11 (Nov. 2007), pp. 2319–2392. DOI: 10.1016/J.NDS.2007.10.001.

[35] William A. Fowler et al. "Neutrino Processes and Pair Formation in Massive Stars and Supernovae." In: *ApJS* 9 (Dec. 1964), p. 201. DOI: 10.1086/190103. URL: https://ui.adsabs.harvard.edu/abs/1964ApJS....9..201F/abstract.

[36] G. Fruet et al. "Advances in the Direct Study of Carbon Burning in Massive Stars". In: *Physical Review Letters* 124.19 (May 2020). DOI: 10.1103/PhysRevLett.124.192701.

[37] Guillaume Fruet. "Structure des Ions Lourds et Nucléosynthèse dans les Étoiles Massives: la Réaction 12C+12C". PhD thesis.

[38] Guillaume Fruet et al. "Fusion cross section measurements of astrophysical interest for light heavy ions systems within the STELLA project". In: *EPJ Web of Conferences* 163 (Nov. 2017), p. 00018. DOI: 10.1051/EPJCONF/201716300018. URL: https://www.epj-conferences.org/articles/epjconf/abs/2017/32/epjconf_fusion2017_00018/epjconf_fusion2017_00018.html.

[39] Guillaume Fruet et al. *Fusion cross section measurements of astrophysical interest for light heavy ions systems within the STELLA project*. Tech. rep.

[40] G. Gamow. "Zur Quantentheorie des Atomkernes". In: *ZPhy* 51.3-4 (Mar. 1928), pp. 204–212. DOI: 10.1007/BF01343196. URL: https://ui.adsabs.harvard.edu/abs/1928ZPhy...51..204G/abstract.

[41] Enrique Garcia-Berro, Claudio Ritossa, and Icko Iben Jr. "On the evolution of stars that form electron-degenerate processed by Carbon burning. III. The inward propagation of a carbon-burning flame and other properties of a 9 Solar Mass model star." In: *The Astrophysical Journal* 485 (1997), pp. 765–784.

[42] R. W. Gurney and E. U. Condon. "Quantum Mechanics and Radioactive Disintegration". In: *Physical Review* 33.2 (Feb. 1929), p. 127. DOI: 10.1103/PhysRev.33.127. URL: https://journals.aps.org/pr/abstract/10.1103/PhysRev.33.127.

[43] K Hagino, K Ogata, and A M Moro. "Coupled-channels calculations for nuclear reactions: From exotic nuclei to superheavy elements". In: *Progress in Particle and Nuclear Physics* 125 (2022), p. 103951. DOI: 10.1016/j.ppnp.2022.103951. URL: https://doi.org/10.1016/j.ppnp.2022.103951.

[44] K. Hagino, N. Rowley, and A. T. Kruppa. "A program for coupled-channel calculations with all order couplings for heavy-ion fusion reactions". In: *Computer Physics Communications* 123.1-3 (Dec. 1999), pp. 143–152. DOI: 10.1016/S0010-4655(99)00243-X.

[45] Hamamatsu. *Si detectors for high energy particles*. 2021. URL: https://www.hamamatsu.com/content/dam/hamamatsu-photonics/sites/documents/99_SALES_LIBRARY/ssd/high_energy_kspd9002e.pdf.

[46] M. Heine et al. "Gamma Efficiency Simulations towards Coincidence Measurements for Fusion Cross Sections". In: *Journal of Physics: Conference Series*. Vol. 763. 1. Institute of Physics Publishing, Oct. 2016. DOI: 10.1088/1742-6596/763/1/012005.

[47] M. Heine et al. "The STELLA Apparatus for Particle-Gamma Coincidence Fusion Measurements with Nanosecond Timing". In: (Feb. 2018). DOI: 10.1016/j.nima.2018.06.058. URL: http://arxiv.org/abs/1802.07679%20http://dx.doi.org/10.1016/j.nima.2018.06.058.

[48] Ernest M. Henley and Alejandro Garcia. "Subatomic physics: Third edition". In: *Subatomic Physics: Third Edition* (Jan. 2007), pp. 1–620. DOI: 10.1142/6263/SUPPL{_}FILE/6263{_}CHAP06.PDF.

[49] M. D. High and B. Čujec. "The 12C + 12C sub-coulomb fusion cross section". In: *Nuclear Physics A* 282.1 (May 1977), pp. 181–188. DOI: 10.1016/0375-9474(77)90179-8.

[50] P. Holl et al. "A Double-Sided Silicon Strip Detector with Capacitive Readout and a New Method of Integrated Bias Coupling". In: *IEEE Transactions on Nuclear Science* 36.1 (Feb. 1989). URL: https://ieeexplore.ieee.org/stamp/stamp.jsp?arnumber=34444.

[51] F. Hoyle. "The Synthesis of the Elements from Hydrogen". In: *Monthly Notices of the Royal Astronomical Society* 106.5 (Oct. 1946), pp. 343–383. DOI: 10.1093/MNRAS/106.5.343. URL: https://academic.oup.com/mnras/article/106/5/343/2601776.

[52] F. Hoyle et al. “Nucleosynthesis in Supernovae.” In: *ApJ* 132 (Nov. 1960), p. 565. DOI: 10.1086/146963. URL: https://ui.adsabs.harvard.edu/abs/1960ApJ...132..565H/abstract.

[53] IAEA. *Livechart - Table of Nuclides - Nuclear structure and decay data*. URL: https://nds.iaea.org/relnsd/vcharthtml/VChartHTML.html.

[54] IAEA Nuclear Data Sheet 138 Ba. *ENSDF source for 138Ba*. URL: https://nds.iaea.org/relnsd/NdsEnsdf/showensdfdata.html#NUCID=138BA&SEQNO=101699&SOURCE=ensdf.

[55] IAEA Nuclear Data Sheet 138Ce. *ENSDF source for 138Ce*. URL: https://nds.iaea.org/relnsd/NdsEnsdf/showensdfdata.html#NUCID=138CE&SEQNO=101701&SOURCE=ensdf.

[56] C L Jiang et al. “Unexpected Behavior of Heavy-Ion Fusion Cross Sections at Extreme Sub-Barrier Energies”. In: (2002). DOI: 10.1103/PhysRevLett.89.052701.

[57] C. L. Jiang et al. “Expectations for C12 and O16 induced fusion cross sections at energies of astrophysical interest”. In: *Physical Review C - Nuclear Physics* 75.1 (2007). DOI: 10.1103/PhysRevC.75.015803.

[58] C. L. Jiang et al. “Measurements of fusion cross-sections in 12C 12C at low beam energies using a particle-γ coincidence technique”. In: *Nuclear Instruments and Methods in Physics Research, Section A: Accelerators, Spectrometers, Detectors and Associated Equipment* 682 (Aug. 2012), pp. 12–15. DOI: 10.1016/j.nima.2012.03.051.

[59] C. L. Jiang et al. “Reaction rate for carbon burning in massive stars”. In: *Physical Review C* 97.1 (Jan. 2018). DOI: 10.1103/PhysRevC.97.012801.

[60] Valentin T Jordanov and Glenn F Knoll. “Digital synthesis of pulse shapes in real time for high resolution radiation spectroscopy”. In: *Nuclear Instruments and Methods in Physics Research A* 345 (1994), pp. 337–345.

[61] K. U. Kettner, H. Lorenz-Wirzba, and C. Rolfs. “The12C+12C reaction at subcoulomb energies (I)”. In: *Zeitschrift für Physik A Atoms and Nuclei 1980 298:1* 298.1 (Mar. 1980), pp. 65–75. DOI: 10.1007/BF01416030. URL: https://link.springer.com/article/10.1007/BF01416030.

[62] K. U. Kettner et al. “Study of the Fusion Reaction 12C+12C below the Coulomb Barrier”. In: *Physical Review Letters* 38.7 (Feb. 1977), p. 337. DOI: 10.1103/PhysRevLett.38.337. URL: https://journals.aps.org/prl/abstract/10.1103/PhysRevLett.38.337.

[63] Glenn F. Knoll. *Radiation Detection and Measurement, 3rd ed.* 3rd. Wiley, 2000.

[64] Yosio Kondo, Takehiro Matsuse, and Yasuhisa Abe. "A Study of Resonances in the Sub-Coulomb 12C-12C Reaction from the Viewpoint of Nuclear Molecule". In: *Progress of Theoretical Physics* 59.2 (Feb. 1978), pp. 465–479. DOI: 10.1143/PTP.59.465. URL: https://dx.doi.org/10.1143/PTP.59.465.

[65] L. D. Landau. "On the theory of stars". In: *Physicalische Zeitschrift Der Sowjetunion* 1 (1932), p. 285.

[66] LCG ROOT MathLib Team. *ROOT: Special functions*. 2005. URL: https://root.cern/doc/master/group__SpecFunc.html#ga0e6c218274375c03a81402af953ea682.

[67] William R. Leo. "Scintillation Detectors". In: *Techniques for Nuclear and Particle Physics Experiments* (1994), pp. 157–175. DOI: 10.1007/978-3-642-57920-2{_}7. URL: https://link.springer.com/chapter/10.1007/978-3-642-57920-2_7.

[68] A Lépine-Szily and R Lichtenthäler. "Coupled channels effects in heavy ion reactions". In: *Eur. Phys. J. A* 57 (2021), p. 99. DOI: 10.1140/epja/s10050-021-00412-z. URL: https://doi.org/10.1140/epja/s10050-021-00412-z.

[69] Michael G Mazarakis and William E Stephens. *Experimental Measurements of the C+ C Nuclear Reactions at Low Energies*. Tech. rep.

[70] Michael G. Mazarakis and William E. Stephens. "Experimental Measurements of the 12C+ 12C Nuclear Reactions at Low Energies". In: *Physical Review C* 7.4 (Apr. 1973), p. 1280. DOI: 10.1103/PhysRevC.7.1280. URL: https://journals.aps.org/prc/abstract/10.1103/PhysRevC.7.1280.

[71] M K Mehta and S Kailas. "Proton-nucleus optical model potential at low energies, a review". In: *Phys* 27.2 (1986), pp. 139–160.

[72] Mesytec. *mesytec - MPR-16*. URL: https://www.mesytec.com/products/nuclear-physics/MPR-16.html.

[73] Micron. *S3 | Micron Semiconductor Ltd*. URL: http://www.micronsemiconductor.co.uk/product/s3/.

[74] Micron. *S3 Micron Semiconductor Ltd*. 2022. URL: http://www.micronsemiconductor.co.uk/product/s3/.

[75] MIDAS. *Multi Instance Data Acquisition System (MIDAS)*. 2005. URL: http://npg.dl.ac.uk/MIDAS/.

[76] B D Milbrath et al. "Characterization of alpha contamination in lanthanum trichloride scintillators using coincidence measurements". In: *Nuclear Instruments and Methods in Physics Research A* 547 (2005), pp. 504–510. DOI: 10.1016/j.nima.2004.11.054. URL: www.elsevier.com/locate/nima.

[77] A. Mişicu and H. Esbensen. "Hindrance of heavy-ion fusion due to nuclear incompressibility". In: *Physical Review Letters* 96.11 (Mar. 2006), p. 112701. DOI: 10.1103/PHYSREVLETT.96.112701/FIGURES/3/MEDIUM. URL: https://journals.aps.org/prl/abstract/10.1103/PhysRevLett.96.112701.

[78] A. M. Mukhamedzhanov, A. S. Kadyrov, and D. Y. Pang. "Trojan horse method as an indirect approach to study resonant reactions in nuclear astrophysics". In: *The European Physical Journal A 2020 56:9* 56.9 (Sept. 2020), pp. 1–44. DOI: 10.1140/EPJA/S10050-020-00214-9. URL: https://link.springer.com/article/10.1140/epja/s10050-020-00214-9.

[79] K. Nomoto. "Evolution of 8-10 solar mass stars toward electron capture supernovae. I - Formation of electron-degenerate O + NE + MG cores." In: *The Astrophysical Journal* 277 (Feb. 1984), pp. 791–805. DOI: 10.1086/161749. URL: https://ui.adsabs.harvard.edu/abs/1984ApJ...277..791N/abstract.

[80] K. Nomoto et al. "Accreting white dwarf models for type I supern. III. Carbon deflagration supernovae." In: *The Astrophysical Journal* 286 (Nov. 1984), pp. 644–658. DOI: 10.1086/162639. URL: https://ui.adsabs.harvard.edu/abs/1984ApJ...286..644N/abstract.

[81] Nuclear Data. *NuDat 3*. URL: https://www.nndc.bnl.gov/nudat3/.

[82] J. R. Patterson et al. "Experimental Investigation of the Stellar Nuclear Reaction 12C+12C at Low Energies". In: *ApJ* 157 (July 1969), p. 367. DOI: 10.1086/150073. URL: https://ui.adsabs.harvard.edu/abs/1969ApJ...157..367P/abstract.

[83] M Pesaresi et al. "The FC7 AMC for generic DAQ & control applications in CMS". In: (2014), pp. 22–26. DOI: 10.1088/1748-0221/10/03/C03036. URL: http://iopscience.iop.org/1748-0221/10/03/C03036.

[84] Luciano Piersanti et al. "Carbon-Oxygen White Dwarf Accreting CO-Rich Matter. II. Self-Regulating Accretion Process up to the Explosive Stage". In: *The Astrophysical Journal* 598.2 (Dec. 2003), pp. 1229–1238. DOI: 10.1086/378952/FULLTEXT/. URL: https://iopscience.iop.org/article/10.1086/378952%20https://iopscience.iop.org/article/10.1086/378952/meta.

[85] F. G.A. Quarati et al. “Study of 138La radioactive decays using LaBr 3 scintillators”. In: *Nuclear Instruments and Methods in Physics Research, Section A: Accelerators, Spectrometers, Detectors and Associated Equipment* 683 (Aug. 2012), pp. 46–52. DOI: 10.1016/J.NIMA.2012.04.066.

[86] H. Reeves and E. E. Salpeter. “Nuclear Reactions in Stars. IV. Buildup from Carbon”. In: *Physical Review* 116.6 (Dec. 1959), p. 1505. DOI: 10.1103/PhysRev.116.1505. URL: https://journals.aps.org/pr/abstract/10.1103/PhysRev.116.1505.

[87] P. H. Regan. “Precision measurement of sub-nanosecond lifetimes of excited nuclear states using fast-timing coincidences with LaBr3(Ce) detectors”. In: *Radiation Physics and Chemistry* 116 (Nov. 2015), pp. 38–42. DOI: 10.1016/j.radphyschem.2015.01.029.

[88] J. M. Régis et al. “The generalized centroid difference method for picosecond sensitive determination of lifetimes of nuclear excited states using large fast-timing arrays”. In: *Nuclear Instruments and Methods in Physics Research Section A: Accelerators, Spectrometers, Detectors and Associated Equipment* 726 (Oct. 2013), pp. 191–202. DOI: 10.1016/J.NIMA.2013.05.126.

[89] J. M. Régis et al. “The mirror symmetric centroid difference method for picosecond lifetime measurements via γ–γ coincidences using very fast LaBr3(Ce) scintillator detectors”. In: *Nuclear Instruments and Methods in Physics Research Section A: Accelerators, Spectrometers, Detectors and Associated Equipment* 622.1 (Oct. 2010), pp. 83–92. DOI: 10.1016/J.NIMA.2010.07.047.

[90] J. M. Régis et al. “The time-walk of analog constant fraction discriminators using very fast scintillator detectors with linear and non-linear energy response”. In: *Nuclear Instruments and Methods in Physics Research Section A: Accelerators, Spectrometers, Detectors and Associated Equipment* 684 (Aug. 2012), pp. 36–45. DOI: 10.1016/J.NIMA.2012.04.088.

[91] M Reinecke et al. “A new model for deflagration fronts in reactive fluids”. In: *Astron. Astrophys* 347 (1999), pp. 724–733.

[92] Oliver J. Roberts et al. “A LaBr3: Ce fast-timing array for DESPEC at FAIR”. In: *Nuclear Instruments and Methods in Physics Research, Section A: Accelerators, Spectrometers, Detectors and Associated Equipment* 748 (June 2014), pp. 91–95. DOI: 10.1016/j.nima.2014.02.037.

[93] Rogers Corp. *RO4000® Series Laminates*. URL: https://www.rogerscorp.com/advanced-electronics-solutions/ro4000-series-laminates.

[94] Claus E. Rolfs and William S. Rodney. *Cauldrons in the cosmos: nuclear astrophysics*. Chicago: University of Chicago Press, 1988, p. 561.

[95] Saint-Gobain Crystals. *BrilLanCe TM Scintillators Performance Summary Scintillation Products Technical Note*. Tech. rep. URL: www.detectors.saint-gobain.com..

[96] K. S. Shah et al. "LaBr3:Ce Scintillators for Gamma-Ray Spectroscopy". In: *IEEE Transactions on Nuclear Science* 50.6 II (Dec. 2003), pp. 2410–2413. DOI: 10.1109/TNS.2003.820614.

[97] T. Spillane et al. "C12+C12 fusion reactions near the Gamow energy". In: *Physical Review Letters* 98.12 (Mar. 2007). DOI: 10.1103/PhysRevLett.98.122501.

[98] H. Spinka and H. Winkler. "Experimental Determination of the Total Reaction Cross-Section of the Stellar Nuclear Reaction O-16 + O-16". In: *Nucl.Phys.A* 233.2 (Nov. 1974), pp. 456–494. DOI: 10.1016/0375-9474(74)90469-2.

[99] C. Spitaleri et al. "The Trojan Horse Method in nuclear astrophysics". In: *Physics of Atomic Nuclei* 74.12 (Dec. 2011), pp. 1725–1739. DOI: 10.1134/S1063778811110184/METRICS. URL: https://link.springer.com/article/10.1134/S1063778811110184.

[100] *Stopping-Power & Range Tables for Electrons, Protons, and Helium Ions | NIST*. URL: https://www.nist.gov/pml/stopping-power-range-tables-electrons-protons-and-helium-ions.

[101] O Straniero, L Piersanti, and S Cristallo. "Do we really know Mup (i.e. the transition mass between Type Ia and core-collapse supernova progenitors)?" In: *Journal of Physics: Conference Series* 665.1 (Jan. 2016), p. 012008. DOI: 10.1088/1742-6596/665/1/012008. URL: https://iopscience.iop.org/article/10.1088/1742-6596/665/1/012008%20https://iopscience.iop.org/article/10.1088/1742-6596/665/1/012008/meta.

[102] Ian J. Thompson. "Coupled reaction channels calculations in nuclear physics". In: *Computer Physics Reports* 7.4 (Apr. 1988), pp. 167–212. DOI: 10.1016/0167-7977(88)90005-6.

[103] Livius Trache. "Indirect methods for nuclear astrophysics with radioactive nuclear beams". In: *AIP Conference Proceedings* 1213 (2010), pp. 125–136. DOI: 10.1063/1.3362561. URL: https://www.researchgate.net/publication/228556121_Indirect_Methods_For_Nuclear_Astrophysics_With_Radioactive_Nuclear_Beams.

[104] A. Tumino et al. "An increase in the 12C + 12C fusion rate from resonances at astrophysical energies". In: *Nature 2018 557:7707* 557.7707 (May 2018), pp. 687–690. DOI: 10.1038/s41586-018-0149-4. URL: https://www.nature.com/articles/s41586-018-0149-4.

[105] Aurora Tumino et al. "The trojan horse method: A nuclear physics tool for astrophysics". In: *Annual Review of Nuclear and Particle Science* 71 (2021), pp. 345–376. DOI: 10.1146/ANNUREV-NUCL-102419-033642.

[106] UHV Design. *Rotary feedthroughs | UHV Design*. URL: https://www.uhvdesign.com/products/rotary-feedthroughs/.

[107] P. Vichoudis et al. "The Gigabit Link Interface Board (GLIB), a flexible system for the evaluation and use of GBT-based optical links". In: *Journal of Instrumentation* 5.11 (Nov. 2010). DOI: 10.1088/1748-0221/5/11/C11007. URL: https://www.researchgate.net/publication/230901463_The_Gigabit_Link_Interface_Board_GLIB_a_flexible_system_for_the_evaluation_and_use_of_GBT-based_optical_links.

[108] A. H. Wapstra and G. Audi. "The 1983 atomic mass evaluation. (I). Atomic mass table". In: *Nuclear Physics, Section A* 432.1 (Jan. 1985), pp. 1–54. DOI: 10.1016/0375-9474(85)90283-0.

[109] James Zickefoose. "12C+12C Fusion: Measurement and Advances Toward the Gamow Energy". PhD thesis. Connecticut: University of Connecticut, 2011. URL: https://www.proquest.com/docview/908637546?parentSessionId=81sie%2FgKzrlHwYG7HhnaQ8WoBn%2Brpm59F0I489XGHwU%3D.